Theoretical methods for studying charge and spin separation in excited states of large molecules and condensed phase

Dissertation
zur
Erlangung des Doktorgrades (Dr. rer. nat.)
der
Mathematisch-Naturwissenschaftlichen Fakultät
der
Rheinischen Friedrich-Wilhelms-Universität Bonn

vorgelegt von
Vafa Ziaei
aus Gonbadkavoos/Iran

Bonn, September 2017

Angefertigt mit Genehmigung der Mathematisch-Naturwissenschaftlichen Fakultät der
Rheinischen Friedrich-Wilhelms-Universität Bonn

1. Gutachter: Professor Dr. Thomas Bredow
2. Gutachter: Professor Dr. Stefan Grimme
Tag der Promotion: 19.12.2017
Erscheinungsjahr: 2018

Acknowledgments

I deeply thank Prof. Dr. Thomas Bredow for giving me the unique opportunity to enter the interesting field of quantum chemistry, and getting involved in an extremely exciting research area.

I sincerely thank Prof. Dr. Stefan Grimme for accepting to act as second reviewer of my dissertation.

I thank the whole YAMBO team, in particular Andrea Marini, Daniele Varsano, Davide Sangalli, Claudio Attaccalite, Andrea Ferretti and Conor Hogan for the insight- and useful workshop in CECAM/LAUSANNE (2015) in which I had the chance to deepen my understanding and skills in the field of quantum many-body theory.

I sincerely thank Fabien Bruneval for many stimulating and fruitful discussions regarding MOLGW code.

I gratefully thank the Jülich and Paderborn Supercomupting Center for providing valuable computing time making this work possible.

I wish to thank my parents for all their supports and encouragements.

Finally, I want to thank the Deutsche Forschungsgemeinschaft for financial support for this work within the Collaborative Research Center SFB 813: Chemistry at Spin Centers.

Abstract

In recent years the GW/BSE approach as a sophisticated many-body method gained considerable attention for ab-initio calculations of a range of properties in finite and infinite systems. For instance, several benchmarks exist for ionization potentials, electron affinities, (band) gaps, and electronically excited states demonstrating an overall good performance of the GW/BSE approach at a computational cost comparable to time-dependent density functional theory (TD-DFT) which is a widely applied method in quantum chemistry. The GW/BSE method outperforms TD-DFT for accurate description of charge-transfer states due to explicit capture of non-local electron-hole interaction mediated by the screened Coulomb potential $W(r, r', \omega)$. Furthermore, dynamical correlation is properly described through explicit frequency dependency of $W(r, r', \omega)$. Long-range dispersion effects are accounted for by infinite summation of non-local electron correlation contributions; the so-called ring diagrams within the random-phase approximation (RPA). Therefore, the GW/BSE method provides a reliable theoretical tool with a satisfactory prediction power for electronic and optical properties of materials at different phases, and hence is consistently used in this thesis for different types of problems.

In the first part of this thesis, the effect of electron-electron correlation, electron-phonon coupling and vertex corrections on the electronic band structure of ice and liquid water within the many-body Green's function formalism (the GW method) is investigated. Furthermore, within the same methodology and based on the Bethe-Salpeter equation (BSE) linear optical absorption spectra of antiferromagnetic zinc ferrite, water and ammonia in the condensed phase are calculated and analyzed in detail. Here, the electron-hole correlation which is responsible for the observed red-shift of absorption peaks and spectral weight redistributions is explicitly taken into account. The electron-hole effects are also of extreme importance for the non-linear absorption spectrum of liquid water (two-photon spectrum) in combination with quasi-particle (QP) effects.

The good performance of the GW/BSE methodology is also shown on large donor-acceptor-type molecules, demonstrating its reliability for finite systems where the screening effects are much lower than in periodic systems and a correct description of the long-range behaviour

of the exchange-correlation functional is essential. In order to enhance the predictive power of the GW/BSE theory for molecular systems starting from self-interaction free orbitals, a many-body based screening mixing scheme is introduced which remarkably improves the agreement of calculated excitation energies with reference data.

In the second part, non-adiabatic excited-state dynamics of condensed water is studied. A combination of ab-initio Born-Oppenheimer molecular dynamics and time-dependent density functional theory is applied. The complex proton dynamics is investigated by large-scale excited-state calculations. It is found that instantaneous concerted hops of protons to the neighboring water molecules (Grotthuss mechanism) are highly unlikely. Furthermore, the solvated electron formed upon proton transfer in the excited state is not fully localized within a cavity-like environment as a consequence of attractive interaction with the surrounding water molecules.

Publication List

1) **Red and blue-shift of liquid water's excited states: A many-body perturbation study**, V. Ziaei, and T. Bredow, JCP **145**, 064508 (2016)

2) **Giant many-body effects in liquid ammonia absorption spectrum**, V. Ziaei, and T. Bredow, JCP **145**, 174502 (2016)

3) **GW/BSE approach on S_1 vertical transition energy of large charge transfer compounds: A performance assessment**, V. Ziaei, and T. Bredow, JCP **145**, 174305 (2016)

4) **Large-scale quantum many-body perturbation on spin and charge separation in the excited states of the synthesized donor-acceptor hybrid PBI-macrocycle complex**, V. Ziaei, and T. Bredow, ChemPhysChem **18**, 1439-7641 (2017)

5) **Ab-initio optical properties and dielectric response of open-shell spinel zinc ferrite**, V. Ziaei, and T. Bredow, Eur. Phys. J. B **90**, 29 (2017)

6) **Dynamical electron-phonon coupling, GW self-consistency, and vertex effect on the electronic band gap of ice and liquid water**, V. Ziaei, and T. Bredow, Phys. Review B **95**, 235105 (2017)

7) **Simple many-body based screening mixing ansatz for improvement of GW/BSE excitation energies of molecular systems**, V. Ziaei, and T. Bredow, Phys. Review B **96**, 195115 (2017)

8) **Qualitative assessment of ultra-fast non-Grotthuss proton dynamics in S_1 excited state of liquid H_2O from ab-initio time-dependent density functional theory**, V. Ziaei, and T. Bredow, Eur. Phys. J. B **90**, 224 (2017)

9) **Two-photon absorption spectrum of liquid water and the effect of non-diagonal self-energy elements in the self-consistent GW approach on the band gap**, V. Ziaei, and T. Bredow, Phys. Review B **96**, 245109 (2017)

Contents

Chapter 1

Introduction

Nowadays, ab-initio calculation of material's properties is of paramount importance in order to gain a deeper understanding of the physical properties in many-body ensembles. A wealth of advanced theoretical methods for the calculation of electronic, electron-phonon, (non)-linear optical properties, and quantum dynamics in excited states of large molecules and condensed phase is presently available.

The main subject of this thesis is the accurate ab-initio calculation of many-body effects such as electron-electron (e-e), electron-phonon (e-ph), and electron-hole (e-h) interaction. A reliable assessment of the impact of e-e, e-ph, and e-h effects on the electron levels (one-particle levels) is of utmost importance since they considerably renormalize the fundamental gap, upon which optical properties are based. Hence, an accurate quantification of the involved effects is required to be able to reliably put the puzzle of many-body contributions together and to build up the whole picture in an ab-initio manner. This goal is achieved by means of the ab-initio Green's function formalism which takes into account many-body effects. This unique methodology provides access to static properties such as single-particle excitations observed in photo-emission spectra as well as the 2-particle excitations determining optical spectra. Furthermore, within the Green's function methodology, it is possible to account for non-linear phenomena, such as high harmonic generations and two-photon absorption spectra, resulting in fundamentally different spectral weight distributions relative to the corresponding linear spectra due to different selection rules. The impact of correlation approximations on the non-linear spectrum is assessed in this thesis.

Traditionally the GW/BSE approach has been applied to solids. In order to obtain biased-free spectra for finite systems, the many-body scheme is reformulated from the plane waves to localized basis set representation. This basis set change allows to circumvent the supercell approach, and to investigate spectra of large molecular systems without being hampered by artificial interaction of periodic images, as encountered in the plane wave formalism.

Dynamic properties of excited states are studied using time-dependent density functional theory (TD-DFT) combined with DFT Born-Oppenheimer molecular dynamics. TD-DFT is in comparison to Green's functions a lower cost method, and hence very appealing for analysing quantum dynamics of large systems in excited states. As an example, the quantum dynamics of liquid water in its excited states is investigated, showing an unusual ultra-fast proton transfer.

The work is organized as follows:

Chapter 2 presents an overview of the theoretical methods used in this thesis.
In **Chapter 3**, the importance of electron-hole correlation effects, the so-called excitonic effects, is demonstrated which is of importance for a realistic distribution of spectral weights. Further, ab-initio calculations of dynamic electron-phonon coupling effects on the band gap of ice and liquid water are presented and discussed. The impact of GW correlation on the band gap is calculated and analyzed. **Chapter 4** deals with non-linear absorption spectrum of liquid water. The importance of GW self-consistency and excitonic effects on the non-linear spectrum is shown.
In **Chapter 5** a reformulation of the Bethe-Salpeter equation from plane waves to localized basis sets is presented for molecular systems. The predictive power of the GW/BSE formalism in large charge-transfer molecular systems is demonstrated. Furthermore, in order to avoid self-interaction errors and to considerably reduce the computational cost a screening mixing GW/BSE ansatz is presented. **Chapter 6** concerns with quantum excited-state dynamics of liquid water, and the corresponding excited-state chemical processes based on time-dependent density functional theory. The work is closed in **Chapter 7** by a summary and an outlook for future research in the many-body field.

Chapter 2

Theoretical methods

2.1 Introduction

In the beginning of the 20th century with the advent of quantum mechanics the laws to exactly describe the way particles interacting in a many-particle ensemble were established at microscopic level through the electronic time-independent Schrödinger equation.

$$\left[\sum_{i}^{N}\left(-\frac{1}{2}\nabla_i^2 + V_{ext}(\mathbf{r}_i)\right) + \frac{1}{2}\sum_{i\neq j}^{N} v(|\mathbf{r}_i - \mathbf{r}_j|)\right]\Psi(\mathbf{r}_1,\ldots,\mathbf{r}_N) = E\Psi(\mathbf{r}_1,\ldots,\mathbf{r}_N) \qquad (2.1)$$

The Eq. (2.1) describes the correlated movement of N electrons in an external static potential V_{ext} created by the presence of N nuclei with the assumption that the electrons move much faster, and hence at much shorter time scales than the nucleus, and can instantly adjust to a change of the nuclear configuration (adiabaticity principle). This leads to decoupling of the electronic and nuclear wave functions (known as the Born-Oppenheimer (BO) approximation [1]) and hence to a major simplification. Therefore, Eq. (2.1) is an eigenvalue equation providing the spectrum of eigenvalues (E_i) of an electronic system at fixed ionic positions $\mathbf{R} = \mathbf{R}_1,\ldots,\mathbf{R}_{N_{atom}}$. This approximation is only valid if the adiabatic states are not degenerated. In case of degeneracy, non-adiabatic effects (Jahn-Teller effects [2]) have to be taken into account.

Even within the BO approximation, Eq. (2.1) still poses a major challenge, as due to presence of the Coloumb interaction v, the complexity of the solution of the Schrödinger equation (2.1) is massive. In case of absence of the Coulomb interaction, the Schrödinger equation reduces to a set of N independent one-electron equations. Therefore, since the many-body wave function, $\Psi(\mathbf{r}_1,\ldots,\mathbf{r}_N)$, is a function of $3N$ variables, where N is of the order of the Avogadro's number in solids, an exact solution to the many-body Eq. (2.1) is impossible, and indeed finding approximations to Eq. (2.1) is the only way to get out of

this immense complexity.

The first crude approximation is to consider the electrons, moving in a periodic potential (generated by the ions) in a solid, to be independent particles. This assumption led to the concept of energy bands $\epsilon_{n\mathbf{k}}$ and Bloch states [3], $\psi_{n\mathbf{k}}(\mathbf{r}) = u_{nk}(\mathbf{r}) \exp^{i\mathbf{kr}}$; which are solutions of the single-particle Schrödinger equation :

$$\Big(-\frac{1}{2}\nabla^2 + V_{ext}(\mathbf{r}) \Big) \psi_{n\mathbf{k}}(\mathbf{r}) = \epsilon_{n\mathbf{k}} \psi_{n\mathbf{k}}(\mathbf{r}) \tag{2.2}$$

where $V_{ext}(\mathbf{r})$ and $u_{nk}(\mathbf{r})$ have the same spatial periodicity. Based on this assumption, there have been some major successes, such as providing a first description of the low-temperature limit of the metallic resistance, a first explanation of the different Hall coefficients and a first classification of metal and insulators of solids at low temperatures [4]. However, as of any other models in solid state physics, this one-particle Bloch band structure theory suffers from its too simple physical structure, leading, for instance, to a rough electron-counting in distinguishing metals and insulators or to improper capturing of the electronic localization for a more realistic description of an insulator.

2.2 Hartree-Fock Theory

The next level of approximation to Eq. (2.1) to better describe many electron-electron interactions is the Hartree-Fock approximation [5,6] in which one considers the electrons as independent but the classical Coulomb and exchange effects are taken into account. However, in the HF approximation correlation effects are neglected.

In Hartree-Fock (HF) theory the many-body wave function is given as a single Slater determinant

$$\Psi(\mathbf{r}_1, \ldots, \mathbf{r}_N) = \sum_P sgn(P) \prod_{i=1}^{N} \psi_i(\mathbf{r}_{P(i)}) \tag{2.3}$$

The HF equations determine the set of one-particle orbitals ψ_i that minimizes the total energy of the system :

$$\Big[-\frac{1}{2}\nabla^2 + V_{ext}(\mathbf{r}) \Big] \psi_i(\mathbf{r}) + V_H(\mathbf{r})\psi_i(\mathbf{r}) + \int d\mathbf{r}' V_x(\mathbf{r}, \mathbf{r}')\psi_i(\mathbf{r}') = E_i \psi_i(\mathbf{r}) \tag{2.4}$$

where Hartree and exchange potential are given by :

$$V_H(\mathbf{r}) = \sum_j \int d\mathbf{r}' \psi_j^*(\mathbf{r}') \frac{1}{|\mathbf{r} - \mathbf{r}'|} \psi_i(\mathbf{r}') \tag{2.5}$$

$$\int d\mathbf{r}' V_x(\mathbf{r}, \mathbf{r}')\psi_i(\mathbf{r}') = -\sum_j \delta_{\sigma_i\sigma_j} \int d\mathbf{r}' \psi_j^*(\mathbf{r}') \frac{1}{|\mathbf{r} - \mathbf{r}'|} \psi_j(\mathbf{r})\psi_i(\mathbf{r}') \tag{2.6}$$

In essence, HF theory describes an independent electron moving in a mean-field potential created by the other electrons. The Hartree potential V_H in Eq. (2.5) is the classic Coulomb interaction between the electrons, and V_x in Eq. (2.6) is the non-local exchange potential reflecting the quantum nature of the underlying electronic system as a consequence of the Pauli exclusion principle. Although the HF-approximation performs reasonable for atomic total energies or molecular equilibrium geometries, the lack of correlation effects has dramatic consequences on the accurate or even qualitative prediction of system properties.

2.3 Density Functional Theory

For a more realistic modelling of the behavior of electrons in solids the quality of the approximations has to be improved. One way is to map the original wave function based equation (Schrödinger equation) onto a single-particle equation which allows for a better approximation of the many-body effects. This starts from the general Hamiltonian

$$H = T + V + H_{Coul} \tag{2.7}$$

in which T is the kinetic energy functional, V specifies the external potential and H_{Coul} describes the Coulomb interaction.

The mapping from the highly correlated many-body Schrödinger equation onto a one-particle equation is key to be able to develop a computationally tractable method. The theoretical framework was given in 1964 by P. Hohenberg und W. Kohn [7] in their seminal paper, where they presented the basic principles of the density functional theory (DFT) in which three fundamental theorems are stated :

1) The ground-state expectation value of any observable is a unique functional of the exact ground-state density n :

$$\langle \Psi[n]|\hat{O}|\Psi[n]\rangle = \hat{O}[n] \tag{2.8}$$

And from the knowledge of the ground-state density the external potential V_{ext} of the system is determined by the inverse map of the product of A and B :

$$A : V \to \Psi \tag{2.9}$$

$$B : \Psi \to n \tag{2.10}$$

$$(AB)^{-1} : n(\mathbf{r}) \to V(\mathbf{r}) \tag{2.11}$$

and hence the entire Hamiltonian (2.7), once the kinetic energy and the Coulomb interaction are specified.

2) The ground-state energy E_0 of N electrons system is found by minimizing the energy functional with respect to the density.

$$E_{V_{ext}}[n] \equiv \langle \Psi[n]|T + V_{ext} + H_{coul}|\Psi[n]\rangle \tag{2.12}$$

$E[n]$ has the property that

$$E_0 < E_{V_{ext}}[n] \tag{2.13}$$

with

$$E_0 = E_{V_0}[n_0] \tag{2.14}$$

Thus, the minimization of the energy functional $E_V[n]$ leads to the exact ground-state density of an interacting N-electron system.

3) The mapping (2.11) is independent of the V_{ext} of the particular system and consequently the Hohenberg-Kohn functional $F_{HK}[n]$ is a universal functional given as :

$$F_{HK}[n] = \langle \Psi[n]|T + H_{coul}|\Psi[n]\rangle \tag{2.15}$$

in

$$E[n] = F_{HK}[n] + \int d\mathbf{r} V_{ext}(\mathbf{r}) n(\mathbf{r}) \tag{2.16}$$

The three statements of invertibility, variationality and universality are at the heart of the DFT formulation; however still some efforts are necessary for its practical realization.

The KS equation

In order to implement the ideas of Hohenberg and Kohn in a practical form, Kohn and Sham (KS) suggested an alternative efficient strategy [8] in which one considers an auxiliary system of N non-interacting particles subjected to an effective external potential, V_{KS}, with the property that it yields the same density as the real interacting system. Defining the energy functional :

$$E[n] = T[n] + U[n] + \int V(\mathbf{r}) n(\mathbf{r}) d^3\mathbf{r} \tag{2.17}$$

with T as kinetic and U as nuclear attraction, and further differentiating Eq. (2.17) with

respect to the non-interacting Kohn-Sham density n_{ks}:

$$V_{KS}(\mathbf{r}) = V_{ext}(\mathbf{r}) + V_H(\mathbf{r}) + V_{xc}[n_{ks}(\mathbf{r})] \tag{2.18}$$

One obtains the definition for the effective single-particle potential V_{KS} in terms of the external potential V_{ext}, the Hartree potential V_H :

$$V_H(\mathbf{r}) = \int d\mathbf{r}^{'} v(|\mathbf{r} - \mathbf{r}^{'}|) n(\mathbf{r}^{'}) \tag{2.19}$$

and the exchange-correlation potential V_{xc} :

$$V_{xc}(\mathbf{r}) = \frac{\delta E_{xc}}{\delta n(\mathbf{r})} \tag{2.20}$$

According to the second Hohenberg-Kohn statement, the variation of the energy functional is performed in terms of the single-particle Kohn-Sham orbitals ϕ_i under orthogonality constraint :

$$\frac{\delta}{\delta \phi_i}\left[E - \sum_{k,l}^{N} \epsilon_{kl}\left(\int d\mathbf{r}\phi_k^*(\mathbf{r})\phi_k(\mathbf{r}) - \delta_{kl}\right)\right] = 0 \tag{2.21}$$

resulting in the Kohn-Sham equations :

$$\left[-\frac{1}{2}\nabla_i^2 + V_{KS}[n](\mathbf{r})\right]\phi_i(\mathbf{r}) = \epsilon_i \phi_i(\mathbf{r}) \tag{2.22}$$

whose solutions give the density of the N electron system :

$$n(\mathbf{r}) = \sum_{i}^{N} |\phi_i(\mathbf{r})|^2 \tag{2.23}$$

Therefore, in order to obtain a practical and computationally tractable formulation of the quantum physics of the many-electron system, the solution of the many-body Schrödinger equation (2.1) is elegantly converted into a set of self-consistent one-particle Schrödinger-like equations with the effective single-particle potential V_{KS}.

2.3.1 Approximations to the exchange-correlation functional

LOCAL DENSITY APPROXIMATION (LDA)

In the Kohn-Sham formulation of DFT the whole complexity of the many-body system is downfolded into V_{xc}. However, the exact form of the exchange-correlation potential in Eq. (2.20) is not known. The most simple formulation of E_{xc} is the local-density approximation (LDA)

$$E_{xc}^{LDA}[n] = \int d\mathbf{r} n(\mathbf{r}) \epsilon_{xc}^{HEG}(n(\mathbf{r})) \tag{2.24}$$

As can be seen from the Eq. (2.24), the true interacting density is approximated via the local homogeneous electron gas (HEG) density. ϵ_{xc}^{HEG} is composed of

$$\epsilon_{xc}^{HEG} = \epsilon_{x}^{HEG} + \epsilon_{c}^{HEG} \tag{2.25}$$

with ϵ_{x}^{HEG} being the exchange and ϵ_{c}^{HEG} the correlation energy density.
The ϵ_{x}^{HEG} is an analytic function of n [9] :

$$\epsilon_{x}^{HEG} = -\frac{3}{4}\left[\frac{3n}{\pi}\right]^{1/3} \tag{2.26}$$

whereas the correlation part can be calculated approximately using many-body perturbation theory [10] or via Quantum Monte Carlo methods [11]. Despite the locality of the density, LDA provides surprisingly good results. This accuracy follows from error cancellations in the approximation of the exchange and correlation terms (LDA overestimates exchange and underestimates correlation [12]) and further from the fact that LDA satisfies the sum rules for the exchange-correlation hole n_{xc} [13, 14].

GRADIENT CORRECTED APPROXIMATION (GGA)

In order to account for the spatial variation of the density (or in other words for density inhomogeneities), one goes a step forward and generalizes LDA to the so called generalized-gradient approximation (GGA) [15]. Within the GGA scheme, ϵ_{xc} from Eq. (2.24) becomes a function of the density and its gradients, with some free parameters that are obtained either from sum rules or fitting to experiments.

$$E_{xc}^{GGA}[n] = \int d^3\mathbf{r} \epsilon_{xc}(n(\mathbf{r}), \overrightarrow{\nabla} n(\mathbf{r})) n(\mathbf{r}) \tag{2.27}$$

The GGA-type functionals are widely used in chemistry as they improve for instance the dissociation energies over LDA and give a good description of hydrogen bonding [16]. How-

ever, a systematic improvement relative to LDA was not found. In particular, both LDA and GGA functionals suffer from self interaction error, as the V_{xc} does not exactly cancel the Hartree potential, or in other words the electron in the effective potential interact with all electrons instead of all the other electrons.

META GGA - HYBRIDS - DOUBLE HYBRID APPROXIMATIONS

A more sophisticated approximation to V_{xc} is denoted as meta GGA which additionally includes the second derivative of the density

$$E_{xc}^{MGGA}[n] = \int d^3\mathbf{r}\epsilon_{xc}(n(\mathbf{r}), \overrightarrow{\nabla} n(\mathbf{r}), \tau_s(\mathbf{r}))n(\mathbf{r}) \tag{2.28}$$

with $\tau_s(\mathbf{r})$ defined as :

$$\tau_s(\mathbf{r}) = \frac{1}{2}\sum_{i}^{occ} |\nabla\phi_i(\mathbf{r})|^2 \tag{2.29}$$

The TPSS functional [17] is an example of such kind of meta-GGA functional which performs well for molecules in gas-phase and for determination of hydrogen bonded structures. Another popular approximation to V_{xc} are hybrid functionals where a fraction of Hartree-Fock exchange is added to the GGA exchange functional :

$$E_{xc}^{HYBRID} = E_x^{GGA} + \alpha(E_x^{HF} - E_x^{GGA}) + E_c^{GGA} \tag{2.30}$$

For instance the PBE0 functional [18, 19] which is frequently applied in physics and chemistry is constructed by a GGA type functional (PBE) with a HF exchange fraction of 25%. This type of functionals results in much better description of band gaps relative to GGAs due to better error cancellations between HF-exchange and GGA correlation effects.

The most accurate approximation of V_{xc} is represented by the double hybrid functionals in which a combination of HF exchange fraction, GGA exchange-correlation potentials and many-body correlation from the second order perturbation theory is taken into account, leading to an even better description of electronic properties at the expense of higher complexity and computational cost. The double hybrid scheme is given by

$$E_{xc}^{D-HYBRID} = E_x^{GGA} + \alpha(E_x^{HF} - E_x^{GGA}) + bE_c^{GGA} + cE_c^{PT2} \tag{2.31}$$

where E_c^{PT2} is the second-order correlation energy.

2.3.2 The Bloch-Theorem and plane wave basis

Beside a proper choice for the exchange-correlation potential, one also needs a proper representation for the Kohn-Sham orbitals ϕ_i in a finite basis set for practical reasons. To this end, one takes advantage of the Bloch-Theorem $\phi(\mathbf{r}) = u(\mathbf{r})\exp(i\mathbf{kr})$ with $u(\mathbf{r})$ as lattice periodic function with the property : $u(\mathbf{r}) = u(\mathbf{r}+\mathbf{R})$ and $\mathbf{R}$ as the Bravais lattice vector

$$\mathbf{R} = n_1\mathbf{a_1} + n_2\mathbf{a_2} + n_3\mathbf{a_3} \tag{2.32}$$

with $\mathbf{a}$ as lattice vectors and n as integers.
The Bloch wave function can be expanded in terms of plane waves :

$$\phi_{n\mathbf{k}}(\mathbf{r}) = \frac{1}{\sqrt{N_\mathbf{k}\Omega_c)}}\sum_\mathbf{G} u_{n\mathbf{k}}(\mathbf{G})\exp^{i(\mathbf{k}+\mathbf{G})\mathbf{r}} \tag{2.33}$$

with

$$u_{n\mathbf{k}}(\mathbf{G}) = \frac{1}{\Omega_c}\int_{\Omega_c} d\mathbf{r}\exp^{-i\mathbf{Gr}} u_{n\mathbf{k}}(\mathbf{r}) \tag{2.34}$$

$\mathbf{G}$ is a reciprocal lattice vector while $\mathbf{k}$ is a general vector in reciprocal space. From Eq. (2.33) it is obvious that the quality of the KS wave function (represented by plane waves) depends solely on the number of $\mathbf{G}$ vectors which are controlled by a single parameter, i.e., the kinetic energy cutoff E_{cut} :

$$\frac{(\mathbf{k}+\mathbf{G})^2}{2} < E_{cut} \tag{2.35}$$

Thus, systematic improvement of the wave function can be easily achieved by increasing E_{cut}. Further, the local one particle density $n(\mathbf{r})$ in DFT is given as :

$$n(\mathbf{r}) = \sum_n \int_{\Omega_k} d\mathbf{k} f(\epsilon_F - \epsilon_{n\mathbf{k}})\phi^*_{n\mathbf{k}}(\mathbf{r})\phi_{n\mathbf{k}}(\mathbf{r}) \tag{2.36}$$

with ϵ_F Fermi energy and Fermi-distribution f, assuring the inclusion of only occupied states in the sum over the bands. The k integration in Eq. (2.36) is further replaced by a finite sum over special k points in the irreducible Brillouin zone (IBZ). Such special k points can be generated using the recipe presented by Monkhorst and Pack [20]. Plugging the Bloch representation of the KS wavefunctions in Eq. (2.33) into Eq. (2.36), one explicitly obtains the density of the system $n(\mathbf{r})$ in terms of plane waves :

$$n(\mathbf{r}) = \sum_n \sum_\mathbf{k}^{IBZ} \sum_{\mathbf{G}\mathbf{G}'} \omega_\mathbf{k} f(\epsilon_F - \epsilon_{n\mathbf{k}}) u^*_{n\mathbf{k}}(\mathbf{G}) u_{n\mathbf{k}}(\mathbf{G}')\exp^{i(\mathbf{G}-\mathbf{G}')\mathbf{r}} \tag{2.37}$$

where $\omega_\mathbf{k}$ determines the weights of the special k points in irreducible BZ. The density in Eq. (2.37) represents the whole electronic density of the system. However, in order to

be able to efficiently use the plane wave basis set, one typically adopts a pseudopotential approximation (PPA). In the PPA, the electronic system is divided into the core and valence regions with interaction between the separated parts. Because the core electrons do not take part in chemical bonding, the frozen-core approximation can be used. This allows to massively reduce both the number of electrons in the system and the $\mathbf{G}$ vectors (needed for convergence of the wave function and density). Throughout this work, ab-initio norm-conserving pseudopotentials [21] are employed to mimic the core effect on the valence electrons. There are many ways to construct such ab-initio pseudopotentials, see for instance in Refs. [22, 23]. Finally, the ground-state electronic energy is given by :

$$E_0 = -\frac{1}{2}\sum_i \int d\mathbf{r}\phi_i^*(\mathbf{r})\nabla^2\phi_i(\mathbf{r}) + \frac{1}{2}\int d\mathbf{r}d\mathbf{r}^{'}\frac{n(\mathbf{r})n(\mathbf{r}^{'})}{|\mathbf{r}-\mathbf{r}^{'}|} + \\ + \int d\mathbf{r}V_{ext}(\mathbf{r})n(\mathbf{r}) + E_{xc}[n] \tag{2.38}$$

For the total energy, E_{tot}, one further needs to account for the constant Coulomb repulsion term in Eq. (2.38) between the ions.

DFT is an extremely successful theory for the description of material properties; however since it is a pure ground-state theory, it can capture neither the correct band structures nor the excited states (excitons) of the many-electron systems. Instead, the correct theory for the band structures (single-particle excitations) and optical properties (2-particle excitations) relies upon the Green's-function formalism which is introduced in detail in the next section.

2.4 Green's Function Formalism

In a single-particle reformulation of an interacting many-body system such as DFT, all particles are moving in a mean-field potential independent of the motion of the others, characterized by a set of discrete delta functions in the spectral function. Since DFT as a ground-state theory is unable to describe charged excitations and excitonic effects due to lack of capture of first and higher order particle effects, an effective many-body perturbation methodology within the framework of Green's function formalism was developed. In this approach, a new highly complex quantity, denoted as self-energy $\Sigma(r, r', \omega)$ (an object similar to the exchange-correlation functional of DFT but non-local in space, frequency dependent and non-hermitian) is introduced which contains in principle exactly the many-body physics, such as exchange, correlation, and most importantly screening effects in an exact diagrammatic fashion. This means that the amount of information available in $\Sigma(r, r', \omega)$ is immense but fortunately a full evaluation of the self-energy is not mandatory for charged and excited-state properties for the vast majority of materials. Extracting only the most relevant information from $\Sigma(r, r', \omega)$ provides results in quite satisfactory to excellent agreement with experimental data. To demonstrate this, the theory of Green's functions is presented in depth based on second quantization formulation, and equations for evaluation of the Green's functions aimed at obtaining quasi-particle (QP) energies are derived which are interpreted as corrections to the Kohn-Sham DFT energies. The corrected energies are the basis for calculation of optical absorption spectra of finite and periodic systems.

2.4.1 The GW Theory

The GW methodology is based on the idea of treating electronic correlation not in form of summation of configuration interactions but describing it in the language of Feynman diagrams. These diagrams are the building blocks of the self-energy $\Sigma(r, r', \omega)$ which represents a non-hermitian, non-local and frequency dependent object acting as a sophisticated many-body mean-field potential in an N-particle interacting system. The evaluation of this quantity is important for the theoretical description of band structures and optical properties of both molecular systems and condensed phase at many-body level. The fact that Σ contains in principle the full information about an N-particle interacting system hampers its explicit calculation. Therefore approximations to the self-energy are unavoidable. Fortunately, even the simplest approximation to Σ, namely, the product of a Green's function G and a dynamically screened interaction W, ($\Sigma = GW$) provides remarkably accurate results for the electronic band gaps, ionization potentials, and electron affinity. Furthermore, the performance of the GW method is highly superior to DFT and Hybrid-DFT.

The core question related to many-body problems is how to solve an ensemble of N inter-

acting particles. Since up to now it is impossible to solve the Schrödinger equation (SE) for an N-interacting particle system (N-IPS), an approximative N-particle solution to the SE has to be found. The most effective route is to reduce the N-IPS to an effective problem of a few weakly (or even non-) interacting particles. This leads to the concept of quasi-particles (QPs) or elementary excitations. Once a quasi-particle Hamiltonian containing the self-energy as its most important ingredient is set up, one obtains the QP-eigenstates and eigenenergies through a diagonalization scheme. The obtained quasi-particle states are then approximative N-particle solutions to the N-interacting particle SE. These mostly uncorrelated QPs are known as charged excitation, realized through a change of number of particles to $N+1$ or $N-1$. Furthermore, weak interactions of QPs implicate their peculiar property of exhibiting complex energies, given as poles of the one-particle Green's function (GF) in the complex plane. The imaginary part of the GF pole represents the lifetime of the particles, and the real part gives the energy of the single-particle excitations.

GFs such as retarded, advanced, temperature dependent, N-particle, equilibrium or non-equilibrium are extensively used in the applications of many-body perturbation theory (MBPT) [24]. Due to the complex internal mathematical structure (coupled chains of N-particle GFs) a direct access to the photon-mediated excited states for N-electron system as in time-dependent density functional theory (TD-DFT) is not possible, and thus, the quasi-particle states and energies corresponding to $N+1$ and $N-1$ electron system have to be first calculated as an intermediate step for subsequent optical response calculations.

To achieve this, one defines one-particle Green's function as the time-ordered product of the creation and annihilation field operators $\Psi(x,t)$ and $\Psi(x,t)^\dagger$ acting on the fully interacting N-particle ground-state of an electronic system, representing the quantum amplitude of an injected particle into the N-IPS at (x',t') that propagates to (x,t), if $t > t'$; corresponding to a $N+1$ system, or propagation of a hole forward in time from (x,t) to (x',t') , if $t < t'$; corresponding to a $N-1$ system.

$$G(x,t;x',t') = -i\,\langle N|T\{\Psi(x,t)\Psi^\dagger(x',t')\}|N\rangle \tag{2.39}$$

This mathematical object embodies basically all many-body interactions, a test particle through its path into the N-particle system "acts and feels" [24].

In Eq. 2.39 the one-electron quantum amplitude or the one-electron GF is presented in the Heisenberg representation through time-dependent field operators $\psi(x,t)$, x symbolising space (r) and spin (σ) coordinates, and T ensures time ordering of the operators. From the one-particle GF a series of one-particle system properties such as electronic and spin

densities or total energy is deducible. For instance, the local charge density n is directly extractable through performing the integration and taking the infinitesimal imaginary time limit (τ) of the propagation (2.39), as shown in Eq. (2.40)

$$n(r,t) = -i \lim_{\{\tau \to 0+\}} \int G(x,t;x,t+\tau)dt \tag{2.40}$$

or the ground-state total energy of the system is given by the Galitskii-Migdal Equation (2.41):

$$E_0 = \int dx \lim_{\{x \to x'\}} \lim_{\{\tau \to 0+\}} [\frac{\partial}{\partial t} - ih(x)]G(x,t;x',t+\tau) \tag{2.41}$$

with

$$h(x) = -\frac{1}{2}\nabla^2 + V_{ext}(x) \tag{2.42}$$

as the one-particle Hamiltonian.
Now in order to obtain a practical expression for the GF an equation of motion for the Green's function (eom-GF) is necessary. The eom-GF is strongly coupled to the Heisenberg equation of motion (2.43) for the field operators.

$$i\frac{\partial \Psi(x,t)}{\partial t} = [\Psi, H] \tag{2.43}$$

with $H = T + W + V$ (Hamilton operator) given as the sum of kinetic, external potential and Coulomb interaction formulated in second quantization :

$$T = -\frac{1}{2}\int d\mathbf{r}\Psi^\dagger(\mathbf{r})\nabla^2\Psi(\mathbf{r}) \tag{2.44}$$

$$W = \int d\mathbf{r}\Psi^\dagger(\mathbf{r})V_{ext}(\mathbf{r})\Psi(\mathbf{r}) \tag{2.45}$$

$$V = \frac{1}{2}\int d\mathbf{r}d\mathbf{r}'\Psi^\dagger(\mathbf{r})\Psi^\dagger(\mathbf{r}')v(\mathbf{r}-\mathbf{r}')\Psi(\mathbf{r}')\Psi(\mathbf{r}) \tag{2.46}$$

From Eq. (2.43) the equation of motion for the GF is derived as :

$$[i\frac{\partial}{\partial t} - h(x)]G(x,t;x',t') + i\int dx'' v(x',x'') \langle N|T\{\Psi^\dagger(x'',t)\Psi(x'',t)\Psi(x,t)\Psi^\dagger(x',t)\}|N\rangle = \delta(x,x')\delta(t,t') \tag{2.47}$$

The second term of Eq. (2.47) (l.h.s) involves a 2-particle GF. Its physical interpretation is that if an electron is injected into the system, it creates and annihilates bound electron-hole pairs along its path. From Eq. (2.47) is obvious that the one-particle GF couples to the 2-particle GF. The time evolution or the equation of motion (EOM) of the 2-particle GF

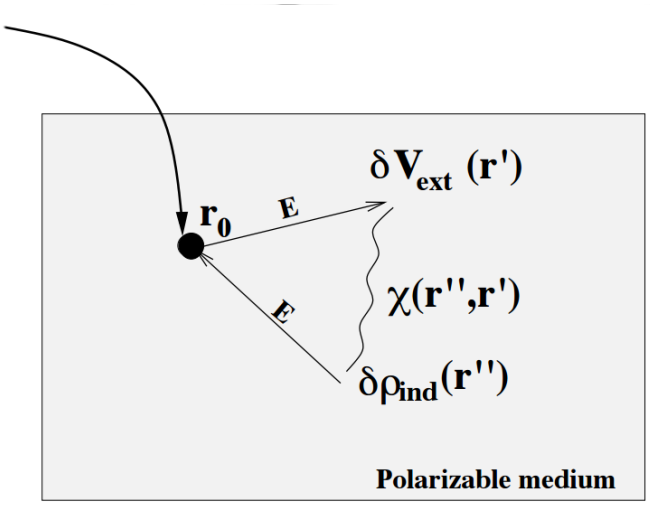

Figure 2.1: Schematic representation of the potential felt by an extra particle at $\mathbf{r_0}$ which induces an external potential δV_{ext} in a polarizable medium, which on its turn, induces charge variations $\delta\rho_{ind}$. The latter works back on the introduced point charge. The straight arrows labeled **E** represent the interaction due to classical electric field. The wiggly line represents the polarizability. Figure adopted from Ref. [25].

again couples to the 3-particle GF which again creates or annihilates further electron-hole pairs from the electron-hole pairs of the 2-particle GF. Therefore, the EOM of GF generates an infinite cascade of higher order GFs in the following connected way :
$G_1 \rightarrow G_2$, $G_2 \rightarrow G_3$, $G_3 \rightarrow G_4$, ...
Since such a set of chained equations for each particle order of GF is practically non-solvable, the EOMs have to be truncated at an order. The mathematical structure of Eq. (2.47) shows that an injected extra electron in a N-electron system polarizes its surroundings by change of the electronic density, as shown in Fig. 2.1.

Now, based on Schwinger's trick [26] the same polarization (induced by propagation of an extra electron) can be mimicked using a time-dependent external perturbation potential V_{pert} which will be set to 0 at the end of the derivation of an equation for the one-particle GF which will be decoupled from the (higher order) n-particle GFs. Thus, the chain of evolution equations for GFs in (2.47) is then properly truncated, and hence the evaluation of the one-particle GF is massively facilitated, since it no longer depends on the information from higher order GFs.

From now on for the sake of simplicity, the notation of $G(x,t,\sigma;x',t',\sigma')$ is changed to $G(1,2)$ with 1 and 2 respresenting the space, time and spin degrees of freedom.

It can be shown that the variation of G with respect to V_{pert} is :

$$\frac{\delta G(1,2)}{\delta V_{pert}(3)} = G(1,2)G(3,3^+) - G_2(1,3,2,3^+) \tag{2.48}$$

By plugging Eq. (2.48) into (2.47), one finds :

$$[i\frac{\partial}{\partial t_1} - h(1) + i\int d3v(1,3)G(3,3^+)]G(1,2) = \delta(1,2) + i\int d3v(1^+,3)\frac{\delta G(1,2)}{\delta V_{pert}(3)} \tag{2.49}$$

According to Eq. (2.40) : $-iG(3,3^+) = n(3)$, one hence identifies the third term of Eq. (2.49) from l.h.s as the classical Hartree potential :

$$-i\int d3v(1,3)G(3,3^+) = V_H(1) \tag{2.50}$$

Thus, upon perturbation V_{pert} one obtains a classical Hartree term, and a second purely quantum contribution which is related to the $\frac{\delta G(1,2)}{\delta V_{pert}(3)}$ term of (2.49). This quantum term can be further reformulated as the product of the self-energy and one-particle Green's function:

$$i\int d3v(1^+,3)\frac{\delta G(1,2)}{\delta V_{pert}(3)} = \int d3\Sigma(1,3)G(3,2) \tag{2.51}$$

In this way a 2-particle GF, as appearing in Eq. (2.47) is decomposed in (2.51) into the product of 2 one-particle objects, namely Σ and G. The self-energy $\Sigma(1,3)$ is an effective non-local and frequency dependent (dynamical) potential which an injected electron 'feels'. The unique property of Σ is that it accounts for higher-order particle effects (electron-hole pairs) as a single-particle object, because the self-energy is a functional of the Green's function ($\Sigma[G(1,2)]$).

By introducing the Hartree potential V_H and the self-energy Σ, Eq. (2.49) can now be presented in one-particle form, as follows :

$$[i\frac{\partial}{\partial t_1} - h(1) + V_H(1)]G(1,2) = \delta(1,2) + \int d3\Sigma(1,3)G(3,2) \tag{2.52}$$

By setting $\Sigma = 0$, one finds the equation of motion for a Hartree Green's function :

$$[i\frac{\partial}{\partial t_1} - h(1) + V_H(1)]G_H(1,2) = \delta(1,2) \tag{2.53}$$

with G_H being a non-interacting (independent particle) propagation. Now, the combination of Eqs. (2.53) and (2.52) results in :

$$\Sigma(1,2) = G_H^{-1}(1,2) - G^{-1}(1,2) \tag{2.54}$$

Therefore, the self-energy is a renormalization term, describing the difference between an independent particle propagating freely through the system, and a particle interacting with the other electrons, and polarizing its surroundings.

Equation (2.54) can be rewritten as a non-linear integral Dyson equation, connecting a non-interacting G_H with a fully interacting G :

$$G(1,2) = G_H(1,2) + \int d34\, G_H(1,2)\Sigma(3,4)G(4,2) \tag{2.55}$$

Eq. (2.55) is an equation in a tractable form which is used for evaluation of the Green's function. However, for practical purposes an explicit expression for Σ is needed.
This is obtained by solving Eq. (2.51) with respect to Σ :

$$\Sigma(1,2) = i \int d34\, v(1^+,3)\frac{\delta G(1,4)}{\delta V_{pert}(3)}G^{-1}(4,2) \tag{2.56}$$

and because :

$$\frac{\delta G(1,2)}{\delta V_{pert}(3)} = -\int d45\, G(1,4)\frac{\delta G^{-1}(4,5)}{\delta V_{pert}(3)}G(5,2) \tag{2.57}$$

from Eq. (2.56) one gets :

$$\Sigma(1,2) = -i \int d34\, v(1^+,3)G(1,4)\frac{\delta G^{-1}(4,2)}{\delta V_{pert}(3)} \tag{2.58}$$

with

$$\Gamma(1,2,3) = -\frac{\delta G^{-1}(1,2)}{\delta V_{pert}(3)} \tag{2.59}$$

as reducible vertex Γ. Finally, Eq. (2.58) gets the form :

$$\Sigma(1,2) = -i \int d34\, v(1^+,3)G(1,4)\Gamma(4,2,3) \tag{2.60}$$

and is used for the calculation of the self-energy.
Furthermore, by use of Dyson equation (2.54), the chain rule for the self-energy

$$\frac{\delta\Sigma(1,2)}{\delta V_{pert}(3)} = \int d45\, \frac{\delta\Sigma(1,2)}{\delta G(4,5)}\frac{\delta G(4,5)}{\delta V_{pert}(3)} \tag{2.61}$$

(2.57), and the definition (2.59), the final equation for the reducible vertex Γ is obtained :

$$\begin{aligned}\Gamma(1,2,3) = \delta(1,3)\delta(1,2) + \int d4567\, [-iv(1,4)\delta(1,4)\delta(1,2)\delta(4,5) + \frac{\delta\Sigma(1,2)}{\delta G(4,5)}] \\ G(4,6)\Gamma(6,7,3)G(7,5)\end{aligned} \tag{2.62}$$

The vertex function Γ accounts for all changes that an injected electron induces to all other particles which in turn 'adjust' self-consistently the potential that the injected particle 'feels'. In other words, Γ captures polarization and relaxation processes which are created by an additional particle in an electronic many-body system.

So far, integro-differential equations are derived for the *Green's function* represented through the Dyson equation. Furthermore, the *self-energy* Σ is given as the product of the bare Coulomb potential v, the Green's function G and the *vertex function* Γ, which itself is obtained from a 4-point Dyson-like equation (2.62). The equations for G, Σ, and Γ are corners of a Pentagon known as Hedin-Pentagon which is solved in a self-consistent manner.
Now, in order to reduce the mathematical and most importantly computational complexity of computing G, one introduces various kinds of approximations. The simplest one is to neglect higher-order corrections to the self-energy. By assuming $\Gamma(1,2,3) = \delta(1,3)\delta(1,2)$, the following simple approximation is obtained for the self-energy :

$$\Sigma(1,2) = iG(1,2)v(1^+,2) \tag{2.63}$$

This assumption corresponds to the Hartree-Fock approximation, and reduces the total self-energy to the Fock exchange self-energy operator Σ^x. However, Hartree-Fock self-energy includes no correlation effects, and is ill-defined regarding an expansion in orders of v as shown for the homogeneous electron gas [27]. Instead, Lars Hedin's revolutionary idea [43] was to screen the non-local bare Coulomb interaction v by the inverse of the microscopic dielectric function ϵ. Thus, an order by order expansion of the self-energy is now possible and carried out in terms of screened potential W :

$$W(1,2) = \int d3\, \epsilon^{-1}(1,3)v(3,2) \tag{2.64}$$

in order to prevent divergencies in the expansion series, as otherwise induced by v.
Furthermore, the screened potential W is related to the polarization P, which is again connected to the vertex Γ. Therefore, one encounters here a set of inter-connected equations. By introducing screening (2.64), the screened form of Hedin-Eqs. is obtained :

$$\Sigma(1,2) = i \int d34\, G(1,4)W(3,1^+)\Gamma_{irred}(4,2,3) \tag{2.65}$$

$$G(1,2) = G_H(1,2) + \int d34\, G_H(1,3)\Sigma(3,4)G(4,2) \tag{2.66}$$

$$\Gamma_{irred}(1,2,3) = \delta(1,2)\delta(1,3) + \int d4567\, \frac{\delta\Sigma(1,2)}{\delta G(4,5)} G(4,6)G(7,5)\Gamma_{irred}(6,7,3) \tag{2.67}$$

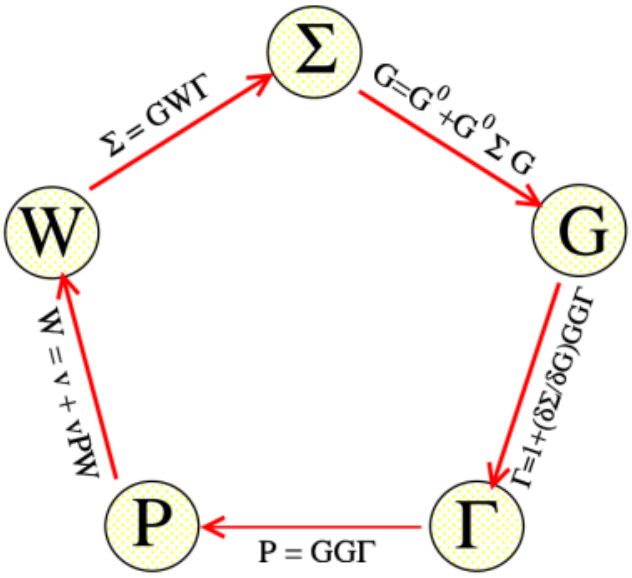

Figure 2.2: Hedin-pentagon gives a self-consistent solution to the many-electron system through five inter-connected fundamental ingredients. Thus, N-particle complexity is reduced to one-particle simplicity.

$$P_{irred}(1,2) = -i \int d34\, G(2,3)G(4,2)\Gamma_{irred}(3,4,1) \tag{2.68}$$

$$W(1,2) = v(1,2) + \int d34\, v(1,3)P_{irred}(3,4)W(4,2) \tag{2.69}$$

These equations describe exactly the physics of many-electron systems upon injection of an additional electron (charge excitation) self-consistently, as illustrated in Fig. 2.2.

An important point is that in the screened form of Hedin-Eqs. (2.65-2.69), the reducible Γ_{red} is replaced by the irreducible vertex Γ_{irred}, since the total classical potential $V_{tot} = V_{pert} + V_{Hartree}$ now replaces the perturbation potential V_{pert} giving :

$$\Gamma_{irred}(1,2,3) = -\frac{\delta G^{-1}(1,2)}{\delta V_{tot}} = \delta(1,3)\delta(1,2) + \frac{\delta\Sigma(1,2)}{\delta V_{tot}} \tag{2.70}$$

$$P_{irred}(1,2) = \frac{\delta n(1)}{\delta V_{tot}(2)} \tag{2.71}$$

From (2.70) one sees, that the irreducible vertex Γ_{irred} describes the variation of the self-energy with respect to the change of total classical potential. However, the effect of irreducible Γ_{irred} is smaller than that of the reducible one because in Γ_{red} the variation of the self-energy is performed with respect to the V_{pert}. By contrast, the induced Hartree potential in the total classical potential V_{tot} counteracts the time-dependent external perturbing potential V_{pert} and hence the change of the potential in Γ_{irred} becomes smaller with

respect to V_{tot}. In other words, the neglect of variation of the self-energy potential in (2.70) with respect to V_{tot}, is a better approximation than with respect to V_{pert}, since $V_{tot} < V_{pert}$. Following this, the irreducible polarizability (2.71) describes the change of the electronic density with respect to the change of V_{tot}, and accounts for polarization of a fully interacting system, as can be seen in (2.68). Now, if the vertex function or equivalently higher-order effects such as interactions in the electron-hole pairs are simplified by setting :

$$\Gamma_{irred}(1,2,3) = \delta(1,2)\delta(1,3) \tag{2.72}$$

in both P_{irred} and Σ, one ends up with the famous GW approximation to the self-energy, as introduced by Hedin [43] :

$$\Sigma(1,2) = iG(1,2)W(1^+,2) \tag{2.73}$$

which contains polarization and dynamical effects explicitly through W in contrast to (2.63) where the self-energy is static, and hence no relaxation of the system is permitted once an extra electron is injected to the system. The Eq. (2.73) is the best paradigm for a different and unique way of capturing electronic correlation (static and dynamic) in many-body systems through screening of the non-local bare Coulomb interaction $v(1,2)$ in contrast to the wave function-based methods where electronic correlation is described through sums of n-particle excited Slater determinants on top of the HF reference state. Therefore, one of the advantages of many-body methodology is simplifying the general evaluation of correlation in terms of dynamically screened interaction W. For a visual understanding of many-body interactions contained in the self-energy (2.73), the schematic representations of Hartree, exchange and correlation interactions based on Feynman diagrams are illustrated in Ref. [24].

2.4.2 GW self-energy approximations

The many-body perturbation theory as a high-level theory encapsulates in principle all the physics of a many-particle system. The complex formalism makes an understanding of the physical principles difficult. Therefore, a reduction of the amount of information contained in the self-energy by means of approximations is a necessary step in order to be able to gain an idea of the underlying fundamental interactions. In the following, an overview is presented of the frequently applied approximations to the self-energy, and ways of how to improve accuracy or to massively speed up calculations.

Hartree-Fock self-energy

By setting $\Sigma = 0$, one receives the known Hartree approximation, while the Hartree-Fock approximation is reproduced by replacing the dynamically screened interaction $W(1,2)$ by the static electron-electron interaction $v(1,2)$:

$$\Sigma_x = iv(1,2)\, G(1,2) \tag{2.74}$$

with Σ_x as Hartree-Fock self-energy. From (2.73) it can be seen that the GW approximation is nothing else but a dynamically screened version of the HF theory, allowing a many-electron system to respond, and thus relax upon an external perturbation potential (beyond Koopmans theorem). The Hartree-Fock self-energy causes massive overestimation of the electronic band gap of materials due to too strong exchange effects. Thus, finding a more reasonable approximation is mandatory to reach a better level of agreement with experimental data.

COHSEX self-energy

The Coulomb-hole screened exchange (COHSEX) approach is a very delicate approximation to the self-energy Σ due to reduction of computational complexity to a large degree. It is static (no frequency sampling) and summation over empty bands is eliminated. The COHSEX self-energy is composed of quantum and classical terms. The first one is the *screened exchange* term :

$$\Sigma^{SEX}(1,2) = -G(1,2)\, W(1,2,\omega=0) = -\sum_i \phi_i(1)\, \phi_i(2)\, W(1,2,\omega=0) \tag{2.75}$$

This is identical to (2.74), except v is replaced by W, which decreases HF-exchange effects by taking into account polarization (exchange damping). The screened exchange term accounts for the Pauli principle, and thus the fermionic nature of electrons. The sum in (2.75) for the Green's function represented by KS-wave functions ϕ_i runs only over the occupied

bands, which is the massive benefit of this approximation. However, unoccupied bands are only eliminated in the Green's function and have to be taken into account in the calculation of polarization function explicitly.

The second part of COHSEX is the *Coulomb hole* term :

$$\Sigma^{COH}(1,2) = \frac{1}{2}\delta_{1,2}\, W_p(1,2,\omega=0) \tag{2.76}$$

with $W_p = W - V$ as a local and static polarization. The Coulomb hole term is a classical term, representing a shift in energy due to instantaneous polarization, once an electron is added or removed. Approximations (2.75) and (2.76) can be used to either solve Eqs.(2.65-2.69) for the self-energy fully iteratively or in a non-self consistent manner within the COHSEX approximation.

An interesting aspect of COHSEX is that it is capable of describing band structures of different structural phases of electronically correlated materials properly, for instance, in the case of VO_2, where LDA or GGA's are not able to capture the true nature of the band structure of low temperature anti-ferromagnetic monoclinic phase of VO_2, which incorrectly predict a metallic band structure. By contrast, it's been shown by Gatti [29] that the full self-consistent COHSEX scheme captures the correct band structure of both high and low temperature phases of VO_2 through successive update of the KS-wave functions. Therefore, COHSEX is capable of restoring the true character of the band structure and is further a good starting point for more accurate calculations targeting dynamical correlations in solids.

single-shot GW

Based on the fundamental set of equations (2.65- 2.69) in the GW approximation, one solves the Hedin-Pentagon for a dynamical self-energy in a one-shot manner. Strinati, Mattausch and Hanke [30], Hybertsen and Louie [31,32] and Godby, Schlutier and Sham [33,34], used the best possible initial guess for G and W from mean field theories, such as LDA, or semi-local functionals, and performed only one cycle of the self-consistent Hedin-Equations. This approach is known as one-shot GW or G_0W_0, which is frequently used for the calculation of band structure of various materials with remarkable success. After performing a single-shot of Hedin-Pentagon, the QP energies for band structures of semi-conductors and insulators are calculated within the GW-approximation as first-order corrections to the Kohn-Sham energies. Through linearization of the self-energy around the KS-energies, one obtains a

perturbative expression for QP energies :

$$\epsilon_n^{QP} = \epsilon_n^{KS} + Z \ \langle\psi_n|(\Sigma(\epsilon^{KS}) - V_{xc}^{KS})|\psi_n\rangle \tag{2.77}$$

with Z as the renormalization factor ranging from 0 to 1, describing the correlation grade in materials. Values close to 1 indicate an electronically less correlated system, meaning that a simple QP description of the many-electron system is justified to properly account for charged excitations. Furthermore, as obvious from (2.77) the quality of the results heavily depends on the starting point. Usually, as mentioned above, G_0W_0 is started from the local or semi-local DFT reference orbitals (LDA,GGA), leading to a considerable improvement of band gaps compared to DFT-hybrid functionals, for instance. Hence, the G_0W_0 approach is way superior to all DFT-hybrid functionals in terms of accuracy. However, it is computationally costly due to explicit frequency sampling of the dielectric matrix $\epsilon(\omega)$, inversion of a potentially large $\epsilon(\omega)$ matrix, and summation over empty bands at each frequency point. Nevertheless, the computational load is affordable on today's computers.

The dependency of G_0W_0 results on the choice of starting wave functions is an issue; however it is considerably reduced by iterating the Hedin-Pentagon multiple times, instead of running only one iteration. This is discussed in the following.

multi-shot GW's

To further increase the accuracy, a partial self-consistent scheme is employed, as systematically applied for the first time by Kresse et al. [35] on a number of semi-conductors and insulators with promising results. Partial self-consistency of Hedin-Eqs. means performing a full self-consistent cycle in G but keeping the dynamical screened interaction W at the mean-field level. This scheme is known as GW_0, and proved to be a promising approach for accurate prediction of the band gaps of a wide range of solids [35], probably due to fortuitous systematic error cancellations [37].

Further iteration both in G and W leads to the fully self-consistent scheme which is from computational point of view the most time consuming GW variant. Within the fully self-consistent GW scheme band widths and gaps are typically overestimated in comparison to experimental references. The overestimation is due to underscreening of $W(\omega)$ caused by spectral weight transfer from the QP peak to the satellite part of the spectral function, as illustrated in Fig. 2.3. This is a direct consequence of inclusion of Z factor in the Green's function ($G = Z_i/(\omega - \epsilon_i - \Gamma)$), constructing the polarization function ($P = -iG\,G$) which is then wrongly attenuated by a factor of Z^2 upon each iteration. The weight transfer is enhanced upon self-consistency resulting in too strong $W(\omega)$, and finally overestimation of

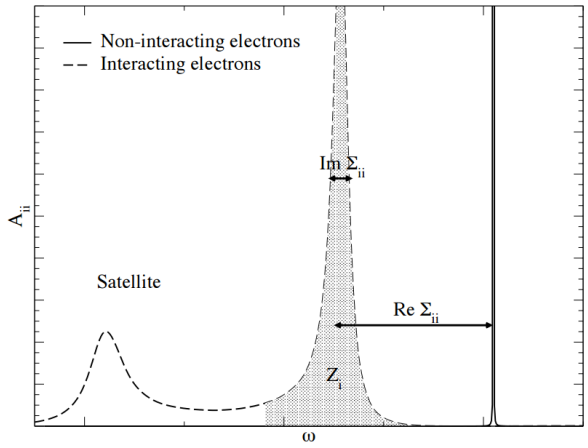

Figure 2.3: Typical features of a diagonal spectral function A_{ii} in the GW theory are shown, namely, a QP peak and a satellite at lower energies. The spectral weight Z under the QP peak determines the validity of the QP approximation. For Z far from 1 the QP approximation should be abandoned. In the case of non-interacting electrons the spectral function has no broadening and is characterized by a delta peak. Figure adopted from Ref. [25].

band widths and gaps. The extreme case is HF where there is no screening in $W(\omega)$ causing massive overestimation of the gaps. One way to solve the underscreening of $W(\omega)$ is to include vertex corrections Γ in $\Sigma = G\,W\,\Gamma$ and in the screening P. However, until now there is no convenient way of how to treat vertex corrections in both Σ and P simultaneously and properly. However, an approximation using test charges was introduced by Kresse [36].

Plasmon Pole Approximation

The dynamic character of W imposes a cumbersome computational burden. In order to reduce the computational load related to frequency dependency of the dielectric function $\epsilon(\omega)$, one proceeds with the single pole approximation, provided the dielectric function is not too structured. This allows to practically skip the computationally most demanding part of the GW calculations, as otherwise for each frequency point of the dielectric function $\epsilon(\omega)$, an inversion of a quite large matrix and a summation over a large number of empty bands have to be performed. However, in the Plasmon Pole approximation (PPA), inversion and summation are carried out only at two frequencies, namely, at zero and plasma frequency according to the following fit scheme :

$$\epsilon^{-1}_{\mathbf{G}\mathbf{G}'}(\mathbf{q},\omega) = \delta_{\mathbf{G}\mathbf{G}'} + \frac{\Omega^2_{\mathbf{G}\mathbf{G}'}}{\omega^2(\mathbf{q}) - (\widetilde{\omega}_{\mathbf{G}\mathbf{G}'} - i\eta)^2} \tag{2.78}$$

where $\Omega(\mathbf{q})$ and $\widetilde{\omega}(\mathbf{G}\mathbf{G}')$ are the two fit parameters.
The small parameter η in the denominator ensures the correct time-ordering.

The justification for PPA is that the general behavior of the dielectric function $\epsilon^{-1}(\omega)$ can exhibit a single pole character which can simply be approximated by a model dielectric function at zero and an imaginary frequency according to the Godby-Needs [37] or Hybertsen and Louie [32] PP schemes. Furthermore, Eq. (2.78) allows to calculate $\epsilon^{-1}(\omega)$ everywhere in the complex plane analytically.

The critical point of PPA is that if results depend on the imaginary frequency, PPA is no longer adequate, and an explicit frequency sampling of the dielectric function is indeed unavoidable. This is the consequence of many poles or poles lower than the electronic band gap appearing in $\epsilon^{-1}(\omega)$, leading to a breakdown of the PP approximation.

2.4.3 The Bethe-Salpeter Equation (BSE)

The so far derived single-particle picture in GW is adequate for description of photo-emission spectra; however in case of optical excitation, one has to go beyond this one-particle scheme. The adequate picture for the optical (neutral) excitations involves propagation of a correlated quasi-electron and quasi-hole (electron-hole pair or exciton).

In the MBPT framework, this correlated motion of quasi-particles is described by the 2-particle Green's function L which is generally defined as the functional derivative with respect to a non-local perturbation :

$$L(1,2,3,4) = -i\frac{\delta G(1,2)}{\delta V_{pert}(3,4)} \tag{2.79}$$

Equation (2.79) can be rewritten as :

$$L(1,2,3,4) = -i\int d56 G(1,5)\frac{G^{-1}(5,6)}{\delta V_{pert}(3,4)}G(6,2) \tag{2.80}$$

Using the Dyson equation

$$G^{-1}(5,6) = G_H^{-1}(5,6) - V_{pert}(5,6) - \Sigma(5,6) \tag{2.81}$$

for $G(5,6)$, the equation of motion for the fully interacting propagator L is obtained :

$$\begin{aligned} L(1,2,3,4) = i\int d56 G(1,5)\Bigg[&- \delta(3,5)\delta(4,6) + \\ &- \frac{\delta[V_H(5)\delta(5,6) + \Sigma(5,6)]}{\delta V_{pert}(3,4)}\Bigg]G(6,2) \end{aligned} \tag{2.82}$$

Then, using the functional chain rule $\delta\Sigma/\delta V_{pert} = (\delta\Sigma/\delta G)(\delta G/\delta V_{pert})$, one obtains :

$$\begin{aligned} L(1,2,3,4) = -iG(1,3)G(4,2) + -i\int d5678 G(1,5)G(6,2) \\ \frac{\delta[V_H(5)\delta(5,6) + \Sigma(5,6)]}{\delta G(7,8)}L(7,8,3,4) \end{aligned} \tag{2.83}$$

with $L_0(1,2,3,4) = -iG(1,3)G(4,2)$ describing the free propagation of an electron and a hole that do not interact. Consequently, one arrives at the final expression for the Bethe-Salpeter equation :

$$L(1,2,3,4) = L_0(1,2,3,4) + \int d5678 L_0(1,2,5,6) \Big[v(5,7)\delta(5,6)\delta(7,8) + \Xi(5,6,7,8) \Big] L(7,8,3,4) \tag{2.84}$$

where Ξ is the four-point non-local many-body kernel given as :

$$\Xi(5,6,7,8) = i\frac{\delta\Sigma(5,6)}{\delta G(7,8)} \tag{2.85}$$

The kernel explicitly captures the exchange and correlation effects of the 2-interacting quasi-particles propagating in time and space, or in other words, the kernel links the non-interacting with the fully interacting propagation. Furthermore, a connection between L and the reducible vertex $\Gamma_{red}(1,2,3) = -\frac{\delta G^{-1}(1,2)}{\delta V_{pert}(3)}$ can be established for a local perturbation potential $V_{pert}(3)$ in the definition (2.79) of L :

$$\begin{aligned} L(1,2,3,3^+) = -i\frac{\delta G(1,2)}{\delta V_{pert}(3)} &= i\int d45 G(1,4)\frac{\delta G^{-1}}{\delta V_{pert}(3)} G(5,2) = \\ &= -i\int d45 G(1,4)\Gamma_{red}(4,5,3)G(5,2) \end{aligned} \tag{2.86}$$

This means that L is indeed a vertex correction, if one would have run a second iteration in Hedin-Pentagon, and avoid setting Γ to unity. Finally, the two-point response function χ as measured in spectroscopy experiments reads as :

$$\chi(1,2) = \frac{\delta n(1)}{\delta V_{pert}(2)} \tag{2.87}$$

Reformulation of BSE

The Bethe-Salpeter equation (2.84) in the above form is very cumbersome to solve due to the high complexity of the non-local four-point kernel. Therefore, several approximations facilitating the practical work are introduced. The standard approximation to the kernel is the GW self-energy. Consequently, the kernel Ξ becomes :

$$\Xi(5,6,7,8) = i\frac{\delta\Sigma(5,6)}{\delta G(7,8)} = -\frac{\delta[G(5,6)W(5,6)]}{\delta G(7,8)} \tag{2.88}$$

Taking the functional derivative with respect to G, one gets two terms : W and $G\delta W/\delta G$; the former describes the dynamically screened interaction and the latter captures the change of the dynamically screened interaction with respect to G. $G\delta W/\delta G$ is a second-order term, and can be safely neglected. With this approximation, the Bethe-Salpeter equation

simplifies to :

$$\begin{aligned} L(1,2,3,4) = L_0(1,2,3,4) + + \int d5678 L_0(1,2,5,6) \\ \Big[v(5,7)\delta(5,6)\delta(7,8) - W(5,6)\delta(5,7)\delta(6,8)\Big] L(7,8,3,4) \end{aligned} \tag{2.89}$$

Thus, as a result, one obtains a non-linear equation of motion which connects the free L_0 with the fully interacting 2-particle L through the non-local kernel which consists of two terms: The first one is the unscreened exchange term v which is repulsive in nature. The second one accounts for the screened Coulomb electron-hole interaction W and is attractive in nature. To further reduce the complexity and computational cost of Eq. (2.89), a static screened interaction is assumed : $\frac{1}{2\pi} W(\mathbf{r_1}, \mathbf{r_2}, \omega = 0)\delta(t_1 - t_2)$.
This approximation is justified by the fact that in semi-conductors the dynamic effects in W and G tend to cancel [39, 40], and hence they are often neglected in both W and G.
Equation (2.89) is then projected onto the transition space which is spanned by either quasi-particle or Kohn-Sham wave functions ϕ_v and ϕ_c. The transfer of L into transition space follows from the fact that for each excitation only a limited number of electron-hole pairs contributes, and hence the sum in the transformation (2.90) is finite.

$$\chi(1,2,3,4,\omega) = \sum_{n_1..n_4} \phi^*_{n_1}(1)\phi_{n_2}(2)\phi^*_{n_3}(3)\phi_{n_4}(4)\chi_{(n_1,n_2),(n_3,n_4)} \tag{2.90}$$

In this way and after some algebra, an effective 2-particle Hamiltonian H is obtained from which information about the excitonic eigenenergies and eigenstates can be gained.

$$\sum_{n_3 n_4} H^{2p}_{(n_1 n_2),(n_3 n_4)} A^{n_3 n_4}_{\lambda} = E_{\lambda} A^{n_1 n_2}_{\lambda} \tag{2.91}$$

In other words, in transition space the Bethe-Salpeter equation is converted to a Schrödinger-like equation with H given as :

$$H^{2p}_{(n_1 n_2),(n_3 n_4)} = (\epsilon_{n_2} - \epsilon_{n_1})\delta_{n_1 n_3}\delta_{n_2 n_4} + (f_{n_2} - f_{n_1})(v_{(n_1 n_2),(n_3 n_4)} - W_{(n_1 n_2),(n_3 n_4)}) \tag{2.92}$$

The exchange v and correlation W in the product basis ϕ_v ϕ_c read as :

$$v_{(vc),(v'c')} = 2 \int d\mathbf{r_1} d\mathbf{r_2} \phi^*_v(\mathbf{r}_1)\phi_c(\mathbf{r}_1) v(|\mathbf{r}_1 - \mathbf{r}_2|)\phi_{v'}(\mathbf{r}_2)\phi^*_{c'}(\mathbf{r}_2) \tag{2.93}$$

$$W_{(vc),(v'c')} = \int d\mathbf{r_1} d\mathbf{r_2} \phi^*_v(\mathbf{r}_1)\phi_{v'}(\mathbf{r}_1) W(\mathbf{r_1}, \mathbf{r_2}, \omega = 0)\phi_c(\mathbf{r}_2)\phi^*_{c'}(\mathbf{r}_2) \tag{2.94}$$

The factor 2 in exchange (2.93) comes from spin degeneracy. The v corresponds to dipole interaction between valence-conduction charge fluctuations, whereas W accounts for direct

(screened) interaction between valence and conduction charge densities.

Now, in order to gain access to eigenenergies and eigenstates of the effective 2-particle Hamiltonian, Eq. (2.91) has to be diagonalized. However, since the diagonalization can become time consuming, depending on the dimension of the matrix, there are much more efficient methods, such as the Haydock recursive algorithm [41–43] or k-point interpolation procedures [44] allowing for a fast calculation of the absorption spectra.
Once the excitonic Hamiltonian is diagonalized, the optical absorption intensities can be calculated from :

$$\epsilon_2(\omega) = \lim_{q\to 0} \frac{8\pi}{q^2} \sum_{\lambda} \left| \sum_{vc} A_{\lambda}^{vc} \langle v| \exp^{-i\mathbf{qr}} |c\rangle \right|^2 \delta(\omega - E_{\lambda}) \tag{2.95}$$

For simplicity, only the resonant contributions ($v \to c$) in (2.95) are taken into account.

A comparison of Eq. (2.95) with Fermi's Golden rule formula

$$\epsilon_2(\omega) = \frac{8\pi^2}{\Omega\omega^2} \sum_{ij} \left| \langle \Psi_j | \hat{\mathbf{e}}.\mathbf{v} | \Psi_i \rangle \right|^2 \delta(E_j - E_i - \omega) \tag{2.96}$$

reveals important implications of the BS equation :

1) Inclusion of excitonic effects in (2.95) results in E_{λ} which is in general different than the independent-particle difference energies $E_c - E_v$ in (2.96).
2) The eigenstates of the effective Hamiltonian A_{λ}^{vc}, the so-called coupling coefficients, mix the independent-particle transitions $|v\rangle \to |c\rangle$.
3) The Bethe-Salpeter equation reduces to the usual independent-particle picture (RPA), if the electron-hole interaction is neglected.

Bibliography

[1] M. Born and R. Oppenheimer, Ann. Phys. **84**, 457 (1927).

[2] H. Jahn and E. Teller, Proc. Roy. Soc. A **161**, 220 (1937).

[3] F. Bloch, Z. Phys. **52**, 553 (1928).

[4] A. H. Wilson, Proc. Roy. Soc. A **133**, 458 (1931).

[5] D. Hartree, Proc. Cambridge Philos. Soc. **24**, 89 (1928).

[6] V. Fock, Z. Phys. **61**, 126 (1930).

[7] P. Hohenberg and W. Khon, Phys. Rev. **136**, B864 (1964).

[8] W. Khon and L. J. Sham, Phys. Rev. **140**, A1113 (1965).

[9] L. Fetter and J.D. Walecka Quantum theory of Many–Body Systems, McGrawHill, New York, N.Y. 1981.

[10] L. Hedin and B. I. Lundqvist, J. Phys. C. **4**, 2064 (1971).

[11] D.M. Ceperley and B.I. Alder, Phys. Rev. Lett. **45**, 566 (1980).

[12] K. Burke, The ABC of DFT, 2003, (unpublished), http://dft.rutgers. edu/kieron/beta.

[13] O. Gunnarsson and B. I. Lundqvist, Phys. Rev. B **13**, 4274 (1976).

[14] R. O. Jones and O. Gunnarsson, Rev. Mod. Phys. **61**, 689 (1989).

[15] J. P. Perdew, K. Burke, and M. Ernzerhof, Phys. Rev. Lett. **77**, 3865 (1996).

[16] D. R. Hamann, Phys. Rev. B **55**, 10157-10160 (1997).

[17] J. Tao, J. P. Perdew, V. N. Staroverov, and G. E. Scuseria Phys. Rev. Lett. **91**, 146401 (2003).

[18] J. P. Perdew, M. Ernzerhof, and K. Burke, J. Chem. Phys. **105** (22): 9982-9985 (1996).

[19] C. Adamo, and B. Vincenzo, J. Chem. Phys. **110** (13): 6158-6170 (1999)

[20] H. J. Monkhorst and J. D. Pack, Phys. Rev. B **13**, 5188 (1976).

[21] G. B. Bachelet, D. R. Hamann, and M. Schlüter, Phys. Rev. B **26**, 4199 (1982).

[22] S. Albrecht, Ph.D. thesis, Palaiseau (France), (1999).

[23] S. Botti, Ph.D. thesis, Pavia (Italy), (2002).

[24] R. D. Mattuck, Guide to Feynman Diagrams in the Many-Body Problem, (1992).

[25] F. Bruneval, Ph.D. thesis, Palaiseau (France), (2005).

[26] J. Schwinger, Proc. Nat. Accad. Sci. **37**, 452 (1951).

[27] B. Holm and U. von Barth, Phys. Rev. B 57, 2108 (1998).

[28] L. Hedin, Phys. Rev. Lett. **139**, A796 (1965).

[29] M. Gatti, Ph.D. thesis, Palaiseau (France), (2007).

[30] G. Strinati, H. J. Mattausch, and W. Hanke, Phys. Rev. B **25**, 2867 (1982).

[31] M. S. Hybertsen and S. G. Louie, Phys. Rev. Lett. **55**, 1418 (1985).

[32] M. S. Hybertsen and S. G. Louie, Phys. Rev. B **34**, 5390 (1986).

[33] R. W. Godby, M. Schlüter, and L. J. Sham, Phys. Rev. B **36**, 6497 (1987).

[34] R. W. Godby, M. Schlüter, and L. J. Sham, Phys. Rev. B **37**, 10159 (1988).

[35] M. Shishkin and G. Kresse, Phys. Rev. B **75**, 235102 (2007).

[36] A. Grüneis, G. Kresse, Y. Hinuma, and F. Oba, Phys. Rev. Lett. **112**, 096401 (2014)

[37] H. N. Rojas, R. W. Godby, and R. J. Needs, Phys. Rev. Lett. **74**, 1827 (1995)

[38] F. Bruneval, and M. Gatti, Springer Berlin Heidelberg **347**, 99-135 (2014).

[39] A. Marini and R. Del Sole, Phys. Rev. Lett. **91**, 176402 (2003).

[40] F. Bechstedt, K. Tenelsen, B. Adolph, and R. Del Sole, Phys. Rev. Lett. **78**, 1528 (1997).

[41] R. Haydock, Comput. Phys. Comm. 20, **11** (1980).

[42] L. X. Benedict, E. L. Shirley, and R. B. Bohn, Phys. Rev. Lett. **80**, 4514 (1998).

[43] M. Marsili, Ph.D. thesis, Università di Roma Tor Vergata, Roma (Italy), (2005).

[44] M. Rohlfing and S. G. Louie, Phys. Rev. Lett. **80**, 3320 (1998).

Chapter 3

Linear absorption spectra of condensed phases, GW self-consistency and electron-phonon coupling

In this chapter, applications of the many-body perturbation methods described in chapter 2 on disordered systems, liquid water and ammonia are presented. Important implications from many-body effects on the absorption spectra are revealed, explaining non-trivial features such as massive spectral weight redistributions and blue-shift of the peaks from gas to liquid phase. The impact and importance of electron-hole correlations on the spectra of open-shell spinel zinc ferrite solid are shown. Further, the effects of electron-phonon coupling and GW self-consistency on the band gap of liquid water is studied.

3.1 Red and blue-shift of liquid H_2O excited states

Abstract

The optical absorption spectrum of liquid H_2O is calculated in the energy range of 5–20 eV to probe the nature of water's excited states by means of many-body perturbation theory. The main features of recent inelastic X-ray measurements [1] are well reproduced, such as a bound excitonic peak at 7.9 eV with a shoulder at 9.4 eV as well as the absorption maximum at 13.9 eV, followed by a broad shoulder at 18.4 eV. The spectrum is dominated by excitonic effects impacting the structures of the spectrum in the low- and high-energy regimes and also by single-particle effects at high energies. The exciton density of the low-energy states, in particular of S_1, is highly anisotropic and localized mostly on one water molecule. The S_1 state is essentially a HOCO-LUCO (highest occupied crystal orbital - lowest unoccupied crystal orbital) transition and of intra-molecular type, showing a localized valence character. In the higher excited states, a significant change in the character of the electronically

excited states occurs, shown by emergence of multiple peaks at 7.9 eV in the quasi-particle (QP) transition profile and in the delocalized exciton density, spread over several water molecules. The exciton delocalization of excited states at 7.9 eV causes a blue-shift of the first absorption band with respect to the S_1 state of the water monomer. However, due to reduction of the electronic band gap from gas to liquid phase as a consequence of enhanced screening upon condensation, the localized S_1 state of liquid water is red-shifted with respect to the S_1 state of the water monomer. For higher excitations near the vertical ionization energy (11 eV), quasi-free electrons emerge, in agreement with the conduction band electron picture. Furthermore, the occurring red and blue shifts of the excited states are independent of the coupling of resonant and anti-resonant contributions to the spectrum.

Introduction

The optical spectra of ice and liquid water have been studied extensively, both experimentally [1, 1, 2, 4–7] and theoretically [9–11, 13, 21, 23]. The absorption spectrum of hexagonal ice (ice Ih) at 80 K shows seven peaks between 8 and 25 eV [6], at 8.65 eV, 10.4 eV, 12.4 eV, 14.5 eV, 17.9 eV, 19.8 eV, and 24.7 eV. An experimentally determined absorption spectrum of liquid water was later obtained based on inelastic X-ray scattering measurement [1] which avoids a number of shortcomings of the usual UV spectroscopy such as surface reflections and use of vacuum. The general features of the optical absorption spectrum of both ice Ih and liquid water are rather similar with the main differences being the peak positions.

In both condensed phases, solid and liquid, a significant blue-shift of the S_1 state of molecular water (7.46 eV [14]) toward higher energies is observed. The blue-shift concerns the shift of the maximum of the first absorption band of liquid water with respect to molecular water's S_1, while the absorption onset of liquid water, i.e. the first excited state with non-zero oscillator strength (the so-called Urbach tail [15]) lies at an energy below the molecular water's S_1 state and thus it is red-shifted.

The occurring blue-shift from gas to liquid-phase has been explained by several approaches, such as electrostatic, the hydrogen bond network, Ry and molecular excitonic effects [2]. Hermann et al. [10] explained the blue-shift by purely electrostatic effects by embedding a water monomer in a finite point charge array, with excitation energies of 8.2, 10.5 and 13.9 eV for liquid water, in good agreement with experiment, but with an unsatisfactory distribution of spectral weights due to neglect of many-body effects and limitations of the applied theoretical approach.

In a further study, Tavernelli used real time-dependent density-functional theory (RTD-DFT) to calculate the optical absorption of liquid water [11]. He was indeed able to

qualitatively reproduce the measured optical absorption spectrum and energy-dependent dielectric function. However, the RTD-DFT spectrum has some deficiencies, such as an underestimation of the first absorption band by more than 1 eV, appearance of multiple peaks near 10 eV and a sharp dip at 18 eV. The shortcomings can be traced back to the use of the semi-local BLYP GGA functional. The deficiencies of TD-DFT based on adiabatic local density approximation (ALDA) for the calculation of optical spectra of liquid water were discussed by Garbuio et al. [12]. They compared DFT gaps with those obtained with the Green's function approach (GW) where electron-electron interaction is explicitly taken into account and found a remarkable improvement of GW gaps over DFT ones. The GW/BSE ansatz considerably changed the energy positions and the shape of the TDDFT-ALDA spectrum.

However, still the energy of the first main peak is underestimated by more than 1 eV in Ref. [12], and the mid- to high-energy part of the calculated spectrum lacks accuracy. Therefore, the aim of the present study is to accurately calculate the optical absorption spectrum of liquid water over a wide energy range, and extract the significance of the related effects, underlying specific features of the spectrum. Furthermore, the nature of the electronically excited states is analysed in terms of energy dependent quasi-particle (QP) transition profile and exciton localization. By accurate calculation of excited-state energies, QP transition spectrum as well as the degree of exciton localization, the mechanism behind the red- and blue-shift of water's excited states upon condensation is revealed.

After analysis of the water spectrum, the validity of the approximations used so far in the literature for calculation of electronic and optical properties of liquid water is assessed to explain discrepancies and to show that the shifts of the excited states are independent of the coupling effects in the BSE. The GW/BSE as a state-of-the-art methodology is employed without further approximations.

Technical details

In order to obtain a reasonable description of the structure of liquid water within periodic boundary conditions, a large supercell has to be considered to obtain statistically representative results and thus reducing numerical noise [16]. While large simulation boxes with thousands of atoms are accessible for modern ab initio MD techniques, many-body perturbation theory (MBPT) calculations are out of reach for large water boxes (128 or 256 water molecules) due to unfavorable scaling with system size. The present simulations of liquid water were therefore restricted to supercells containing 8, 27 and 64 water molecules in cubic boxes of side length 6.2091, 9.3137, and 12.4183 Å, respectively, corresponding to densities of $\rho \approx 1.0$ g/cm^3. The smaller 8-water molecule box was sampled by a relatively dense

k-point grid of 36 points in the irreducible Brillouin zone (IBZ), while 8 special k-points were used for the 27- and 64-water molecule boxes. Results obtained from the different water box sizes (8, 27, 64) are employed to investigate the importance of long-range order and artificial periodic boundary conditions on the spectra.

Careful equilibration of the liquid water structure is of utmost importance for the reliability of the calculated spectra, since the structure strongly impacts the peak positions and spectral structures. To this aim, periodic ab-initio BOMD simulations were performed in NVT ensemble at 300 K using the Quickstep module of CP2k [14] adopting the Nosé-Hoover thermostat, with the PBE density functional [16] which was shown to give a good account of hydrogen bonding [9]. Goedecker-Teter-Hutter (GTH) pseudopotentials were used for the core-electron description and the Grimme D3 correction [15] was used to account for dispersion interactions. Wave functions were expanded in an optimized Gaussian polarized double-zeta split-valence (OPT-DZVP) basis set, whereas the electronic density was represented using an auxiliary plane-wave basis, and a density cutoff of 400 Ry. 30 water configurations were randomly selected from 15 ps production run for the water ensemble. For each configuration a DFT-PBE calculation using QUANTUM ESPRESSO [11] with a cutoff of 100 Ry was performed. On top of the PBE wavefunctions, a full-frequency dependent G_0W_0 calculation was carried out. Excitation energies and spectra were computed in the regime of vanishing momentum transfer $q \to 0$ using YAMBO [12].

Accurate calculation of the electronic structure and hence the electronic band gap of liquid water within the framework of the GW formalism is of utmost importance serving as the basis of subsequent spectroscopic calculations. The experimental reference is 8.7±0.5 eV [23]. Our calculated electronic band gap averaged over 30 configurations of liquid water at G_0W_0 level is 8.58 eV for the 8-water molecule box and 8.71 eV for the 27-water molecule box, both at the Γ-point. The obtained values are rather similar and within the experimental range which indicates that disorder effects are short-range in nature. Furthermore, the electronic band gap determines to a large extent (besides excitonic effects) the location of the energies of the electronically excited states, as the difference of single-particle energies directly enter the BS matrix. Therefore, a good agreement of the calculated electronic band gap with experiment is a necessary prerequisite for accurate spectra calculations.

In the GW calculations for the 8- and 27-water box, 200 (32 occupied) and 600 (112 occupied) bands were considered, respectively and sampled to integrate the frequency-dependent dielectric function $\epsilon(G, G', \omega)$ at 30 frequencies to capture dynamical effects. Furthermore, 50 and 5 Ry for the exchange and correlation part of the self energy were used, respectively. Regarding BSE calculations, 91 transition bands (68 unoccupied) were

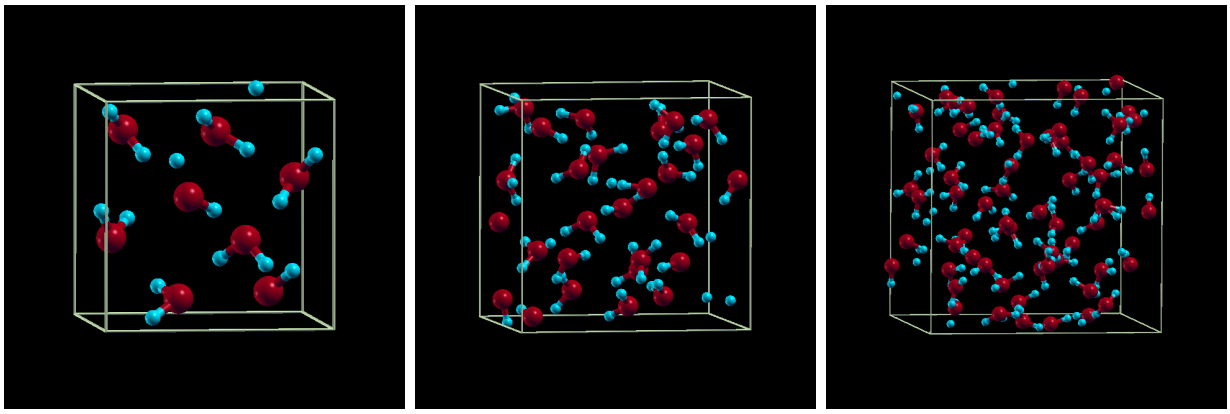

Figure 3.1: Liquid water structures for the 8-,27-, and 64-box used in this study.

considered in the case of the 8-water box, and 228 bands (144 unoccupied) were taken into account for the 27-water box. A sufficiently large number of transition bands is crucial to resolve the relative intensities, in particular for higher-lying excited states up to 20 eV. Furthermore, all optical calculations were performed in the adiabatic limit (static kernel) and within the Tamm-Dancoff approximation (TDA). Liquid water structures are shown in Fig. 3.1. Convergence tests are provided in Appendix A.

Results and discussion

In Figs. 3.2 and 3.3 the optical absorption spectra of water for 8- and 27-molecule boxes obtained at G_0W_0-BSE level are shown. The calculated spectra are compared with inelastic X-ray scattering (IXS) measurements [1] which are considered as the most accurate reference available. The G_0W_0-BSE-spectra of all 30 selected configurations show similar features (Fig. 3.2). The averaged spectrum (black line) for the 27-molecule box has the lowest excited state (S_1) at 5.7 eV, a bound excitonic state at 7.9 eV (exp. 8.1 eV [1]), a shoulder at 9.4 eV (exp. 9.6 eV [24]), a global absorption maximum at 13.9 eV (exp. 14.1 eV [1]) and a second broad shoulder at around 18.4 eV (exp. 18.5 eV [1]). Beyond 18.4 eV the intensity monotonically decreases to zero. As can be seen in Fig. 3.3 the spectrum of the 8-water molecule box is not size-converged. However, the essential features are similar to those of the 27-box. The first absorption band is shifted upwards by about 0.1 eV, the global maximum is stretched by 0.5 eV, and for higher-lying excitations a shift of up to 1.2 eV in the larger cell is observed. The agreement with the measured spectrum is considerably improved with the larger supercell containing 27 molecules. The observed blue-shift of the main features of the calculated absorption spectrum of the 27-water box with respect to the 8-water box is mainly due to reduction of finite size errors introduced by the periodic boundary conditions. An important question is whether the present results are converged regarding the cell size, as GW/BSE calculations for a 64-water box in the 20

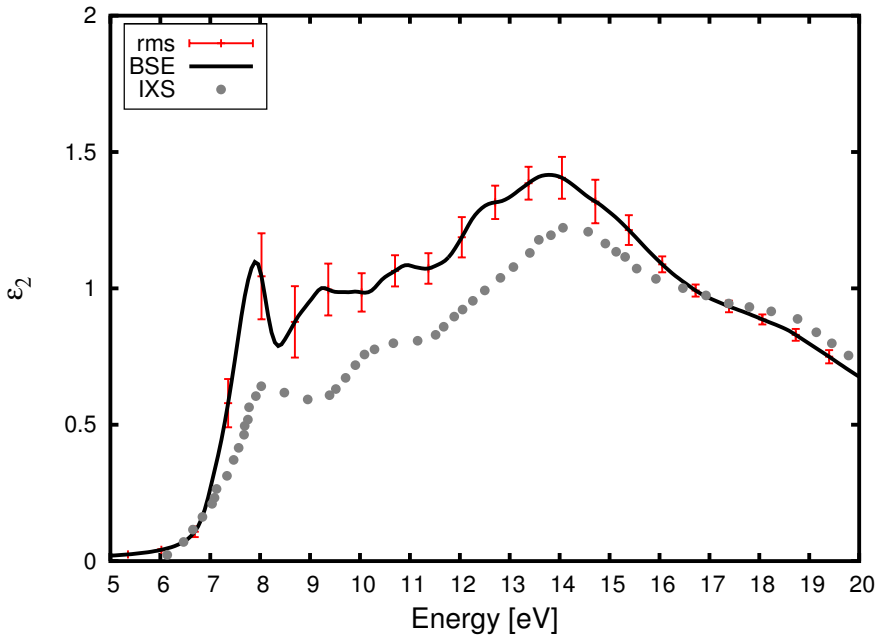

Figure 3.2: G_0W_0-BSE absorption spectra for 30 configurations of the 27-molecule box; A Gaussian broadening of the calculated peaks with a half-width of 0.3 eV has been applied. The calculated spectra are compared to IXS measurements [1].

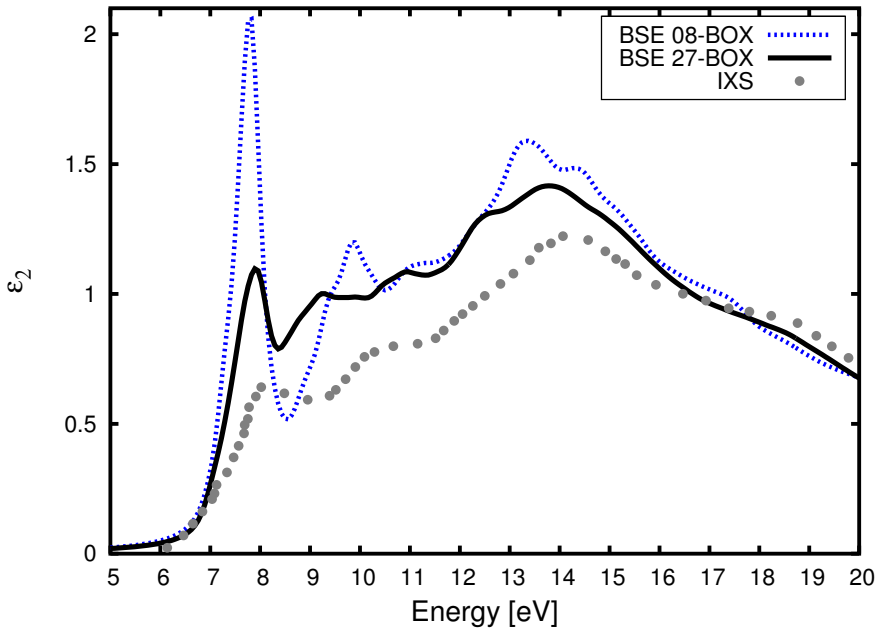

Figure 3.3: G_0W_0-BSE absorption spectra averaged over 30 configurations for 8- and 27-molecule boxes. The calculated spectra are compared to IXS measurements [1].

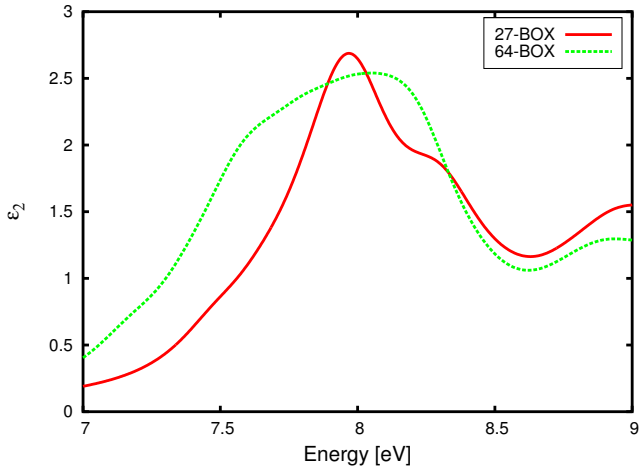

Figure 3.4: Comparison of the first absorption band calculated for the 27- and 64-cells for one configuration.

eV energy range are presently not possible due to drastically increased computational cost as the GW/BSE parameters have to be scaled up considerably for all water trajectories, i.e. a large number of pseudo potential (PP) projectors (depending on the number of atoms) for non-local PP contributions in the computation of dipole matrices should be calculated explicitly, and a 2x2x2 Brillouin zone k-grid sampling is still mandatory for convergence of quasi-particle energies and optical spectra in the 64-cell water. For even more robust results, larger boxes such as 125 or 216-water ensembles would be required but are impossible to treat with the present computer resources.

The position of the first excitonic absorption band located at 7.9 eV is strongly dependent on the GW band gap [4, 5, 25, 26] and electron-hole correlation effects (BSE). GW/BSE contributions are not affected by long-range but mostly by local screening effects, showing the importance of nearest and next nearest water molecules on the electronic and optical structure. This supports the assumption that a larger box, containing for instance 216 molecules, has a minor effect on the band gap and excitonic contributions. Consequently, the position of the first absorption band is hardly altered. To prove this, the quasi-particle band gap of the 64-water ensemble was calculated for a few samples. The obtained band gap of 8.75 eV is very similar to that of the 27-water box of 8.71 eV. If one considers the result obtained for the 64-water box as more precise, it is possible to infer that the position of the first absorption band with respect to the box size is converged. As shown in Fig. 3.4 the location and the magnitude of the first main peak in the 27 and 64-water cells coincide. However, the absorption band of the 64-water cell is broadened. This broadening stems from periodic boundary conditions (PBC) artifacts in the 27-water box. It should be noted that boxes 8 and 27 used in this work are employed for demonstration of changes

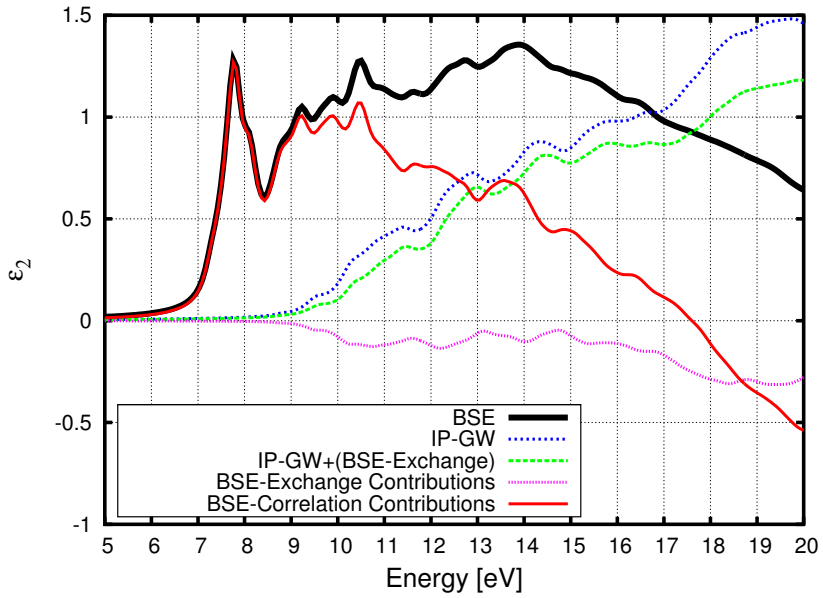

Figure 3.5: For one configuration (27-water box) different contributions to the BSE spectrum are presented. The GW effects from the independent-particle spectrum (blue line), and electron-hole contributions from the difference of TDA-BSE and IP-GW (black line) are illustrated.

over the entire range of energy up to 20 eV with respect to an enhanced environment, and to exhibit a decent cell-size convergence regarding low-, mid- and at least partially in the high-energy area of the spectrum. The positions of excited states are changed by about 0.5 eV in the mid-, and by 1.2 eV in the high-energy range, once a larger 27-water box is taken, due to decrease of PBC artifacts. The low-energy part of the spectrum in the 27- and 64-water boxes is nearly insensitive to the box size beside of a small broadening, providing a strong evidence for the local nature of the electronic band gap and electron-hole contributions. In Fig. 3.5 excitonic and independent particle GW contributions to the spectrum are illustrated. The independent-particle GW spectrum (IP-GW) mainly represents a rigid blue-shift of the IP-DFT spectrum consistent with the increased electronic band gap. By contrast, the excitonic effects introduced by the attractive part of the BSE kernel leads to a red-shift. They have a large contribution to the first absorption band as well as to the high-energy regime of the spectrum. Exchange contributions of the BSE kernel have no major impact on the shape of the IP-G_0W_0 spectrum, beside of a very small blue-shift of about 0.04 eV, and a decrease of spectral weights. Exchange contributions are quite small over the full energy-range. They are responsible for some of the features in the high-energy regime, such as the second shoulder, mixed by G_0W_0 and BSE correlation effects. The Fig. 3.5 illustrates the importance of exciton correlation (attractive part of BS kernel) in formation of the first absorption band.

Table 3.1: S_1 excitation, first absorption band (AB) and exciton binding energies (BE) (in eV) of water are provided in gas and liquid phase based on IP-G_0W_0, IP-G_nW_0 with 5 self-consistent iterations and BSE. The exciton BE is calculated as G_nW_0@BSE subtracted from IP-G_nW_0. Previous works are also given for comparison. The experimental water monomer S_1 energy refers to the adiabatic excitation energy.

	S_1 (gas phase)	S_1 (liq. phase)	First AB (liq. phase)
IP-G_0W_0	12.5	8.7	8.7
G_0W_0@BSE	7.2	5.7	7.9
Exciton BE	5.3	3.0	0.8
G_0W_0@BSE	—	—	7.0 (Garbuio [12])
EOM-CCSD	7.71 (Chipman [21])	—	—
Exp.	7.4 [14]	5.7 [1]	8.1 [1]

Concerning the high energy regime, GW effects start dominating, however, BSE correlation is still of importance as it contributes significantly to the rise of the global maximum at 13.9 eV. The first absorption band is built up entirely upon electron-hole correlation effects (attractive part the of BSE kernel). The first shoulder mainly stems from the BSE correlation accompanied by the GW and small BSE exchange effects. The global maximum is equally due to GW and BSE correlation contributions. The second shoulder is mostly based on GW effects with contributions from negative correlation and exchange contributions of the BSE kernel.

Having verified the significance of various contributions to the liquid water spectrum, now condensation effects on water optical properties are discussed. As outlined in the introduction of this work, the blue-shift of the first absorption band of the water spectrum from gas (7.46 eV) to liquid phase (8.1 eV) of about 0.6 eV has been explained in the previous works based on different approaches. The IP-G_0W_0 spectrum which accounts for electrostatics, exchange and correlation effects (environmental effects) in a non-self-consistent manner, induces a blue-shift on the entire spectrum in comparison to the IP-DFT spectrum. This repulsion or Ry effect (destabilization of the excited state through overlap of diffuse s-wave functions of the surrounding solvent molecules with the excited state) is partially compensated by excitonic effects (pair effects) from BSE, resulting in a red-shift. The excitonic effects are much larger in the gas phase than in liquid phase due to smaller screening, as shown in Fig. 3.6 for the IP-G_0W_0 spectrum of the water monomer. Therefore, the amount of screening contained in G_0W_0 and BSE gives rise to the observed total shift on the ab-

sorption band from gaseous to liquid phase, as it decreases the electronic band gap of the water monomer from 12.5 eV to 8.7 eV in liquid water in the G_0W_0 method. The enhanced screening in the condensed phase delocalizes the exciton associated with the first absorption allowing for an effective interaction of the electron-hole pair with the surrounding water solvent shells. Thus, a mixture of reduction of the G_0W_0 band gap due to enhanced screening and excitonic effects in condensed phase results in the total red-shift of the S_1 excitation energy of liquid water from 8.7 eV to 5.7 eV (Urbach tail) in the BSE spectrum relative to the IP-G_0W_0 spectrum This effect (the exciton binding energy (BE)) is much larger in the isolated water molecule. The S_1 energy decreases from 12.5 (IP-G_0W_0) to 7.2 eV (BSE). The electronic band gaps, excited state energies as well as exciton binding energies are compiled in Table 3.1 for molecular and liquid water.

The excitonic red-shift is about 3 eV in case of liquid water and 5.3 eV for the isolated water molecule. Despite these large excitonic contributions for isolated water, its S_1 energy is not lower than the onset of liquid water's optical gap. This is due to the larger G_0W_0 band gap of the water monomer of 12.5 eV. This suggests that the red-shift of the S_1 energy and blue-shift of the first absorption band of liquid water relative to the S_1 energy of the water monomer depends on a counterbalance of the G_0W_0 and excitonic effects, in other words the decrease of the electronic band gap (-3.8 eV) is much larger than the decrease of the exciton binding energy from gas to liquid phase (-2.3 eV). Therefore, the first absorption band of liquid water is blue-shifted due to decreased exciton binding energy allowing for an enhanced and efficient interaction of the bound electron-hole pair with the surrounding water molecules through the self-energy. On the contrary, the S_1 state of liquid water (Urbach tail) is red-shifted with respect to the S_1 state of the water monomer, despite having a lower exciton binding energy than S_1 of the water monomer. This is due to the reduction of electronic band gap of liquid water as a result of enhanced inter-molecular interactions (screening) upon condensation.

To give an illustration of the blue-shift of liquid water, energetic composition (transition profile) of liquid water excited states is investigated. The electronic transition profiles of selected excited states for one water configuration are presented in Fig. 3.7. The contributions shown in Fig. 3.7 represent the energy-dependent amplitudes of quasi-particles (QP) transitions to the associated excited state, providing information about the character of the excited states. The weights of inter-band QP transitions show that mainly one QP transition (HOCO-LUCO) contributes to the excitonic state S_1 at 7.3 eV, 5-6 QP transitions from a wide energy range between 9 and 12 eV participate in S_{12} at 7.9 eV (the first maximum), and several QP transitions in form of one broad single Lorentzian peak in the range of 11–13 eV contribute to S_{752} at 10.6 eV (the third maximum). The transition

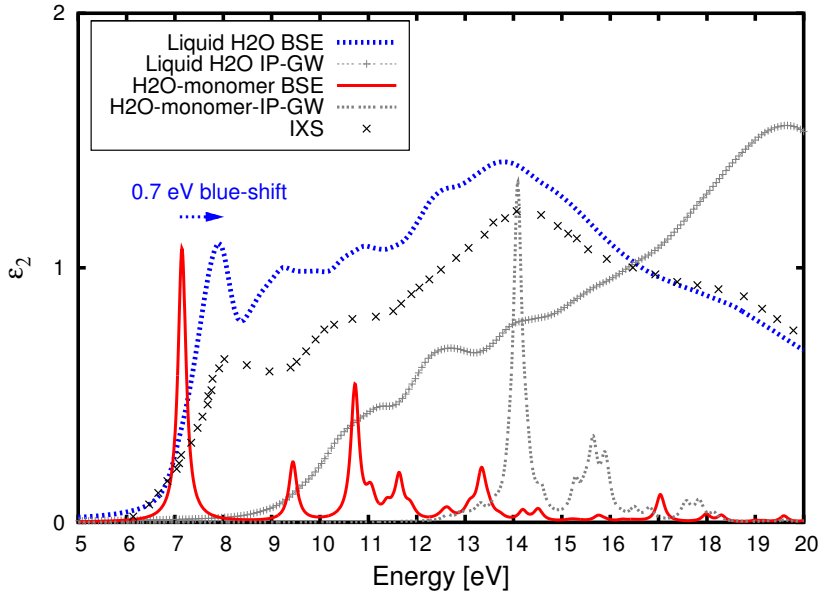

Figure 3.6: The net blue-shift of the first absorption band of water from gas to liquid phase of about 0.7 eV due to the counterbalance of single-particle (repulsive) and excitonic effects (attractive) is illustrated. The spectra of water in gaseous and liquid phase without excitonic effects are shifted by up to 7 eV and 3 eV to higher energies, respectively.

profile indicates that the blue-shift of the first absorption band is strongly connected to the change of the character of the excited states following emergence of multiple QP peaks at 7.9 eV.

The change of the character of the excited states is further visualized by the exciton density distribution. Visualization of the exciton density distribution is of particular interest, as it describes the degree of localization of the excited states in dependence of photon energy. As shown in Fig. 3.8 a highly anisotropic and – in particular for the S_1 state at 7.3 eV – localized exciton distribution on a single water molecule, upon excitation is observed. Localization of the exciton density of the S_1 state, essentially within one water molecule, shows that the excitation is mainly of intra-molecular type, with localized valence character containing some small additional Ry contributions. The S_{12} state at 7.9 eV is more delocalized with an exciton binding energy of 0.8 eV. The higher-lying excited states are even more delocalized, in line with the picture of quasi-free conduction band electrons. The exciton density distribution from S_1 to S_{752} delocalizes upon increase of excitation energy. Thus, the blue shift of the first absorption band indeed reflects a change of nature of the excited state in terms of delocalizing exciton distribution, with a character changing from valence to Ry to a fully free electronic state.

It should be noted that the S_1 state of liquid water for the selected water configuration

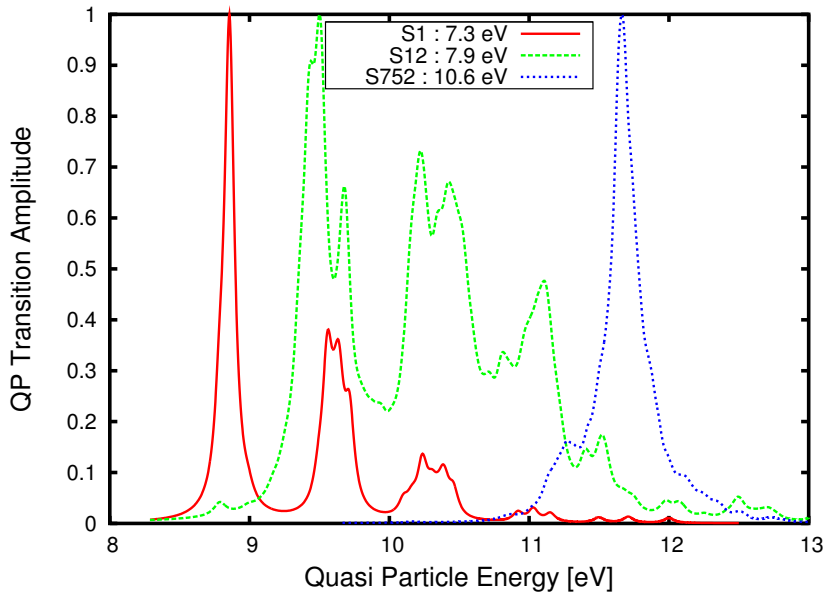

Figure 3.7: The amplitudes of quasi-particle energies to the excitonic states S_1, S_{12} and S_{752} for a selected configuration of the 27-water box are shown. The change of the character of the excited states is apparent as the number of peaks changes upon increase of excitation energy. For S_1, mainly a sharp narrow peak followed by smaller peaks from higher energy regimes is emerged. In case of S_{12}, a collection of peaks distributed over a relatively wide energy range (9-12 eV) is observed. This is a significant change in the transition profile and hence the character of S_{12} in comparison to S_1. At energies near the vertical ionization energy of liquid water, a single broad peak is observed, indicating at approximately homogeneous exciton density distribution over nearly all water molecules in S_{752}.

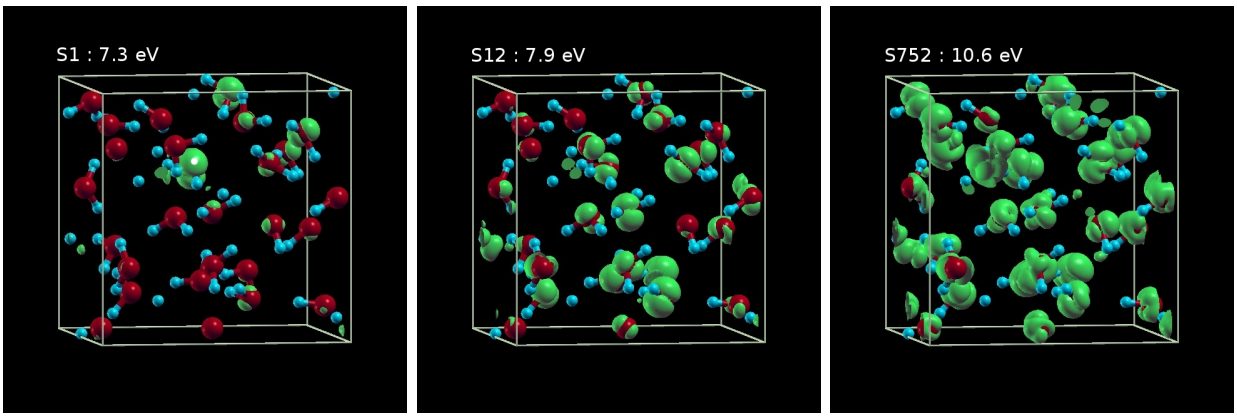

Figure 3.8: Exciton density distribution of liquid water (27-water box) at 7.3 (S_1), 7.9 (S_{12}) and 10.6 eV (S_{752}) for a selected configuration. The S_1 state of liquid water for the selected water configuration is higher than that of the S_1 state of the water monomer due to the chosen water snap-shot. The localization of distributions decreases toward higher energies. The hole is fixed on the oxygen atom indicated by the white sphere near the center of the box.

is higher than that of the S_1 state of the water monomer. This is because of the chosen water snap-shot. The S_1 state for other water configurations was calculated and found to be clearly at lower energies than the S_1 state of the water monomer.

Discussion

The results of Garbuio [12] based on the same MBPT as applied in the present study show substantial deviation from experimental and the present results. In particular, the first absorption band is more than 1 eV off the experimentally measured band and an artificial double peak located between 8.4-8.7 eV appeares which is not observed experimentally. In the following the reliability of approximations made in the previous study concerning energy positions and intensities of the excited states is checked in order to explain the discrepancies.

1) As previously mentioned, the present calculations of water are based on Born-Oppenheimer ab-initio molecular dynamics simulation for the configuration sampling. A good simulation is of importance as the electronic distribution extremely depends on the structures. Furthermore, Grimme D3 dispersion correction is applied as non-local electron correlation is of high relevance impacting water structures and hence the spectral features. The effect of intra-molecular geometry was analysed in a previous study of water electronic structure [25]. The structural aspects of water such as variation of OH bond length was found to be significant for the band gap. Upon decrease of OH length from 1.0 in SPC/E to 0.957 Å in TIP3P and TIP4P empirical force field potentials, an increase in gap of 0.5 eV has been observed [25]. However, since in the present study Garbuio's water band gap of 8.4 eV can be reproduced in the non-self consistent variant of GW (G_0W_0), it is justified to assume that the overall structural effects are not decisive for the present discrepancies.

2) In this study nuclear quantum effects (NQEs) are neglected. Spura et al. [31] performed path integral molecular dynamics (PIMD) on PBE-D3 water structures and found only slight changes of OH bond lengths and H-O-H angles. The slight change of the water structure upon performance of PIMD support the assumption that NQEs on the electronic band gap are small.

Furthermore, Pham et al. [25] simulated liquid water (64 box) at 390 K in order to recover the experimental structures of liquid water, and hence to capture NQE. They calculated the electronic band gap with many-body perturbation theory. The G_0W_0-PBE band gap is 8.1 eV, however with 0.3 eV total convergence error, neglect of dispersion effects, neglect of non-local pseudo-potential contributions (increasing the gap by about 0.2 eV), sampling of the BZ by the Γ-point only as well as use of a different GW implementation. Summing up the mentioned contributions and reduction of convergence error would result in a gap

which is quite close to the present gap of 8.4 eV in the G_0W_0 approach, indicating a small NQE on the gap. In contrast, in the study of Del ben et al. [32] NQEs cause a sizeable electronic shift by -0.6 eV at DFT-hybrid level. However, the effect of dynamic correlation at G_0W_0 level and GW self-consistency (adding further non-local dynamic electron correlation contributions) on the 0.6 eV reduction of the gap were not taken into account.

In this regard, Shishkin and Kresse [41] have shown for insulators that *scGW* increases the gap. Thus, the increase of the gap by self-consistency and decrease of the gap by NQE cancel each other to some extent leading to a net fundamental gap which is equivalent to the gap calculated at G_0W_0 level of theory on top of PBE-D3 structures. Since it is possible to reproduce the experimental electronic band gap of 8.7 eV with the non-self-consistent GW approach on the PBE-D3 structures, it is safe to further calculate the optical absorption spectrum on top of the G_0W_0@PBE-D3 QP energies. It should be noted that the main effect of reduction or increase of the gap is a red- or blue-shift of the entire spectrum, and has no major impact on the optical weights and hence intensities.

3) In Garbuio's study a constant screening is used in BSE for all configurations to reduce computational cost. According to our result, the low-energy part of the spectrum is relatively insensitive to the use of a constant screening. A red-shift of about 0.1 eV as well as a moderate increase of the intensity of the first absorption band are the main differences. For the mid-range (8.5−10.5 eV) peak magnitudes are increased, and the positions of the peaks are moderately stretched. Regarding higher-energy areas, the spectral features are affected significantly. As illustrated in Fig. 3.9 the global maximum is red-shifted by 1.5 eV, once a screening calculated for a configuration was applied to another one. Thus at high energies, a constant screening induces a compression on the spectrum, and therefore, it should not be applied for mid- and higher-lying excited states as possible modifications of the spectrum over the full energy range depend on the explicit structure of the screening of the individual configurations. Due to the increase of intensities in the range of 5-14 eV a constant screening assignment is an error source for emergence and artificially huge intensity of the peaks. The recommendation is to avoid this approximation, in particular for higher-energy regimes.

4) To account for dynamical effects Garbuio used the plasmon pole approximation (PPA). The quality of PPA is checked for one water configuration. The G_0W_0@PBE approach based on PPA leads to a band gap of 8.3 eV. However, a full frequency-dependent G_0W_0@PBE results in a 8.8 eV gap. As shown in Fig. 3.10, the PPA based G_0W_0-BSE method is capable of describing the features of the standard frequency-dependent G_0W_0-BSE spectrum.

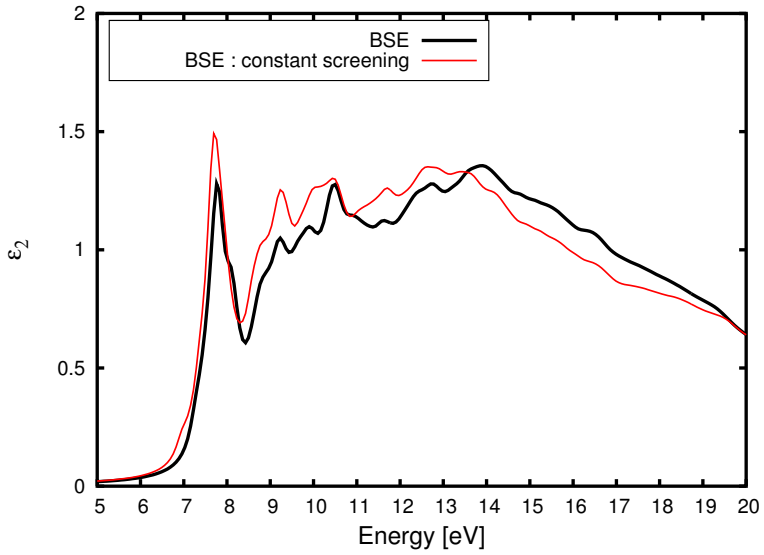

Figure 3.9: BSE spectrum with constant screening approximation versus BSE with own screening for one configuration.

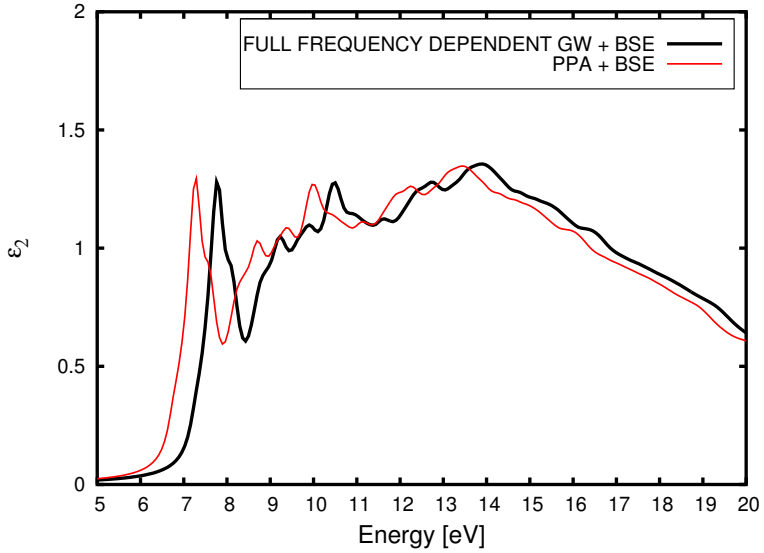

Figure 3.10: The comparison between PPA and full frequency-dependent G_0W_0-BSE is shown.

This 0.5 eV shift of the spectrum to higher energies in Fig. 3.10 is a direct reflection of the increased electronic band gap. Thus, for an accurate calculation of excited states an explicit sampling of dynamical correlation is mandatory. PPA is therefore undoubtedly the main error source explaining the present discrepancy between our and Garbuio's result. It should be emphasized that the general features of the spectrum obtained from full frequency-dependent sampling over the full energy range is nearly one to one reproduced using PPA, which means that PPA is applicable for water with the exception of a constant blue-shift of 0.5 eV. This result is in contrast to the finding of Vinson et al. [34] where the authors present a stretching of the spectrum of about 1 eV in the mid energy range based on many pole self-energy (MPSE) approximation.

5) The impact of a finite simulation cell on energy positions is minor for the energetically low lying states but considerably large for higher lying excited states, as QP energies are subject to finite size effects. The insensitivity of the position of the first absorption band regarding size of the box is investigated by GW/BSE calculation on an even larger 64-water box for one configuration. As shown in Fig. 3.4, no position change concerning the first absorption band is observed, confirming that the 27-water box is a reasonable model for low- and to a large degree for high-energy regimes.

6) The neglect of the commutator of the non-local pseudo potential V_{nl} with the position operator r in the optical limit in the course of calculation of dipole matrices in BSE enhances the intensities over the entire range of energy, and in particular for the first absorption band giving rise to a very intense peak, as illustrated in Fig. 3.11. Furthermore, a blue shift of 0.2 eV for all energy regimes is observed, once non-local pseudo potential contributions are excluded. Therefore, for optical properties explicit calculation of the commutator $[V_{nl}, r]$ is of importance to obtain the correct spectral weight distributions.

7) Regarding the higher-energy regime, the missing weight in Tavernelli's work [11] at 18.6 eV due to the use of a semi-local exchange-correlation functional is restored using an advanced non-local BS kernel. Furthermore, a pronounced artificial peak at around 21 eV arises. At this energy area the experimental spectrum has a monotonically decreasing behavior which is correctly reproduced in our study.

8) In the work of Hermann et al. [10] the water spectrum is described purely through electrostatic effects by embedding a water monomer in a dynamic array of dipole fields. Due to the use of a fit parameter for adjustment of the magnitude of the electrostatic dipole field, Hermann obtained transitions at correct energies but with totally unsatisfactory spectral weight distributions (for instance, the global maximum has the lowest weight of all peaks).

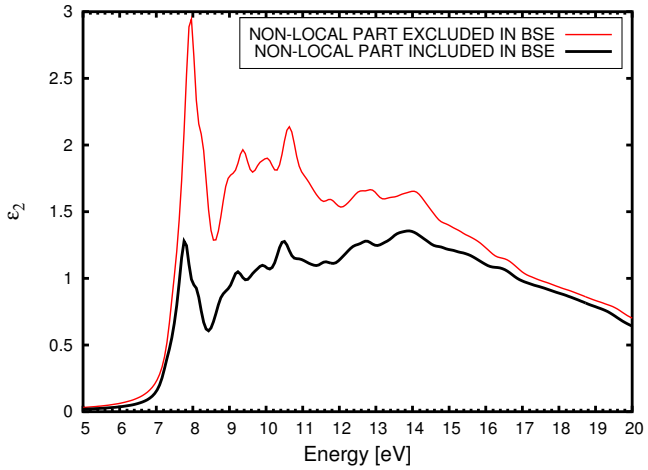

Figure 3.11: Non-local part of the pseudo-potential excluded versus included in the G_nW_0-BSE optical spectra for a 27-water box. Exclusion of non-local parts induces an intense first absorption peak, accompanied by a blue-shift of 0.2 eV.

Furthermore, this concept of embedding a water monomer in an electrostatic environment offers no reliable and comprehensive information about the nature, character, localization and importance of specific contributions such as single-particle and electron-hole effects in build up of excited states due to lack of explicit inclusion of many-body effects. This simple model calculation was however used to explain the water blue-shift from gas to solid phase. According to the present results, the shift and the correct spectral weights distribution are a product of the interplay of electron-electron and electron-hole interactions.

9) The coupling effect on the optical spectrum obtained with BSE calculations is investigated by going beyond the frequently applied Tamm-Dancoff approximation (TDA). It was shown that in case of finite systems coupling of resonant and anti-resonant parts of the BS matrix result in dramatic modification of the spectrum [35]. Since liquid water is at the same time a molecular and extended system, it is of particular interest to check the validity of the TDA. As shown in Fig. 3.12. coupling effects do not impact the BSE spectrum, and thus the occurring red- and blue-shift of the excited state in the condensed phase are fully independent of the coupling effects. This once again confirms that the TDA is a reliable approximation for periodic systems.

The above analysis shows that only a proper capture of the frequency-dependent dynamical effects, environmental interaction (by the many-body self-energy), individually calculated screening, finite size and structural effects provide significantly less biased results for the water optical spectrum over a wide range of energy up to 20 eV. As demonstrated above, accurate calculation of single-particle energies with an individually calculated screening in

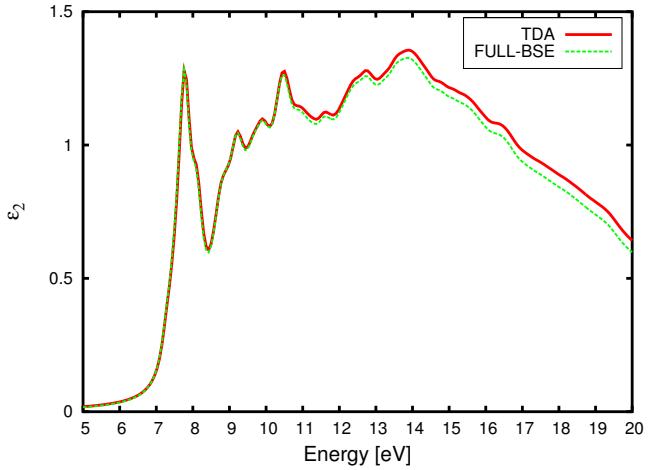

Figure 3.12: The liquid water spectrum is over wide energy range insensitive to the coupling effects of BSE.

G_0W_0@BSE on the 27-water cell improves the location of the first absorption band by up to 0.9 eV to 7.9 eV (exp. IXS: 8.15 eV) with respect to the Garbuio's result of 7.0 eV. Moreover, the shift of the first absorption band to 7.9 eV decreases its exciton binding energy from 1.4 eV in Garbuio's work to 0.8 eV in this study.

Conclusions

The calculated electronic structure of liquid water, employing the GW methodology and periodic boundary conditions, is nearly insensitive to the cell size. Therefore, it is concluded that disorder effects are short-range in nature and that the electronic structure is influenced mostly by nearest or next-nearest water neighbors. The essential features of the spectrum are also reproduced with a small 8-water molecule cell. The changes of the peaks from 8- to 27-water molecule cell by 0.1, 0.5 and 1.2 eV stems from structure effects due to periodic boundary conditions. The small changes regarding the location of the first absorption band between 8-, 27- and 64-molecule cells indicate that size-convergence is reached with a decent accuracy.

The liquid water spectrum is massively affected by excitonic effects, in particular in the low- and mid-energy area. Higher lying excited states are more subject to single-particle than excitonic effects. It is further observed that condensation leads to a splitting of the monomer S_1 state, containing excited states lower than the water monomer S_1 energy and those lying at higher energies due to many-body effects.

The degree of localization and anisotropy of the exciton density distribution decreases with increasing excitation energy. The lowest excited state is essentially localized on a single water molecule, exhibiting an intra-molecular valence character. Upon increase of excitation energy a change of the character to Ryization occurs, responsible for the observed blue-shift of the first absorption band. Furthermore, these character changes of the excited states are fully independent of coupling contributions in the Bethe-Salpeter matrix.

Bibliography

[1] H. Hayashi, N. Watanabe, Y. Udagawa, and C.-C. Kao, Proc. Natl. Acad. Sci. U. S. A. **97**, 6264-6266 (2000).

[2] Y. Ozaki, Y. Morisawa, A. Ikehata, and N. Higashi, Appl. Spectrosc. **66**, 1-25 (2012).

[3] C. G. Elles, C. A. Rivera, Y. Zhang, P. A. Pieniazek, and S. E. Bradforth, J. Chem. Phys. **130**, 084501 (2009).

[4] H. Buiteveld, J. M. H. Hakvoort, and M. Donze, in SPIE Proceedings on Ocean Optics XII, edited byJ. S. Jaffe (SPIE digital library, 1994), Vol. **2258**, pp. 174-183.

[5] M. R. Querry, D. M. Wieliczka, and D. J. Segelstein, Handbook of Optical Constants of Solids II (Academic Press, 1991), pp. 1059-1077.

[6] K. Kobayashi, J. Phys. Chem. **87**, 4317-4321 (1983).

[7] G. M. Hale and M. R. Querry, Appl. Opt. **12**, 555-563 (1973).

[8] P. C. do Couto and D. M. Chipman, J. Chem. Phys. **137**, 184301 (2012).

[9] A. Hermann and P. Schwerdtfeger, Phys. Rev. Lett. **106**, 187403 (2011).

[10] A. Hermann, W. G. Schmidt, and P. Schwerdtfeger, Phys. Rev. Lett. **100**, 207403 (2008).

[11] I. Tavernelli, Phys. Rev. B **73**, 094204 (2006).

[12] V. Garbuio, M. Cascellai, L. Reining, R. D. Sole, and O. Pulci, Phys. Rev. Lett. **97**, 137402 (2006).

[13] P. Hahn, W. Schmidt, K. Seino, M. Preuss, F. Bechstedt, and J. Bernholc, Phys. Rev. Lett. **94**, 037404 (2005).

[14] R. Mota, R. Parafita, A. Giuliani, M.-J. Hubin-Franskin, J. Lourenco, G. Garcia, S. Hoffmann, N. Mason, P. Ribeiro, M. Raposo, and P. Limao-Vieira, Chem. Phys. Lett. **416**, 152-159 (2005).

[15] T. Goulet, A. Bernas, C. Ferradini, and J.-P. Jay-Gerin, Chem. Phys. Lett. **170**, 492-496 (1990).

[16] J. VandeVondele, F. Mohamed, M. Krack, J. Hutter, M. Sprik, and M. Parrinello, J. Chem. Phys. **122**, 014515 (2005).

[17] J. VandeVondele, M. Krack, F. Mohamed, M. Parrinello, T. Chassaing, and J. Hutter, J. Comput. Phys. Commun. **167**, 103-128 (2005).

[18] J. P. Perdew, K. Burke, and M. Ernzerhof, Phys. Rev. Lett. **77**, 3865-3868 (1996).

[19] D. R. Hamann, Phys. Rev. B **55**, 10157-10160 (1997).

[20] S. Grimme, J. Antony, S. Ehrlich, and H. Krieg, J. Chem. Phys. **132**, 154104 (2010).

[21] P. Giannozzi et al., J. Phys.: Condens. Matter **21**, 395502 (2009).

[22] A. Marini, C. Hogan, M. Gruening, and D. Varsano, Comput. Phys. Commun. **180**, 1392-1403 (2009).

[23] A. Bernas, C. Ferradini, and J.-P. Jay-Gerin, Chem. Phys. **222**, 151-160 (1997).

[24] L. R. Painter, R. N. Hamm, E. T. Arakawa, and R. D. Birkhoff, Phys. Rev. Lett. **21**, 282–284 (1968).

[25] T. Anh Pham, E. S. Cui Zhang, and G. Galli, Phys. Rev. B **89**, 060202 (2014).

[26] M. Govoni and G. Galli, J. Chem. Theory Comput. **11**, 2680-2696 (2015).

[27] F. Bruneval, J. Chem. Phys. **142**, 244101 (2015).

[28] I. D. Denis Jacquemin and X. Blase, J. Chem. Theory Comput. **11**, 5340-5359 (2015).

[29] F. Bruneval, https://github.com/bruneval/molgw, 2015.

[30] R. A. Kendall, T. H. Dunning, Jr., and R. J. Harrison, J. Chem. Phys. **96**, 6796 (1992).

[31] T. Spura, C. John, S. Habershon, and T. D. Kühne, Mol. Phys. **113**, 808-822 (2015).

[32] M. Del Ben, J. Hutter, and J. VandeVondele, J. Chem. Phys. **143**, 054506 (2015).

[33] M. Shishkin and G. Kresse, Phys. Rev. B **75**, 235102 (2007).

[34] J. Vinson, J. J. Kas, F. D. Vila, J. J. Rehr, and E. L. Shirley, Phys. Rev. B **85**, 045101 (2012).

[35] M. Grüning, A. Marini, and X. Gonze, Nano Lett. **9**, 2820-2824 (2009).

3.2 Large many-body effects in liquid NH_3 spectrum

Abstract

In the following, the absorption spectrum of liquid ammonia is calculated up to 13 eV using again the many-body perturbation approach applied in the previous section. The electronic band gap of liquid NH_3 (exp. $\Gamma \rightarrow \Gamma$: 7.8 - 8.0 eV [1]) is perfectly described by the energy-only self-consistent approach G_nW_n (7.99 eV), both in the Green's function G and the dynamically screened interaction W. The same ansatz as in chapter 3.1, i.e. the non-self-consistent G_0W_0 method leads to a considerable underestimation of the experimental gap by up to 1.7 eV for liquid ammonia. This can be traced backed to the possible inaccurate description of liquid ammonia structures by the PBE + D3 method in the molecular dynamics simulation or screening effects which depend on the electronic distribution. However, the latter is likely the correct answer based on the many-body calculations on the experimental crystalline ammonia. In order to counter band gap underestimation in liquid ammonia by the G_0W_0 approach, a self-consistent eigenvalue scheme G_nW_n is now employed to be able to reproduce the experimental band gap. With respect to the NH_3 optical properties, the entire spectrum, in particular the low-lying first absorption band, is extremely affected by electron-hole interactions, leading to a fundamental redistribution of spectral weights of the independent-particle spectrum. Three well separated but broad main peaks are identified at 7.0, 9.8 and 11.8 eV with steadily increasing intensities in excellent agreement with the experimental data [1]. Furthermore, a large net blue-shift of the first absorption peak of about 1.4 eV is observed from gaseous to liquid phase as a direct consequence of many-body effects, which lead to a delocalization of the associated liquid ammonia absorption band exciton and to an increase of the repulsion effects imposed by the surrounding solvent shells. The spectrum is insensitive to the coupling of resonant and anti-resonant contributions as also found for liquid water.

Introduction

As mentioned in the previous section, accurate ab-initio calculation of quasi-particle and optical excitation energies is of utmost importance to reliably predict the absolute position of the excited states. Since the G_0W_0 and G_nW_0 on top of the PBE orbital energies and wave functions considerably underestimates the QP-gap of liquid NH_3 due to screening effects, the full energy-only self-consistent G_nW_n method is employed to further decrease the initial screening or in other words to increase the exchange effects. This ansatz improves the description of the QP-gap which is now in excellent agreement with the experimental gap, as shown in the following.

Technical details

A cubic box of side length of 10.3391 Å containing 27 NH_3 molecules (108 atoms in the unit cell) is used. Under periodic boundary conditions by using the CP2k program package [14] a Born-Oppenheimer molecular dynamics simulation of 15 ps productive run is performed after having equilibrated the ammonia box for 5 ps. The molecular dynamics simulation is based on the same PBE-D3 method as used for water. The simulation is performed in the NVT ensemble at 193 K at a density of 0.6903 g/cm^3. A cutoff of 400 Ry is used for the density whereas the electronic wave function is expanded by atom-centered optimized double zeta with polarization quality basis set (ODZVPP). Due to the disordered nature of the system, 30 independent configurations are selected over which results are averaged. For each snapshot a ground-state calculation with 14 special k-points in the irreducible Brillouin zone (IBZ), and a cutoff of 100 Ry is carried out using QUANTUM ESPRESSO [11]. The effect of core electrons is treated by norm-conserving Troullier-Martins pseudo-potentials [18]. BSE calculations are performed in the regime of vanishing momentum transfer q $\rightarrow$ 0 using YAMBO [12]. The G_nW_n method is run on top of the Kohn-Sham (KS) orbital energies and wave functions for each independent configuration. The dielectric function is further sampled by 30 frequency points. The screening is calculated individually for each snapshot with 512 bands in the polarization and Green's function. A cutoff of 50 and 8 Ry for the exchange and correlation part of the self-energy is set, respectively, to converge the QP-energies within 0.02-0.03 eV accuracy. In the optical response calculations (BSE) 181 transition bands are considered with 81 occupied and 100 unoccupied bands for accurate spectral weight distributions and hence reliable relative intensities. In the case of molecular NH_3, a box of side length of 30 Bohr is used, and further the Coulomb cutoff technique by Varsano et al [18] is applied to avoid artificial screening of the periodic images of the isolated NH_3 molecule. For the polarization and Green's function 750 bands with a dielectric matrix cutoff of 2500 G vectors, and 150000 exchange components are used. The dynamical character of the dielectric function is sampled by 100 frequency points. Due to extreme dependency of the position of the first absorption peak of the molecular NH_3 (S_1) on the number of transition bands in the BSE, a large number of transition bands is mandatory. Convergence is reached with 500 transition bands with an accuracy of 0.02 eV for the S_1 energy. All BSE calculations are performed in the static adiabatic limit and within the Tamm-Dancoff approximation (TDA). The S_1 state of the NH_3 monomer is negligibly affected by the TDA.

Results and discussion

In Table 3.2 an overview of the applied methods for calculations of the electronic band gap is given. As expected, the PBE functional is not able to capture the many-body physics

Table 3.2: The averaged electronic band gap of liquid ammonia is given for the 27-box in eV at the PBE, G_0W_0, G_nW_0, G_nW_n as well as the experimental gap of amorphous solid ammonia [1] which is an alternative experimental reference for liquid ammonia due to lack of experimental data.

Fundamental band gap of liquid NH_3	$\Gamma \rightarrow \Gamma$
PBE	3.52
G_0W_0@PBE	6.32
G_nW_0@PBE	6.67
G_nW_n@PBE	7.99
Experiment	7.8–8.0 [1]

properly (fundamental band gap : 3.52 eV), and hence massively underestimates the experimental gap. The non-self consistent GW variant (G_0W_0) with an explicit frequency sampling of the dielectric function on top of the PBE reference wave functions and energies opens up the gap to 6.32 eV. However, the G_0W_0@PBE gap still underestimates the experimental gap of 7.8 eV considerably. The underestimation of the PBE and G_0W_0@PBE gap might be due to inaccurate description of liquid ammonia structures (bond lengths and angles) by the PBE + D3 method in the molecular dynamics simulation. However, G_0W_0@PBE calculation on the crystalline ammonia based on the experimental structure (due to lack of experimental references for liquid ammonia) showed a band gap of 7.02 eV, and much smaller than the experimental gap of the amorphous solid ammonia (8.0 eV). It should be noted that the experimental gap of the ordered crystalline phase should be larger than the amorphous solid ammonia due to absence of disorder effects, and hence further decreasing of the accuracy of the G_0W_0@PBE method is expected. This observation strongly suggests that screening effects in liquid ammonia are different than in liquid water, even if the number of the electrons are equal. The difference in the impact of screening effects is due to a distinct electronic distribution in both systems. The underestimation of the electronic gap consequently gives rise to underestimated excitation energies. Thus, in order to improve the gap, the partial self-consistent G_nW_0 is applied, where the initial screening is fixed at the mean-field level. The G_nW_0 increases the gap only by 0.35 eV, and hence still the underestimation is large. This can be further improved by performing full energy-only self-consistent G_nW_n method to decrease the effect of the PBE-screening. As compiled in Table 3.2 a converged gap of 7.99 eV is obtained after 5 iterations.

In Fig. 3.13 the density of states (DOS) of liquid NH_3 is illustrated including perturbatively corrected QP energies within the GW approximation. The QP corrections result in an increase of the splitting of unoccupied and occupied bands with the valence band top being less affected, both with respect to position and magnitude. The DOS of liquid

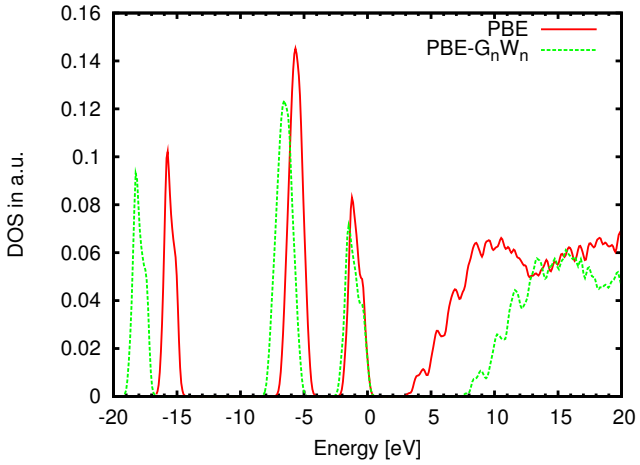

Figure 3.13: Density of states (DOS) of liquid ammonia based on PBE and G_nW_n@PBE level of theory.

NH_3 consists of highly localized occupied bands while the unoccupied states are delocalized. The magnitude of the occupied G_nW_n@PBE DOS is slightly reduced due to changes in QP-energies but also slightly broadened with respect to its PBE pendant, while it is nearly identical for unoccupied DOS between PBE and G_nW_n@PBE, however, the latter is significantly upshifted. In Fig. 3.14 the calculated optical absorption spectra are presented and compared to an experimental spectrum of amorphous solid ammonia [1] due to lack of experimental data for liquid ammonia. It however represents a reasonable alternative experimental reference for liquid ammonia due to its disordered structure.

The spectrum consists of three well separated broad bands. The first main peak is located at 7.0 eV, followed by peaks at 9.8 and 11.8 eV with increasing intensities. Interestingly, the correct asymmetry of the first main peak is fully captured by BSE. The IP-G_nW_n spectrum which is equivalent to a photo-electron spectrum fully misses the first main band due to lack of excitonic effects. However, once the electron-hole interaction is introduced, the IP-G_nW_n spectrum gets red-shifted with a fundamental redistribution of spectral weights. The peak at 7.0 eV is a bound excitonic peak lying below the electronic gap with an exciton binding energy of 1.0 eV, indicating that the exciton associated with the first absorption band is not tightly bound, and to some extent distributed over the nearest and next nearest NH_3 molecules, with which it then effectively interacts. This repulsive interaction with the surrounding NH_3 molecules leads to a net blue-shift of the first main peak of about 1.4 eV with respect to the S_1 energy of the isolated NH_3 molecule at 5.6 eV as shown in Fig. 3.15. The experimental 0-0 transition of the isolated NH_3 molecule is 5.7 eV.

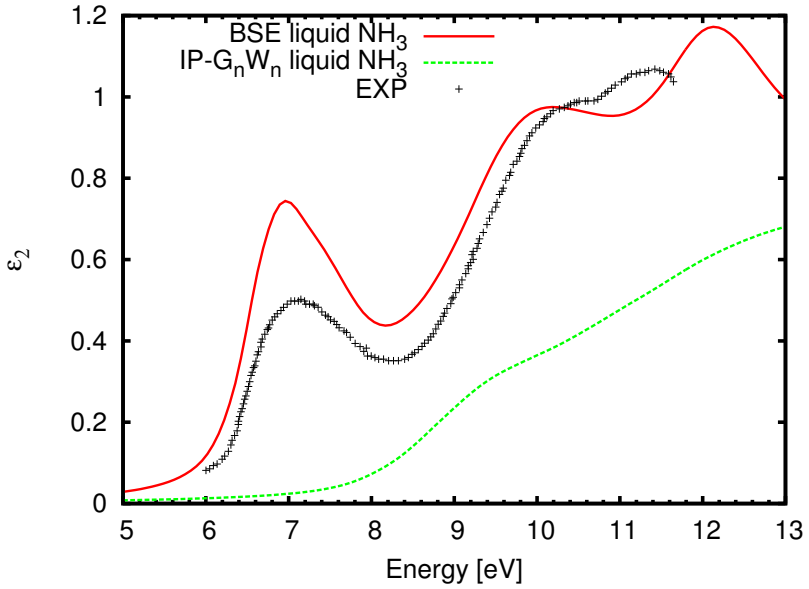

Figure 3.14: BSE (red) and nearly structureless IP-G_nW_n(green) optical absorption spectrum of liquid ammonia. Black dots are the experimental data of amorphous solid ammonia [1].

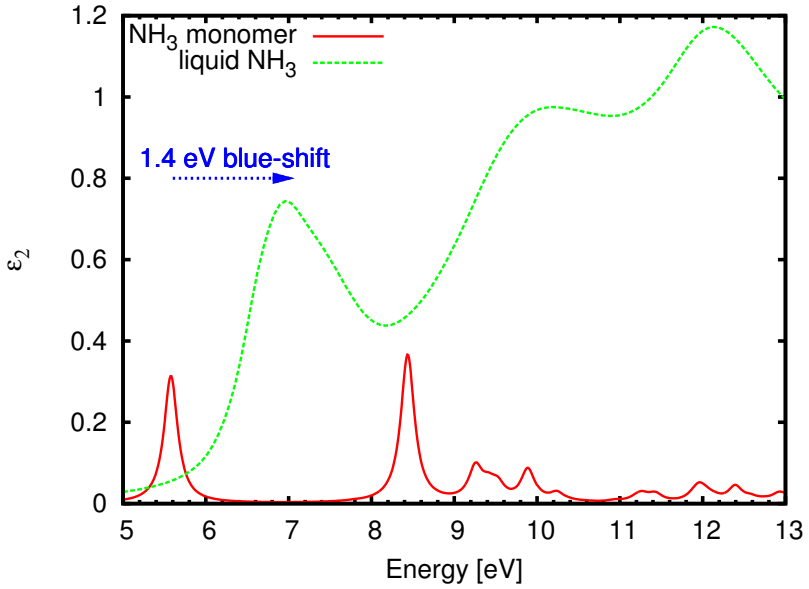

Figure 3.15: BSE spectra of ammonia monomer (red) and liquid ammonia (green) are presented. For better comparison the intensities of the ammonia monomer spectrum is scaled by a factor of 10; however the first monomer peak at 5.6 eV has a low but non-zero oscillator strength.

The blue-shift in liquid ammonia is larger by about 0.7 eV in comparison to the previously studied blue-shift in liquid water from gaseous (GW+BSE : 7.2 eV) to liquid phase (GW+BSE : 7.9 eV) [25] although the hydrogen bond is weaker in liquid NH_3, indicating that approaches explaining the shift based on hydrogen bond network effects [21] are at least incomplete. From the many-body perspective the occurring blue-shift is a direct consequence of an interplay between Pauli repulsion and excitonic effects. It can be explained in terms of enhanced overlap of the excitonic (excited) state with diffuse s-wave functions of the surrounding NH_3 molecules. An overlap without excitonic effects leads to the IP-G_nW_n spectrum, however, the destabilization of the excited state following overlapping with Rydberg wave functions is partially counterbalanced by electron-hole correlation effects resulting in a net blue-shift of 1.4 eV. Therefore, correlated motion of electron and hole (e-h) while interacting with its surrounding is key for an explanation of the observed net blue-shift of the main first band. In other words, the 1.4 eV blue-shift is due to the more extended electron distribution in liquid than gas-phase ammonia, which leads to a reduced e-h binding energy. As can be seen in Fig. 3.16, the electronic density of the first absorption band considerably delocalizes over the nearest and next nearest ammonia molecules to effectively overlap with the diffuse states of the surrounding molecules. In case of zero e-h binding energy, the electron freely moves around and interacts with solvent spheres giving rise to the IP-G_nW_n spectrum which is a reflection of the full Pauli exchange effects. Furthermore, beside of the blue-shift in the low energy part of the spectrum, many-body effects are of importance over the full energy range as with respect to the higher energy regimes excitonic effects are decisive for building up important features of the liquid NH_3 spectrum (peaks at 9.8 and 11.8 eV) together with single-particle effects which are increasingly contributing upon increasing energy.

A further important property of liquid NH_3 is the frequency-dependent dielectric constant obtained from the real part of the macroscopic dielectric function. This quantity shown in Fig. 3.17. describes the response of the electronic degree of freedom of the solvent spheres to photo-excitation or in other words a fast electronic response to external perturbation. The static dielectric constant sets on at about 1.4 and peaks at 6.9 and 9.5 eV. Therefore, liquid NH_3 is quite responsive in the energy range of 6-10 eV to photo-excitation, however ϵ_1 considerably decreases at higher energy regimes. From the many-body point of view, liquid ammonia is similar to liquid water [23, 25]. In both systems strong excitonic effects play a decisive role for the appearance of typical features in the optical and electronic response spectrum. Regarding coupling effects in the Bethe-Salpeter transition matrix, it was shown in the previous section for liquid water that mixing of resonant and anti-resonant electron-hole pairs leaves the spectrum unaffected over the full energy range. The same result is also obtained for liquid NH_3. Thus, in contrast to molecular systems [23] where pair and

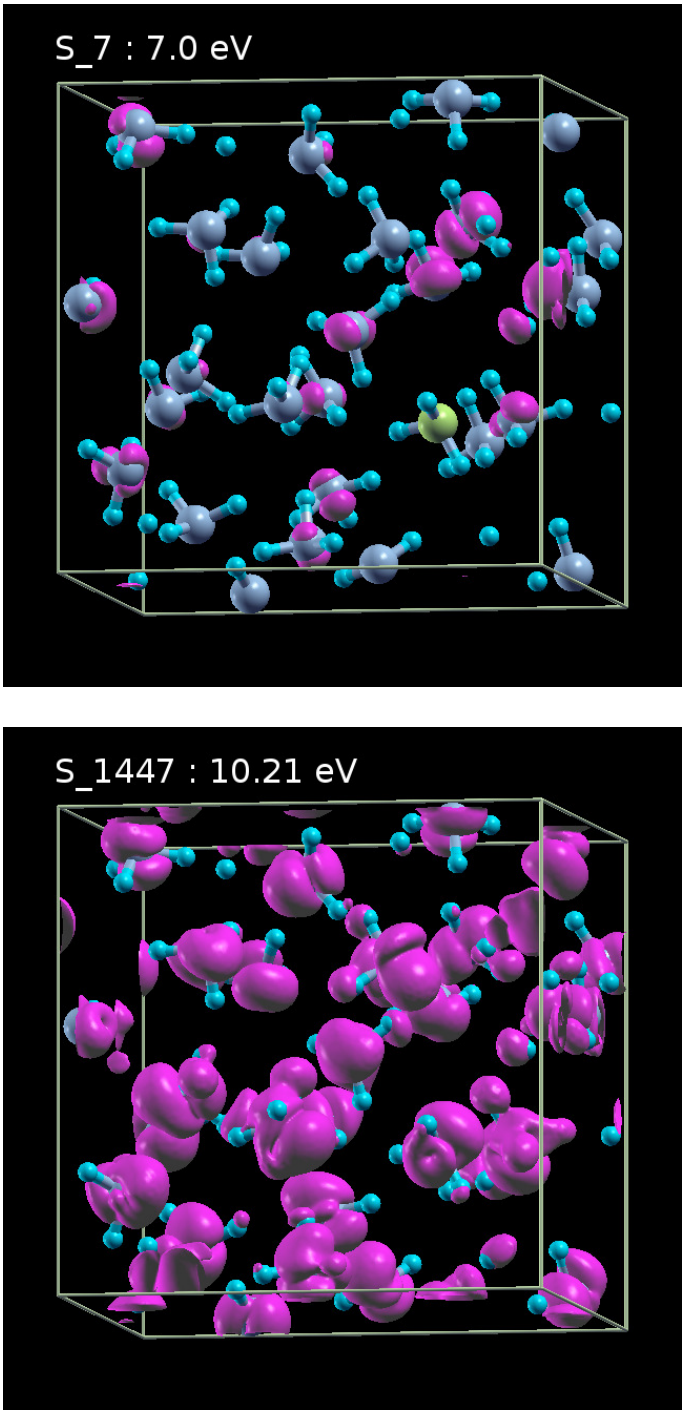

Figure 3.16: Exciton density distribution for the first absorption band (AB) edge at 7.0 eV (left), and the second peak at 10.21 eV (right) for a selected configuration. At the first AB the electronic density is delocalized over the nearest and next nearest ammonia molecules, while at the second peak (at an energy higher than the direct electronic band gap) it is fully delocalized over the whole system, in agreement with the free conduction band electron picture. The hole is indicated by the yellow sphere placed on an N atom.

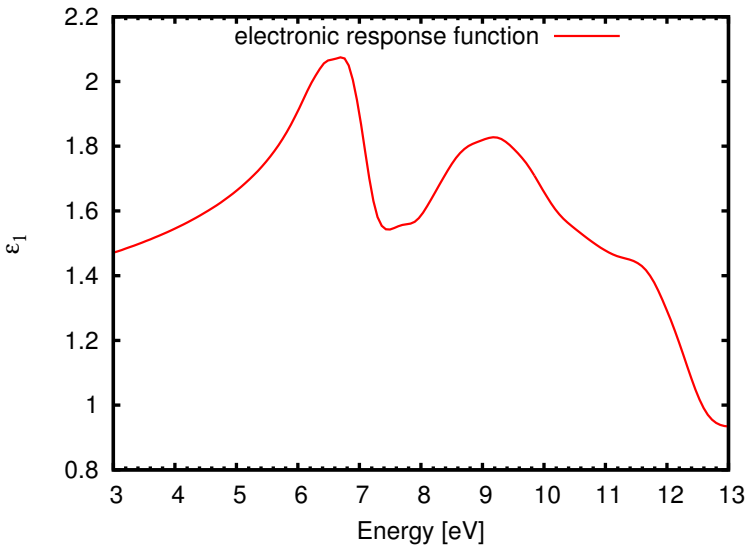

Figure 3.17: The real part of the macroscopic dielectric function of liquid ammonia. The ϵ_1 function has two responsive peaks at 6.9 and 9.5 eV, showing that liquid NH_3 is most sensitive to photo-excitations at energies lower than the electronic band gap.

anti-pair mixing can dramatically reshape spectra, causing exciton-plasmonic excitations, for hydrogen bonded extended molecular systems such a behaviour is absent.

Conclusions

The many-body perturbation methods were applied to gain a deeper understanding of the electronic, optical and electronic response structure of liquid NH_3. In order to obtain an accurate electronic band gap, capturing of exchange and screening effects are of high importance. This was done by performing a frequency-dependent energy-only self-consistent G_nW_n on top of the PBE orbital energies and wave functions resulting in an excellent agreement with the experimental gap due to optimal modification of the initial PBE screening. The G_nW_n ansatz was used because the G_0W_0@PBE method considerably underestimated the band gap of liquid NH_3 in contrary to liquid water based on PBE + D3 structures, leading to underestimation of excitation energies.

Further, it was found that exchange effects at single-particle level are stronger in liquid NH_3 than in liquid water, due to a larger blue-shift of the first absorption band relative to the S_1 energy of the molecular NH_3 of about 1.4 eV, which is two times larger than in liquid water. The NH_3 BSE spectrum consists of an excitonic broad band at 7.0 eV with an asymmetrical weight distribution, followed by further broad and slightly more intense absorption bands.

Bibliography

[1] P. Voehringer, Annu. Rev. Phys. Chem. **66**, 97–118 (2015).

[2] M. Shishkin and G. Kresse, Phys. Rev. B **75**, 235102 (2007).

[3] V. Garbuio, M. Cascellai, L. Reining, R. Del Sole and O. Pulci, Phys. Rev. Lett. **97**, 137402 (2006).

[4] F. Bruneval, S. M. Hamed, and J. B. Neaton, J. Chem. Phys. **142**, 244101 (2015).

[5] D. Jacquemin, I. Duchemin, and X. Blase, J. Chem. Theory Comput **11**, 5340-5359 (2015).

[6] L. Hedin, Phys. Rev. Lett. **139**, A796 (1965).

[7] J. VandeVondele, M. Krack, F. Mohamed, M. Parrinello, T. Chassaing, and J. Hutter, J. Comput. Phys. Commun. **167**, 103–128 (2005).

[8] J. P. Perdew, K. Burke, and M. Ernzerhof, Phys. Rev. Lett. **77**, 3865-3868 (1996).

[9] D. R. Hamann, Phys. Rev. B **55**, 10157-10160 (1997).

[10] S. Grimme, J. Antony, S. Ehrlich, and H. Krieg, J. Chem. Phys. **132**, 154104 (2010).

[11] P. Giannozzi, S. Baroni, N. Bonini, M. Calandra, R. Car, C. Cavazzoni, D. Ceresoli, G. L. Chiarotti, M. Cococcioni, I. Dabo, A. Dal Corso, S. de Gironcoli, S. Fabris, G. Fratesi, R. Gebauer, U. Gerstmann, C. Gougoussis, A. Kokalj, M. Lazzeri, L. Martin-Samos, N. Marzari, F. Mauri, R. Mazzarello, S. Paolini, A. Pasquarello, L. Paulatto, C. Sbraccia, S. Scandolo, G. Sclauzero, A. P. Seitsonen, A. Smogunov, P. Umari, and R. M. Wentzcovitch, J. Phys. Condens. Matter **21**, 395502 (2009).

[12] N. Troullier and J. L. Martins, Phys. Rev. B **43**, 1993-2006 (1991).

[13] A. Marini, C. Hogan, M. Gruening, and D. Varsano, Computer Phys. Commun. **180**, 1392-1403 (2009).

[14] M. S. Hybertsen and S. G. Louie, Phys. Rev. B **34**, 5390 (1986).

[15] F. Bruneval, N. Vast, and L. Reining, Phys. Rev. B **74**, 045102 (2006).

[16] M. Gatti, F. Bruneval, V. Olevano, and L. Reining, Phys. Rev. Lett. **99**, 266402 (2007).

[17] F. Trani, J. Vidal, S. Botti, and M. A. L. Marques, Phys. Rev. B **82**, 085115 (2015).

[18] C. A. Rozzi, D. Varsano, A. Marini, E. K. U. Gross, and A. Rubio, Phys. Rev. B **73**, 205119 (2006).

[19] A. Kokalj, Comp. Mater. Sci., **28**, 155 (2003).

[20] V. Ziaei and T. Bredow, J. Chem. Phys. **145**, 064508 (2016).

[21] P. C. do Couto and D. M. Chipman, J. Chem. Phys. **137**, 184301 (2012).

[22] M. Gruening, A. Marini, and X. Gonze, Nano Lett. **9**, 2820-2824 (2009).

3.3 Spectrum of open-shell spinel zinc ferrite

Abstract

In this section the optical properties and electronic response spectrum of the spinel zinc ferrite $Zn_2Fe_4O_8$ as an example of a crystalline system are studied, and in particular the impact of many-body effects on the absorption spectrum are shown using the same many-body perturbation approach as before. The excitonic effects remarkably redistribute the spectral weights causing a red-shift of 1.6 eV of the maximum of the independent particle G_0W_0 (IP-G_0W_0) towards electron-hole interaction affected spectrum. The excitation spectrum of zinc ferrite exhibits a low-lying doubly degenerated bound dark exciton at 1.84 eV with a fully symmetric excited-state density, and a narrow optical gap setting on at 1.93 eV. The electronic transitions and exciton density distributions giving insights to the nature of excitations are further analysed. The dielectric response of $Zn_2Fe_4O_8$ is calculated, showing a particular sensitivity to excitations higher than the electronic band gap, however at high-energy regime it abruptly becomes passive to the incoming electro-magnetic wave and propagates to the negative regions.

Spinel ferrites are magnetic materials being used in spintronics [1, 2], in the area of the electrochemical energy storage (batteries and electrochemical capacitors) and photocatalysis [3–5]. The ferrites photoelectrochemical (PEC) activities originate from i) a narrow optical band gap (< 2.2 eV), which allows for an efficient visible light harvesting of the solar spectrum, ii) multiple oxidation states stabilized by the spinel structure with the individual transition metals of known catalytic properties. Further, as the constituting transition metals are abundant and low cost they are promising candidates for large-scale PEC applications. Spinel ferrites are ternary transition metals oxides with the general formula

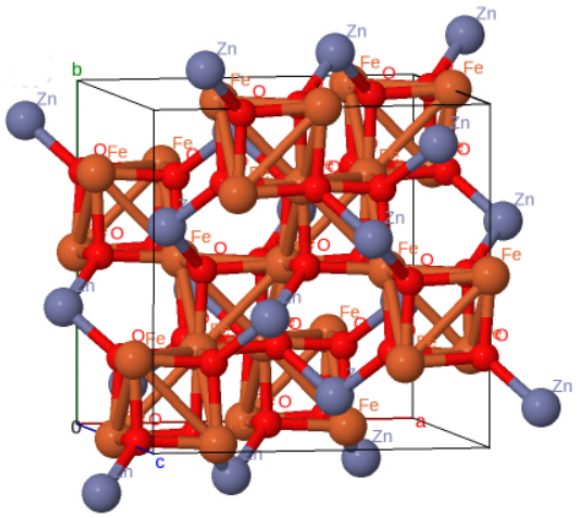

Figure 3.18: Cubic structure of the spinel zinc ferrite.

$X_2Fe_4O_8$, where X (X = Zn, Ga, Cr, etc) and Fe are divalent and trivalent metal cations, respectively. The oxygen anions are arranged in a cubic closed-packed lattice and the cations Zn and Fe are located at two different crystallographic subsites, namely, the tetrahedral (A) and octahedral (B) sites. The crystal structure of the zinc ferrite is illustrated in Fig. 3.18. Fe exhibits a high-spin d^5 configuration, giving rise to an antiferromagnetic ground-state of $Zn_2Fe_4O_8$.

Technical details

DFT ground-state calculations are conducted for the experimental structure [7] based on the PBE formalism of the generalized gradient approximation (GGA) [8] using the QUANTUM ESPRESSO package [11]. Wave functions are expanded in plane waves with a cutoff of 80 Ry. A 4x4x4 Γ-centered k-grid is adopted to accurately converge quasi-particle (QP) energies and absorption spectrum. Standard norm-conserving Troullier-Martins pseudopotentials [18] are used to treat core electrons. On top of the ground-state reference wave functions, a one-shot full frequency-dependent G_0W_0 calculation is carried out with 30 frequency points to properly sample the dynamical character of the dielectric function. The exchange and correlation parts of the self-energy are described by a cutoff of 50 and 8 Ry, respectively, with 300 bands included in the Green's function. For the optical response calculations 300 bands are used for the static polarization function and further 18 occupied and 18 unoccupied bands in the transition space are taken into account to accurately resolve spectral weight distributions and hence relative intensities over 10 eV energy range. The BSE calculations are performed in the limit of adiabatic (static) kernel within the Tamm-Dancoff approximation (TDA) using YAMBO [12].

Results and discussion

In Table 3.3 the DFT, QP indirect, direct and optical band gaps of $Zn_2Fe_4O_8$ are compiled. The single-shot frequency-dependent G_0W_0 provides a very slight correction to the PBE electronic gaps. According to Table 3.3, zinc ferrite is an indirect antiferromagnetic insulator based on PBE. The indirect nature of the electronic gap is maintained upon many-body corrections. Furthermore, an optical gap of 1.93 eV is obtained in excellent agreement with the experimental references.

In order to further characterize the nature of the electronic transitions in the excitation spectrum, in Fig. 3.19 orbital resolved total density of states (T-DOS) at Γ-point is computed. As illustrated the top valence bands mostly consist of O 2p orbitals while the low lying unoccupied bands mainly stem from the O 2p and Fe 3d-orbitals, indicating that

Table 3.3: The PBE, QP electronic (in)direct band gaps and BSE optical gap of $Zn_2Fe_4O_8$ with the experimentally measured gaps are listed. All gaps are in eV.

PBE-indirect/direct gap	G_0W_0-indirect/direct gap	BSE-Optical gap
1.97/2.07	2.02/2.15	1.93
Experimental gaps :		1.9[1], 1.90[2], 1.92[3], 1.93[4]

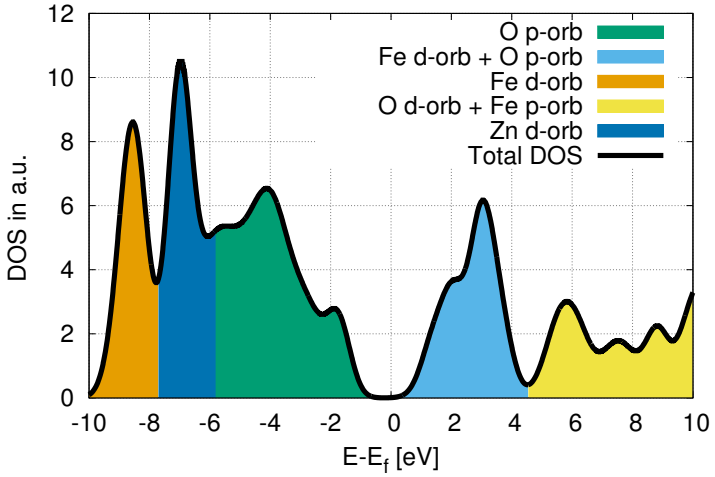

Figure 3.19: PBE total DOS at Γ-point. Only most relevant orbital contributions to the T-DOS are colored.

most of the energetically low-lying transitions have strong p-d or hybridized p-p and p-d character. The occupied Fe and Zn 3d-orbitals are located at much deeper energies, and are not relevant for transitions.

In Fig. 3.20 the calculated absorption spectrum of zinc ferrite is presented. The excitonic effects are rather large, and a red-shift of about 1.6 eV of the global maximum of the independent particle G_0W_0 (IP-G_0W_0) towards fully interacting spectrum with a remarkable spectral weight redistribution upon excitonic effects is observed. Furthermore, the $Zn_2Fe_4O_8$ spectrum possesses a doubly degenerated bound dark exciton at 1.84 eV, and an optical gap setting on at 1.93 eV. The spectrum shows a relatively rich pattern of excitations with the main peaks located at 2.84 (P1), 3.48 (P2), 4.41 (P3), 6.19 (P4), and 7.29 (P5) eV.

To gain more information about the nature of transitions, the QP transition profile (QPTP) and the electronic density distribution are analysed for the dark exciton (S_1) and P1, P2,

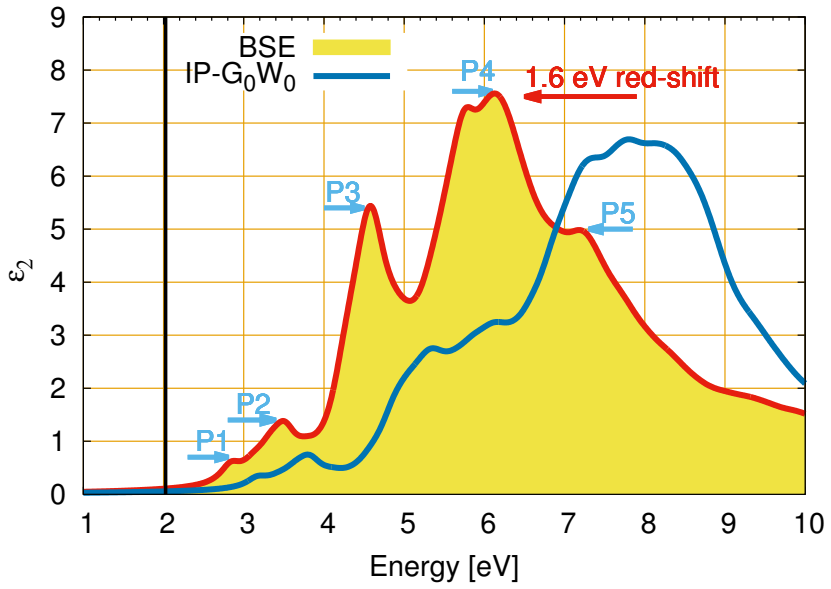

Figure 3.20: BSE and IP spectra of the spinel zinc ferrite are shown. The black vertical line specifies the position of the indirect gap. A red-shift of about 1.6 eV from the maximum of the IP to the BSE spectrum and a considerable spectral weight redistribution are induced upon exciton effects.

P3, P4, and P5 peaks located at different energy ranges up to 7.6 eV. As shown in Fig. 3.21 for the dark state S_1 a single narrow QP peak arises at 2.15 eV with a fully symmetric excited-state density, describing a forbidden Γ-point pure highest occupied crystal orbital (HOCO) to lowest unoccupied crystal orbital (LUCO) O intra-atomic p-p and Fe d-d (central Fe atom) transitions. Furthermore, the dark state represents mainly a spin up-spin up transition. The P1 peak exhibits in the transition profile a single sharp narrow QP peak at 3.16 eV (Fig. 3.21) related to an enhanced symmetric density distribution at four O atoms connected to the central Fe atom (Fig. 3.22), originating from a HOCO – LUCO inter-atomic O-O p-p transition at a non-Γ point. The P2 shows again a single sharp QP peak at 3.79 eV with a distinct symmetric electronic density topology relative to P1, arising upon a Γ-point HOCO - 4 – LUCO transition with an inter-atomic O-O P-P character. The P3 QPTP at 4.76 eV is less narrow and mainly consists of non-gamma point HOCO – LUCO and HOCO – LUCO + 1 transitions with an excited-state density concentrated more on the upper-half of the unit cell (non-symmetric distribution) on the O and Fe atoms, showing a hybrid inter-atomic p-p and p-d character. The P4 QP peak at 6.43 eV is much more broadened, reflecting multi-band transitions at many k-points including the Γ-point, each of which contributing with small to large weights to the excitonic state. The P4 state maintains a large density concentration in the upper-half of the unit cell (non-symmetric distribution), with delocalizations between O and Fe atoms, exhibiting a strong mixed inter

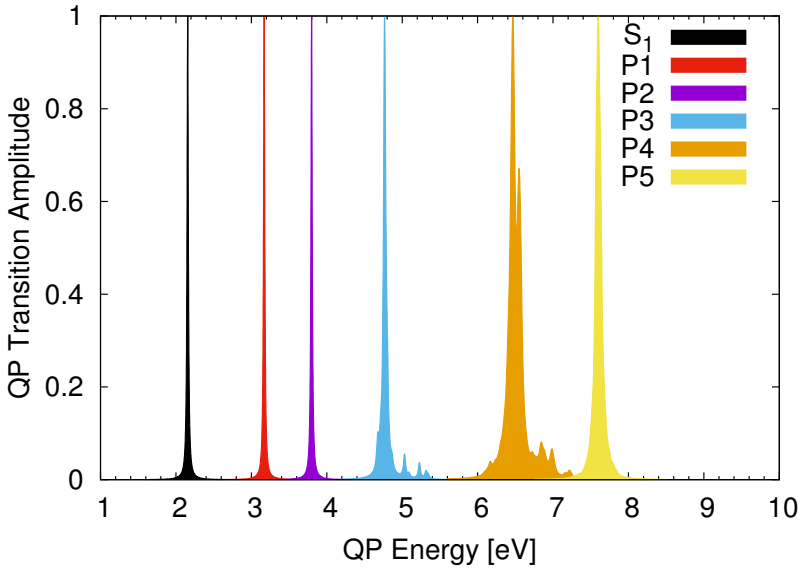

Figure 3.21: QP transition profile of the dark exciton and five intense representative peaks (P1-P5). S_1 gives rise to a forbidden Γ-point Fe intra-atomic d-d transition. P1 and P2 consist of sharp peaks with dominant single band transition at a single k-point, whereas P4 and P5 show multi-band character at many k-points. P3 is a single k-point double band pure spin down-down transition, while all the other peaks (P1,P2,P4,P5) are mainly spin up-spin up transitions.

p-d and p-p character. The P5 QP peak at 7.61 eV gives rise to a delocalized excitonic state with multi-band transitions at many non-gamma k-points. As illustrated in Fig. 3.22, the P5 density is distributed over O, O-Fe and Fe atoms, forming a mixed inter-atomic p-p and inter-atomic p-d character. Interestingly, the density of S_1, P1, and P2 give rise to a symmetric distribution, whereas P3, P4, and P5 densities represent a shift of charge to a particular part of the unit cell.

One further important property of the spinel is the instantaneous frequency-dependent dielectric response upon external perturbation which is given as the real part of the macroscopic dielectric function. This is presented in Fig. 3.23 and describes how the electronic degrees of freedom of the anti-ferromagnetic system responds to photo-excitations. As can be seen, the static dielectric constant given as $\epsilon_1(\omega = 0)$ sets on at 2.5 and increases to the high magnitude peaks at 4.3 and 5.4 eV. It is therefore most responsive to photo-excitations higher than the electronic band gap. At higher energies it however rapidly drops and becomes considerably passive to excitations. At about 6.2 eV a sign change occurs, and ϵ_1 propagates to the negative regions, meaning electrons act in a repulsive way to the incoming electro-magnetic wave.

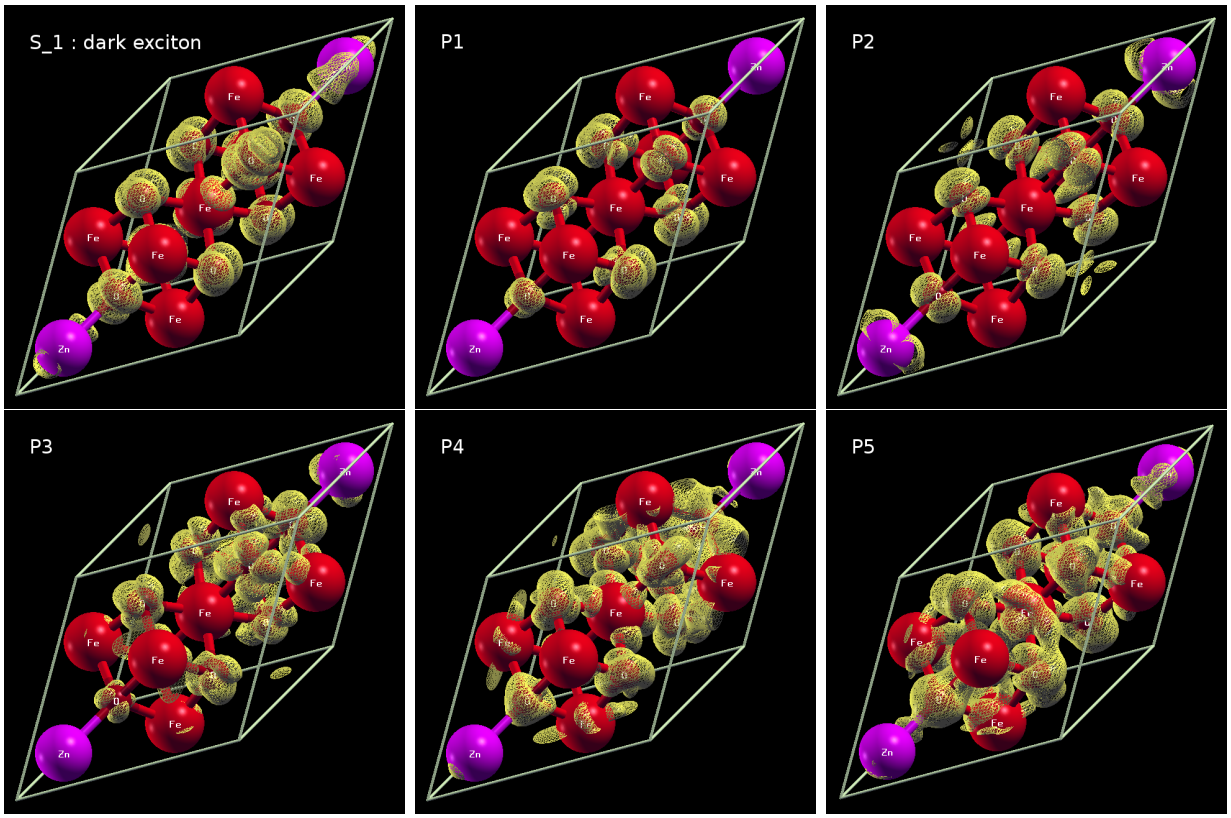

Figure 3.22: FULL (spin up and down) excited-state electronic density of the dark exciton at 1.84 eV (Γ-point transition), P1 at 2.84 eV, P2 at 3.48 eV, P3 at 4.41, P4 at 6.19 eV, and P5 at 7.29 eV.

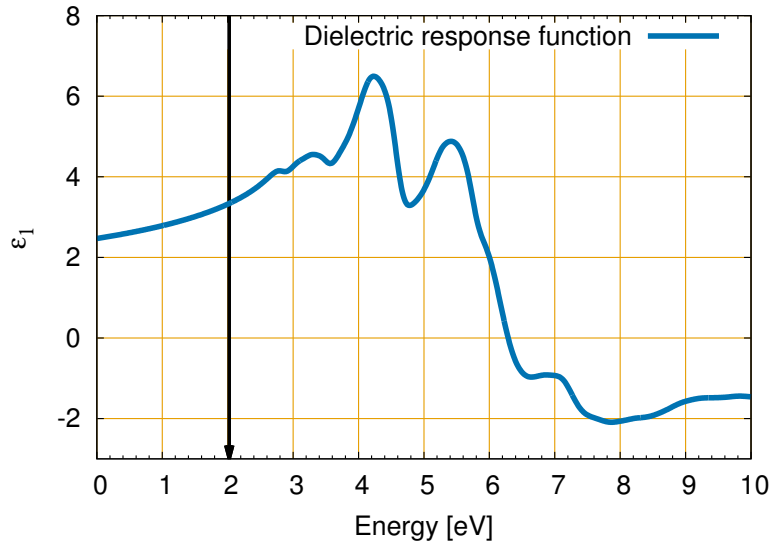

Figure 3.23: Dielectric response function of the spinel zinc ferrite is presented. It shows high sensitivity to the excitations higher than the indirect electronic gap (black arrow). ϵ_1 however rapidly decreases above 6 eV.

Conclusions

In this section the GW/BSE method was applied to compute the optical properties and dielectric response spectrum of the spinel zinc ferrite. It was shown that the upper valence bands mainly consist of O 2p-orbitals, whereas low-lying conduction bands are combinations of O 2p- and Fe 3d-orbitals. As demonstrated, many-body effects are extremely important for the occuring red-shift compared to the independent-particle spectrum and a realistic redistribution of the spectral weights towards low- and mid-range energy area. A doubly degenerated dark exciton was found showing a fully symmetrically distributed excited-state density stemming from intra-atomic p-p and intra-atomic d-d transitions at Γ-point. The P1 and P2 peaks are of single band inter-atomic (O-O) p-p character, while the higher lying excitation peaks (P4 and P5) are multi-band inter-atomic p-p/p-d transitions at many k-points. The P3 peak is a double band single non-gamma point transition.

The dielectric function goes through three phases: a responsive, a passive (ϵ_1 less than 1), and a repulsive area. ϵ_1 is highly responsive to photo-excitations between 3 - 6 eV, after which it abruptly drops into negative regions.

Bibliography

[1] M. Sugimoto, Journal of the American Ceramic Society **82**, 269 (1999).

[2] D. S. Mathew, R. S. Juang, Chem. Eng. J. **129**, 51 (2007).

[3] C. Z. Yuan, H. B. Wu, Y. Xie, X. W. Lou, Angewandte Chemie-International Edition **53**, 1488 (2014).

[4] M. S. Park, J. Kim, K. J. Kim, J. W. Lee, J. H. Kim, Y. P. Yamauchi, Phys. Chem. Chem. Phys. **17**, 30963 (2015).

[5] E. Casbeer, V. K. Sharma, X. Z. Lee, Sep. Purif Technol. **87**, 1 (2012).

[6] L. Hedin, Phys. Rev. Lett. **139**, A796 (1965).

[7] Szytula et al., Acta Physica Polonia. **5**, 583-591 (1904)

[8] J. P. Perdew, K. Burke, and M. Ernzerhof, Phys. Rev. Lett. **77**, 3865-3868 (1996).

[9] P. Giannozzi, S. Baroni, N. Bonini, M. Calandra, R. Car, C. Cavazzoni, D. Ceresoli, G. L. Chiarotti, M. Cococcioni, I. Dabo, A. Dal Corso, S. de Gironcoli, S. Fabris, G. Fratesi, R. Gebauer, U. Gerstmann, C. Gougoussis, A. Kokalj, M. Lazzeri, L. Martin-Samos, N. Marzari, F. Mauri, R. Mazzarello, S. Paolini, A. Pasquarello, L. Paulatto, C. Sbraccia, S. Scandolo, G. Sclauzero, A. P. Seitsonen, A. Smogunov, P. Umari, and R. M. Wentzcovitch, J. Phys. Condens. Matter **21**, 395502 (2009).

[10] N. Troullier and J. L. Martins, Phys. Rev. B **43**, 1993-2006 (1991).

[11] A. Marini, C. Hogan, M. Gruening, and D. Varsano, Computer Phys. Commun. **180**, 1392-1403 (2009).

[12] Y. Matsumoto, M. Omae, I.Watanabe, E. Sato, Journal of the Electrochemical Society **133**, 711 (1986).

[13] P. H. Borse et al., Journal of the Korean Physical Scoiety **55**, 1572 (2009).

[14] S. Boumaza et al., Applied Energy **87**, 2230 (2010).

[15] R. Dom et al, Rsc Advances **2**, 12782 (2012).

[16] A. Kokalj, Comp. Mater. Sci., **28**, 155 (2003).

3.4 Electron-phonon coupling

Abstract

In this section, the impact of dynamic electron-phonon (el-ph) effects on the electronic band gap of ice and liquid water is investigated by accounting for frequency-dependent Fan contributions in the el-ph mediated self-energy within the many-body perturbation theory (MBPT). It is found that the dynamic el-ph coupling effects significantly reduce the static el-ph band gap correction of crystalline ice from -2.46 eV to -0.23 eV in contrast to the result of Monserrat et al. [1]. This is of particular importance as otherwise the static el-ph gap correction would considerably reduce the electronic band gap, leading to strong underestimation of optical excitation energies and deteriorating the agreement with the experimental references. By contrast, the static el-ph gap correction of liquid water is moderate (-0.32 eV), and inclusion of dynamical effects slightly reduces the gap correction to -0.19 eV. Further, the diverse sensitivity of ice and liquid water to the GW self-consistency is determined and it is shown that the energy-only self-consistent approach (G_nW_n) exhibits large implicit vertex character in comparison to the Quasi-Particle Self-Consistent (QSGW) approach, for which an explicit calculation of vertex corrections is necessary for good agreement with experiment.

Introduction

In recent years, effects arising from electron-phonon (el-ph) coupling attracted much interest, as nuclear vibrations coupled with the electronic degrees of freedom were found to have a great impact on the electronic structure, and in particular on the band gap of a range of materials [2–5] and even further on the build up of excitons in phonon-mediated optical excitations in semi-conductors [6, 7].

Recently, el-ph coupling effects in hydrogen-rich molecular crystals such as ice and NH_3 were subject to a first principles investigation by Monserrat et al. [1]. They found that the commonly used Allen-Heine-Cardona (AHC) theory is insufficient in capturing the strength of el-ph coupling, and hence going beyond the AHC theory is a mandatory step for accurate description of zero point effects. Monserrat et al. started both from

$$E_g = \langle \phi(q) | E_g(q) | \phi(q) \rangle \tag{3.1}$$

and

$$E_g = E(0) + \sum_{n,k} a_{nk}^2 \langle \phi(q) | q_{nk}^2 | \phi(q) \rangle + \mathcal{O}(q^4) \tag{3.2}$$

to calculate vibrational effects. Here E_g is the electronic band gap expanded around the equilibrium position in terms of harmonic vibrational mode amplitudes q_{nk}, k is the vibrational Brillouin zone wave vector and n is the branch index. Further, a^2_{nk} are the diagonal quadratic expansion coefficients.

The Eq. (3.1) is exact, whereas the Eq. (3.2) is perturbative and represents the quadratic contribution to gap correction and hence is equivalent to the AHC theory. Now, in order to account for higher-order terms, Eq. (3.1) was sampled by Monserrat using a Monte Carlo approach, resulting in large static el-ph band gap corrections of -1.0 eV in NH_3 to -1.52 eV in H_2O.

However, since these corrections lead to massive band gap reductions, the optical absorption spectra of the investigated molecular crystals which build upon previously calculated quasi-particle (QP) energies inevitably suffer a red-shift to much lower excitation energies. Low-lying intense excitation peaks in case of ice for instance, were however never observed experimentally [see section 3.1]. Consequently, in order to be able to reproduce the experimental first intense peak of hexagonal ice (ice-Ih) which lies at 8.65 eV [8] an electronic band gap of about 9.7 eV is necessary as otherwise the first absorption band would be underestimated by 1.52 eV if the static el-ph gap correction of ice as calculated by Monserrat were taken into account. The same red-shift of the optical peaks as a result of inaccurate computation of el-ph effects can also be observed on ammonia absorption peaks [9], if the large static el-ph gap correction of -1.01 eV is considered. This means that a key term is still missing in order to reduce the large static el-ph gap corrections, and hence improving the agreement with experiment.

To clarify this non-trivial issue, one goes beyond the AHC theory and identifies the missing term with the dynamic electron-phonon contribution by including the extremely important dynamic structure of the Fan term in the el-ph mediated self-energy within the many-body Green's function formalism.

A direct comparison to optical peak positions is justified, even if the exciton-phonon coupling is not included explicitly in our study, since dynamic el-ph massively reduces the static band gap correction. Possible effects of phonon modes mediated exciton build up (the so-called coherent contributions in the BSE or exciton-phonon interaction neglected here) which lead to a blue-shift of optical peak positions must be rather small, as otherwise the peak positions will be blue-shifted to much higher excitation energies, in disagreement with experimental references.

In the following ab-initio many-body perturbation theory (MBPT) electron-phonon calculations are performed on ice and liquid water including dynamic effects to demonstrate its massive impact on the static el-ph gap correction. Phonon mode contributions to the gap are analysed by inspecting the corresponding Eliashberg spectral functions.

For a deeper theoretical understanding of the applied methodology the reader may consult references [10–12].

Theoretical background

In the following a very short overview of the theory of electron-phonon coupling within the MBPT framework is provided. In this many-body description the el-ph interaction is treated perturbatively and its corresponding el-ph Green's function contains a static term called Debye-Waller (DW) (a second-order term in nuclear displacement) and a dynamic term known as Fan (a first-order term in nuclear displacement), which build up the el-ph interacting Green's function

$$G_n(\omega, T) = [\omega - \epsilon_n - \Sigma_n^{DW}(T) - \Sigma_n^{Fan}(\omega, T)]^{-1} \tag{3.3}$$

The poles of (3.3) directly correspond to the QP excitations. Eq. (3.3) contains ϵ_n as the ground-state Kohn-Sham (KS) frozen atom eigenenergies, obtained from plane wave DFT. The $\Sigma^{DW}(T)$ term is the temperature-dependent Debye-Waller contribution

$$\Sigma_n^{DW}(T) = -\frac{1}{2}\sum_{n'\lambda} \frac{\Lambda^{\lambda}_{nn'}}{N}[\frac{2N_\lambda(T)+1}{\epsilon_n - \epsilon_{n'}}] \tag{3.4}$$

and the $\Sigma_n^{Fan}(\omega, T)$ term is the frequency- and temperature-dependent Fan contribution

$$\Sigma_n^{Fan}(\omega, T) = \sum_{n'\lambda} \frac{|g^{\lambda}_{nn'}|^2}{N}\left[\frac{N_\lambda(T)+1-f_{n'}}{i\omega - \epsilon_{n'} - \omega_\lambda} - \frac{N_\lambda(T)-f_{n'}}{i\omega - \epsilon_{n'} + \omega_\lambda}\right] \tag{3.5}$$

where N_λ and $f_{n'}$ represent the Bose-Einstein and Fermi-Dirac distribution functions, while ω_λ and N are the phonon frequencies and number of q-points in the Brillouin zone. Further, $g^{\lambda}_{nn'}$ are the electron-phonon matrix elements, representing the scattering probability amplitude of an electron with emission or absorption of phonons which is given by

$$g^{\lambda}_{nn'} = \sum_{s\alpha} (2M_s\omega_\lambda)^{-\frac{1}{2}} e^{iq\tau_s} \langle n'|\frac{\partial V_{scf}(r)}{\partial R_{s\alpha}}|n\rangle \, \zeta_\alpha(\lambda|s) \tag{3.6}$$

where M_s is the atomic mass, τ_s is the position of the atomic displacement in the unit cell, $\zeta_\alpha(\lambda)$ are the components of the phonon polarization vectors, and $V_{scf}(r)$ is the self-

consistent DFT ionic potential.

By linearising the frequency dependency of the Fan self-energy around the KS energies, one arrives at the final perturbative temperature-dependent expression for the el-ph mediated QP energies

$$E_n(T) \approx \epsilon_n + Z_n(T)[\Sigma_n^{DW}(T) + \Sigma_n^{Fan}(\epsilon_n, T)] \tag{3.7}$$

which contains the temperature-dependent renormalization factor $Z_n(T) = [1 - \frac{\partial \Sigma_n^{Fan}(\omega,T)}{\partial \omega}|_{\omega=\epsilon_n}]^{-1}$.

Technical details

The ice geometry is taken from the HIRSCH-I model [13] and liquid water configurations are obtained for 8 and 27 water boxes from ab-initio Born-Oppenheimer Molecular Dynamics (BOMD) using CP2K [14]. After an initial equilibration of 10 ps, a 30 ps productive MD at 300 K is run with the PBE functional and Grimme D3 dispersion correction [15].

On top of the structures, ground-state calculations are conducted using the PBE [16] functional as implemented in QUANTUM ESPRESSO [11]. Core electrons are simulated by norm-conserving Troullier-Martins pseudo-potentials [18]. A kinetic cutoff of 60 (240) and 70 (280) Ry is chosen to represent the wave functions (densities) in terms of plane waves for ice and liquid water, respectively, with a tight convergence criterion of 1.0E-14 Ry. In order to properly sample the Brillouin zone a Γ-centered k-grid of 4x4x4 is used. On top of the ground-state energies and wave functions, electron-phonon calculations are performed with a tight convergence criterion of 1.0E-12 Ry for ice 36 and liquid water 72 phonon branches within the density functional perturbation theory (DFPT). The electron-phonon matrix elements are calculated for 50 and 25 randomly generated q-points for ice and liquid water, respectively, to reach a faster convergence with respect to the number of vibrational Brillouin zone q-points.

The el-ph self-energy calculations are performed with 10^6 random q-points for the random integration method in order to boost the convergence and 200 bands using YAMBO [12]. Convergence is further checked with 300 bands showing no notable impact. Self-consistency is again performed by YAMBO and vertex calculations are carried out using ABINIT [20,21] with non-local parts of pseudo-potential accounted for in the calculation of dipole matrices in GW. The vertex calculations are performed for the 8-water box due to the local nature of the vertex correction, and as it will be shown the obtained value is very comparable to the result reported in literature.

Further, to avoid finite size effects and having comparable results, the larger 27-box is

used instead of the 8-water box in the GW calculations, for which a kinetic energy cutoff of 100 and 400 Ry is used for the wave functions and densities, respectively. The GW and vertex results are averaged over only 5 water snapshots, since the main focus is on relative effects, such as dynamical versus static el-ph coupling, self- versus non-self-consistency and vertex effects, and not on absolute values.

Results and discussion

In Table I the results of the static and dynamic approaches to electron-phonon coupling effects on the electronic band gap of ice and liquid water at Γ-point are shown. As can be seen, the el-ph gap corrections of ice based on static corrections from the Debye-Waller contributions result in a gap reduction of -2.48 eV. However, dynamical effects arising from the Fan contributions massively reduce the gap correction to -0.23 eV.

For liquid water the static DW gap reduction is interestingly only -0.32 eV (much smaller than in ice) and dynamical effects slightly further reduce the static gap correction to -0.19 eV. The small static el-ph gap correction of liquid water is directly related to its disordered structure, and hence the coupling of lattice vibrations with the electronic degrees of freedom is much less effective than in ice.

Furthermore, an important numerical G-damping parameter dependency for gap corrections on the Green's function damping is observed having a great impact on the absolute position of the valence band energy correction (VBEC), while absolute conduction band energy correction (CBEC) is largely insensitive to damping effects as shown in Table 3.4. Such a dramatic numerical effect was shown to increase the lifetimes of Quasi-Particles of copper by 50% [22]. This calls for a careful convergence check with respect to the G-damping parameter in the Fan and Debye-Waller self-energies in future studies.

Interestingly, the el-ph gap correction of ice based on DW contributions is much larger than the Monserrat gap correction based on Monte Carlo sampling of Eq. (3.1), indicating that the higher-order terms (non-quadratic contributions) in Eq. (3.1) indeed reduce the DW gap corrections from -2.46 eV to -1.52 eV. However dynamic Fan el-ph effects massively further reduce the static DW corrections, and exactly this massive reduction of the static band gap correction explains why the intense peaks in the optical absorption spectrum of ice are not underestimated by 1.52 eV for instance.

Now, in order to determine the importance of each energy-dependent vibrations contributing to the gap correction, phonon modes are further analysed by calculating and inspecting

the generalized Eliashberg spectral function (ESF) given by

$$g^2F_n(\omega) = \sum_{\lambda n'} \left[\frac{|g^{\lambda}_{nn'}|^2}{\epsilon_n - \epsilon_{n'}} - \frac{1}{2} \frac{\Lambda^{\lambda}_{nn'}}{\epsilon_n - \epsilon_{n'}} \right] \delta(\omega - \omega_{\lambda}) \tag{3.8}$$

which is further connected to the gap correction $\Delta E_n(T)$ by

$$\Delta E_n(T) = \int d\omega g^2F_n(\omega)[2N_{\lambda}(\omega, T) + 1] \tag{3.9}$$

where $N_{\lambda}(\omega, T)$ is the Bose-Einstein distribution, ω_{λ} are the phonon frequencies, $g^{\lambda}_{nn'}$ and $\Lambda^{\lambda}_{nn'}$ are the first and second order electron-phonon matrix elements which are directly linked to the Fan and DW contributions.

An extremely important aspect of Eq. (3.8) is its sign which is determined by its denominator, describing emission or absorption of phonons after scattering of an electron. Typically, the ESF (3.8) in semi-conductors is positive at the valence band maximum (VBM) and negative at the conduction band minimum (CBM), causing the usual observed reduction of the band gap upon el-ph scattering effects. Hence, ESF is an insightful tool helping to further gain access to the details of build up of el-ph mediated gap corrections.

In Fig. 3.24 the dynamic ESFs of ice for the VBM and CBM states are shown. Phonon contributions are observed over a large energy scale up to 450 meV. In particular, for the VB state low frequency modes are dominant, whereas for the CB state intense peaks appear at much higher energies around 400-450 meV.

Interestingly, the VB ESF is not an entirely positive function, and particularly at low-energy regime multiple sign changes occur. For the CB ESF, the function is not negative over the full energy range exhibiting positive contributions in the high-energy regime (425 meV). Thus, the ESF of ice for both VB and CB states shows anomalous regions. The VB anomaly region is responsible for the negligible energy correction to the Kohn-Sham VB state due to nearly full compensation of all phonon mode contributions. By contrast, although the ESF of the CB state also exhibits an anomaly region at high energies, however the overall compensation is not that effective as for the VB states, because the high-frequency positive contributions at 425 meV are much less weighted by the Bose-Einstein distribution function and hence nearly the whole gap correction stems from the negative contributions of lower CB modes distributed up to 200 meV.

In Fig. 3.25 the dynamic ESFs for liquid water are shown. Low-energy modes are dom-

inant for the VB states, while for the CB states phonon mode contributions are quite distributed over wide energy regimes. Again for the VB state a sign change occurs at about 25 meV, leading to negative contributions which are much more weighted than the other high-frequency modes. This gives rise to nearly full compensation of positive and negative contributions to the VB energy correction. By contrast, for the CB states, no sign change is observed up to 300 meV and hence contributions are negative in nature causing the gap reduction.

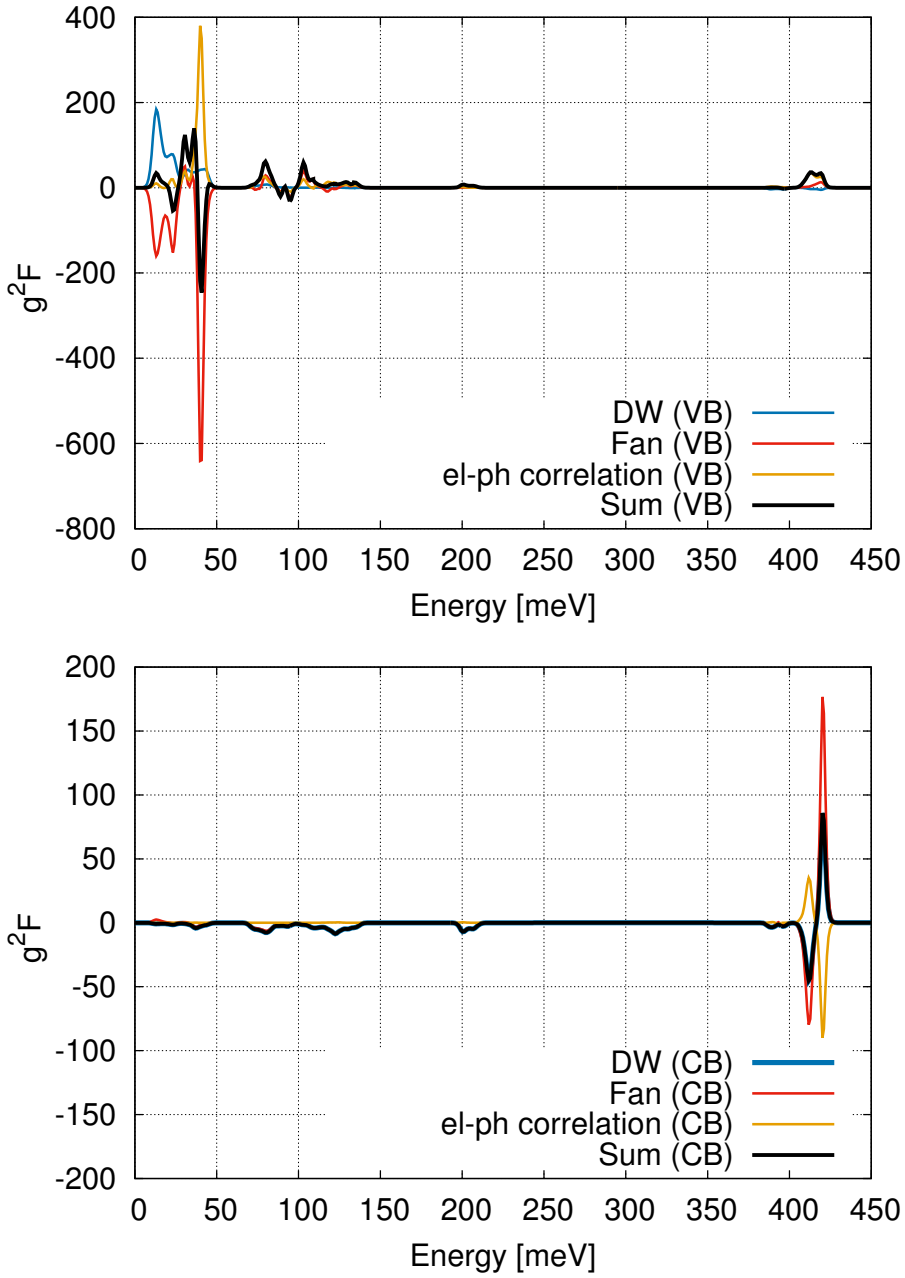

Figure 3.24: The dynamic Eliashberg spectral functions of ice at Γ-point for the valence and conduction band (VB,CB) are shown. For the VB state low frequency modes are dominant; however positive and negative contributions cancel each other, while for the CB state, the phonon modes are distributed up to 450 meV, and compensation of negative and positive contributions is much less effective, since the high frequency positive contributions are much less weighted by the Bose-Einstein distribution function, and hence larger el-ph correction to the CB states is obtained.

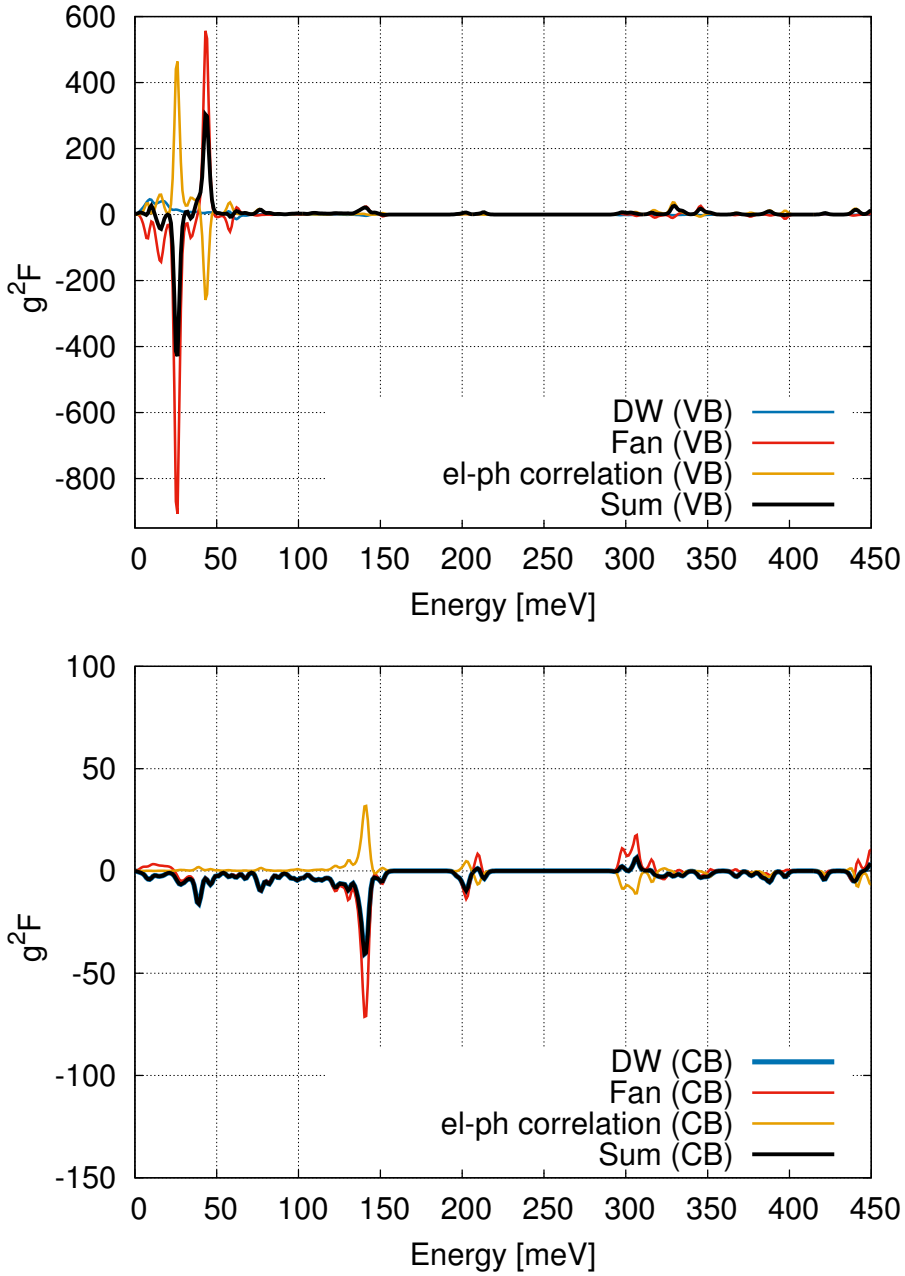

Figure 3.25: The dynamic Eliashberg spectral functions of liquid water box at Γ-point for the valence and conduction band (VB,CB) are shown. A full compensation of positive and negative areas below the black line (DW+Fan contributions) can be seen, and hence nearly no contribution to the VB correction, while for the CB states negative contributions distributed over wide energy ranges are dominant and responsible for the CB el-ph energy correction.

Table 3.4: Static and dynamic el-ph mediated band gap corrections at Γ-point for ice at 0 K and liquid water at 300 K. The Green's function damping parameter, absolute valence and conduction band energy corrections (VBEC and CBEC) and el-ph band correction are given in eV. Furthermore, a fine frequency grid of 0.001 eV is used for accurate integrations. Parenthesis indicates sign change of energy corrections depending on damping parameter.

Static el-ph approach on ice (DW + Fan)			
G-damping	VBEC	CBEC	$\Delta E(T = 0K)$
0.1	0.8159	-0.2586	-1.0745
0.01	1.1420	-0.2595	-1.4015
0.001	1.5470	-0.2590	-1.8060
0.0001	2.2190	-0.2595	-2.4785
1.0E-05	2.2206	-0.2590	-2.4796
1.0E-06	2.2100	-0.2593	-2.4693
Dynamical el-ph approach on ice (DW + Fan)			
G-damping	VBEC	CBEC	$\Delta E(T = 0K)$
0.1	0.2700	-0.2346	-0.5046
0.01	0.0016(-)	-0.2346	-0.2330
0.001	0.0089	-0.2348	-0.2437
0.0001	0.0040	-0.2345	-0.2385
1.0E-05	0.0012(-)	-0.2343	-0.2331
1.0E-06	0.0016(-)	-0.2345	-0.2329
Static el-ph approach on water (DW + Fan)			
G-damping	VBEC	CBEC	$\Delta E(T = 300K)$
0.1	1.1220	-0.6566	-1.7786
0.01	2.0750	-0.7090	-2.7840
0.001	2.0940	-0.7157	-2.8097
0.0001	1.8070	-0.7086	-2.5156
1.0E-05	0.6107	-0.7260	-1.3367
1.0E-06	0.3299(-)	-0.7147	-0.3848
1.0E-07	0.3900(-)	-0.7103	-0.3203
1.0E-08	0.3840(-)	-0.7093	-0.3253
Dynamical el-ph approach on water (DW + Fan)			
G-damping	VBEC	CBEC	$\Delta E(T = 300K)$
0.1	0.1266	-0.2901	-0.4167
0.01	0.0434	-0.2667	-0.3101
0.001	0.0075(-)	-0.2282	-0.2207
0.0001	0.0009(-)	-0.1935	-0.1926
1.0E-05	0.0003(-)	-0.1920	-0.1917
1.0E-06	0.0008	-0.1916	-0.1924
1.0E-07	0.0008	-0.1900	-0.1908
1.0E-08	0.0008	-0.1923	-0.1916

Table 3.5: An overview of the effects on the electronic band gap of ice and liquid water with respect to energy update in G and W in combination with approximated vertex corrections via the local static kernel f_{xc} is given. Calculations are performed on a 4x4x4 Γ-centered k-grid with 20 frequencies, 10 Ry energy cutoff for the dielectric matrix, 300 bands and n=8 iterations in the Hedin self-consistent Pentagon for ice, and on a 2x2x2 k-grid with 20 frequencies, 8 Ry dielectric cutoff, 400 bands and n=8 for the 27-water box. The given ice gap reference value was measured for hexagonal ice. All numbers are given in eV.

	Ice (HIRSCH-I)	**Liquid H_2O**
PBE	5.79	5.25
G_0W_0	8.81	8.21
G_nW_n(Energy-only)	10.76	9.77
f_{xc}	-0.93	-0.85
NQE	——	-0.7 [32]
el-ph	-0.23	-0.19
exp.	9.7 [33]	8.7 [34]

3.5 GW self-consistency and vertex effects

In this section, electron-electron many-body contributions to the electronic band gap are analysed in a self-consistent manner. In particular, the effect of vertec corrections approximated by exchange-correlation kernel f_{xc} is shown. The electronic band gap of ice and liquid water was in recent years subject to high level many-body calculations in its non-self consistent G_0W_0 implementation [23–25] (see section 3.1).

As shown in Table 3.5. the G_0W_0 method considerably increases the Kohn-Sham DFT gap of ice from 5.79 to 8.81 eV. Energy-update in G and W further increases the gap by about 2 eV. The effect of wave function update in G and W is a -4 meV reduction of the gap, and hence negligible. In contrary to the self-consistency (SC) effects, the vertex correction f_{xc} reduces the gap by -0.93 eV, and hence SC effect is nearly halved by strong vertex effects. However, the G_nW_n approach can be regarded as an already vertex-corrected approach in an implicit manner, since in this approach the errors associated with the neglect of the off-diagonal elements in the self-energy Σ, the Green's function G and update of the wave functions (or in other words neglect of FULL sc-GW effects) are cancelled out by the errors associated with the neglect of higher-order diagrams in the self-energy and polarizability P to a high degree. Therefore, the vertex mediated gap reduction of -0.93 eV within the f_{xc} approximation causes a vertex double counting problem, if it is added to an approach which already intrinsically contains vertex effects. Other self-consistent approaches such as Quasi-Particle Self-Consistent [35] (QSGW) may also have to some degrees vertex-corrected character, but probably to a lesser extent than G_nW_n, since QSGW and fully self-consistent

GW (sc-GW) produce nearly the same results for large band gap insulators.

The implicit vertex character of QSGW stems from the fact that the Z factor is cancelled out in order to avoid spectral weight transfer to the incoherent part of the Green's function (effective vertex simulation) [35]. The f_{xc} approximation combined with QSGW was applied by Shishkin et al. [36] to a number of semi-conductors and insulators producing promising results; however the success of QSGW + f_{xc} approximation also relies to some extent on simplifications and hence error compensations, as for instance in QSGW the Quasi-Particle-approximation is used and vertex corrections are not included in the self-energy. Grüneis et al. [37] included second-order exchange diagrams for the vertex function in the self-energy (to reduce self-interaction and restore the antisymmetry of the many-body electron wave function), resulting in an increase of the band gaps of semi-conductors and insulators with respect to the experimental references, worsening the agreement. Further, inclusion of vertex corrections in the self-energy and W with a dynamic or static W can cause either a reduction or an increase of the gaps, respectively.

Unfortunately due to immense complexity of the vertex contributions there is no definite answer to the question of how to treat vertices properly. What can be said unambiguously is that the present local f_{xc} approximation to the vertex function in W results in a large vertex mediated band gap correction, and consequently to a large decrease of the gap, if it is added to the energy-only G_nW_n approach which through fortuitous error compensations already accounts for vertex effects.

In the case of liquid water, self-consistency effects cause a gap increase of about 1.6 eV, which is smaller than for ice. Moreover, the self-consistent vertex contributions within the f_{xc} approximation lead to gap reduction by -0.85 eV, and therefore the self-consistency effect is nearly halved by f_{xc}. Now the inclusion of nuclear quantum effects (NQEs) considerably reduces the gap by up to -0.7 eV [32], which in summary would lead to a band gap of 8.22 eV, almost 0.5 eV smaller than the experimental value.

The energy-only self-consistent liquid water gap of 9.77 eV on classical water structures is not consistent with the result of Chen et al. [32] of 10.5 eV, obtained with QSGW. The large discrepancy of about 0.7 eV between the two methods is indicative that G_nW_n contains implicitly much more vertex character than QSGW. Therefore, addition of f_{xc} to G_nW_n simply overcounts the vertex effect. Consequently, the f_{xc} should be added to a self-consistent approach which either has no or less vertex character to avoid biased results. As a final point regarding vertex corrections, it is mentioned that the present vertex result of -0.85 eV on the 8-water box is comparable to the result of Chen [32] of -0.9 eV for a

32-water box.
Recently, Kutepov [38, 39] presented a fully diagrammatic (in principle exact) approach avoiding the Quasi-Particle approximation in the Green's function, and most importantly the problem of vertex double counting. In his approach Hedin's equations are solved exactly and self-consistently, with inclusion of vertex corrections both in the self-energy and W, together with full capture of frequency dependency of the dynamical screened interaction W, obtaining promising results for the band gaps of a number of semi-conductors and insulators without relying on error compensations.

There are also other important effects impacting the gap which are briefly mentioned. In the case of liquid water finite size and nuclear quantum effects (NQEs) are neglected in DFT-based simulations, as this study is primarily concerned with the intrinsic many-body electron-phonon and electron-electron effects. However, it was shown in Chapter 3 that finite size effects are negligible based on a comparison between the gap of 27- and 64-water box. Hence the convergence is reached using a 27-water box [25]. This strongly indicates that the electronic band gap of water is rather a local quantity, and its renormalization with respect to the size of the box stems mostly from the nearst and next nearst water molecules.

Regarding NQE, Del Ben et al. [40] based on the approximated (accelerated) Path-Integral Molecular Dynamics (PIMD) on top of hybrid density functional, estimated the effect of proton delocalization to -0.6 eV decrease in the electronic band gap. A similar result, i.e. a gap reduction by -0.7 eV, also based on boosted PIMD but on top of G_0W_0 was found by Chen et al. However, comparison of our G_0W_0 calculations on the 27-water box based on the structures obtained from ab-initio BOMD at 300 K and 390 K (simulating the experimental structure of liquid water at 300 K; the so-called temperature trick [24]) show a gap reduction of only -0.2 eV. This indicates that the thermal effects can not fully account for quantum fluctuations by a simple temperature increase in molecular dynamics.

Further, the impact of NQE is starting point energy or in other words starting point exchange dependent, as NQE increases in 0.1 eV steps from Kohn-Sham PBE to hybrid-DFT (PBE0) to GW (i.e. a gap correction by -0.5, -0.6, -0.7 eV, as found by Del Ben and Chen). The NQE of ice-Ih is presently not known; however a zero-point correction of about -0.7 to -1.0 eV with the full energly-only self-consistent scheme would produce an experimentally consistent band gap. It should be mentioned that the self-consistency and vertex effects are independent of NQE, and hence these effects are solely intrinsic.

To summarize the contributing effects to the band gap : if one ignores the contributions of f_{xc} for the vertex function in order to avoid vertex double counting, and subtract the nuclear

quantum and electron-phonon effects from the G_nW_n gap, one ends up with a final liquid water band gap of 8.9 eV in good quantitative agreement with the experimental gap of 8.7 eV. Therefore, the G_nW_n approach makes explicit calculation of vertex correction in the self-energy and W unnecessary. This could be of enormous importance for computational efficiency when calculating large liquid boxes.

Conclusions

The importance of dynamic effects arising from Fan self-energy was shown for the accurate calculation of the el-ph mediated gap correction in ice with implications to other hydrogen-rich molecular systems. Assessment of dynamical effects is of particular importance as otherwise static el-ph gap corrections are overestimated for ice, and consequently the corresponding peaks in the optical absorption spectra building upon the el-ph mediated QP energies suffer a tremendous artificial red-shift. Furthermore, for liquid water static el-ph effects lead to considerably smaller gap corrections, and further inclusion of dynamical effects only slightly reduce the gap correction. This is because of ineffective electron-lattice vibration coupling due to disordered structure of water. Furthermore, in both systems the phonon modes of the CB states up to 200 meV are the driving force for el-ph gap reduction.

Further checks on solid ammonia and on molecular systems (not shown here) revealed that the dynamical structure of the self-energy indeed has a strong impact on the static el-ph band gap corrections, hence the presented result on crystalline ice gap is general in nature. Also Antonius et al [4] found a large impact of dynamic el-ph coupling by -50% on the gap of LiF and MgO, indicating that frequency dependency of the self-energy should not be neglected even in solids.

It was further demonstrated that the energy-only self-consistency in G and W (as expected) increases the G_0W_0 gap of ice and water by 2 eV and 1.6 eV, respectively. Furthermore, the approximated vertex correction by f_{xc} in W for the G_nW_n approach causes a vertex double counting problem leading to an overestimation of gap reduction.

Bibliography

[1] B. Monserrat, E. A. Engel, R. J. Needs
Phys. Rev. B **92**, 140302 (2015).

[2] H. Kawai, K. Yamashita, E. Cannuccia, and A. Marini
Phys. Rev. B **89**, 085202 (2014).

[3] C. E. P. Villegas, A. R. Rocha, and A. Marini,
Phys. Rev. B **94**, 134306 (2016).

[4] G. Antonius, S. Poncé, P. Boulanger, M. Côté, and X. Gonze, Phys. Rev. Lett **112**, 215501 (2014).

[5] S. Ponc, Y. Gillet1, J. Laflamme Janssen, A. Marini, M. Verstraete, and X. Gonze, J. Chem. Phys. **143**, 102813 (2015).

[6] A. Marini, Phys. Rev. Lett. **101**, 106405 (2008).

[7] A. Molina-Sánchez, M. Palummo, A. Marini, and L. Wirtz , Phys. Rev. B **93**, 155435 (2016).

[8] Masami Seki, Koichi Kobayashi, and Junichiro Nakahara, J. Phys. Soc. Jpn. **50**, 2643-2648 (1981).

[9] V. Ziaei and T. Bredow, J. Chem. Phys. **145**, 174502 (2016).

[10] A. Marini, S. Poncé, and X. Gonze,
Phys. Rev. B **91**, 224310 (2015).

[11] F. Giustino, Rev. Mod. Phys. **89**, 015003 (2017).

[12] M. T. Dove, Introduction to lattice dynamics (Cambridge university press, 1993).

[13] Tomas K. Hirsch, and Lars Ojamäe, J. Phys. Chem. B, **108**, 15856-15864 (2004).

[14] J. VandeVondele, M. Krack, F. Mohamed, M. Parrinello, T. Chassaing, and J. Hutter, J. Comput. Phys. Commun. **167**, 103–128 (2005).

[15] S. Grimme, J. Antony, S. Ehrlich, and H. Krieg, J. Chem. Phys. **132**, 154104 (2010).

[16] J. P. Perdew, K. Burke, and M. Ernzerhof, Phys. Rev. Lett. **77**, 3865-3868 (1996).

[17] P. Giannozzi, S. Baroni, N. Bonini, M. Calandra, R. Car, C. Cavazzoni, D. Ceresoli, G. L. Chiarotti, M. Cococcioni, I. Dabo, A. Dal Corso, S. de Gironcoli, S. Fabris, G. Fratesi, R. Gebauer, U. Gerstmann, C. Gougoussis, A. Kokalj, M. Lazzeri, L. Martin-Samos, N. Marzari, F. Mauri, R. Mazzarello, S. Paolini, A. Pasquarello, L. Paulatto, C. Sbraccia, S. Scandolo, G. Sclauzero, A. P. Seitsonen, A. Smogunov, P. Umari, and R. M. Wentzcovitch, J. Phys. Condens. Matter **21**, 395502 (2009).

[18] N. Troullier and J. L. Martins,
Phys. Rev. B **43**, 1993-2006 (1991).

[19] A. Marini, C. Hogan, M. Gruening, and D. Varsano, Computer Phys. Commun. **180**, 1392-1403 (2009).

[20] ABINIT: First-principles approach to material and nanosystem properties, X. Gonze, B. Amadon, P.M. Anglade, J.-M. Beuken, F. Bottin, P. Boulanger, F. Bruneval, D. Caliste, R. Caracas, M. Cote, T. Deutsch, L. Genovese, Ph. Ghosez, M. Giantomassi, S. Goedecker, D. Hamann, P. Hermet, F. Jollet, G. Jomard, S. Leroux, M. Mancini, S. Mazevet, M.J.T. Oliveira, G. Onida, Y. Pouillon, T. Rangel, G.-M. Rignanese, D. Sangalli, R. Shaltaf, M. Torrent, M.J. Verstraete, G. Zérah, J.W. Zwanziger. Computer Phys. Commun. **180**, 2582-2615 (2009).

[21] X. Gonze, G.-M. Rignanese, M. Verstraete, J.-M. Beuken, Y. Pouillon, R. Caracas, F. Jollet, M. Torrent, G. Zerah, M. Mikami, Ph. Ghosez, M. Veithen, J.-Y. Raty, V. Olevano, F. Bruneval, L. Reining, R. Godby, G. Onida, D.R. Hamann, and D.C. Allan, Zeit. Kristallogr. **220**, 558-562 (2005).

[22] A. Marini, R. Del Sole, A. Rubio, and G. Onida, Phys. Rev. B **66**, 161104 (2002).

[23] V. Garbuio, M. Cascellai, L. Reining, R. Del Sole and O. Pulci, Phys. Rev. Lett. **97**, 137402 (2006).

[24] T. Anh Pham, C. Zhang, E. Schwegler, and G. Galli,
Phys. Rev. B **89**, 060202 (2014).

[25] V. Ziaei and T. Bredow, J. Chem. Phys. **145**, 064508 (2016).

[26] L. Hedin, Phys. Rev. Lett. **139**, A796 (1965).

[27] G. Strinati, Riv. Nuovo Cimento 11, 1 (1988)

[28] L. Reining et al., Phys. Rev. Lett. **88**, 066404 (2002).

[29] G. Adragna, R. Del Sole, and A. Marini, Phys. Rev. B **68**, 165108 (2003).

[30] F. Sottile, V. Olevano, and L. Reining, Phys. Rev. Lett. **91**, 056402 (2003).

[31] F. Bruneval et al., Phys. Rev. Lett. **94**, 186402 (2005).

[32] W. Chen, F. Ambrosio, G. Miceli, and A. Pasquarello, Phys. Rev. Lett. **117**, 186401 (2016).

[33] K. Kobayashi, J. Phys. Chem. **87**, 4317–4321 (1983).

[34] A. Bernas, C. Ferradini, and J.-P. Jay-Gerin, Chem. Phys. **222**, 151–160 (1997).

[35] S. V. Faleev, M. van Schilfgaarde, and T. Kotani, Phys. Rev. Lett. **93**, 126406 (2004).

[36] M. Shishkin, M. Marsman, and G. Kresse, Phys. Rev. Lett. **99**, 246403 (2007).

[37] A. Grüneis, G. Kresse, Y. Hinuma, and F. Oba, Phys. Rev. Lett. **112**, 096401 (2014).

[38] Andrey L. Kutepov, Phys. Rev. B **94**, 155101 (2016).

[39] Andrey L. Kutepov, Phys. Rev. B **95**, 195120 (2017).

[40] M. Del Ben, Jürg Hutter, and J. VandeVondele, J. Chem. Phys. **143**, 054506 (2015).

Chapter 4

Non-linear optics from a real-time ab-initio many-body approach

Introduction

The ab-initio Green's function theory presented in Chapter 2 proved to be a powerful and reliable method for calculations of linear response optical properties beyond the independent-particle approximation (IPA). The ab-initio Green's function approach accounts for important many-body effects, such as single-particle and excitonic effects through the self-energy and its derivative with respect to the Green's function. However, in contrast to the linear response Green's function theory, the inclusion of many-body effects for non-linear optical susceptibilities in the frequency-domain turns out to be an extremely difficult and challenging task, as the complexity of the corresponding non-linear expressions grows with increasing perturbation order. In order to reduce computational complexity introduced by higher-order non-linear expressions, a time-domain based approach is used [2–8], instead of operating in the usual frequency-domain (like in the standard GW/BSE approach discussed in Chapters 3).

In this time-domain approach the non-linear susceptibility is obtained from the dynamical polarization P of the system which is expanded in powers of the external field ε :

$$P = \chi(1)\varepsilon^1 + \chi(2)\varepsilon^2 + \chi(3)\varepsilon^3 + \dots \tag{4.1}$$

This domain transformation enormously simplifies the complexity allowing for an efficient calculation of non-linear optical spectra because of the following major advantages : (i) Crucial many-body effects can be easily taken into account by adding the corresponding operator to the effective Hamiltonian. (ii) The time-domain approach is not perturbative, meaning that the non-linear susceptibilities can be calculated on any external field order without increasing the computational cost.

However, one major problem still remains for both frequency and real-time based approaches. That is the correct definition of the position operator (length gauge) within the Born-von-Kàrmàn periodic boundary condition (PBC) for calculation of dipole matrix elements between the periodic part of the Bloch functions. A correct definition of the position operator within PBC was introduced by means of the geometric Berry phase in the modern theory of polarization [8]. This definition is used in the following.

To better understand this ab-initio real-time approach, in the following the fundamental equations are presented, and further the non-linear two-photon absorption spectrum of liquid water is shown, demonstrating the reliability of the real-time approach in predicting the experimental two-photon spectrum, and hence in general the non-linear phenomena.

4.1 Theoretical background

In the time-domain approach, a set of coupled one-particle effective time-dependent Schrödinger equations is solved :

$$i\hbar\frac{d}{dt}\left|v_{mk}\right\rangle = \left(H_k^{\mathrm{sys}} + i\varepsilon\,.\,\partial_k\right)\left|v_{mk}\right\rangle \tag{4.2}$$

where $|v_{mk}\rangle$ is the periodic part of the time-dependent Bloch functions, determining the system polarization, H_k^{sys} stands for the system Hamiltonian, and $\varepsilon\,.\,\partial_k$ describes the coupling with the external field ε in the dipole approximation. This coupling is gauge invariant and takes the form of a k-derivative ∂_k, since Born-von-Kàrmàn periodic boundary conditions are imposed.

By integrating Eq. (4.2), and from $|v_{mk}\rangle$, the time-dependent polarization of the system $P_{||}$ along the lattice vector $\mathbf{a}$ is calculated as:

$$P_{||} = -\frac{ef|\mathbf{a}|}{2\pi\Omega_c}\Im\log\prod_{i=k}^{N_k-1}\det S(k,k+q) \tag{4.3}$$

where $S(k,k+q)$ is the overlap matrix between the valence states $|v_{nk}\rangle$ and $|v_{mk+q}\rangle$, Ω_c is the unit cell volume, f is the spin degeneracy, N_k is the number of k points along the polarization direction, and $q = 2\pi/(N_k a)$. In Eq. (4.2) the system Hamiltonian incorporates different levels of approximation such as the following:

1) The independent-particle approximation:

$$H_k^{\mathrm{IP}} \equiv H_k^{\mathrm{KS}} \tag{4.4}$$

where H_k^{KS} is the unperturbed KS Hamiltonian.

2) The QP approximation:

$$H_k^{\mathrm{QP}} \equiv H_k^{\mathrm{KS}} + \Delta H_k \tag{4.5}$$

where a scissor operator shift ΔH_k is added to the KS Hamiltonian, estimated from the many-body perturbation theory in order to account for QP effects.

3) The full GW+BSE approximation:

$$H_k^{\mathrm{GW+BSE}} \equiv H_k^{\mathrm{KS}} + \Delta H_k + V_h(\mathbf{r})[\Delta\rho] + \Sigma_{SEX}[\Delta\gamma] \tag{4.6}$$

where $V_h(\mathbf{r})$ is the time-dependent Hartree term as a functional of density variation:

$$\Delta\rho \equiv \rho(\mathbf{r};t) - \rho(\mathbf{r};t=0) \tag{4.7}$$

The Hartree term describes the local-field effects arising from inhomogenities in crystal densities. Σ_{SEX} term is the screened exchange self-energy and accounts for the electron-hole effects (as known from the BSE in chapters 2 and 3). It is a functional of the variation of the density matrix induced by the external field ε. $\Delta\gamma$ is given as:

$$\Delta\gamma \equiv \gamma(\mathbf{r},\mathbf{r}';t) - \gamma(\mathbf{r},\mathbf{r}';t=0) \tag{4.8}$$

The terms beyond the KS Hamiltonian describe correlation effects impacting the non-linear spectra. It should be noted that in the limit of small perturbation Eq. (4.6) reproduces the standard GW + BSE optical absorption spectra. A schematic representation of the workflow of non-linear calculations is illustrated in Fig. 4.1 for a visual understanding.

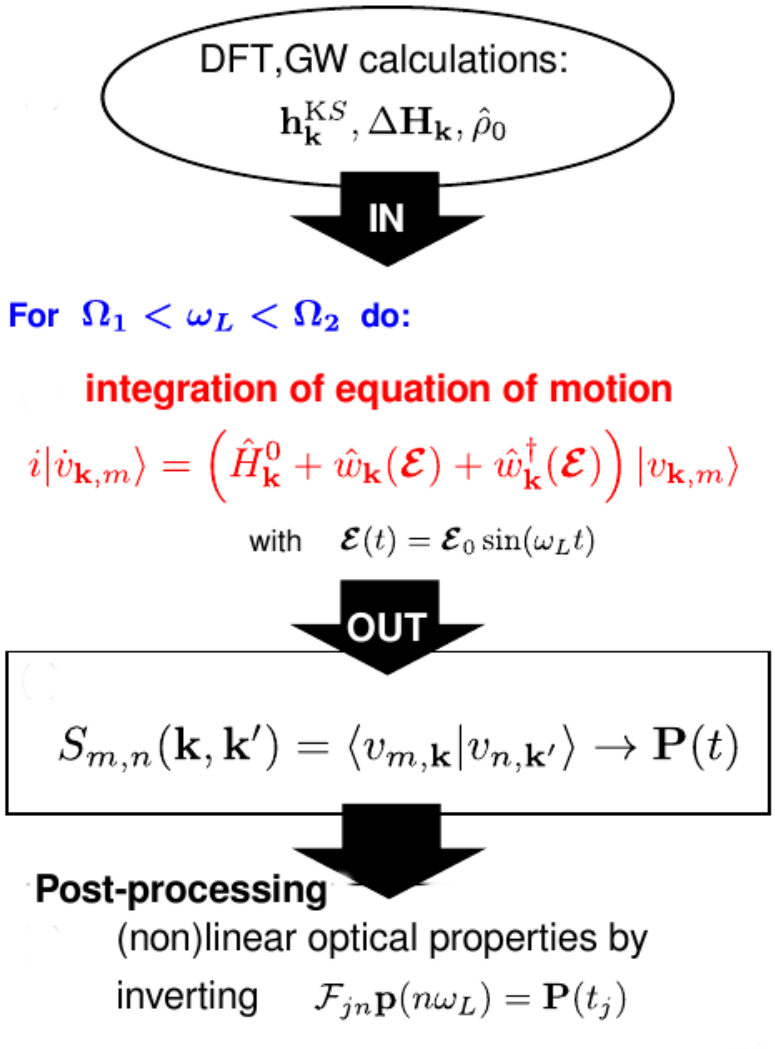

Figure 4.1: A real-time flowchart for ab-initio non-linear optical susceptibilities of periodic systems is shown. First, KS-DFT and QP energies are calculated. Then the effective one-particle Schrödinger equation is integrated in the time intervall $[\Omega_1, \Omega_2]$ for a small time step Δt to obtain the eigenvectors. Then, the overlap matrix S is constructed which further corresponds to polarization $P(t)$. The non-linear properties are then obtained in post-processing by Fourier-transformation of $P(t)$. Figure adopted from Ref. [8].

4.2 Two-photon absorption spectrum of liquid H_2O

Abstract

The two-photon absorption spectrum of liquid water is calculated using an ab-initio many-body real-time approach. Correlation effects, such as single-particle and excitonic effects are included, with the latter showing notable impact both on the structure and the peak positions of the two-photon spectrum. A broad absorption band at 10.0 eV is obtained, in excellent agreement with the experimental reference [1].

Introduction

The two-photon absorption (TPA) was first predicted by Göppert-Mayer in 1931 in her doctoral thesis. Thirty years later by invention of the laser the first experimental confirmation of the TPA was reported when two-photon-excited fluorescence was detected in a europium-doped crystal [13, 14].

TPA is a non-linear phenomenon which is related to the imaginary part of the third-order non-linear susceptibility. TPA follows different selection rules than one-photon absorption (1-PA). This stems from the fact that photons have spin of ± 1, therefore, one-photon absorption involves an electron changing its molecular orbital by an angular momentum of ± 1, while two-photon absorption requires a change of +2, 0, or -2, because of the involvement of two simultaneously incoming photons each of which with spin ± 1.

Since TPA is a third-order optical process and hence quite weak, a very high laser field intensity is required in order to realize a much faster increase of the strength of the interaction with the electric field of the light than in the linear process. Here for liquid water, the field intensity is set to 100000 kWL/m^2 in the calculations to simulate the experimental condition, and a monochromatic light with an energy of 6.2 eV is chosen to calculate the non-linear response.

Technical details

In the following the two-photon absorption spectrum of liquid water is calculated both at independent-particle with QP-energies and excitonic level. A ground-state calculation is performed with a density cutoff of 400 Ry using QUANTUM ESPRESSO [11], and the QP-energies are calculated within the frequency-dependent Green's function formalism using YAMBO [12]. In order to integrate Eq. (4.2), a polarization simulation is run for a time interval of 60 fs using the numerical approach described in Refs. [9, 10], with a time step of $\Delta t = 0.01$ fs which guarantees numerically stable and sufficiently accurate simulations.

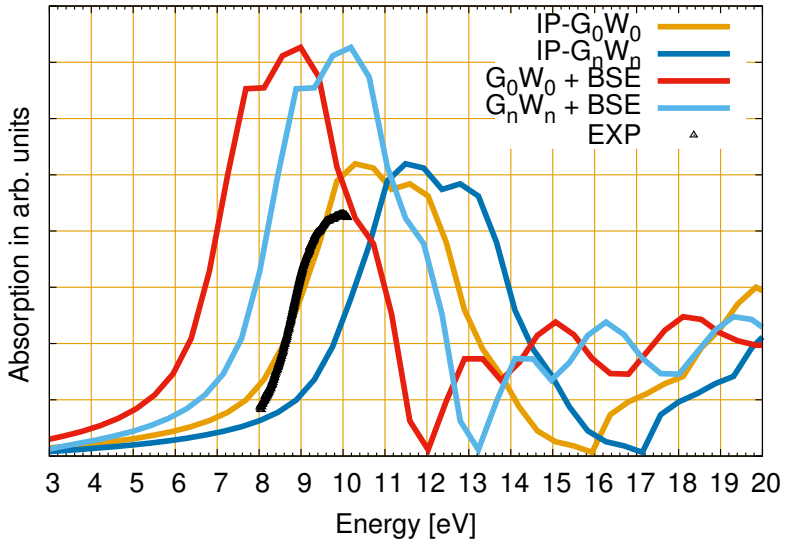

Figure 4.2: The calculated two-photon absorption spectra of liquid water (27-water box) based on the IP + G_0W_0, IP + G_nW_n, G_0W_0 + BSE, and G_nW_n + BSE methods are shown. A broad main peak at about 10 eV (fully consistent with the experimental reference (black tile)) followed by a shoulder at about 12 eV is observed based on the G_nW_n + BSE method. 64 (un)occupied bands are used as transition bands to achieve convergence for spectral weights.

A dephasing of 0.4 eV is used to simulate the experimental finite broadening. Simulation of time-dependent polarization is performed using LUMEN [8] which is a subprogram of YAMBO.

Correlation effects on non-linear spectrum

The effect of correlation on the TPA spectrum of water is analysed. The correlation terms included in the calculation of the TPA spectrum of water are listed as follows:

i) **IPA + QP**; ii) **IPA + QP + BSE (excitonic effects)**

The TPA spectra of the 27-water system averaged over only 5 configurations are shown in Fig. 4.2 within the independent-particle approximation with QP-energies, and screened exchange effects or equivalently excitonic effects (BSE). As can be seen, the IP@G_0W_0 and IP@G_nW_n methods overestimate the experimental broad band at 10.0 eV by 0.4 and 1.4 eV, respectively. Only if the excitonic effects are explicitly taken into account in combination with update of QP-energies in G and W, a quantitative agreement is reached with the experimental reference measured by Elles et al. [1] at 10.0 eV (the experimental spectrum was measured only between 8 and 10 eV). This underlines the fact that as for the linear

spectrum of water where excitonic correlations (coupled motion of electron-hole pairs) are of extreme importance for a quantitative description of the spectrum, such a two-particle correlation is important for the 3-order excitation (TPA) as well, altering weight distributions and peak positions.

An interesting point is that unlike the linear spectrum of liquid water where BSE on top of the G_0W_0 QP-energies was sufficient to quantitatively describe the experimental spectrum, for the non-linear spectrum, update of the QP energies (G_nW_n) is inevitable for an accurate agreement with experiment, since the BSE@ G_0W_0 method underestimates the experimental absorption band by about 1 eV. The averaged band gap calculated for this set of five water snapshots is 8.5 eV, and update of the QP energies results in a gap of 9.69 eV. This gap increase of almost 1.2 eV is reflected in the non-linear spectrum as a rigid blue-shift of the spectrum, improving considerably the agreement with the experimental reference in combination with excitonic effects.

This change of ansatz from G_0W_0 to G_nW_n for QP-energies in case of liquid water might be traced back to different selection rules required for non-linear spectra, i.e. excited states contributing to the broad absorption band at 10.0 eV have different character than those contributing in the first absorption band of the linear spectrum at 8.1 eV. In other words, in the two-photon spectroscopy higher lying states are excited.

Conclusions

The non-linear two-photon absorption spectrum of liquid water was calculated using an ab-initio many-body real-time approach which includes the single-particle and excitonic effects through addition of the corresponding Hamiltonians. In TPA the absorption band at 10.0 eV is blue-shifted by 1.9 eV compared to the absorption band of the linear spectrum at 8.1 eV. This shift is attributed to different states at different energies which are excited during two-photon excitation.

It was shown that the IP approximation with QP corrections overshoots the experimental absorption band. Inclusion of screened exchange or excitonic effects with update of QP-energies (BSE@G_nW_n) improves the spectrum remarkably compared to BSE@G_0W_0 spectrum, in which the absorption band is underestimated by about 1 eV. The TPA spectrum is considerably affected by higher-order correlation (excitonic) effects and hence they have to be explicitly taken into account in order to reach a quantitative agreement with exterimental references. Therefore, the importance of excitonic effects are not only constrained to the linear spectra but also to non-linear phenomena, altering weight distributions and peak positions.

Bibliography

[1] C. G. Elles, C. A. Rivera, Y. Zhang, P. A. Pieniazek, and S. E. Bradforth, J. Chem. Phys. **130**, 084501 (2009).

[2] C. Attaccalite, E. Cannuccia, M. Grüning, Phys. Rev. B **95**, 125403 (2017).

[3] C. Attaccalite, arXiv preprint arXiv:1609.09639

[4] M. Grüning, D Sangalli, C Attaccalite, Phys. Rev. B **94** (3), 035149 (2016).

[5] M. Grüning, C. Attaccalite, Phys. Chem. Chem. Phys. **18** (31), 21179-21189 (2016).

[6] C. Attaccalite, A. Nguer, E. Cannuccia, M. Grüning, Phys. Chem. Chem. Phys. **17** (14), 9533-9540 (2015).

[7] M. Grüning, C. Attaccalite, Phys. Rev. B **89** (8), 081102 (2014).

[8] C. Attaccalite, M. Grüning, Phys. Rev. B **88** (23), 235113 (2013).

[9] I. Souza, J. Iniguez, and D. Vanderbilt, Phys. Rev. B **69**, 085106 (2004).

[10] S. E. Koonin and C. M. Dawn, eds., Computational Physics: Fortran Version (Perseus Books, 2008).

[11] P. Giannozzi et al., J. Phys.: Condens. Matter **21**, 395502 (2009).

[12] A. Marini, C. Hogan, M. Grüning, and D. Varsano, Comput. Phys. Commun. **180**, 1392-1403 (2009).

[13] W. Kaiser, C. G. B. Garrett, Phys. Rev. Lett. **7** (6), 229 (1961).

[14] I. D. Abella, Phys. Rev. Lett. **9** (11), 453 (1962).

Chapter 5

GW/BSE with localized basis sets

In this chapter, it will be shown how the so far applied many-body equations (GW and BSE) translate, if finite basis sets are used.

The reason for the basis set change from the delocalized plane wave to the localized atom-centered basis functions follows from the fact that for finite systems artificial interactions with their periodic images become increasingly a problem. This hinders to calculate the electronic and optical properties of atoms, molecules and clusters. The issue of artificial interactions can not be solved by simply increasing the size of the simulation box, as the electrostatic potental is long-range in nature, and the undesired effect increases with system size.

Furthermore, such periodic box calculations with large amount of vacuum require a high energy cutoff, i.e. a large number of G vectors, rendering the computations intractable, even for small molecular systems. Beside this, parallel to the increase of box volume, the GW and BSE parameters, such as number of unoccupied bands, cutoff of the dielectric matrix, exchange components and unoccupied bands (due to increase of the number of empty states upon increasing the volume) have to be accordingly scaled up, restricting massively the range of applicability of GW/BSE theory due to very slow convergence.

Therefore, the only way to get rid of such plane wave related shortcomings is to represent the self-consistent quantum field equations (Hedin equations) in terms of localized basis functions [1].

5.1 Theoretical background

5.1.1 Gaussian basis set

In both Hartree-Fock and Kohn-Sham theory one starts with a ground-state calculation which gives access to the electronic structure of the system. To do so, one has to first find a proper basis set representation for the wave functions. A good ansatz is to expand the electronic wave function as linear combinations of atomic orbitals ϕ_μ :

$$\varphi_n^\sigma(\mathbf{r}) = \sum_\mu C_{\mu n}^\sigma \phi_\mu(\mathbf{r}) \tag{5.1}$$

with ϕ_μ represented by linear combinations of Gaussian orbitals or "contracted Gaussians" given by :

$$\phi_\mu(\mathbf{r}) = x^{l_x} l^{n_y} l^{n_z} \sum_b c_b e^{-\alpha_b r^2} \tag{5.2}$$

Now in order to calculate the wavefunction's coefficients C^σ introduced in Eq. (5.1), one has to solve the non-linear Roothaan-Hall equations :

$$H^\sigma C^\sigma = S C^\sigma \epsilon^\sigma \tag{5.3}$$

where S is the basis function overlap matrix :

$$S_{\mu\nu} = \int d\mathbf{r} \phi_\mu(\mathbf{r}) \phi_\nu(\mathbf{r}) \tag{5.4}$$

and H is the spin-dependent Hamiltonian, describing formally all interactions in the many-body ensemble

$$H_{\mu\nu}^\sigma = T_{\mu\nu} + (V_{ext})_{\mu\nu} + J_{\mu\nu} - \alpha K_{\mu\nu}^\sigma - (\alpha - 1)(V_x^\sigma)_{\mu\nu} + (V_c^\sigma)_{\mu\nu} \tag{5.5}$$

with the kinetic energy :

$$T_{\mu\nu} = -\frac{1}{2} \int d\mathbf{r} \lim_{\mathbf{r}' \to \mathbf{r}} \phi_\mu(\mathbf{r}) \nabla_{\mathbf{r}'}^2 \phi_\nu(\mathbf{r}') \tag{5.6}$$

the external potential energy term :

$$(V_{ext})_{\mu\nu} = -\sum_a \int d\mathbf{r} \phi_\mu(\mathbf{r}) \frac{Z_a}{|\mathbf{r} - \mathbf{R}_a|} \phi_\nu(\mathbf{r}) \tag{5.7}$$

with Z_a, $\mathbf{R}_a$ and $\mathbf{r}$ as the charge and the position of the nuclei, and the electrons. Further, the classical electrostatic interaction $J_{\mu\nu}$ reads as :

$$J_{\mu\nu} = \sum_{\lambda\tau} (\mu\nu|\lambda\tau) \sum_{\sigma} P^{\sigma}_{\lambda\tau} \tag{5.8}$$

where P is the density matrix, constructed out of the coefficients of the expanded wave functions :

$$P^{\sigma}_{\mu\nu} = \sum_{n} f^{\sigma}_{n} C^{\sigma}_{\mu n} C^{\sigma}_{\nu n} \tag{5.9}$$

with f^{σ}_{n} as the occupation number, as well as the electron-electron repulsion integral in Mulliken notation :

$$(\mu\nu|\lambda\tau) = \int\int d\mathbf{r} d\mathbf{r}^{'} \phi_{\mu}(\mathbf{r}) \phi_{\nu}(\mathbf{r}) \frac{1}{|\mathbf{r} - \mathbf{r}^{'}|} \phi_{\lambda}(\mathbf{r}^{'}) \phi_{\tau}(\mathbf{r}^{'}) \tag{5.10}$$

The exchange interactions $K^{\sigma}_{\mu\nu}$

$$K^{\sigma}_{\mu\nu} = \sum_{\lambda\tau} P^{\sigma}_{\lambda\tau} (\mu\lambda|\tau\nu) \tag{5.11}$$

And finally the exchange and correlation potentials $V_{x,c}$ (in the case of DFT hybrid methods [1]):

$$(V^{\sigma}_{x,c})_{\mu\nu} = \langle\mu| \, v_{x,c}[n^{\sigma}(\mathbf{r}), \nabla_{\mathbf{r}} n^{\sigma}(\mathbf{r})] \, |\nu\rangle \tag{5.12}$$

with the density and density gradient obtained from :

$$n^{\sigma}(\mathbf{r}) = \sum_{\mu\nu} P^{\sigma}_{\mu\nu} \phi_{\mu}(\mathbf{r}) \phi_{\nu}(\mathbf{r}) \tag{5.13}$$

$$\nabla_{\mathbf{r}} n^{\sigma}(\mathbf{r}) = \sum_{\mu\nu} P^{\sigma}_{\mu\nu} \nabla_{\mathbf{r}} [\phi_{\mu}(\mathbf{r}) \phi_{\nu}(\mathbf{r})] \tag{5.14}$$

The evaluation of the repulsion molecular integrals (written in Mulliken notation) is done by using recursion formulas [2] as implemented e.g. in the libint library [3].

Furthermore, the integration in the exchange-correlation potential (Eq. 5.12) is performed numerically by partitioning the space in smooth regions around each atom using Becke [4] or SSF schemes [5] and then discretizing the space around each atom by a radial and angular mesh [6, 7].

Finally, due to the non-linear nature of the eigenvalue equation (Eq. 5.3) (dependence of the terms J, K, V_{xc} on the density matrix), the Roothaan-Hall equations are solved

self-consistently to obtain the one-electron wave functions and energies.

Auxiliary basis set

The appearance of 4-center molecular integrals in Hartree and exchange terms poses a great deal of difficulty in terms of computational efficiency and memory consummation for evaluation of the molecular integrals. Therefore, auxiliary basis sets have been proposed [8–10] to massively reduce the costs. This technique, also known as the resolution-of-the-identity, replaces the 4-center molecular integrals in terms of the product of 2- and 3 center integrals, as

$$(\mu\nu|\lambda\tau) \approx \sum_{PQ} (\mu\nu|P)(P|Q)^{-1}(Q|\lambda\tau) \tag{5.15}$$

where the 3-center integrals read

$$(\mu\nu|P) = \int\int d\mathbf{r}d\mathbf{r}^{'}\phi_{\mu}(\mathbf{r})\phi_{\nu}(\mathbf{r})\frac{1}{|\mathbf{r}-\mathbf{r}^{'}|}\phi_{P}(\mathbf{r}^{'}) \tag{5.16}$$

and the 2-center integrals are

$$(P|Q) = \int\int d\mathbf{r}d\mathbf{r}^{'}\phi_{P}(\mathbf{r})\frac{1}{|\mathbf{r}-\mathbf{r}^{'}|}\phi_{Q}(\mathbf{r}^{'}) \tag{5.17}$$

The capital letters P and Q are the auxiliary basis indexes.

Due to the approximative nature of this technique, good auxiliary basis sets are required. The basis sets proposed by Weigend [10] are of high accuracy for the evaluation of the Hartree J and Fock exchange term K, and are frequently used in quantum chemistry, known as "RI-JK" approximation.

5.1.2 Polarizability in product basis

One of the most important ingredient in many-body perturbation theory is the dynamically screened interaction W which appears in self-energy both within the random phase approximation (RPA) and in BSE. In order to evaluate W, one needs to start from polarization.

As outlined in chapter 2 polarization in many-body perturbation theory is described by the 4-point Green's function equation. This non-linear equation is transformed into matrix form in transition space [1] spanned by occupied and unoccupied orbitals (product basis) :

$$\begin{pmatrix} A & B \\ -B & -A \end{pmatrix} \begin{pmatrix} X^{s} \\ Y^{s} \end{pmatrix} = \begin{pmatrix} X^{s} \\ Y^{s} \end{pmatrix} \Omega_{s} \tag{5.18}$$

where Ω_s are the neutral excitation energies and (X^s,Y^s) are the corresponding eigenvectors

The Eq. (5.18) is a general formulation of neutral excitations and includes all the related theories such as RPA, TD-HF, TD-DFT and BSE, with the only difference being in the specific expression of the matrix elements in A and B. The blocks specified as A and B read :

$$A_{ia\sigma}^{jb\sigma'} = (\epsilon_a^\sigma - \epsilon_i^\sigma)\delta_{ij}\delta_{ab}\delta_{\sigma\sigma\prime} + (ia\sigma|jb\sigma') + \Xi_{ia\sigma}^{jb\sigma'} \tag{5.19}$$

$$B_{ia\sigma}^{jb\sigma'} = (ia\sigma|bj\sigma') + \Xi_{ia\sigma}^{bj\sigma'} \tag{5.20}$$

where the operator Ξ stands for the kernel. In case of RPA, $\Xi = 0$. The integrals in Eq. (5.19 and 5.20) are defined as :

$$(ia\sigma|jb\sigma') = \int\int d\mathbf{r}d\mathbf{r}'\varphi_i^\sigma(\mathbf{r})\varphi_a^\sigma(\mathbf{r})\frac{1}{|\mathbf{r}-\mathbf{r}'|}\varphi_j^{\sigma'}(\mathbf{r}')\varphi_b^{\sigma'}(\mathbf{r}') \tag{5.21}$$

for which the resolution-of-the-identity approximation is used.

After some algebra [11], the Eq. (5.18) can be cast into a more compact form :

$$CZ^s = Z^s\Omega_s^2 \tag{5.22}$$

where $C = (A-B)^{1/2}(A+B)(A-B)^{1/2}$ is a symmetric matrix with now the half of the dimension of the initial equation. Further, from the knowledge of the eigenvector Z^s, one can recover X^s and Y^s as :

$$X^s = \frac{1}{2}\left[\Omega_s^{-1/2}(A-B)^{1/2} + \Omega_s^{1/2}(A-B)^{1/2}\right]Z^s \tag{5.23}$$

$$Y^s = \frac{1}{2}\left[\Omega_s^{-1/2}(A-B)^{1/2} - \Omega_s^{1/2}(A-B)^{1/2}\right]Z^s \tag{5.24}$$

Now, with the eigenvalues Ω_s and the eigenvectors (X^s,Y^s) obtained through diagonalization of Eq. (5.22), the matrix multiplications in Eqs. (5.23 and 5.24), the spectral representation of the polarizability and the screened Coulomb interaction, one arrives at the final expression for W :

$$W_{mn\sigma}^{op\sigma'} = (mn\sigma|op\sigma') + \sum_s w_{mn\sigma}^s w_{op\sigma'}^s\left(\frac{1}{\omega-\Omega_s+i\eta} - \frac{1}{\omega+\Omega_s-i\eta}\right) \tag{5.25}$$

where the residues $w_{mn\sigma}^s$ are defined as :

$$w_{mn\sigma}^s = \sum_{ia\sigma'}(mn\sigma|ia\sigma')(X_{ia\sigma'}^s + Y_{ia\sigma'}^s) \tag{5.26}$$

The first term on the r.h.s. of the Eq. (5.25) is the Fock exchange term, and the second term refers to the dynamic correlation part.

5.1.3 GW self-energy

Based on the spectral decomposition of W (Eq. (5.25)) and the residuum theorem, the GW self-energy can be calculated analytically, meaning that it is computed exactly at each frequency point. The correlation part of the self-energy Σ_c (diagonal components) reads as

$$\Sigma^{\sigma}_{c,nn} = \sum_{is} \frac{w^s_{ni\sigma} w^s_{ni\sigma}}{\omega - \epsilon^{\sigma}_i + \Omega_s - i\eta} + \sum_{ms} \frac{w^s_{nm\sigma} w^s_{nm\sigma}}{\omega - \epsilon^{\sigma}_m + \Omega_s - i\eta} \tag{5.27}$$

with the convention that index a runs over unoccupied orbitals and i runs over occupied orbitals. Hedin's static approximation to GW; "Coulomb-hole plus screened exchange" (COHSEX) as introduced in Chapter 2, can now be deduced from Eq. (5.27) by considering the limit of $\Omega_s \gg |\omega - \epsilon^{\sigma}_m|$:

$$\Sigma^{\sigma}_{c,nn} = 2\sum_{is} \frac{w^s_{ni\sigma} w^s_{ni\sigma}}{\Omega_s} - \sum_{ms} \frac{w^s_{nm\sigma} w^s_{nm\sigma}}{\Omega_s} \tag{5.28}$$

The first term in Eq. (5.28) is the screened exchange (a quantum contribution), whereas the second one is the Coulomb hole which is a pure classical term, inducing a rigid energy shift.

5.1.4 Excitation energies from BSE

Regarding optical excitations, BSE is a particular case of the polarizability equation written in Eqs. (5.18,5.19,5.20). In the standard static BSE, the kernel Ξ reduces to

$$\Xi^{jb\sigma'}_{ia\sigma} = -\delta_{\sigma\sigma'} W^{ab\sigma'}_{ij\sigma}(\omega = 0) \tag{5.29}$$

with $W(\omega = 0)$ as the RPA screened Coulomb interaction evaluated at $\omega = 0$. Because $W(\omega = 0)$ is already calculated in the GW part, it can be reused for the BSE kernel Ξ by plugging (5.25) into (5.29) :

$$\Xi^{jb\sigma'}_{ia\sigma} = -\delta_{\sigma\sigma'} \left[(ij\sigma|ab\sigma) - 2\sum_{s} \frac{w^s_{ij\sigma} w^s_{ab\sigma}}{\Omega_s} \right] \tag{5.30}$$

After build up of the BS matrix and its diagonalization, one obtains the excitation energies which can be directly compared with experiment. For instance, the photo-absorption cross

section tensor $\sigma_{xx'}(\omega)$ [73] is given as :

$$\sigma_{xx'}(\omega) = -\frac{4\pi\omega}{c} \sum_s f_x^s f_{x'}^s \left(\frac{1}{\omega - \Omega_s + i\eta} - \frac{1}{\omega + \Omega_s + i\eta} \right) \tag{5.31}$$

with the oscillator strength f_x^s :

$$f_x^s = \sum_{ia\sigma} \langle i\sigma | \hat{x} | a\sigma \rangle \left(X_{ia\sigma}^s + Y_{ia\sigma}^s \right) \tag{5.32}$$

The symbol $\hat{x}$ is the position operator along the x direction in space.
In the limit of a complete basis set, the sum of the oscillator strengths equals the number of electrons in the system (Reiche-Kuhne sum rule [11]).

After this practical introduction into the formulation of the GW/BSE theory within localized basis set, in the following some crucial applications and performance of the methodology are presented on large molecular systems with some thousands auxiliary basis functions, and it is shown how this methodology manages to correctly predict excitation energies with high accuracy in a fully parameter-free manner.

Bibliography

[1] F. Bruneval, T. Rangel, S.M. Hamed, M. Shao, C. Yang, and J.B. Neaton, Comput. Phys. Commun. **208**, 149 (2016).

[2] S. Obara, A. Saika, J. Chem. Phys. **84** (7), 3963-3974 (1986).

[3] E. F. Valeev, http://libint.valeyev.net/ (2016).

[4] A. D. Becke, J. Chem. Phys. **88**, (4) 2547-2553 (1988).

[5] R. Stratmann, G. E. Scuseria, M. J. Frisch, Chem. Phys. Lett. **257**, 213-223 (1996).

[6] V. I. Lebedev, and D. N. Laikov, Doklady Mathematics **59** (3) 477-481 (1999).

[7] M. E. Mura, and P. J. Knowles, J. Chem. Phys. **104** (24), 9848-9858 (1996).

[8] K. Eichkorn, O. Treutler, H. hm, M. Hser, R. Ahlrichs, Chem. Phys. Lett. **240** (4), 283-290 (1995).

[9] K. Eichkorn, F. Weigend, O. Treutler, R. Ahlrichs, Theor. Chem. Acc. **97** (1-4), 119-124 (1997).

[10] F. Weigend, Phys. Chem. Chem. Phys. **4**, 4285-4291 (2002).

[11] C. A. Ullrich, Oxford Graduate Texts, Oxford University Press, Oxford, New York, 2012.

5.2 GW/BSE approach on the vertical S_1 energy of large charge transfer compounds

Abstract

In this section, many-body perturbation theory is applied on large charge-transfer (CT) complexes to assess its performance on the S_1 excitation energy. Since the S_1 energy of CT compounds is strongly dependent on the Hartree-Fock exchange fraction in the reference density functional [1], MBPT opens an alternative way for reliable predictions to hybrid TD-DFT. By starting from a (semi-)local reference functional and performing an update of the Kohn-Sham (KS) energies in the Green's function G while keeping dynamical screened interaction $W(\omega)$ frozen to the mean-field level, it is possible to obtain accurate S_1 energies at slightly higher computational cost in comparison to TD-DFT. However, this energy-only updating mechanism in G fails if the initial guess contains a fraction or 100% HF exchange, and hence considerably inaccurate S_1 energies are obtained. Furthermore, eigenvalue updating both in G and $W(\omega)$ leads to overestimation of the S_1 energy due to enhanced underscreening of $W(\omega)$, independent of the (hybrid-)DFT starting orbitals. A full energy-update on top of HF orbitals, even further overestimates the S_1 energy. An additional update of KS wave functions within the Quasi-Particle Self-Consistent GW (QSGW) deteriorates results. This is in contrast to the good results obtained from QSGW for periodic systems. For the sake of transferability, data of small critical non-charge transfer systems are presented in the last part, confirming the outcomes of the CT-systems.

Introduction

The high relevance of donor-acceptor compounds for applications in organic photonics and electronics requires theoretical methods with reliable prediction power for charge-transfer (CT) excitation energies. Time-dependent density functional theory (TD-DFT) [17, 18] is the most widely used theoretical tool for prediction of excited-state properties from small to large molecules. However the calculated transition energies of CT compounds are heavily dependent on the fraction of HF exchange in the underlying density functional. Therefore a theoretical method is required that does not contain the HF exchange component as adjustable parameter. In recent years, MBPT [1–4, 19] attracted much interest for calculation of finite systems electronic and optical properties such as total energy, ionization potentials, electron affinity and excitation energies [5–12, 12, 13, 25, 26]. It was shown that MBPT with update of molecular orbital energies (known as eigenvalue self-consistency) diminishes the aforementioned functional dependency in organic systems to a large degree [15]. Furthermore, this approach does not require correction concerning the long-range behavior of the TD-DFT exchange functional, avoiding incorporation of further parameters as in range-

separated density functionals.

Concerning CT-systems, Faber et al. [14] demonstrated the potential capabilities of GW/BSE in targeting CT states in form of energy-only update of KS energies for small molecules, leading to a remarkable improvement of excitation energies and correct level alignment.

In this chapter, the reliability and predictive power of the GW/BSE formalism is studied in depth with respect to energy and wave function update both in the Green's function G and dynamically screened interaction $W(\omega)$ for large and critical CT complexes for which sophisticated TD-DFT functionals such as CAM-B3LYP and LC-BLYP miserably fail to predict correct S_1 energies. Possible effects of self-consistency on the HOMO-LUMO gap and S_1 energy in dependence of reference starting points with and without HF-exchange contribution are investigated. For the sake of transferability of results, the same method within the same self-consistency variants is also applied on selected small molecules, water, ammonia, hydrogen fluoride, phosphine and hydrogen sulfide, as their S_1 energies show quite large dependency on the amount of HF exchange.

This study involves thermally activated delayed fluorescence (TADF) materials as schematically depicted in Fig. 5.1 : 4,5-di (9H-carbazol-9-yl) phthalonitrile (2CzPN), phenoxazine-2,4,6-triphenyl-1,3,5-triazine (PXZ-TRZ), and 2',7'-bis (di-p-tolylamino)-9,9'-spirobifluorene-2,7-dicarbonitrile (Spiro-CN). The TADF materials as emitters for fluorescence-based organic light-emitting diodes continue to attract interest because of their high exciton production efficiency which is normally limited in simple fluorescent molecules [23,24]. TADFs are known CT-systems with spatially separated highest occupied molecular orbital (HOMO) and lowest unoccupied molecular orbital (LUMO). The S_1 state energy of these compounds calculated with TD-DFT shows a large dependency on the percentage of HF exchange [1]. The goal is to let GW/BSE find in an automatic and self-regulative manner the proper amount of HF exchange to predict the correct S_1 excitation energy from both HF exchange free (LDA, PBE) and containing (PBE0, HF) starting points.

Technical details

All many-body calculations are performed using MOLGW [29, 30] on top of B3LYP [28] optimized structures taken from Ref. 24. Results are given with respect to three starting density functionals, namely LDA, PBE [29], PBE0 [30] and exact HF with aug-cc-pVDZ basis sets [33] using the resolution of identity (RI) [31, 32] and frozen core approximation. Basis set dependency of the excitation energy (S_1) investigated for 2CzPN using aug-cc-pVDZ and aug-cc-pVTZ basis sets shows a small increase of S_1 energy of about 0.01 eV (Fig. 5.12), indicating that GW/BSE is not highly sensitive to the choice of basis set, as also

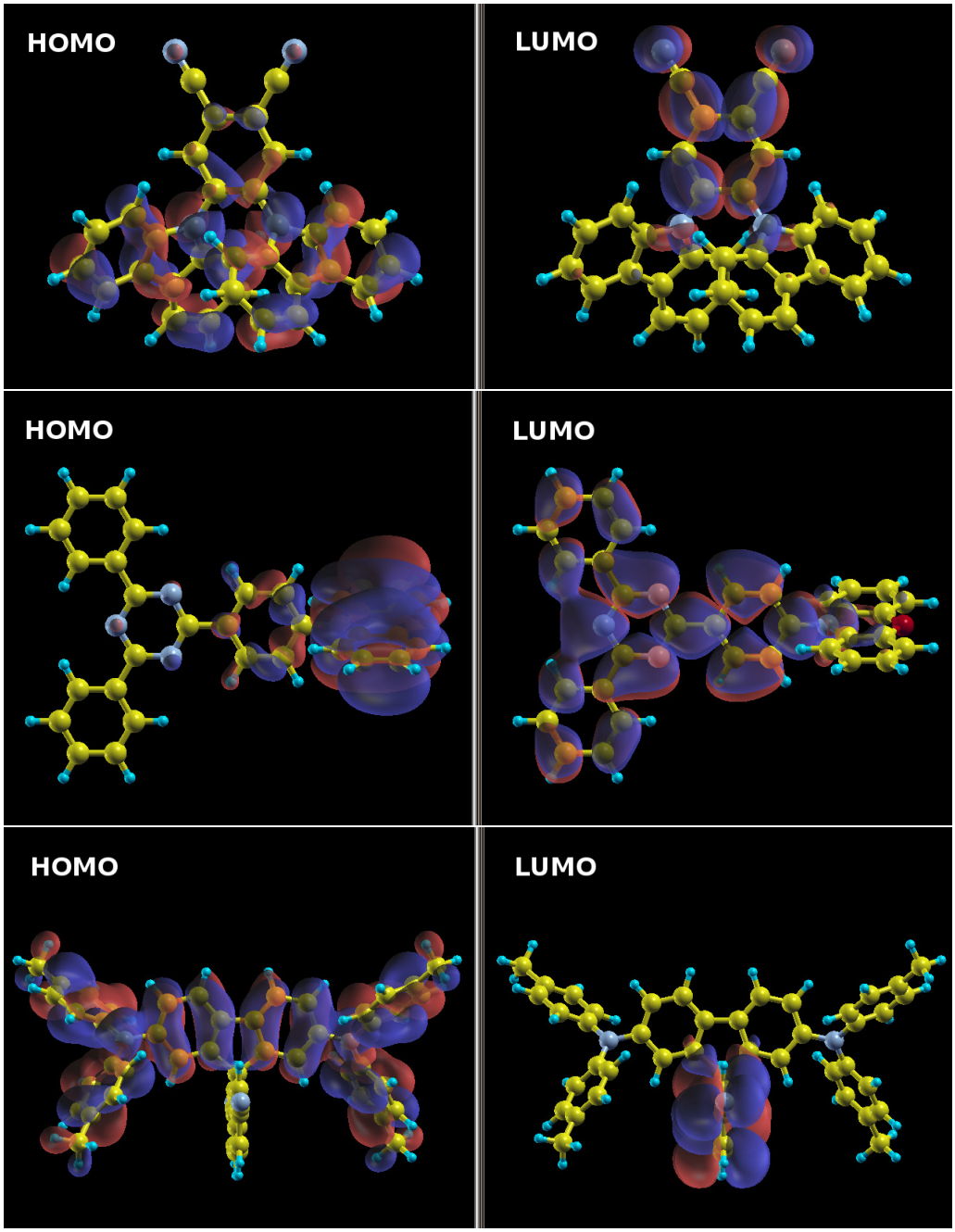

Figure 5.1: HOMO and LUMO PBE orbitals of the TADF systems from up to down : 2CzPN, PXZ-TRZ and Spiro-CN.

verified by Jacquemin et al. [15] for a large set of organic molecules with an average absolute deviation of 0.017 eV between aug-cc-pVDZ and aug-cc-pVTZ. By applying the frozen core approximation, the S_1 energy is decreased by about 0.01 eV with respect to an all-electron calculation in the case of 2CzPN. Therefore, semi-core and valence electrons are sufficient to be taken into account, together with 300 virtual orbitals in G and W to guarantee the convergence of HOMO-LUMO gaps within 50 meV accuracy. Furthermore, the pole structure of the screened interaction W is captured by spectral representation, giving rise to an analytic computation of the G_0W_0 self-energy at any frequency. The Quasi-Particle equation is diagonalized exactly, and thus the usual perturbative treatment of QP energies is avoided in order to reach a high level of accuracy. Concerning self-consistency, update of the wave function is performed only for 2CzPN due to extremely high computational load. Furthermore, the S_1 energy is calculated in the limit of adiabatic (static) kernel for the full Bethe-Salpeter matrix in the transition space, meaning that resonant and anti-resonant contributions are mixed. The results of the small molecules are compared with equation of motion coupled cluster singles and doubles (EOM-CCSD) using PSI4 [34].

Results and discussion

I. 2CzPN

The accuracy of the predicted S_1 energy strongly depends on an accurate calculation of the HOMO-LUMO gap [15,26]. As shown in Table 5.1, plain LDA severely underestimates the gap (2.08 eV compared to the QSGW result 7.18 eV and the reference value of G_nW_0@PBE (6.02 eV)). The non-iterative scheme of GW (G_0W_0) corrects the gap to 5.82 eV leading to a S_1 excitation energy of 2.84 eV (Table 5.2 and Fig. 5.2), with an acceptable error of -0.35 eV with respect to the experimental reference (3.19 eV). However, with energy-update in G while keeping W fixed to LDA, HOMO-LUMO gap is further improved and the S_1 energy is now in much better agreement with the experimental data. The S_1 state based on BSE@G_nW_0@LDA is mainly a HOMO $\rightarrow$ LUMO transition with an amplitude of 0.69, consistent with TD-DFT. Energy-update both in G and W makes the gap and the S_1 energy largely independent of the (hybrid-)DFT starting points. However, the S_1 energy obtained from the full eigenvalue self-consistency on top of (hybrid-)DFT is considerably overestimated due to underscreening of W. This overestimation at molecular level is consistent with the results of Kresse et al. [35] for periodic systems, where electronic band gaps of semiconductors are overestimated upon self-consistency in the Green's function and $W(\omega)$.

Probably the most interesting reference point in view of a critical assessment of different GW variants is HF, as it contains 100% exact exchange. The emerging question is whether GW is able to regulate the exchange by screening through update of KS energies to a proper

Table 5.1: HOMO-LUMO gaps of 2CzPN in eV obtained for different starting functionals and self-consistency levels in GW.

method@	LDA	PBE	PBE0	HF
DFT/HF	2.08	2.12	3.70	8.74
G_0W_0 (n=0)	5.82	4.93	6.13	7.33
G_nW_0 (n=5)	5.97	6.02	6.37	7.26
G_nW_n (n=5)	6.51	6.55	6.61	7.09
QSGW	7.18	—	—	7.17

Table 5.2: S_1 excitation energies of 2CzPN in eV with aug-cc-pVDZ basis set. TD-DFT results (1) are from Ref. 1.

BSE@	G_0W_0@LDA	G_nW_0@LDA	G_nW_n@LDA
S_1	2.84	3.19	3.73
BSE@	G_0W_0@PBE	G_nW_0@PBE	G_nW_n@PBE
S_1	2.14	3.23	3.77
BSE@	G_0W_0@PBE0	G_nW_0@PBE0	G_nW_n@PBE0
S_1	3.28	3.52	3.77
BSE@	G_0W_0@HF	G_nW_0@HF	G_nW_n@HF
S_1	4.40	4.33	4.14
TD-DFT@	CAM-B3LYP[1]	LC-BLYP[1]	LC-wPBE[1]
S_1	3.68	4.35	4.23
TD-DFT@	PBE0[1]	HSE06[1]	EXP.[1]
S_1	2.99	2.86	3.19

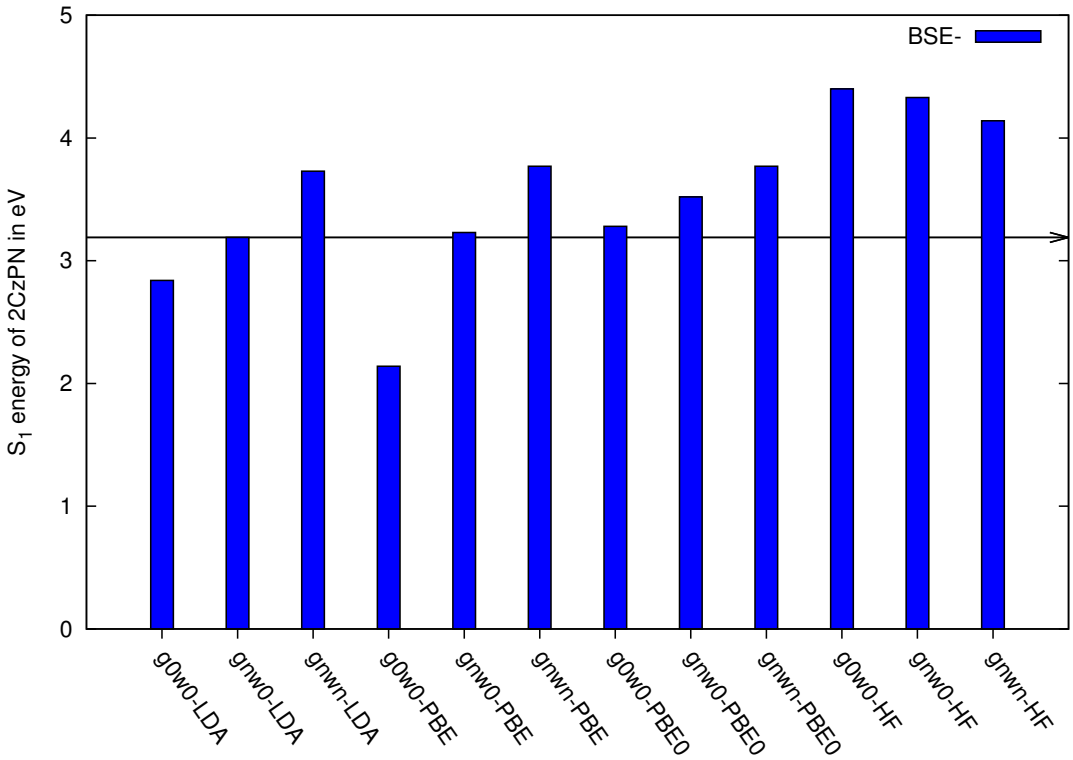

Figure 5.2: S_1 Vertical transition energy of 2CzPN in eV. The black line represents the experimental reference [1].

amount suitable for CT description or not. As can be seen from Table 5.1, G_0W_0@HF dramatically overestimates the QP gap relative to G_nW_0@LDA, and performing eigenvalue self-consistency (G_nW_0@HF and G_nW_n@HF) reduces the G_0W_0@HF QP gap only by 0.24 eV. Thus, the HF reference deteriorates the performance of the G_nW_0 and G_nW_n schemes, and the updating mechanism is not capable of lowering HF starting point dependency. In comparison to LDA, the increase of the QP gap from G_nW_n@LDA (6.51 eV) to G_nW_n@HF (7.09 eV) is due to incorporated exchange, as for both, the screening is treated at the same updating level. Further, as upon photo-excitation orbitals are relaxed, the effect of full self-consistency is investigated, i.e. update of energies and wave functions both in G and W within the Quasi-Particle Self-Consistent method (QSGW) to address possible inadequacies incorporated by HF reference orbitals. According to Table 5.1, even an additional orbital update fails to improve the (G_nW_0,G_nW_n)@HF results, and only a very small correction is obtained. Performing QSGW on top of LDA again yields an overestimated QP gap with respect to G_nW_0@PBE, very similar to QSGW@HF. This shows that QSGW is fully independent of the starting point. Interestingly G_nW_n@HF (7.09 eV) and QSGW (7.17 eV) nearly give the same QP gaps. This suggests that HF and QSGW orbitals largely overlap, and only a minor orbital modification is obtained with QSGW.

The overestimated QSGW QP gap with respect to the G_nW_0@PBE method is however a surprising finding as for periodic systems the deficiencies of the traditional self-consistent GW (sc-GW) are eliminated by introduction of a new kind of self-consistency (QSGW) [36], as otherwise sc-GW leads to underscreening of $W(\omega)$ in solids and hence to overestimation of a range of quantities due to spectral weight transfer to the incoherent part of the Green's function [37]. Therefore, QSGW restores the typical behaviour of sc-GW observed for solids in CT molecular systems. This further deteriorates the accuracy of excitation energies as subsequent optical response calculations strongly depend on QP gaps.

As can be seen from the calculated S_1 energies compiled in Table 5.2, results in excellent agreement with the experimental data are obtained from BSE@G_0W_0@PBE0 and BSE@G_nW_0@(LDA,PBE) strategies. By contrast, BSE@G_nW_n@HF overestimates the S_1 energy by about 1 eV. This means that the incorporated exchange in the underlying HF orbitals can not be properly damped, neither by energy nor by wave function update in G and W to obtain a QP gap similar to G_nW_0@LDA.

II. PXZ-TRZ

For PXZ-TRZ results concerning QP gaps and S_1 energies are compiled in Tables 5.3 and 5.4. Again G_0W_0 improves the DFT HOMO-LUMO gap, and energy-update in G on top of (semi-)local functionals opens the gap further to give a good basis for the subsequent BSE calculations. Furthermore, a full eigenvalue self-consistency largely decreases the (hybrid-)DFT dependency of QP gap and S_1 energy. However, G_nW_n@(LDA,PBE,PBE0,HF) consistently overestimate the G_nW_0@LDA QP gap and consequently the S_1 energy.

The exchange effect in PXZ-TRZ shown by the difference between G_nW_n@LDA (5.66 eV) and G_nW_n@HF (6.44 eV) QP gaps is about 0.8 eV, much larger than 2CzPN, both results leading to overestimated S_1 energies. Again best S_1 predictions are obtained from BSE@G_0W_0@PBE0 and BSE@G_nW_0@(LDA,PBE). The S_1 state based on BSE@G_nW_0@LDA mainly consists of HOMO $\rightarrow$ LUMO and HOMO $\rightarrow$ LUMO + 2 transitions with amplitudes of 0.66 and 0.16, respectively.

Table 5.3: HOMO-LUMO gap of PXZ-TRZ in eV obtained for different starting functionals and self-consistency levels in GW.

Method@	LDA	PBE	PBE0	HF
DFT/HF	1.20	1.27	2.94	7.94
G_0W_0 (n=0)	4.53	4.62	5.31	6.64
G_nW_0 (n=5)	5.09	5.15	5.53	6.56
G_nW_n (n=5)	5.66	5.71	5.81	6.44

Table 5.4: S_1 excitation energies of PXZ-TRZ in eV with aug-cc-pVDZ basis set. TD-DFT results (1) are from Ref. 1.

BSE@	G_0W_0@LDA	G_nW_0@LDA	G_nW_n@LDA
S_1	2.13	2.66	3.26
BSE@	G_0W_0@PBE	G_nW_0@PBE	G_nW_n@PBE
S_1	2.21	2.73	3.30
BSE@	G_0W_0@PBE0	G_nW_0@PBE0	G_nW_n@PBE0
S_1	2.80	3.03	3.28
BSE@	G_0W_0@HF	G_nW_0@HF	G_nW_n@HF
S_1	4.06	3.97	3.83
TD-DFT@	CAM-B3LYP[1]	LC-BLYP[1]	LC-wPBE[1]
S_1	3.31	4.26	4.07
TD-DFT@	PBE0[1]	HSE06[1]	EXP.[1]
S_1	2.31	2.09	2.73

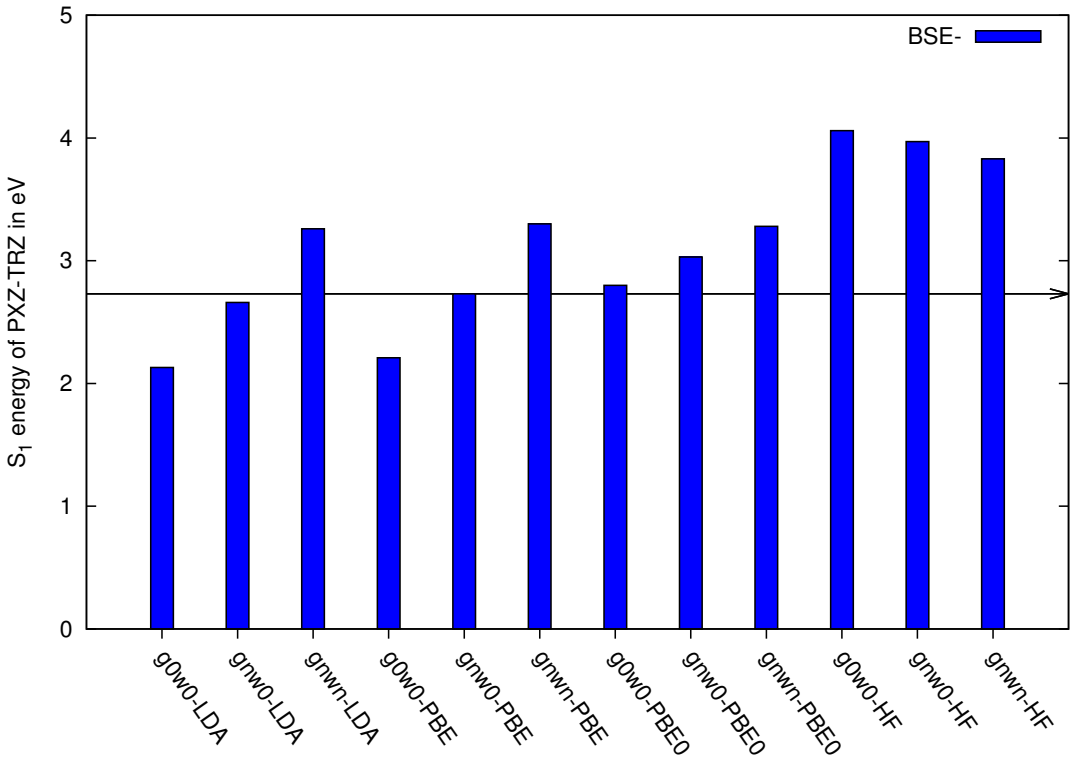

Figure 5.3: S_1 Vertical transition energy of PXZ-PRZ in eV. The black line represents the experimental reference [1].

III. Spiro-CN

For Spiro-CN (99 atoms), as compiled in Table 5.5, the energy-update in G does not result in a further gap opening as G_0W_0@LDA and G_nW_0@LDA yield identical gaps. However, even if the partial energy update has no effect on the QP gap in comparison to the non-iterative GW, it still can change the level alignment and the number of contributing single-particle orbitals to the excited state and thus modifying its character. The orbital composition of S_1 based on BSE@G_0W_0@LDA consists of HOMO $\rightarrow$ LUMO + 3 and HOMO - 1 $\rightarrow$ LUMO + 6, with the transition weights of 0.67 and 0.16, respectively. However, the character of S_1 changes to HOMO $\rightarrow$ LUMO transition with an amplitude weight of 0.7 upon energy-update in G (BSE@G_nW_0@LDA).

Starting from the HF reference, neither partial nor full eigenvalue self-consistency can restore the true nature of S_1 which is a HOMO $\rightarrow$ LUMO charge transfer state, as predicted by the (advanced) TD-DFT functionals. The CT state of Spiro-CN based on BSE@(G_0W_0,G_nW_0,G_nW_n)@HF is shifted from S_1 towards higher lying singlet states. It should be pointed out, that HOMO $\rightarrow$ LUMO transition amplitudes obtained from GW/BSE methodology on TADF systems are decreased relative to TD-DFT.

Table 5.5: HOMO-LUMO gap of Spiro-CN in eV obtained for different starting functionals and self-consistency levels in GW.

Method@	LDA	PBE	PBE0	HF
DFT/HF	1.17	1.22	2.71	7.35
G_0W_0 (n=0)	4.73	4.46	4.99	6.15
G_nW_0 (n=5)	4.73	4.78	5.17	6.07
G_nW_n (n=5)	5.24	5.28	5.42	5.96

Table 5.6: S_1 excitation energies of Spiro-CN in eV using aug-cc-pVDZ basis set. TD-DFT results (1) are from Ref. 1.

BSE@	G_0W_0@LDA	G_nW_0@LDA	G_nW_n@LDA
S_1	2.37	2.65	3.16
BSE@	G_0W_0@PBE	G_nW_0@PBE	G_nW_n@PBE
S_1	2.37	2.70	3.22
BSE@	G_0W_0@PBE0	G_nW_0@PBE0	G_nW_n@PBE0
S_1	2.86	3.04	3.28
BSE@	G_0W_0@HF	G_nW_0@HF	G_nW_n@HF
S_1	3.86	3.80	3.68
TD-DFT@	CAM-B3LYP[1]	LC-BLYP[1]	LC-wPBE[1]
S_1	3.30	4.06	4.00
TD-DFT@	PBE0[1]	HSE06[1]	EXP.[1]
S_1	2.21	2.01	2.69

Furthermore, the slight difference of about 0.05 eV in G_nW_0@LDA and G_nW_0@PBE QP gaps is directly reflected in the difference of the corresponding S_1 excitation energies of about 0.05 eV. Thus, this once again shows the importance of accurate calculation of QP energies.

A further interesting fact for the TADF systems discussed so far is that if the reference starting functional is a (hybrid-)DFT, the S_1 energy keeps increasing, whereas if it is HF, S_1 energy decreases upon self-consistency. This is related to the fact that the initial screening of HF is zero, and gets enhanced upon energy updating, whereas LDA screening is too large, and gets weakened upon energy updating.

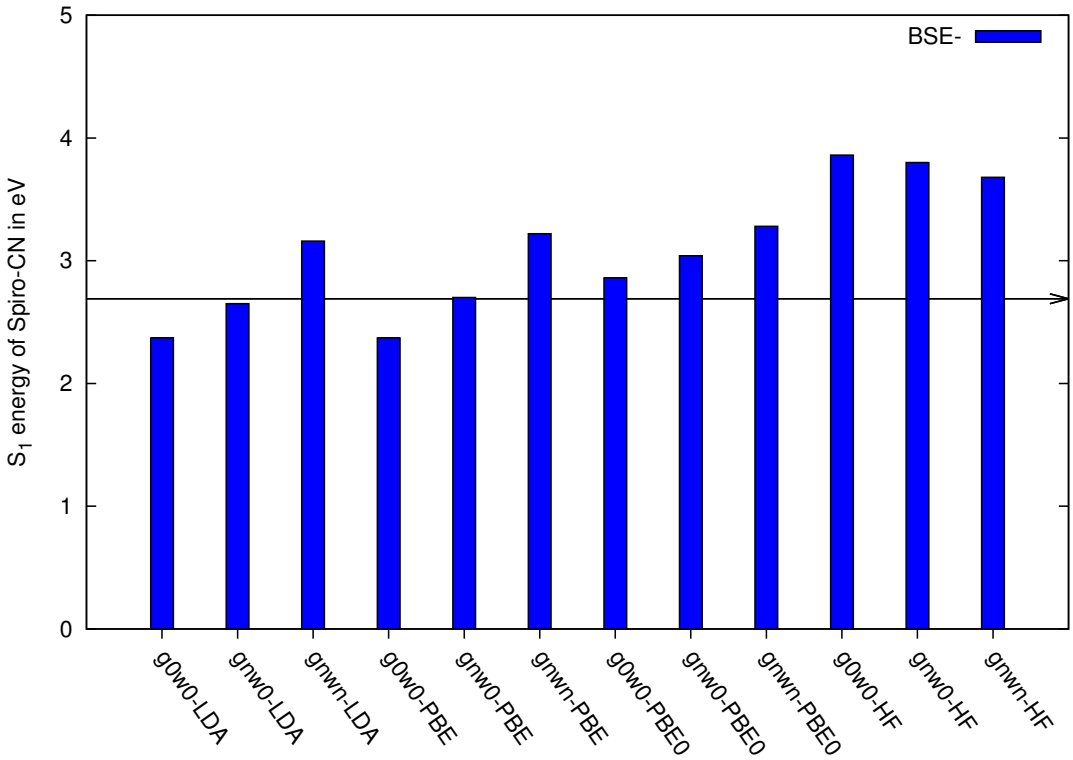

Figure 5.4: Vertical transition energies of Spiro-CN in eV. The black line represents the experimental reference [1].

Transferability

So far it is observed that the S_1 excitation energy does depend on the underlying starting point, as shown in the case of LDA and HF for TADF systems. To further check the transferability of results, the same methodology is applied on small non-charge transfer molecules to study S_1 initial point dependency. Results for water, ammonia, hydrogen fluoride and phosphine are compiled in Table 5.7. For this set of molecules, deviations of S_1 energies obtained from the full eigenvalue self-consistency between LDA and HF are up to 1.2 eV. Neither partial nor full eigenvalue self-consistency is capable of restoring orbital independency. Independent of the type of the molecules under study (CT or non-CT), one indeed observes a LDA and HF dependency of S_1 energy within all GW flavors with a system-dependent magnitude.

Furthermore, with respect to the reference method EOM-CCSD, the neutral excitation energies obtained with BSE@G_nW_n@(LDA,HF) are either under- or overestimated by about 0.5 eV, showing that the GW/BSE methodology fails to accurately predict the S_1 energy due to improper capturing of the screening structure at the various level of many-body approximations. Even starting from G_0W_0@PBE0 which was a perfect strategy for TADF systems is no remedy to address the S_1 inaccuracy. Therefore, none of the presented strate-

gies in Table 5.7 is capable of targeting the S_1 energy, and hence performance of the various variants of GW is found to be system-dependent.

Concerning updating of energies and orbitals both in G and W, as compiled in Table 5.8, the first ionization potential (IP) is computed within QSGW, extracted simply as the negative of HOMO energy for eleven test molecules for which experimental data are available, and further show the effect of larger and more flexible basis sets on IPs. This set of small molecules was previously calculated by Kaplan and coworkers [38] with def2-TZVPP basis sets.

In the present calculations the correlation consistent aug-cc-pVQZ basis sets were used, starting from the same reference geometries. The different basis set leads to a mean absolute error (MAE) of 0.17 eV relative to Kaplan's data. With respect to the experimental data, QSGW IPs observed again performs unsatisfactorily with a MAE of 0.41 eV as for CT-systems. Further increase of the number of basis functions in the basis set still results in slight changes. Therefore, in particular for small molecular systems, it is recommended to use a large basis set for more precise results, as also found by Kaplan et al. Further, the similarity of QSGW and G_nW_n@(LDA,HF) IPs results indicate only a slight modification of orbitals in QSGW, and hence orbital-update can be safely neglected for IPs. Furthermore, based on QSGW IPs results, a strong evidence is observed for systematic underscreening of W within the QSGW methodology in both non-CT and CT systems, independent of the starting point. The experimental IPs are best reproduced with a MAE of 0.14 eV using the G_nW_0@LDA strategy, while G_nW_n@(LDA,HF) and QSGW consistently overestimate the experimental references, and do not represent an alternative for CCSD(T). This perfectly underpins the transferability of the results obtained for the TADF systems, where G_nW_0@LDA provided accurate QP gaps and S_1 excitation energies. Interestingly, full eigenvalue update makes IPs to a large degree independent of both (hybrid-) DFT and HF starting points. By contrast, the full eigenvalue self-consistent QP gap discrepancy between (hybrid-)DFT and HF observed for the TADF systems stems mainly from the change of absolute position of HOMO energy, whereas LUMO energies remain nearly unchanged upon full eigenvalue self-consistency.

In summary, update of screening not necessarily leads to accurate IPs, QP gaps and excitation energies, as it gives rise to underscreening of W in G_nW_n@(LDA,HF) and QSGW, which is most probably a direct consequence of the RPA approximation to the polarization function. It was shown by Shishkin and Kresse [16] that accounting for explicit vertex corrections in the polarization function (beyond RPA) leads to a damping of the overestimated sc-GW QP band gaps of semiconductors due to cancellation effects. However, the effectivity

Table 5.7: S_1 energies in eV calculated with aug-cc-pVQZ basis sets. Full eigenvalue self-consistency largely diminishes initial (hybrid-)DFT orbital dependency, while S_1 energy still depends on HF orbitals, as for CT-systems, with a system-dependent magnitude.

H_2O			
EOM-CCSD(S_1)	7.68		
BSE@	G_0W_0@LDA	G_nW_0@LDA	G_nW_n@LDA
S_1	5.78	6.58	7.14
BSE@	G_0W_0@PBE0	G_nW_0@PBE0	G_nW_n@PBE0
S_1	6.40	6.76	7.09
BSE@	G_0W_0@HF	G_nW_0@HF	G_nW_n@HF
S_1	8.27	8.23	8.18
NH_3			
EOM-CCSD(S_1)	6.67		
BSE@	G_0W_0@LDA	G_nW_0@LDA	G_nW_n@LDA
S_1	5.07	5.78	6.21
BSE@	G_0W_0@PBE0	G_nW_0@PBE0	G_nW_n@PBE0
S_1	5.66	5.97	6.23
BSE@	G_0W_0@HF	G_nW_0@HF	G_nW_n@HF
S_1	7.27	7.25	7.22
HF			
EOM-CCSD(S_1)	10.51		
BSE@	G_0W_0@LDA	G_nW_0@LDA	G_nW_n@LDA
S_1	8.15	9.07	9.73
BSE@	G_0W_0@PBE0	G_nW_0@PBE0	G_nW_n@PBE0
S_1	8.85	9.28	9.67
BSE@	G_0W_0@HF	G_nW_0@HF	G_nW_n@HF
S_1	11.03	10.97	10.88
PH_3			
EOM-CCSD(S_1)	6.23		
BSE@	G_0W_0@LDA	G_nW_0@LDA	G_nW_n@LDA
S_1	4.95	5.32	5.65
BSE@	G_0W_0@PBE0	G_nW_0@PBE0	G_nW_n@PBE0
S_1	5.34	5.52	5.69
BSE@	G_0W_0@HF	G_nW_0@HF	G_nW_n@HF
S_1	6.81	6.83	6.82

Table 5.8: Ionization potentials of a set of small molecules. Performance of QSGW based on aug-cc-pVQZ and def2-TZVPP basis sets is shown. For the sake of comparison, IPs results with respect to partial and full eigenvalue self-consistency are also given. All results are in eV. The superscripts (1) is from Ref. 40 with def2-TZVPP, (2) is this work with aug-cc-PVQZ, and (3) is from Ref. 38 with def2-TZVPP. Experimental values are taken from Ref. 38.

	G_nW_0@LDA	G_nW_n@LDA	G_nW_0@HF	G_nW_n@HF
H_2	16.20	16.54	16.39	16.41
H_2O	12.73	13.19	13.08	13.04
NH_3	10.93	11.29	11.39	11.37
CH_4	14.43	14.71	14.87	14.86
LiH	7.98	8.45	8.25	8.25
BF	11.00	11.22	11.48	11.48
N_2	15.56	15.99	17.18	17.16
Na_2	5.00	5.05	4.99	4.99
Li_2	5.33	5.45	5.36	5.37
CO_2	13.84	14.22	14.38	14.33
F_2	15.68	16.25	16.11	16.03
	G_nW_0@PBE0	G_nW_n@PBE0	G_nW_0@HSE06	G_nW_n@HSE06
H_2	16.26	16.41	16.23	16.41
H_2O	12.76	13.03	12.69	13.02
NH_3	11.01	11.22	10.96	11.21
CH_4	14.50	14.67	14.47	14.67
LiH	8.02	8.29	7.94	8.28
BF	11.13	11.24	11.09	11.24
N_2	15.69	15.97	15.64	15.96
Na_2	5.01	5.03	5.00	5.04
Li_2	5.36	5.40	5.32	5.41
CO_2	13.86	14.11	13.82	14.11
F_2	15.64	16.00	15.59	15.99
	ΔCCSD(T)[1]	QSGW[2]	QSGW[3]	EXP.
H_2	16.21	16.42	16.04	15.42
H_2O	12.61	13.11	12.95	12.62
NH_3	10.85	11.27	11.11	10.85
CH_4	14.36	14.69	14.46	14.35
LiH	7.93	8.22	7.98	7.90
BF	11.14	11.30	11.17	11.00
N_2	15.54	15.98	15.86	15.58
Na_2	4.92	5.02	4.99	4.89
Li_2	5.20	5.35	5.30	5.11
CO_2	13.67	14.15	14.06	13.78
F_2	15.46	16.23	15.91	15.70

of compensation effects in molecular systems remains an issue for further investigations.

Conclusions

For the CT-systems many-body perturbation theory is a reliable alternative for TD-DFT, however with some limitations which need to be taken into account. Upon update of orbital energies in G while freezing W to the mean-field level, accurate S_1 energies are obtained for all the TADF systems independent from the content of HF exchange in the DFT-functional as GW automatically is able to properly screen HF exchange upon energy updating in G. This is a big advantage, as TD-DFT results strongly depend on the HF fraction. However, this kind of partial self-regulation mechanism of GW is activated, when starting from a (semi)-local reference functional. If the initial guess contains 100% exact HF exchange, a deterioration of the accuracy of S_1 energies upon partial self-consistent GW was observed. Further, a full eigenvalue self-consistent GW on top of the (hybrid-)DFT starting points gives rise to considerably overestimated S_1 energies due to underscreening of W. In case of G_nW_n@HF W screening gets moderately weaker, however the S_1 energies are still overestimated. This shows that the accuracy of this approach is very much (hybrid-)DFT and HF initial guess dependent within all GW flavors.

With respect to additional wave function updating, QSGW deteriorates the QP gap relative to G_nW_0@LDA, however this is related to the underscreening of W and not to orbital updating. Further, for the sake of transferability, application of MBPT on S_1 energies of small non-CT systems clearly demonstrated the limitation of GW/BSE in terms of starting point dependency (DFT vs. HF) and accuracy. Application of QSGW on IPs showed that it considerably lacks accuracy. Furthermore, similar QSGW and G_nW_n@(LDA,HF) IPs suggest that update of wave function is of minor importance.

The recommended procedure for TADF or similar CT complexes is to start from a hybrid functional with a single-shot GW or from a (semi-)local functional with energy-only updating in G while keeping W fixed to the mean-field starting guess.

As a final statement, it is pointed out that the partial self-consistent GW scheme on top of GGA performs much better than the standalone long-range corrected DFT functionals such as CAM-B3LYP, LC-BLYP which are generally considered to be ideally suited for non-local excitations such as charge-transfer excitations.

Bibliography

[1] S. Huang, Q. Zhang, Y. Shiota, T. Nakagawa†, K. Kuwabara†, K. Yoshizawa, and C. Adachi, J. Chem. Theory Comput. **9**, 3872–3877 (2013).

[2] E. Runge and E. K. U. Gross, Phys. Rev. Lett. **52**, 997 (1984).

[3] C. A. Ullrich, Time-Dependent Density-Functional Theory: Concepts and Applications, Oxford Graduate Texts (Oxford University Press, Oxford, New York, 2012).

[4] G. Strinati, Riv. Nuovo Cimento 11, 1 (1988)

[5] G. Onida, L. Reining, and A. Rubio, Rev. Mod. Phys. **74**, 601.

[6] L. Hedin, Phys. Rev. Lett., **139**, A796 (1965).

[7] B. Baumeier, D. Andrienko, Y. Ma, M. Rohlfing, J. Chem. Theory Comput. **85**, 323 (2012).

[8] J. C. Grossman, M. Rohlfing, L. Mitas, S. G. Louie, and M. L. Cohen, Phys. Rev. Lett. **2001**, 472 (2001).

[9] S. Körbel, P. Boulanger, I. Duchemin, X. Blase, M. A. L. Marques, and S. Botti, **10**, 3934-3943 (2014).

[10] C. Faber, P. Boulanger, C. Attaccalite, I. Duchemin, and X. Blase, http://dx.doi.org/10.1098/rsta.2013.0271 (2014).

[11] P. Koval, D. Foerster, and D. Sanchez-Portal, Phys. Rev. B **89**, 155417 (2014).

[12] C. Faber, C. Attaccalite, V. Olevano, E. Runge, and X. Blase, Phys. Rev. B **83**, 115123 (2011).

[13] F. Caruso, P. Rinke, X. Ren, M. Scheffler, and A. Rubio, Phys. Rev. B **86**, 081102 (2012).

[14] F. Bruneval and M. A. L. Marques, J. Chem. Theory Comput. **9**, 324324 (2013).

[15] E. Coccia, D. Varsano, and L. Guidoni, J. Chem. Theory Comput. **10**, 501-506 (2014).

[16] X. Blase, P. Boulanger, F. Bruneval, M. Fernandez-Serra, and I. Duchemin, J. Chem. Phys. **144**, 034109 (2016).

[17] N. Marom, F. Caruso, X. Ren, O. T. Hofmann, T. Körzdörfer, J. R. Chelikowsky, A. Rubio, M. Scheffler, and P. Rinke, Phys. Rev. B, **86**, 245127 (2012).

[18] T. Rangel, S. M. Hamed, F. Bruneval, and J. B. Neaton, J. Chem. Theory Comput. **12**, 2834-2842 (2016).

[19] F. Bruneval, S. M. Hamed, and J. B. Neaton, J. Chem. Phys. **142**, 244101 (2015).

[20] C. Rostgaard, K. W. Jacobsen, and K. S. Thygesen, Phys. Rev. B **81**, 085103 (2010).

[21] D. Jacquemin, I. Duchemin, and X. Blase, J. Chem. Theory Comput. **11**, 5340–5359 (2015).

[22] C. Faber, J. L. Janssen, M. Côté, E. Runge, and X. Blase, Phys. Rev. B **84**, 155104 (2011).

[23] H. Tanaka, K. Shizu, H. Miyazakiab and C. Adachi, Chem. Commun. **48**, 11392-11394 (2012).

[24] J. W. Sun, K. Kim, C. Moon, J. Lee, and J. Kim, Appl. Mater. Interfaces **8**, 9806-9810 (2016).

[25] A. Kokalj, Comp. Mater. Sci., **28**, 155 (2003).

[26] F. Bruneval, **https://github.com/bruneval/molgw (2016)**

[27] F. Bruneval, T. Rangel, S. M. Hamed, M. Shao, C. Yang, and J. B. Neaton, Comput. Phys. Commun. **208**, 149 (2016).

[28] C. Lee, W. Yang,and R. G. Parr, Phys. Rev. B **37**, 785–789 (1988).

[29] J. P. Perdew, K. Burke, and M. Ernzerhof, Phys. Rev. Lett. **77**, 3865 (1996).

[30] J. P. Perdew, M. Ernzerhof and K. Burke, J. Chem. Phys. **105**, 9982 (1996).

[31] T. H. Dunning, J. Chem. Phys. **90**, 1007 (1989).

[32] F. Weigend, Phys. Chem. Chem. Phys. **4**, 4285–4291 (2002).

[33] F. Weigend, A. Kohn and C. Hättig, J. Chem. Phys. **16**, 3175-3183 (2002).

[34] "Psi4: An open-source ab initio electronic structure program," J. M. Turney, A. C. Simmonett, R. M. Parrish, E. G. Hohenstein, F. Evangelista, J. T. Fermann, B. J. Mintz, L. A. Burns, J. J. Wilke, M. L. Abrams, N. J. Russ, M. L. Leininger, C. L. Janssen, E. T. Seidl, W. D. Allen, H. F. Schaefer, R. A. King, E. F. Valeev, C. D. Sherrill, and T. D. Crawford, WIREs Comput. Mol. Sci. **2**, 556 (2012). (doi: 10.1002/wcms.93).

[35] M. Shishkin and G. Kresse, Phys. Rev. B **75**, 235102 (2007).

[36] S. V. Faleev, M. van Schilfgaarde, and T. Kotani, Phys. Rev. Lett. **93**, 126406 (2004).

[37] F. Bruneval, and M. Gatti, Springer Berlin Heidelberg **347**, 99-135 (2014).

[38] F. Kaplan, M. E. Harding†, C. Seiler, F. Weigend, F. Evers, and M. J. van Setten, J. Chem. Theory Comput. **12**, 2528-2541 (2016).

[39] M. Shishkin, M. Marsman, and G. Kresse, Phys. Rev. Lett. **99**, 246403 (2007).

[40] K. Krause, M. E. Harding, and W. Klopper, Mol. Phys. **113**, 19521960 (2015).

5.3 Visible and charge-transfer states of a large PBI-macrocycle complex

Abstract

As pointed out in the previous section, reliable calculation of excited states of charge-transfer (CT) compounds poses a major challenge to ab-initio methods, as the frequently employed TD-DFT method massively relies on the underlying density functional, resulting in heavily HF exchange-dependent excited state energies. Instead the many-body perturbation approach is applied to address the encountered unreliabilities and inconsistencies of not optimally tuned (standard) TD-DFT regarding excited-state CT phenomena, and results are presented concerning accurate vertical transition energies and correct energetic ordering of the CT and the first visible singlet state of a recently synthesized perylenebisimide-macrocycle complex. This is a large-scale application of quantum many-body perturbation approach on a technologically relevant CT-system, demonstrating the system size-independence of the high quality of many-body theory derived excitation energies. Furthermore, it is shown that an optimal tuning of the ωB97X hybrid functional can well reproduce the many-body results, making TD-DFT a suitable choice but at the expense of introduction of a range-separation parameter which needs to be optimally tuned.

Introduction

TD-DFT [17,18] as the most widely employed theoretical method for calculation of excited-state phenomena is in general not well suited for CT-systems due to massive reliance of its prediction power on the choice of the density functional, and hence on the amount of incorporated HF exact exchange in the starting reference orbitals. Therefore, it is desirable to perform calculations without such dependence. To this end, by using the many-body perturbation approach described in the previous chapters [1–3, 6, 7, 10–16, 19, 26] on top of LDA orbitals, one aims at accurate computation of singlet excited-state energies, the correct energy ordering of the first bright S and dark CT state, and their separation energy, as the relative energies of CT and S states determine the quantum efficiency of the photovoltaic devices. The challenging compound under study is a recently synthesized donor-acceptor hybrid macrocycle complex [17], as shown in Fig. 5.5 consisting of perylenebisimide (PBI) units as electron accepting building block and a central phenylene-bithiophene macrocycle as donor. The CT character of the hybrid PBI-macrocycle (294 atoms) was verified experimentally, as it showed no fluorescence upon de-excitation as a consequence of a rapid electron transfer from the PBI to the macrocycle, representing a non-radiative pathway towards the ground-state.

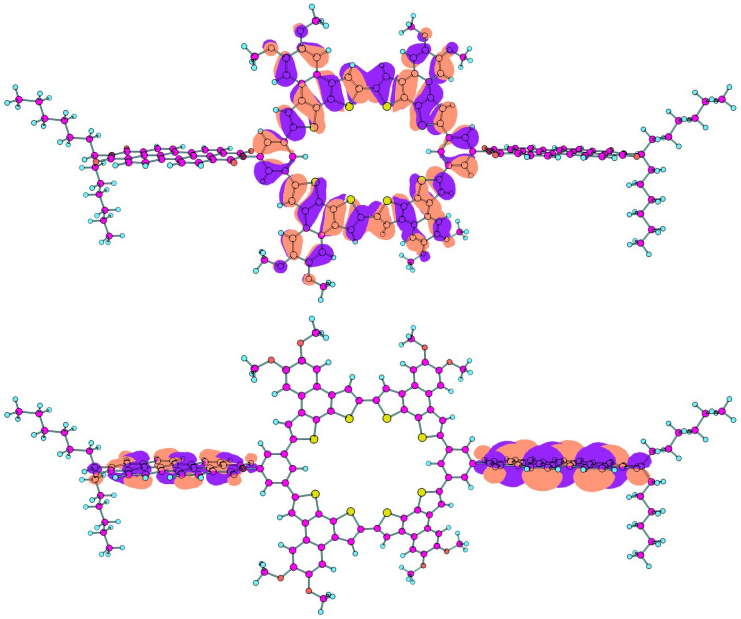

Figure 5.5: Spatially separated LDA highest occupied (up) and lowest unoccupied (down) molecular orbitals of the hybrid macrocycle complex consisting of 294 H, C, N, O, and S atoms.

Technical details

For computation of excited states up to 11 eV a Gaussian basis set implementation of the GW/BSE approach is employed using MOLGW [29, 30] with cc-pVDZ basis sets [33] and resolution of identity [31, 32] starting from the B3LYP optimized structure. It was shown by Jacquemin et al. [15] for a large set of medium-sized molecules that the GW and TD-DFT methods are largely insensitive to the choice of basis set, as also verified here for the large hybrid CT complex using SVP and TZVP basis sets with an error of 50 meV for the first ten excitation energies (Fig. 5.12). Using a more flexible basis set (TZVP) improves the excitation energies only slightly. Nevertheless, all TD-DFT calculations are performed using TZVP basis sets; however due to massive increase in computational load and memory usage, the smaller cc-PVDZ basis set is used for GW/BSE calculations. As shown in the last section GW/BSE is only weakly basis set dependent when applied to large molecular systems such as TADF, 2CzPn and PXZ-TRZ. It is noted that the cc-PVDZ basis set used in GW/BSE gives rise to 11752 auxiliary basis functions (ABF) which is a remarkably large number, while cc-PVTZ leads to 18226 ABFs, making GW/BSE calculations de-facto intractable. As both the Green's function G and dynamically screened interaction W depend on the virtual orbitals, the virtual space is extended to 500 unoccupied orbitals to ensure convergence of the QP HOMO-LUMO (H-L) gap within 1 meV accuracy. As soon as the QP gap converges, no more change in excitation energies is observed. In

Table 5.9: QP HOMO-LUMO gap convergence of the complex in eV in dependence of the number of virtual orbitals based on G_nW_0@LDA (n=5).

Number of virtual orbitals :	300	400	500	600
G_nW_0@LDA	3.73	3.58	3.55	3.55

Table 5.9 the convergence of QP H-L gap with respect to the number of truncated virtual orbitals is presented. As can be seen, convergence is reached at 500 orbitals, proving that the dependency of GW/BSE on virtual orbitals is not critical, and rather moderate.

As a further simplification deeper-lying core electrons are excluded (frozen core approximation) leaving excited-state energies unaffected within 0.02 eV as observed in medium-size TADF molecules of the previous section.

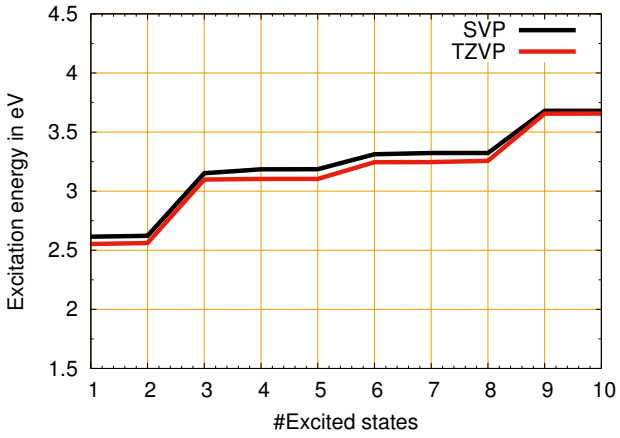

Figure 5.6: Basis set dependency of the first 10 singlet excited states using SVP and TZVP basis sets for CAM-B3LYP TD-DFT. The lines are only guides to the eye.

The self-energy is calculated analytically through the spectral representation of W and the residuum theorem, avoiding numerical errors arising from improper capturing of the frequency dependency of the self-energy. Furthermore, the Quasi-Particle equation is diagonalized exactly, and thus the usual perturbative treatment of QP energies is avoided in order to reach an even higher level of accuracy, as accurate excited state energies massively rely upon accurate relative QP energies.

BSE calculations are performed in the limit of adiabatic static kernel with mixing of resonant and anti-resonant contributions to the absorption spectrum, and thus avoiding the frequently employed Tamm-Dancoff approximation (TDA) which neglects important coupling of electron-hole pairs [23]. The TD-DFT calculations are carried out in solution (dichloromethane) represented by the PCM [24] using Gaussian09 [25].

Results and discussions

In Fig. 5.7 the performance of TD-DFT based on common GGAs, hybrid, (tuned) range-separated hybrid functionals, and quantum many-body perturbation approach is examined for the calculation of the lowest excitation energies. As expected, a strong dependence of the energetic order of the CT state and the lowest singlet state (S) with large oscillator strength from the kernel is observed.

As can be seen in Fig. 5.7, the GGA kernels strongly underestimate the CT state but give reasonable agreement with the experimental S energy (first peak in Fig. 5.8). Global hybrid functionals and short-range screened HSE06 [26,27] moderately reduce the CT-S difference and provide good agreement for the absolute S position. According to BHLYP [28] with 50% HF-exchange, the energetic difference between CT and S states is small; however, it overestimates the experimental excitation energy.

It was shown by Chai and Head-Gordon [20] that functionals with an asymptotically correct potential are essential for a correct prediction of charge transfer with TD-DFT. Stein et al. [21, 32] have shown that this is not a sufficient condition for a quantitative prediction, but such prediction can be obtained if the range-separation parameter in a range-separated hybrid functional is tuned from first principles based on the ionization potential theorem. Their method has since been used successfully for the quantitative prediction of a variety of full and partial charge transfer energies [33–36]. To test the consistency of tuned range-separated functionals, in particular the performance of TD-ωB97X on the macrocycle complex is studied. As expected and shown in Fig. 5.7, the results of TD-ωB97X are parameter-dependent. Starting from the standard range-separation parameter $\mu = 0.3$ Bohr^{-1} the excitation energies are inaccurate but the energy ordering is consistent with CAM-B3LYP [29]. An optimal tuning of the range-separation parameter to $\mu = 0.1$ Bohr^{-1} considerably improves the accuracy of the S energy toward the experimental reference [17] compared to the larger separation values ($\mu = 0.3\,, 0.2$) and CAM-B3LYP. Interestingly, state ordering remains consistent for all separation values.

Concerning many-body approaches, the non-self consistent variant (G_0W_0) predicts the same energy ordering as range-separated functionals, giving a first visible S state at 1.81 eV (carrying large oscillator strength) but with a relatively large error of about 0.5 eV to the experimental S energy and a CT state at 1.99 eV with a small energy difference to the S state. However, the partial self-consistent variant ($\mathrm{G}_n\mathrm{W}_0$) further improves the excitation energies upon updating of KS energies, giving again a visible S state located at 2.31 eV and a nearby HOMO-LUMO CT state at 2.45 eV carrying a very small oscillator strength with a tiny energy separation of 0.14 eV to the S state. These outcomes are consistent with the

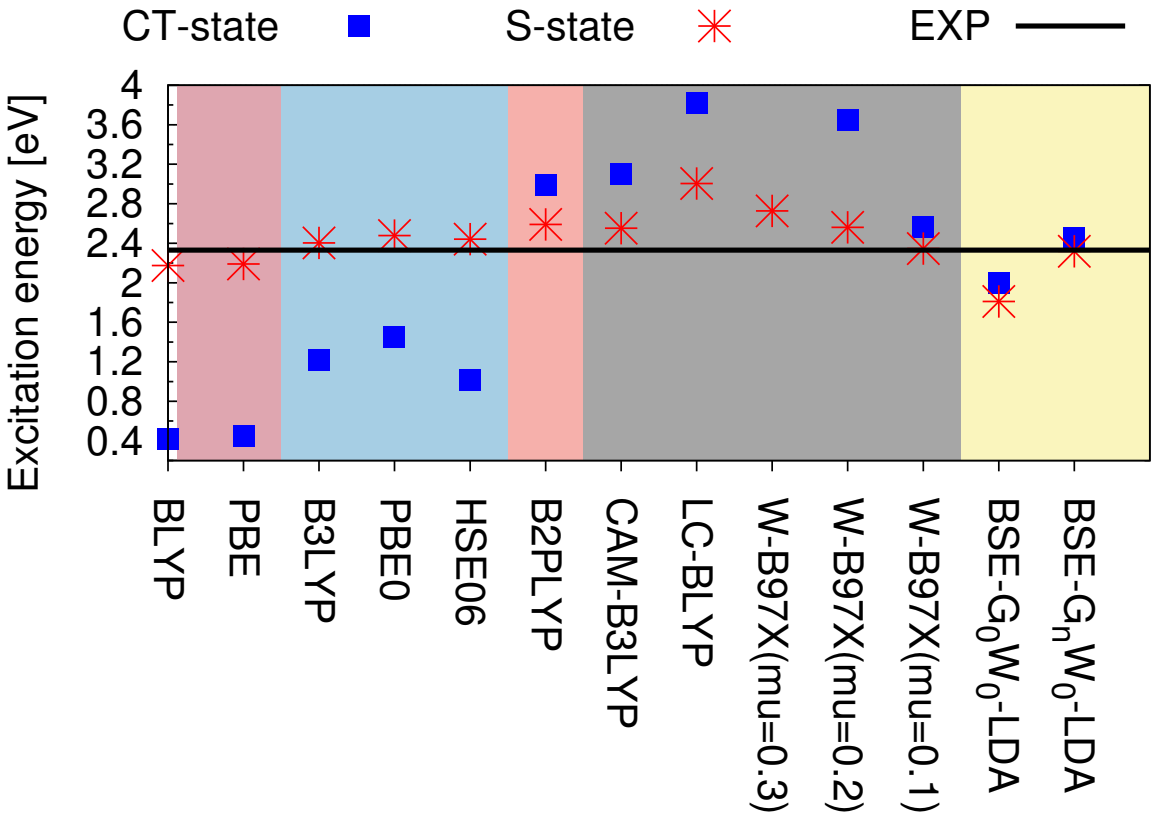

Figure 5.7: Calculated excitation energies for CT and S states at TD-DFT with selected exchange-correlation functionals, and at many-body perturbation level. The results are classified into five regimes: standard GGA functionals, (short-range screened) global, double hybrid, (tuned) range separated functionals, and many-body approach on top of LDA Kohn-Sham energies and orbitals in its non- and partial self-consistent variants. Starting from the CAM-B3LYP functional the energetic order of the CT and S state is observed, with the visible S_1 state coming first, and CT-state as the next nearby lying state, as further confirmed by BSE@G_0W_0@LDA and BSE@G_nW_0@LDA. The black line represents the experimental reference [17].

previously published results in the literature on performance of GW/BSE on CT state of small molecular systems [27, 37–39]

A full eigenvalue self-consistency both in G and W (G_nW_n) was not performed due to high computational cost; however it is very likely that G_nW_n overestimates the excitation energies due to underscreening of W, as also found by Shishkin and Kresse for the band gap of a large number of semi-conductors [41]. Thus, the typical behavior of G_0W_0 and G_nW_0 in solids is observed in the large CT-system.

Concerning energy ordering, since the (tuned) range-separated functionals, the non- and partially self-consistent GW/BSE yield consistent results, it is then likely that the visible state (S_1) has a lower energy than the HOMO-LUMO CT state.

The presented results again demonstrate that the many-body perturbation theory approach is highly reliable in describing non-local CT phenomena, given the fact that the LDA functional is the worst possible starting point. Apparently due to an effective error compensation. LDA orbitals turned out to be a much better starting point than HF orbitals [42].

In Fig. 5.8 the calculated absorption spectrum in gas-phase based on many-body approach is presented. The first peak (S_1) lies at 2.31 eV which is in remarkable agreement with the experimentally visible S_1 state at 2.33 eV in solution [17]. This shows that the S_1 state is nearly insensitive to the environmental effects, as further checked with TD-CAM-B3LYP due to lack of GW/BSE combined with the polarization continuum model (PCM) in MOLGW. The change of the S energy introduced by the solvent effects was only 0.07 eV.

The peaks located at 2.52, 2.68 and 2.88 eV in the experimental spectrum are highly likely vibronic in nature. This was checked by a TD-CAM-B3LYP calculation with and without solvent effects, showing the vibronic origin of the corresponding states. By contrast, the first peak at 2.31 eV and the double peaks at 3.19 and 3.57 eV in the calculated spectrum are vertical states.

The key to the high accuracy of the many-body approach for the singlet and CT states is to find in the following important facts : 1) the long-range Coulomb interaction is correctly captured, avoiding artificial intruder states, 2) the initial LDA molecular orbital energies are properly updated upon the one-particle self-consistent scheme [43]. 3) dynamical effects (correlation) are accounted for through frequency dependency of self-energy giving rise to correct state ordering. 4) Even though the self-energy is approximated by the product of G and W, it however is capable of capturing the essential part of many-body physics

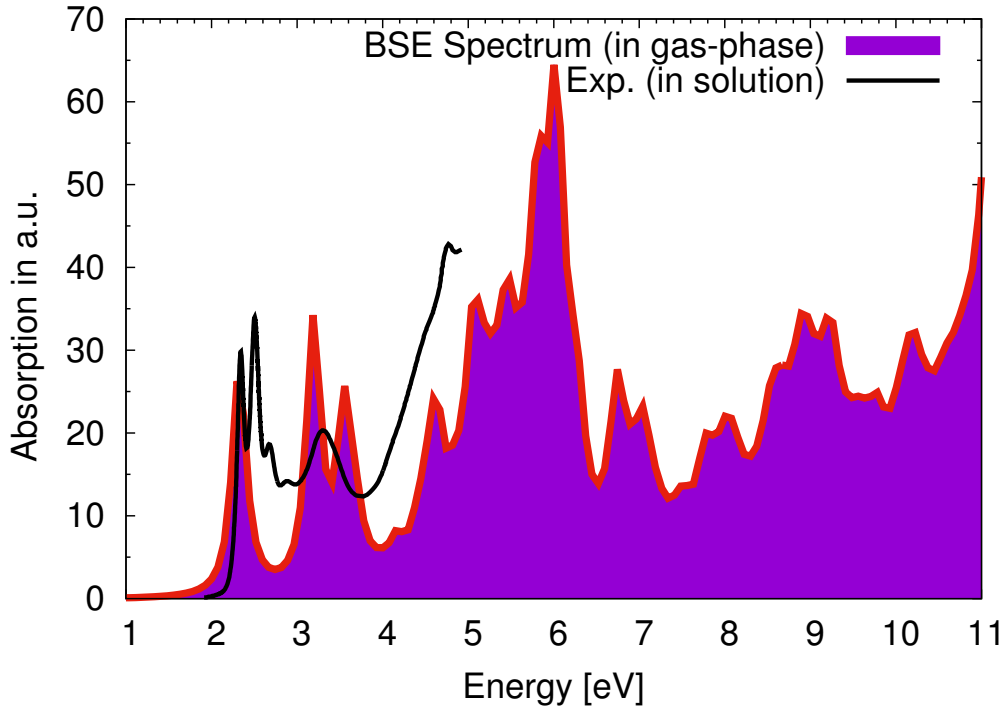

Figure 5.8: Absorption spectrum of the hybrid PBI-macrocycle complex in gas-phase, including important excitonic effects and resonant–anti-resonant mixing of electron-hole pairs. The first most important peak representing the first visible excited state lies at 2.31 eV, in excellent agreement with the experimental reference of 2.33 eV [17]. The black line represents the experimental spectrum in CH_2Cl_2 solution. As expected due to lack of solvent effects, the theoretical gas-phase peaks at 2.52 and 3.33 eV are not accordingly red-shifted. By contrast the first peak is solution insensitive.

of the system. 5) effective capture of vertex corrections in the polarization function by G_nW_0 due to a fortunate effect cancellation. 6) appropriate treatment of excitonic effects (electron-hole interactions) by a spatially non-local four-point kernel.

Conclusions

It is shown that many-body treatment of excited states including CT state as a non-local excitation, is indeed an improvement over TD-DFT as it correctly reproduces the excitation energies and level alignment of a large CT complex. The TD-ω-B97X method with asymptotic correction and tuned range-separation parameter is also able to quantitatively describe the S_1 state but at the expense of parameter tuning. The separation parameter ω can be either obtained in a semi-empirical way or from ab-initio computation based on ionization potential.

The GW/BSE approach also suffers from problems, such as underscreening of W upon full eigenvalue self-consistency, leading to overestimation of excitation energies or the dependence from the initial orbitals.

Bibliography

[1] E. Runge and E. K. U. Gross, Phys. Rev. Lett. **1984**, 52, 997.

[2] C. A. Ullrich, Time-Dependent Density-Functional Theory: Concepts and Applications, Oxford Graduate Texts (Oxford University Press, Oxford, New York, 2012).

[3] G. Strinati, Riv. Nuovo Cimento **1988**, 11, 1.

[4] G. Onida, L. Reining, and A. Rubio, Rev. Mod. Phys. **2002**, 74, 601.

[5] L. Hedin, Phys. Rev. Lett., **1965**, 139, A796.

[6] C. Faber, P. Boulanger, C. Attaccalite, I. Duchemin, and X. Blase, http://dx.doi.org/10.1098/rsta.2013.0271 **2014**.

[7] P. Koval, D. Foerster, and D. Sanchez-Portal, Phys. Rev. B **2014**, 89, 155417.

[8] F. Bruneval and M. A. L. Marques, J. Chem. Theory Comput. **2013**, 9, 324324.

[9] E. Coccia, D. Varsano, and L. Guidoni, J. Chem. Theory Comput. **2014**, 10, 501-506.

[10] T. Rangel, S. M. Hamed, F. Bruneval, and J. B. Neaton, J. Chem. Theory Comput. **2016**, 12, 2834-2842.

[11] F. Bruneval, S. M. Hamed, and J. B. Neaton, J. Chem. Phys. **2015**, 142, 244101.

[12] C. Rostgaard, K. W. Jacobsen, and K. S. Thygesen, Phys. Rev. B **2010**, 81, 085103.

[13] C. Faber, J. L. Janssen, M. Côté, E. Runge, and X. Blase, Phys. Rev. B **2011**, 84, 155104.

[14] B. Baumeier, D. Andrienko, Y. Ma, M. Rohlfing, J. Chem. Theory Comput. **2012**, 85, 323.

[15] D. Jacquemin, I. Duchemin, and X. Blase, J. Chem. Theory Comput. **2015**, 11, 5340–5359.

[16] M. Shishkin, M. Marsman, and G. Kresse, Phys. Rev. Lett. **2007**, 99, 246403.

[17] S. K. Maier, S. S. Jester, U. Müller, W. M. Müllera and S. Höger, Chem. Commun. **2011**, 47, 11023-11025.

[18] F. Bruneval,
https://github.com/bruneval/molgw (2016)

[19] F. Bruneval, T. Rangel, S. M. Hamed, M. Shao, C. Yang, and J. B. Neaton, Comput. Phys. Commun. **2016**, 208, 149.

[20] T. H. Dunning, J. Chem. Phys. **1989**, 90, 1007.

[21] F. Weigend, Phys. Chem. Chem. Phys. **2002**, 4, 4285–4291.

[22] F. Weigend, A. Kohn and C. Hättig, J. Chem. Phys. **2002**, 16, 3175-3183.

[23] M. Gruening, A. Marini, and X. Gonze, Nano Lett. **2009**, 9, 2820-2824.

[24] B. Mennucci and J. Tomasi, J. Phys. Chem. A, **2001**, 106 (25), pp 6102-6113

[25] M. J. Frisch, G. W. Trucks, H. B. Schlegel, G. E. Scuseria, M. A. Robb, J. R. Cheeseman, G. Scalmani, V. Barone, B. Mennucci, G. A. Petersson, H. Nakatsuji, M. Caricato, X. Li, H. P. Hratchian, A. F. Izmaylov, J. Bloino, G. Zheng, J. L. Sonnenberg, M. Hada, M. Ehara, K. Toyota, R. Fukuda, J. Hasegawa, M. Ishida, T. Nakajima, Y. Honda, O. Kitao, H. Nakai, T. Vreven, J. A. Montgomery, Jr., J. E. Peralta, F. Ogliaro, M. Bearpark, J. J. Heyd, E. Brothers, K. N. Kudin, V. N. Staroverov, T. Keith, R. Kobayashi, J. Normand, K. Raghavachari, A. Rendell, J. C. Burant, S. S. Iyengar, J. Tomasi, M. Cossi, N. Rega, J. M. Millam, M. Klene, J. E. Knox, J. B. Cross, V. Bakken, C. Adamo, J. Jaramillo, R. Gomperts, R. E. Stratmann, O. Yazyev, A. J. Austin, R. Cammi, C. Pomelli, J. W. Ochterski, R. L. Martin, K. Morokuma, V. G. Zakrzewski, G. A. Voth, P. Salvador, J. J. Dannenberg, S. Dapprich, A. D. Daniels, O. Farkas, J. B. Foresman, J. V. Ortiz, J. Cioslowski, and D. J. Fox, 09, Revision B.01, Gaussian, Inc., Wallingford, CT, **2010**.

[26] J. Heyd, G. E. Scuseria, M. Ernzerhof, J. Chem. Phys. **2006**, 126, 219906.

[27] J. Heyd, G. E. Scuseria, M. Ernzerhof, J. Chem. Phys. **2003**, 118, 8207-8215.

[28] S. Grimme and F. Neese, J. Chem. Phys., **2007**, 127, 154116.

[29] T. Yanai, D. P. Tew, N. C. Handy, Chem. Phys. Lett. **2004**, 393, 51-57.

[30] Chai and Head-Gordon, J. Chem. Phys. **2008**, 128, 084106.

[31] T. Stein, L. Kronik, R. Baer, J. Chem. Phys. **2009**, 131, 244119.

[32] T. Stein, L. Kronik, R. Baer, J. Am. Chem. Soc. **2009**, 131, 2818-2820.

[33] Karolewski et al., J. Chem. Phys. **2011**, 134, 151101.

[34] S. Zheng, E. Geva, and B. D. Dunietz, J. Chem. Theo. Comp. **2013**, 9, 1125-1131.

[35] C. Zhang et al., J. Chem. Theo. Comp. **2014**, 10, 2379-2388.

[36] R. S. Bhatta, G. Pellicane, M. Tsige, Comp. Theor. Chem. **2015**, 1070, 14-20.

[37] D. Rocca, D. Lu and G. Galli, J. Chem. Phys. **2010**, 133, 164109.

[38] X. Blase and C. Attaccalite, Appl. Phys. Lett. **2011**, 99, 171909.

[39] B. Baumeier, D. Andrienko, and M. Rohlfing, J. Chem. Theo. Comp. **2012**, 8, 2790-2795.

[40] D. Jacquemin, I. Duchemin, A. Blondel, and X. Blase, J. Chem. Theo. Comp. **2016**, 12, 3969-3981.

[41] M. Shishkin and G. Kresse, Phys. Rev. B **2007**, 75, 235102.

[42] V. Ziaei, T. Bredow, J. Chem. Phys. **2016**, 145, 174305.

[43] L. Hedin, Phys. Rev. Lett. **1965**, 139, A796.

5.4 A many-body based screening ansatz for improvement of excitation energies

Abstract

A simple many-body based screening mixing strategy is proposed to enhance the performance of the BSE approach for prediction of excitation energies of molecular systems. This strategy enables to closely reproduce results of highly correlated equation of motion coupled cluster singles and doubles (EOM-CCSD) through optimal exploitation of cancellation effects. Wave function and one-particle energies are obtained from Hartree-Fock (HF), and the screening is calculated with the LDA based random phase approximation (RPA), denoted as W_0-RPA@LDA with W_0 as the dynamically screened interaction which is built upon LDA wave functions and energies. This W_0-RPA@LDA screening is used as an initial screening for calculation of QP energies in the framework of G_0W_0@HF. The W_0-RPA@LDA screening is further injected into the BSE. By applying such an approach on a set of 22 molecules for which the traditional GW/BSE approaches fail, a good agreement with respect to EOM-CCSD references is observed. The reason for the observed good accuracy of this mixing ansatz (scheme A) lies in an optimal damping of HF exchange effects through the strong W_0-RPA@LDA screening, leading to substantial decrease of typically overestimated HF electronic gap, and hence to better excitation energies. Furthermore, a second multi-screening ansatz (scheme B) is presented which is similar to scheme A with the exception that now the W_0-RPA@HF screening is used in the BSE in order to improve the overestimated excitation energies of carbonyl sulfide (COS) and disilane (Si_2H_6). The reason for improvement of the excitation energies in scheme B lies in the fact that W_0-RPA@HF screening is less effective (and weaker than W_0-RPA@LDA) which gives rise to stronger electron-hole effects in the BSE.

Introduction

As shown in the previous sections, application of GW/BSE on small molecular systems, like molecular water or ammonia demonstrated its consistent failure to predict the correct excitation energies regardless of the diverse strategies applied so far, such as full eigenvalue self-consistency (ev-SC) in G and GW on top of DFT or HF initial orbitals [22,25]. Now in order to enhance the accuracy of the GW/BSE approach, a simple straightforward screening mixing scheme is proposed which considerably enhances the low quality of the excitation energies obtained from the standard GW/BSE strategies in a fully ab-initio manner without any empirical parameters.

To show the improved accuracy of the mixing scheme, results concerning the first five

vertical single excitation energies (S_1-S_5) of 20 molecules are presented. The choice of this particular set of molecules was motivated by the fact that the standard GW/BSE method fails to predict the excitation energies of these systems. The consistency and robustness of the proposed screening procedures are checked on the excited states of two large biological systems for which recent EOM-CCSD calculations became possible due to massive algorithmic improvements [24].

5.4.1 Screening mixing

In order to enhance the performance of GW/BSE, it is of utmost importance to adequately increase the screening quality, as the entire theoretical building block of the many-body perturbation approach is based upon screening. To this end, two mixing schemes are proposed which involve the following steps :

Scheme A:

1) A W_0-RPA screening based on LDA wave functions and energies (denoted as W_0-RPA@LDA) is generated. 2) The W_0-RPA@LDA screening is further used as an initial screening guess for W_0 in G_0W_0@HF to obtain Hartree-Fock based G_0W_0 QP energies being now affected by W_0-RPA@LDA screening. 3) The W_0-RPA@LDA screening from step 1 is injected into the BSE and at the same time the G_0W_0@HF QP energies are read from step 2 to proceed further with computation of excitation energies by solving the BS equation.

Because excitation energies strongly depend on accurate relative QP energies [26, 27], this screening modified scheme gives rise to a reduced QP HOMO-LUMO gap serving as an important intermediate step enabling prediction of excitation energies with considerably better accuracy. This scheme is denoted as BSE@G_0W_0@HF/LDA (scheme A), as G_0W_0@LDA screening is injected into the G_0W_0@HF as initial screening and later into the BSE. The flowchart of scheme A is shown in Fig. 5.9.

Scheme B:

It is exactly proceeded as in the steps 1) and 2) of scheme A, except in the step 3) a new calculation is run to obtain the W_0-RPA@HF screening which is then injected into the BSE and with the G_0W_0@HF QP energies of step 2 of scheme A. In other words, in the BSE part of scheme B, the W_0-RPA@HF screening is used instead of the $W0$-RPA@LDA screening. The flowchart of scheme B is shown in Fig. 5.10.

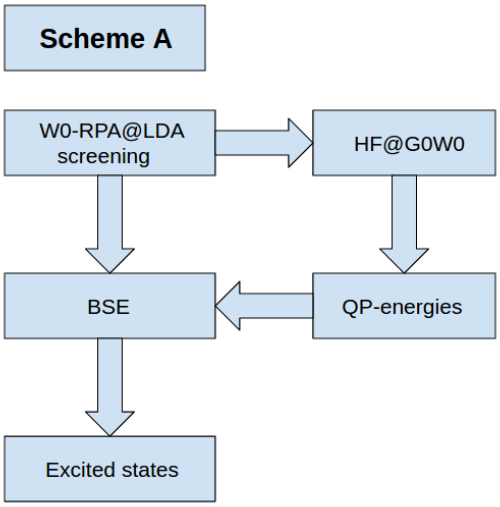

Figure 5.9: The flowchart of scheme A is presented. The G_0W_0@HF QP energies and BSE are both affected by W_0-RPA@LDA screening.

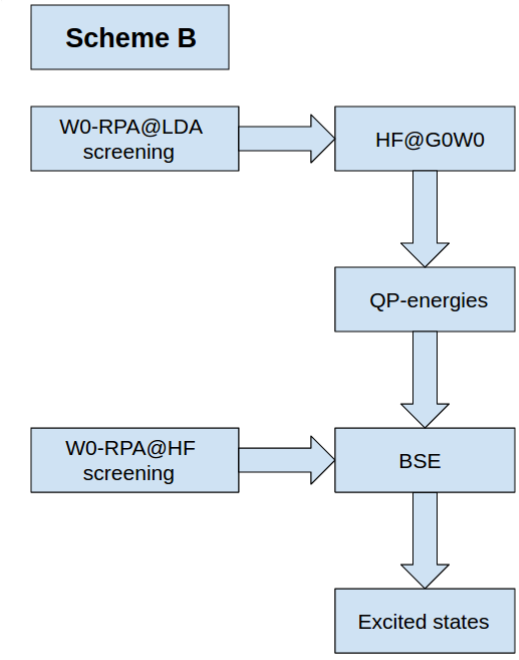

Figure 5.10: The flowchart of scheme B is presented. The W_0-RPA@LDA screening is injected into G_0W_0@HF to obtain the QP energies affected by the W_0-RPA@LDA screening, whereas W_0-RPA@HF screening is injected into the BSE to enhance the electron-hole effect (excitonic red-shift).

Technical details

The many-body calculations are performed using MOLGW [29,30] with frozen core approximation and the resolution-of-the-identity [31, 32]. Depending on computational feasibility whenever possible a flexible basis set (aug-cc-pVQZ) [33] is used for the EOM-CCSD and GW/BSE calculations. Furthermore, as the Green's function G and dynamically screened interaction W strongly depend on the virtual orbitals, hence all unoccupied orbitals are taken into account to fully ensure convergence of HOMO-LUMO QP gaps. As before, the self-energy is calculated analytically through the spectral representation of W and the residuum theorem. BSE calculations are performed in the limit of adiabatic static kernel with mixing of resonant and anti-resonant contributions. Further all coupled cluster calculations (EOM-CCSD) are performed using PSI4 [34].

5.4.2 Improved excitation energies

In Appendix B the results of full eigenvalue self-consistent scheme starting from HF orbitals are presented along with the screening mixed ansatz of scheme A and EOM-CCSD for comparison. As can be seen, the standard method (BSE@G_nW_n@HF) overestimates the singlet transition energies over the entire set of molecular systems by 0.2-0.6 eV on average, which is large given the fact that the molecules are small and simple; however scheme A considerably improves the excitation energies over a large range of energies for each molecule, giving a satisfactory accuracy as presented in Fig 5.11. This underpins the finding that W_0-RPA@LDA screening used as initial screening for W in G_0W_0@HF optimally damps and regulates the HF exchange effect on the QP energies. The standard G_nW_n@HF, as expected, overestimates the HOMO-LUMO gaps (and hence the transition energies) due to underscreening of W upon molecular energy updating.

For extreme cases, a better agreement to the EOM-CCSD excitation energies can be obtained if one uses W_0-RPA@LDA screening for W_0 in G_0W_0@HF, but (in a new calculation) W_0-RPA@HF screening in the BSE (scheme B). The reason for the better agreement is that the W_0-RPA@HF screening is weaker than W_0-RPA@LDA screening, and hence excitonic effects are more effective, leading to a larger red-shift of excitation energies. This multi-screening injection scheme is only an improvement if the scheme A still overestimates the vertical energies, and hence by injection of W_0-RPA@HF screening in the BSE, it is then possible to achieve a further improvement in the BSE, and hence excitation energies.

For carbonyl sulfide (COS) and disilane (Si_2H_6) which have a large mean absolute error of excitation energies, the effect of injection of W_0-RPA@LDA screening in GW and W_0-RPA@HF screening in the BSE is shown in Table 5.10, leading to a further considerable

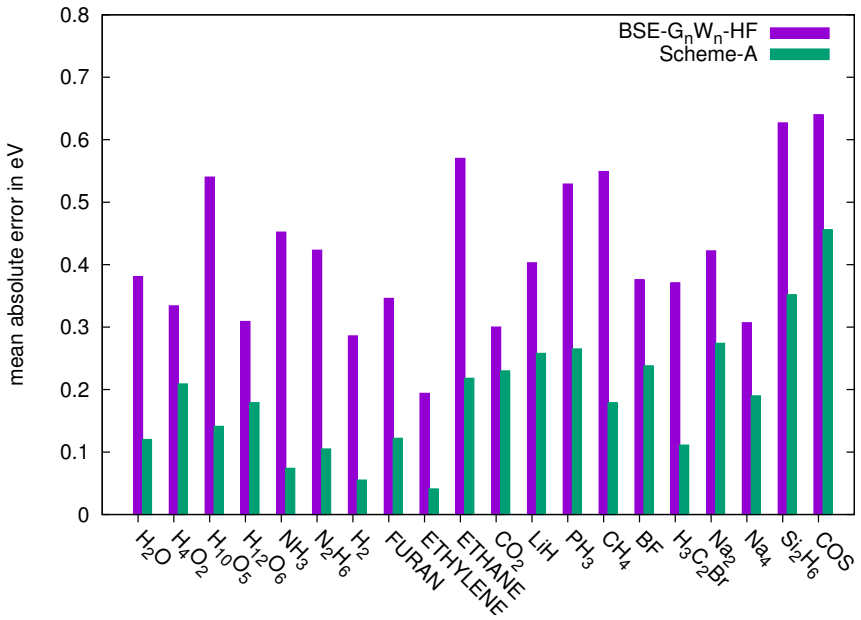

Figure 5.11: Average absolute error (over 5 singlet states) relative to EOM-CCSD for 20 reference molecules is given. Using W_0-RPA@LDA screening as initial screening for G_0W_0@HF considerably reduces the average absolute error over the entire set of molecules, in some cases such as water pentamer and ammonia monomer errors are massively decreased. In extreme cases such as Si_2H_6 and COS the error of scheme A is still considerable.

reduction of the absolute errors, and consequently to much better vertical transition energies. Similar results can also be obtained for other molecules with large excitation energy errors. Therefore, the scheme B is best suited for the cases where the standard GW/BSE approach extremely overestimates the excitation energies due to lack of a proper screening description. This is for instance the case for COS and Si_2H_6.

5.4.3 Consistency and theoretical justification

The success of this ansatz is based on the fact that the traditional eigenvalue self-consistent GW based on HF orbitals (denoted as G_nW_n@HF with n as the iteration number) overestimates the HOMO-LUMO QP gap and consequently the excitation energies. This overestimation is diminished by overscreening nature of the LDA functional in the presented schemes A and B. Therefore, the obtained improvement from this screening mixing procedure is systematic because of the general overestimation of the QP gap by G_nW_n@HF approach.

Regarding the screening itself, the choice of the LDA functional is justified by the fact that its overscreening character is stronger than that of other functionals; however other

Table 5.10: Screening mixing effects for scheme A and scheme B for the five lowest excited states of COS and Si_2H_6.

BSE@ :	G_nW_n@HF	Scheme A	Scheme B	EOM-CCSD
COS (aug-cc-pVQZ)				
S_1 (1A2)	6.26	6.14	5.83	5.76
S_2 (1A1)	6.51	6.38	6.09	5.83
S_3 (2A2)	6.51	6.38	6.09	5.83
S_4 (1B1)	8.19	7.93	7.84	7.53
S_5 (1B2)	8.19	7.93	7.84	7.53
mean absolute error	**0.64**	**0.45**	**0.24**	
Si_2H_6 (aug-cc-pVTZ)				
S_1 (1Ag)	8.21	7.84	7.74	7.63
S_2 (1Au)	8.24	8.07	7.67	7.61
S_3 (1Bu)	8.24	8.07	7.67	7.61
S_4 (2Bu)	8.63	8.27	8.15	7.98
S_5 (2Ag)	8.88	8.56	8.39	8.23
mean absolute error	**0.62**	**0.35**	**0.11**	

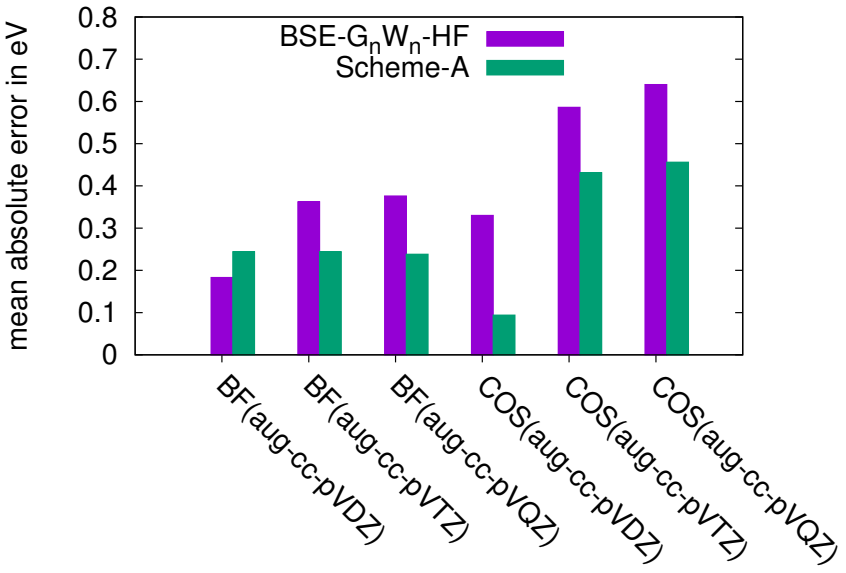

Figure 5.12: Basis set effect on the mean absolute errors. The absolute errors increase upon basis set increase; however the relative absolute error nearly converges with aug-cc-pVTZ and aug-cc-pVQZ.

functionals with a good overscreening grade can also be used.

Furthermore, this ansatz has no straightforward theoretical justification and relies purely on cancellation effects; however one could connect the screening character of the LDA functional with the terms from higher-order correlation diagrams (vertex terms), in the exact theory. This is an important connection since the vertex terms in the screened interaction W are computationally very time-consuming even for the smallest molecules, and the present schemes (A and B) provide indeed a good alternative way of calculating these higher-order correlation terms in a very simple and straightforward fashion.

5.4.4 Basis set effect

In this subsection, the basis effects are investigated on the mean absolute error accuracy of BF and COS molecules of the standard GW/BSE approach and scheme A. As shown in Fig. 5.12 the errors increase with increasing flexibility of the basis sets, and a basis set convergence is obtained with aug-cc-pVQZ basis set. However, the relative mean absolute error is nearly converged even for the less flexible aug-cc-pVTZ basis sets. Nevertheless, the aug-cc-pVQZ basis sets were used whenever the EOM-CCSD calculations were still computationally tractable.

Table 5.11: HOMO-LUMO gaps of COS and Si_2H_6 at different levels of theory in eV. 10 iterations in the self-consistent Hedin-Pentagon (n=10) were performed to ensure convergence of the QP gaps.

	HF	G_0W_0@HF	G_nW_n@HF	Scheme A
COS (aug-cc-pVQZ)				
HOMO-LUMO QP gap	12.604	12.635	12.617	12.274
Si_2H_6 (aug-cc-pVTZ)				
HOMO-LUMO QP gap	11.930	11.784	11.775	11.328

5.4.5 Renormalization effect in GW and BSE

In this subsection, the impact of screening in each calculation part (GW and BSE) is outlined. As shown in Table 5.11, the W_0-RPA@LDA screening reduces the QP gaps. This is demonstrated by injecting of W_0-RPA@LDA screening in G_0W_0@HF, renormalizing considerably the HOMO-LUMO gap of COS and Si_2H_6 by 0.330 and 0.602 eV from HF, respectively. By contrast, W_n-RPA@HF screening only moderately and hence insufficiently damps the HOMO-LUMO HF gap, showing that W_0-RPA@LDA is much stronger than W_n-RPA@HF screening. Furthermore, in the BSE, one can either inject the W_0-RPA@LDA (scheme A) or W_0-RPA@HF screening (scheme B) in the BSE.

5.4.6 Size extensivity

An interesting point is how the quality of excitation energies of the screening mixed GW/BSE (scheme A) behaves upon increase of the number of identical molecules in a cluster. As presented in Table B.1 and Fig. 5.13, the mean absolute error of G_0W_0@HF/LDA relative to EOM-CCSD remains largely unaffected upon cluster size increase, and hence the quality of the excitation energies based on the present screening ansatz does not degrade for larger clusters. This is a good sign for the applicability of this ansatz on larger systems for which wave function based methods are out of reach.

5.4.7 Screening effect on the BSE absorption spectra

The effect of W_0-RPA@LDA screening in scheme A on the absorption spectra of water monomer and dimer is calculated over large energy regimes. As can be seen in Fig. 5.14 injection of W_0-RPA@LDA screening as in G_0W_0@HF results in a consistent red-shift of the

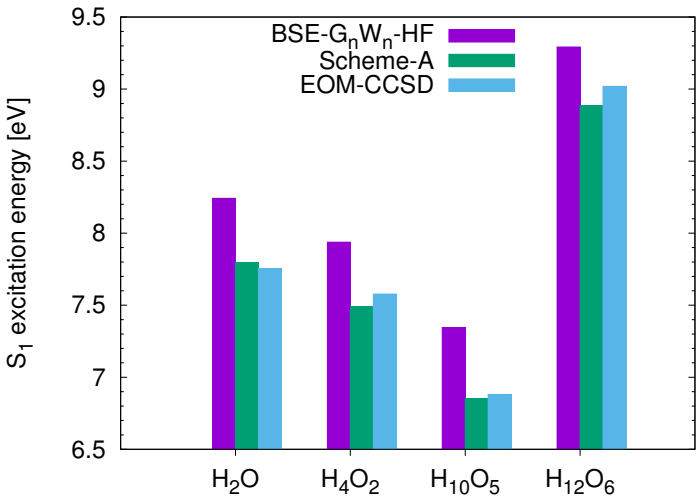

Figure 5.13: Size extensivity of the accuracy of the screening mixed GW/BSE (scheme A) versus BSE@G_nW_n@HF and EOM-CCSD is shown. Upon cluster size increase, the accuracy of the first excitation energy S_1 (optical gap) does not degrade.

entire water spectrum due to a consistent HOMO-LUMO QP gap reduction, leading to an optimal damping of HF exchange effect in all energy ranges. This is also observed for larger water clusters (pentamer and hexamer) and other smaller molecular systems. Furthermore, the intensities of the BSE spectra are moderately reduced; however the spectral weight distributions remain unaffected in all energy scales.

5.4.8 Application to large biological molecules

In this subsection, the many-body screening ansatz is applied on selected large molecular systems for which both experimental and recent EOM-CCSD (bt-PNO-EOMEA-CCSD) results [24] are available. The large systems are biological molecular species, namely, 11-cis-retinal protonated Schiff base (with 156 electrons and 2202 auxiliary basis functions (ABF)) and Chloropyll A (with 340 electrons and 4262 ABFs). The optimized molecular geometries were obtained from Ref. 24. Here different variants of the GW/BSE methodology are compared to demonstrate the screening effects and exhibit the consistency of the screening injected results in comparison to the available experimental and most importantly to the wave function based theoretical data. For both species aug-cc-pVDZ basis sets are used with 400 virtual orbitals in G and W to ensure convergence of the excited-state energies within 50 meV accuracy.

As can be seen from Table 5.12, in the case of retinal the S_1 energies of bt-PNO-EOMEA-CCSD and scheme A are close, whereas for the S_2 energy the deviation is larger. As of

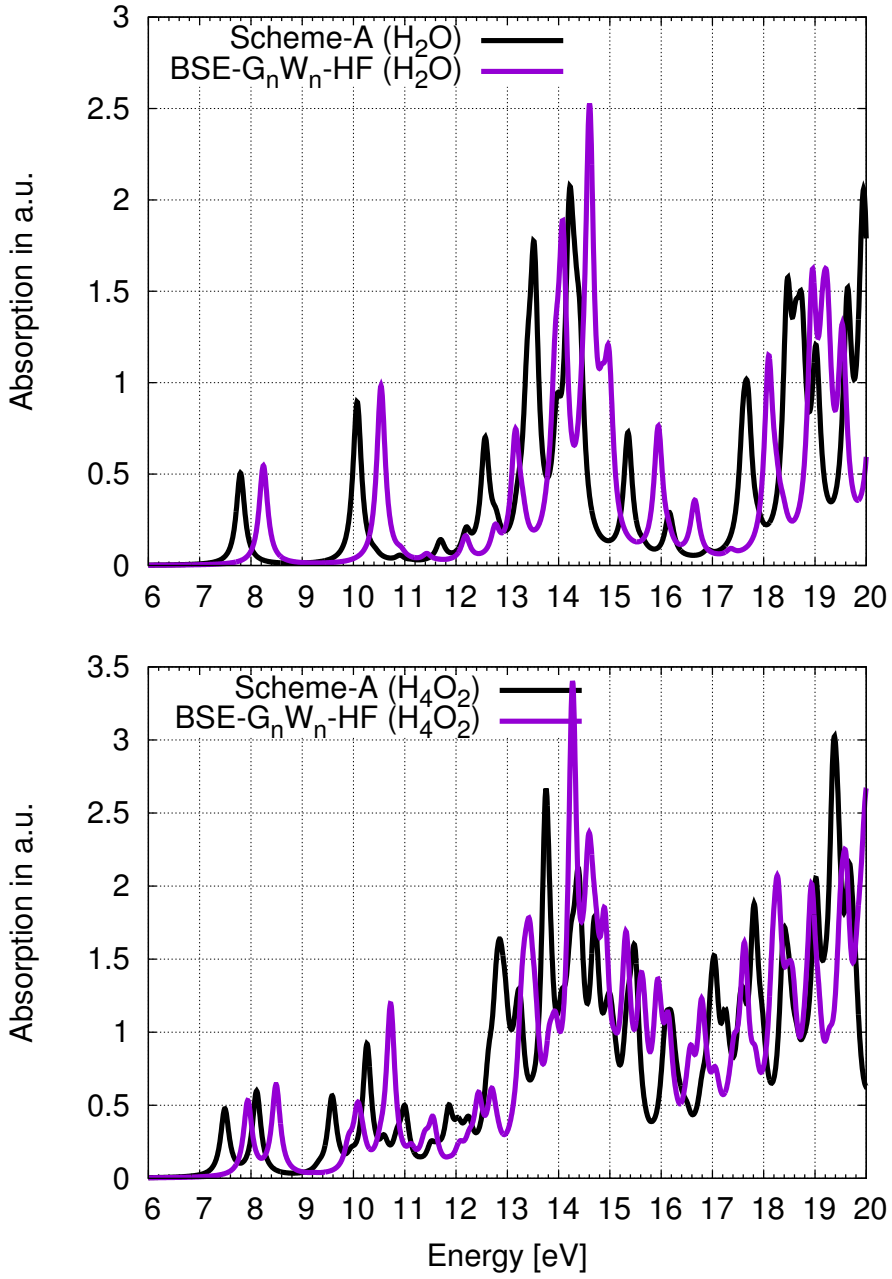

Figure 5.14: The effect of injection of W_0-RPA@LDA screening in G_nW_n@HF on optical absorption spectra of water monomer and dimer is shown. The W_0-RPA@LDA screening consistently red-shifts the standard BSE@G_nW_n@HF spectra over the full energy range towards lower energies.

Table 5.12: Excitation energies of the first two singlet states in eV based on BSE@G_0W_0@HF, BSE@G_nW_n@HF, scheme A, and EOM-CCSD. Calculations were performed with aug-cc-pVDZ basis sets.

BSE@ :	G_0W_0@HF	G_nW_n@HF	Scheme A	EOM-CCSD[1]	EXP[2]
11-cis-Retinal					
S_1 (1A)	2.42	2.23	1.86	1.80	2.03
S_2 (2A)	3.79	3.57	2.80	3.30	3.18
Chloropyll A					
S_1 (1A)	2.18	2.01	1.98	1.70	1.9
S_2 (2A)	2.76	2.55	2.33	2.37	—

BSE@G_nW_n@HF, the excitations energies are consistently overestimated which can be consistently reduced using W_0-RPA@LDA screening within scheme A.

In the case of chloropyll A, BSE@G_0W_0@HF overestimates the experimental S_1 energy by about 0.3 eV; however full update of the orbital energies in G and W (BSE@G_nW_n@HF) improves the agreement. W_0-RPA@LDA screening enhances the agreement only slightly. However, with respect to the S_2 energy, scheme A transition energy is in good agreement with bt-PNO-EOMEA-CCSD, whereas BSE@G_0W_0@HF and BSE@G_nW_n@HF considerably overestimate the S_2 energy.

It must be noted that for larger systems EOM-CCSD and iterative GW schemes become computationally intractable. Therefore, the presented non-iterative screening mixed GW/BSE approaches (schemes A and B) provides a reliable alternative for computing excited-state energies with a good accuracy at much lower cost from an exact self-interaction free reference state (HF).

5.4.9 Conclusions

It was shown that through injection of W_0-RPA@LDA screening to G_0W_0@HF, one can optimally reduce the overestimated HF and HF based QP gaps resulting in a consistent and robust enhancement of the quality of excitation energies, since BSE@G_0W_0@HF and BSE@G_nW_n@HF approach consistently overestimate the excitation energies. In extreme cases such as COS and Si_2H_6, where the mean absolute error was large, it is possible to enhance the performance by injecting W_0-RPA@LDA screening into G_0W_0@HF in GW part to obtain adequate QP energies and in the subsequent BSE step, W_0-RPA@HF screening is injected in the BS equation (scheme B) in order to increase the effect of excitonic red-shift.

The accuracy of screening mixed GW/BSE theory is consistent both in the low and high energy regimes. Furthermore, within this screening scheme, introduction of any kind of parameter as usually encountered for instance in the advanced TD-DFT is strictly avoided.

The screening mixing schemes A and B are -in particular with respect to large molecules- computationally efficient, as they avoid update of W through molecular orbital energies through the iterative self-consistent Hedin-Pentagon.

As a final important remark, the applicability and consistency of the proposed mixing approach strongly relies on cancellation effects between HF exchange and overscreening character of the LDA functional which are crucial for systematic improvement of excitation energies. In general the calculations should be performed based on scheme A. For critical cases where excitation energies show large deviations from the experimental reference, scheme B should be considered.

Bibliography

[1] G. Strinati, Riv. Nuovo Cimento 11, 1 (1988)

[2] G. Onida, L. Reining, and A. Rubio, Rev. Mod. Phys. **74**, 601.

[3] B. Baumeier, D. Andrienko, Y. Ma, M. Rohlfing, J. Chem. Theory Comput. **85**, 323 (2012).

[4] J. C. Grossman, M. Rohlfing, L. Mitas, S. G. Louie, and M. L. Cohen, Phys. Rev. Lett. **2001**, 472 (2001).

[5] S. Körbel, P. Boulanger, I. Duchemin, X. Blase, M. A. L. Marques, and S. Botti, **10**, 3934-3943 (2014).

[6] C. Faber, P. Boulanger, C. Attaccalite, I. Duchemin, and X. Blase, http://dx.doi.org/10.1098/rsta.2013.0271 (2014).

[7] P. Koval, D. Foerster, and D. Sanchez-Portal, Phys. Rev. B **89**, 155417 (2014).

[8] C. Faber, C. Attaccalite, V. Olevano, E. Runge, and X. Blase, Phys. Rev. B **83**, 115123 (2011).

[9] F. Caruso, P. Rinke, X. Ren, M. Scheffler, and A. Rubio, Phys. Rev. B **86**, 081102 (2012).

[10] F. Bruneval and M. A. L. Marques, J. Chem. Theory Comput. **9**, 324324 (2013).

[11] E. Coccia, D. Varsano, and L. Guidoni, J. Chem. Theory Comput. **10**, 501-506 (2014).

[12] N. Marom, F. Caruso, X. Ren, O. T. Hofmann, T. Körzdörfer, J. R. Chelikowsky, A. Rubio, M. Scheffler, and P. Rinke, Phys. Rev. B, **86**, 245127 (2012).

[13] T. Rangel, S. M. Hamed, F. Bruneval, and J. B. Neaton, J. Chem. Theory Comput. **12**, 2834-2842 (2016).

[14] C. Faber, J. L. Janssen, M. Côté, E. Runge, and X. Blase, Phys. Rev. B **84**, 155104 (2011).

[15] Van Setten et al. , J. Chem. Theory Comput., **11**, 5665-5687 (2015).

[16] F. Caruso et al., J. Chem. Theory Comput., **12**, 5076-5087 (2016).

[17] E. Runge and E. K. U. Gross, Phys. Rev. Lett. **52**, 997 (1984).

[18] C. A. Ullrich, Time-Dependent Density-Functional Theory: Concepts and Applications, Oxford Graduate Texts (Oxford University Press, Oxford, New York, 2012).

[19] L. Hedin, Phys. Rev. Lett., **139**, A796 (1965).

[20] Chai and Head-Gordon, J. Chem. Phys. **128**, 084106 (2008).

[21] T. Stein, L. Kronik, R. Baer, J. Chem. Phys. **131**, 244119 (2009).

[22] V. Ziaei, and T. Bredow, J. Chem. Phys. **145**, 174305 (2016).

[23] V. Ziaei, and T. Bredow (2017), Large-Scale Quantum Many-Body Perturbation on Spin and Charge Separation in the Excited States of the Synthesized Donor–Acceptor Hybrid PBI-Macrocycle Complex. ChemPhysChem. doi: 10.1002/cphc.201601244

[24] A. Dutta, F. Neese, and R. Izsákb, J. Chem. Phys. **145**, 034102 (2016).

[25] X. Blase, P. Boulanger, F. Bruneval, M. Fernandez-Serra, and I. Duchemin, J. Chem. Phys. **144**, 034109 (2016).

[26] F. Bruneval, S. M. Hamed, and J. B. Neaton, J. Chem. Phys. **142**, 244101 (2015).

[27] D. Jacquemin, I. Duchemin, A. Blondel, and X. Blase, J. Chem. Theo. Comp. **12**, 3969-3981 (2016).

[28] D. Jacquemin, I. Duchemin, and X. Blase, J. Phys. Chem. Lett. **8**, 1524-1529 (2017)

[29] F. Bruneval,
https://github.com/bruneval/molgw (2016)

[30] F. Bruneval, T. Rangel, S. M. Hamed, M. Shao, C. Yang, and J. B. Neaton, Comput. Phys. Commun. **208**, 149 (2016).

[31] F. Weigend, Phys. Chem. Chem. Phys. **4**, 4285–4291 (2002).

[32] F. Weigend, A. Kohn and C. Hättig, J. Chem. Phys. **16**, 3175-3183 (2002).

[33] T. H. Dunning, J. Chem. Phys. **90**, 1007 (1989).

[34] "Psi4: An open-source ab initio electronic structure program," J. M. Turney, A. C. Simmonett, R. M. Parrish, E. G. Hohenstein, F. Evangelista, J. T. Fermann, B. J. Mintz, L. A. Burns, J. J. Wilke, M. L. Abrams, N. J. Russ, M. L. Leininger, C. L. Janssen, E. T. Seidl, W. D. Allen, H. F. Schaefer, R. A. King, E. F. Valeev, C. D. Sherrill, and T. D. Crawford, WIREs Comput. Mol. Sci. **2**, 556 (2012). (doi: 10.1002/wcms.93).

[35] I. B. Nielsen, L. Lammich, and L. H. Andersen, Phys. Rev. Lett. **96**, 018304 (2006).

Chapter 6

Ab-initio non-adiabatic excited-state dynamics

In this chapter, the complex quantum dynamics of protons in the low-lying excited states of liquid water is investigated. To this end, for a better understanding of the underlying theoretical methods a short review of the basic principles of ab-initio excited-state dynamics and non-adiabatic couplings (NACs) is presented for studying time evolution of photo-excited phenomena in chemical systems. Accordingly, the algorithmic procedures for excited-state time evolution and NACs are derived and described. For further detailed information, in particular with respect to derivation of the equations, the reader is encouraged to consult the references [1–6].

6.1 Born-Oppenheimer approximation and non-adiabatic couplings

One generally starts with a Hamiltonian that describes the physics of the system. The electronic Hamiltonian is defined as :

$$\hat{H}_e = \hat{V}_{NN} + \hat{T}_e + \hat{V}_{Ne} + \hat{V}_{ee} \tag{6.1}$$

where $\hat{V}_{NN}$ denotes the nuclear-nuclear repulsion, $\hat{T}_e$ is the kinetic energy of the electrons, $\hat{V}_{Ne}$ denotes the attraction between nuclei and electrons, and $\hat{V}_{ee}$ is the electron-electron repulsion. Using Eq. (6.1) the time-independent Schrödinger eigenvalue problem reads as :

$$\hat{H}_e(\mathbf{R}, \mathbf{r})\Phi_i(\mathbf{R}, \mathbf{r}) = V_i(\mathbf{R})\Phi_i(\mathbf{R}, \mathbf{r}) \tag{6.2}$$

whose solutions give the adiabatic electronic states $\Phi_i(\mathbf{R}, \mathbf{r})$ and the eigenvalues $V_i(\mathbf{R})$. Here, $\mathbf{R}$ and $\mathbf{r}$ refer to the entire set of the nuclear and electronic coordinates, respec-

tively. By taking the nuclear kinetic degrees of freedom into account, one defines the total Hamiltonian of the many-body system as :

$$\hat{H} = \hat{T}_N + \hat{V}_{NN} + \hat{T}_e + \hat{V}_{Ne} + \hat{V}_{ee} \tag{6.3}$$

upon which the time-independent eigenfunction of the many-body ensemble reads as :

$$\Psi(\mathbf{R}, \mathbf{r}) = \sum_i \Phi_i(\mathbf{R}, \mathbf{r})\chi_i(\mathbf{R}) \tag{6.4}$$

In Eq. (6.4) the total wave function is now separated and expanded in terms of a sum of products of the electronic $\Phi_i(\mathbf{R}, \mathbf{r})$ and nuclear eigenfunctions $\chi_i(\mathbf{R})$. This separation and expansion is justified because i) the electronic and nuclear degrees of freedom are nearly independent due to much smaller mass of the electrons relative to nuclear masses or in other words the electrons instantly adjust to the change of nuclear coordinates, and ii) the adiabatic states $\Phi_i(\mathbf{R}, \mathbf{r})$ form a a complete orthogonal basis set, allowing for an expansion of the total wave function.

Now by plugging Eq. (6.4) into the Schrödinger equation of the total system :

$$\hat{H}(\mathbf{R}, \mathbf{r})\Psi(\mathbf{R}, \mathbf{r}) = E\Psi(\mathbf{R}, \mathbf{r}) \tag{6.5}$$

and further multiplying by Φ_j^* from the left and integrating over the electronic coordinates, one obtains an equation :

$$[\hat{T}_N + V_j(\mathbf{R})]\chi_j(\mathbf{R}) - \sum_i \hat{\Lambda}_{ji}\chi_i(\mathbf{R}) = E\chi_j(\mathbf{R}) \tag{6.6}$$

which can be used to determine the coefficients of $\chi_i(\mathbf{R})$ in the BO expansion [4].
The important aspect of Eq. (6.6) is that the dynamical correlation between the electronic and nuclear motion is now downfolded into the non-adiabatic coupling term :

$$\hat{\Lambda}_{ji} = \delta_{ji}\hat{T}_N - \langle\Phi_j(\mathbf{R})|\hat{T}_N|\Phi_i(\mathbf{R})\rangle \tag{6.7}$$

This can be further reformulated by using the usual expression for the kinetic nuclear operator $\hat{T}_N = -\frac{1}{2M}\nabla^2_{\mathbf{R}}$, and the average nuclear mass M :

$$\hat{\Lambda}_{ji} = \frac{1}{2M}[2\mathbf{d}_{ji}.\nabla_{\mathbf{R}} + G_{ji}] \tag{6.8}$$

with the first derivative non-adiabatic coupling vector $\mathbf{d}_{ji}$ defined as :

$$\mathbf{d}_{ji}(\mathbf{R}) = \langle\Phi_j(\mathbf{R})|\nabla_{\mathbf{R}}\Phi_i(\mathbf{R})\rangle \tag{6.9}$$

and the second derivative scalar non-adiabatic coupling term G_{ji} given as :

$$G_{ji}(\mathbf{R}) = \langle \Phi_j(\mathbf{R}) | \nabla^2_{\mathbf{R}} \Phi_i(\mathbf{R}) \rangle \tag{6.10}$$

Now, if one simplifies Eq. (6.6) by setting Λ to zero, one obtains the original BO-adiabatic equation :

$$[\hat{T}_N + \hat{V}(R)]\chi(R) = E\chi(R) \tag{6.11}$$

The validity of the BO adiabatic approximation can be checked by Eq. (6.8), since Λ is inversely proportional to the nuclear mass M, meaning the larger the mass, the smaller the non-adiabatic coupling, justifying the $\Lambda = 0$.

Semiclassical Non-Adiabatic Molecular Dynamics

Now, in order to be able to describe the evolution of the chemical system on an excited surface, one solves the time-dependent Schrödinger equation :

$$\hat{H}\Psi(\mathbf{R}, \mathbf{r}, t) = i\frac{\partial}{\partial t}\Psi(\mathbf{R}, \mathbf{r}, t) \tag{6.12}$$

However, due to high complexity of the full quantum solution of the system because of explicit correlation between all the particles, one has to apply classical or semiclassical approximations to be able to efficiently describe the evolution in time.

In the classical molecular dynamics (MD) the nuclear degrees of freedom (DOF) are propagated in time using Newton's equation of motion. The shortcoming of the classical approach is that bond breaking or chemical reactions are not captured by this description as the electronic DOFs are completely ignored. A much better alternative, in particular with respect to time evolution of chemical reactions, is the semi-classical approximation where the total system is divided into a classical and quantum part. The classical part represents the slow DOFs, whereas the quantum part stands for the fast electronic DOFs.
One possibility for realization of such an ansatz is the Ehrenfest method with two central equations :

$$F = M\ddot{\mathbf{R}} = -\nabla_{\mathbf{R}} \langle \psi | \hat{H}_e | \psi \rangle \tag{6.13}$$

$$i\frac{\partial}{\partial t}\Psi(r, t) = \hat{H}_e\Psi(r, t) \tag{6.14}$$

with the first equation describes the nuclei propagation and the second equation treats the electronic motion. However, the Ehrenfest method evolves the electronic DOFs into superposition of adiabatic states :

$$\chi(\mathbf{R}, \mathbf{r}, t) = \sum_k C_k(t)\Phi_k(\mathbf{R}, \mathbf{r}) \tag{6.15}$$

leading to unrealistic description of chemical reactions as unphysical nuclear forces are obtained and hence incorrect trajectories are calculated. This problem is remedied by recovering the BO approximation and propagating the system only in one adiabatic state Φ_k. With this solution one might have a good description for a variety of systems, however the non-adiabatic effects are still neglected.

Tully Surface Hopping

To adress this issue, the surface hopping (SH) method was developed. In SH, the slow DOFs are always propagated on a pure adiabatic potential energy surface (PES), and at the same time non-adiabatic effects are accounted for by allowing transitions between the adiabatic states.

In order to obtain the SH equations, the ansatz (6.15) is substituted into the time-dependent Schrödinger equation and with further manipulations [7], one arrives at a first-order differential equation for the expansion coefficients :

$$i\dot{C}_k(t) = \sum_{j=0}^{N_{adia}} C_j(t)[V_{kj} - i\dot{\mathbf{R}} \cdot \mathbf{d}_{kj}] \tag{6.16}$$

with the sum truncated at N_{adia} adiabatic states. Furthermore, V_{kj} is given as the adiabatic matrix element $\langle\Phi_k|\hat{H}|\Phi_j\rangle$ whose diagonal elements represent the excitation energies ω_i. The excitation energies are derived from time-independent KS DFT methods, like ΔSCF or the restricted open shell KS (ROKS) approach [8]. However, these methods are very approximative and restricted in performance due to assumptions that are in general difficult to justify [9,10]. Therefore, in this work, instead time-dependent density functional theory (TD-DFT) was employed which is a more appropriate ansatz for obtaining excitation energies.

Equation (6.16) describes the evolution of the system under influence of the non-adiabatic couplings as previously defined in Eq. (6.9). An interesting feature of Eq. (6.16) is that only the first derivative of the coupling vectors enter the equation and the second derivative scalar couplings as in Eq. (6.10) are avoided. This follows from the fact that the coefficients $C_i(t)$ only depend on time and not on nuclear coordinates in contrast to the $\chi(\mathbf{R}, t)$ in the BO expansion.

Now, with the equality $\sigma_{kj} = \dot{\mathbf{R}} \cdot \mathbf{d}_{kj} = \langle\Phi_k|\frac{\partial}{\partial t}\Phi_j\rangle$, the NAC term in Eq. (6.16) can be

directly approximated by finite differences :

$$\sigma_{ij|t+\Delta/2} = \frac{1}{2\Delta}[\langle\Phi_k(\mathbf{r};\mathbf{R}(t))|\Phi_j(\mathbf{r};\mathbf{R}(t+\Delta))\rangle - \langle\Phi_k(\mathbf{r};\mathbf{R}(t+\Delta))|\Phi_j(\mathbf{r};\mathbf{R}(t))\rangle] \quad (6.17)$$

The coupling σ_{ij} is computed at time steps t and $t+\Delta$ for the adiabatic states Φ_k and Φ_j. Once the time-dependent coefficients and NACs are calculated, one proceeds further with the SH formula developed by Tully [11] to compute probability transitions :

$$g_{k,j}(t,\Delta) = \max\left(0, -2\int_t^{t+\Delta} d\tau \frac{\Re C_j(\tau)C_k^*(\tau)(\dot{\mathbf{R}}\cdot\mathbf{d}_{kj})(\tau)}{C_j(\tau)C_k^*(\tau)}\right) \quad (6.18)$$

Eq. (6.18) is based on the fewest switches criterion between the electronic adiabatic states, i.e. a way to minimize the number of the surface hops by maintaining correct statistical distribution of the trajectories. According to (6.18), at each time step the probability is evaluated and compared to a random number chosen from the interval $\theta \in [0,1]$ by a Monte Carlo algorithm. If $\theta > g_{k,j}$ the system switches from adiabatic state k to j, and the forces are evaluated for the new electronic state until another surface hop occurs.

Now, with the theoretical formulation of non-adiabatic excited-state (NAESD) dynamics at hand, the next section describes the application of NAESD on a liquid water model consisting of a 64-molecule box, in order to unravel the highly non-trivial proton dynamics in excited states.

6.2 Ultra-fast non-Grotthuss proton dynamics in the first excited state of liquid H_2O

Abstract

In this section, ultra-fast proton transfer (PT) is studied in the first singlet (S_1) state of liquid water (absorption onset) through excited-state dynamics by means of time-dependent density functional theory (TD-DFT) and ab-initio Born-Oppenheimer molecular dynamics (BOMD). It is found that after the initial excitation, a proton transfer occurs in S_1 in form of a rapid jump to a neighboring water molecule. There, the proton either may rest for a relatively long period of time (as a consequence of a defect in the hydrogen bond network (HBN)) followed by back and forth hops to its neighboring water molecule or it further moves to the next water molecule accompanied by back and forth movements. In this way the proton may become delocalized over a long water wire branch, followed again by back and forth jumps or short localization on a water molecule for some fs. As a result, the mechanism of PT in S_1 is in most cases highly non-Grotthuss-like, delayed and discrete. Furthermore, upon PT an excess charge is ejected to the solvent trap, the so-called solvated electron. The spatial extent of the ejected solvated electron is mainly localized within one solvent shell with overlappings on the nearest neighbor water molecules and diffuse tails extending beyond the first solvent sphere. During the entire ultra short excited-state dynamics the remaining OH radical from the initially excited water molecule exhibits an extremely low mobility and is non-reactive.

6.2.1 Introduction

By the advent of femtosecond chemistry real-time tracking of ultra-fast processes in excited states of chemical systems became accessible, allowing for exploring a rich scientific area of unprecedented chemical and physical importance. In this regard, one of the most intensively studied systems in almost every aspect is liquid water; however its excited-state dynamics has been much less matter of theoretical investigations. The experimental measurements confirm the occurrence of non-trivial excited-state processes at low and high energies for which theoretical data based on fully quantum mechanical treatment is still lacking. Therefore, in order to deepen the understanding, a qualitative but insightful theoretical investigation of excited-state processes is performed using combined ab-initio techniques.

The vertical transition energy of bulk liquid water from valence to conduction band continuum is reported at 11.1 eV at ambient temperature [12,13], meaning that at this energy and above, the initially produced non-thermal conduction band electron and the valence band

hole are formed by a direct photo-ionization process, such as the intermediate reaction:

$$H_2O + nh\nu \rightarrow e_{CB} + H_2O^+ \tag{6.19}$$

followed by further relaxation of the highly unstable H_2O^+, and hence a proton transfer to a nearby water molecule according to :

$$H_2O^+ + H_2O \rightarrow OH + H_3O^+ \tag{6.20}$$

resulting in a thermalized hydrated electron, a hydronium cation and a hydroxyl radical. However, the most striking point from excitation perspective is that such above-band-gap processes with exactly the same final net products have also been observed experimentally at energies far below the electronic band gap, extending to the optical absorption band edge of water [14–16], indicating that below-band gap processes are possible through an explicit involvement of solvent nuclear motions [17], as otherwise low-energy processes would have not been energetically feasible. Currently two mechanisms are debated as the most relevant candidates for below-band gap excitations, namely, proton-coupled electron transfer (PCET) and hot hydrogen atom (HHA) mechanism [18–20, 22, 23].

PCET involves a proton transfer to a neighboring water molecule, as well as the injection of an electron into a preformed solvent trap, stabilizing the excess charge, i.e. :

$$2\,H_2O + nh\nu \rightarrow H_2O^* + H_2O \rightarrow e^-_{aq} + H_3O^+ + OH \tag{6.21}$$

while in HHA process, due to the dissociative character of the excited states of water [22, 24], a translationally hot hydrogen atom according to : $H_2O^* \rightarrow H$ (hot) + OH with a high kinetic energy is ejected which subsequently collides with a water molecule from its surrounding, leading to formation of a hydrated electron, hydronium cation and hydroxyl radical, i.e. :

$$H_2O^* \rightarrow H_{hot} + OH \xrightarrow{H_2O} e^-_{aq} + H_3O^+ + OH \tag{6.22}$$

Both low-energy pathways (representing indirect ionisations) need a significant change of water solvent network to produce the hydrated electron, serving as an important criterion for the feasibility of the reactions. In both reactions (PCET or HHA) the same net products are generated but on different pathways. Now, in order to find out which one of the reaction candidates (PCET or HHA) is the most probable one, low-energy excited-state ultra-fast

dynamics of liquid water is analysed in its first excited singlet state by means of a TD-DFT approach combined with ab-initio Born-Oppenheimer Molecular Dynamics (BOMD) [25–29] under periodic boundary conditions (PBC) using plane waves. Employing state-of-the-art excited-state TD-DFT-BO dynamics paves the way to gain a deeper understanding of the excited-state processes in condensed water and a fully parameter-free verification of the spatial extension of spin density of the solvated electron formation, known as the "mother of all spin centers in chemistry" [18].

Technical Details

Imposing PBC is of utmost importance to avoid undesirable surface effects. Furthermore, a plane wave description of the electronic wave function and density is used to ensure basis set independence of the wave function and hence a reliable description of the solvated electron spatial extension in the liquid, as for instance use of a localized basis set would artificially localize the solvated electron in a particular region of the simulation cell.

Resolving the spatial extent of the solvated electron is of importance as it represents a long-standing problem which has been a matter of controversial debates in literature [30–34]. Therefore, a full quantum mechanical treatment of the underlying physico-chemical problem is an important step to verify the possibility of an extension of the spin density beyond the first solvent shell after being ejected and thermalized. To achieve this, excited-state dynamics simulations are performed using the PBE exchange-correlation functional on top of 30 snapshots of the 64-water box (see section 3.1) obtained from a 40 ps BOMD ground-state productive run at 300 K, after equilibration for 10 ps. Both the ground- and excited-state dynamics are performed in an NVT ensemble with Nosé-Hoover thermostat. The electronic wave function and density are expanded in plane waves using cutoffs of 100 and 400 Ry, respectively. A convergence criterion of 10^{-8} Ry is used for the wave function optimization, ground- and excited-state run. For both the ground- and excited-state run an integration time step of 0.5 fs is chosen. Core electrons are taken into account by norm-conserving Troullier-Martins pseudo-potentials [35].

In the next step, the 64-water box (with a side length of 12.4 Å) is simulated in the S_1 state and analysed for 116 femtoseconds, before hopping back to the ground-state occurs. The S_1 energy is at about 5 eV, far lower than the electronic band gap 8.7 eV [36–38] (these values differ from those obtained in chapter 3 due to the use of the PBE functional). The ground- and excited-state dynamics are performed using CPMD [39].

In order to show the relaxation dynamics upon surface hoppings and the rest times from higher to lower states, Born-Oppenheimer non-adiabatic excited-state dynamics simulations

are performed for the smaller 8- and 27-water boxes (with side lengths of 6.21 and 9.31 Å) because of extremely high computational costs for calculations of non-adiabatic couplings for the larger 64-water box. The 8- and 27-water box snapshots are also obtained from BO ground-state molecular dynamics simulation run with the same setup as above.

6.2.2 Proton transfer and solvated electron

First the non-adiabatic excited-state dynamics of the 8-water box starting from 3 different initial configurations is analysed.

In Fig. 6.1 the non-adiabatic dynamics of water starting from S_{10} (a state which lies nearly 1 eV above S_1) for PBE [40] and PBE0 [41] functionals is presented. Consecutive fast hoppings from S_{10} to S_1 are observed within a few femtoseconds, but with a relatively long rest of the system in S_1 of about 100 to 500 fs before relaxation to S_0 is achieved. Variation of the rest time of S_1 depends on the initial configurations and more importantly on the functional. The hybrid approach (PBE0) enhances the S_1 rest lifetime, whereas PBE relaxes the system from S_1 to the ground-state S_0 in a shorter time; however both functionals lead to similar results, such as fast initial consecutive relaxations and a relatively long period of rest time in S_1 and hence an ultra-fast transfer of the proton to a neighboring molecule. This underlines the fact that proton transfer is independent of the description of the exchange-correlation potential, and the observed complex dynamics of the photo-generated proton indeed stems from the intrinsic physics of the system.

A further important consequence of the rapid transition to S_1 shown in Fig. 6.1 is that explicit calculation of non-adiabatic couplings (NACs) at each molecular dynamics step is not necessary. That is particularly important for the larger 64- water box, as explicit computation of the couplings is computationally intractable. Therefore, because the system remains on S_1 for about 150 fs on average (PBE approach), explicit calculation of NACs is omitted in the following calculations of excited-state dynamics in S_1 for the larger and more realistic 64-water system for about 150 fs.

It should be noted that the 8-water box can not be considered as a perfect model for liquid water. Therefore, non-adiabatic molecular dynamics based on the PBE approach are also performed for the 27-water box. Very similar results are obtained (not shown in the Figure) in comparison to the 8-water box.

Based on the present results of the excited-state dynamics simulations the following possibilities can occur :

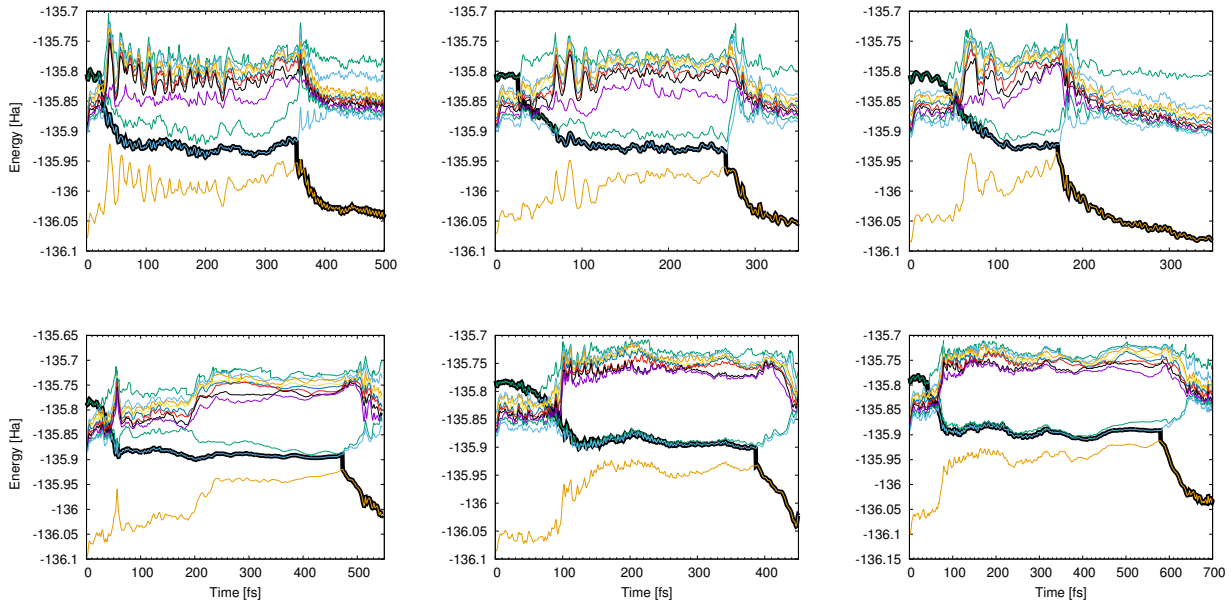

Figure 6.1: Non-adiabatic dynamics of the 8-water box for 3 independent initial configurations from S_{10} to S_0 (ground-state) using PBE in the upper and PBE0 in the lower panel. The consecutive hoppings to lower states were found through explicit ab-initio computation of non-adiabatic couplings at each step of excited-state dynamics and tracked by the thick black line (representing the total energy of the running state). The black line describes how state hopping from higher to lower states at what times occurs. The other colors describes the dynamics in the corresponding excited states if hopping is not taken into account. The first yellow line describes the ground-state dynamics (S_0). Depending on the initial snapshots the rest time of the excited-state dynamics on S_1 varies between 100-250 fs for the PBE and 300-500 fs for the PBE0 functional, respectively.

1) upon excitation of a single water molecule (surrounded by a solvent shell) a fast proton transfer to a nearby water molecule occurs within 12 fs followed by a localization (on that molecule) of about 53 fs, after which a full PT to a third water molecule is accomplished (76 fs) on which the proton becomes delocalized over a water wire for a very short period of time (92 fs), and again localizes on the third water molecule, followed by short delocalizations on a nearby lying forth water molecule (128 fs) (See Fig. 6.2).

2) after the initial excitation an instantaneous PT from the first to a second and from the second to a third water molecule occurs within less than 11 fs in a Grotthuss-like fashion. Once the proton reaches the third molecule, it becomes delocalized over the second and third molecule for a short time, after which it again becomes localized on the third molecule. However, due to a creation of a water chain, it delocalizes over 4 water molecules for a short time (56 fs). After this massive delocalization, it again localizes on the third molecule, from which consecutive hops to a fourth and fifth molecule occur (114 fs) (See Fig. 6.3).

3) after a rapid PT to the neighboring water molecule (8 fs), the proton rests there for a relatively long period of time of about 106 fs, followed by forward and backward hops between a second and third molecule, until finally a full PT to the third molecule is accomplished (191 fs), from which it can further jump to the neighboring molecules (See Fig. 6.4).

4) breaking of both O-H bonds followed by fast recombination. Thus, after the initial excitation, a solvated oxygen atom can be formed which again rapidly recombines with its protons, after which a discrete PT follows as described above.

5) successive jumps of the proton over the hydrogen bonded molecules with almost no delay along a suddenly formed water chain in a Grotthuss-like fashion. These direct instantaneous jumps require however formation of a specific hydrogen bond network (HBN) with nearly no defects, enhancing the probability of a fast proton propagation along the water chain. This possibility was however not observed in the configurations that were studied. Nevertheless, it can not be ruled out, since such a unique formation of a water chain is not entirely impossible; however a Grotthuss dynamics in S_1 seems to be not likely.
Generally speaking, the proton seeks for the best available water chain to perform hoppings. If such a chain is not present, the proton rests on the molecule until a surrounding molecule or an accidentally created water chain provides the possibility for a PT. However, the PT is not necessarily performed along one specific water chain. According to the present observation of the proton dynamics, such a PT can occur along different water chains. Therefore, the proton dynamics is massively dependent on the complexity of the HBN and therefore

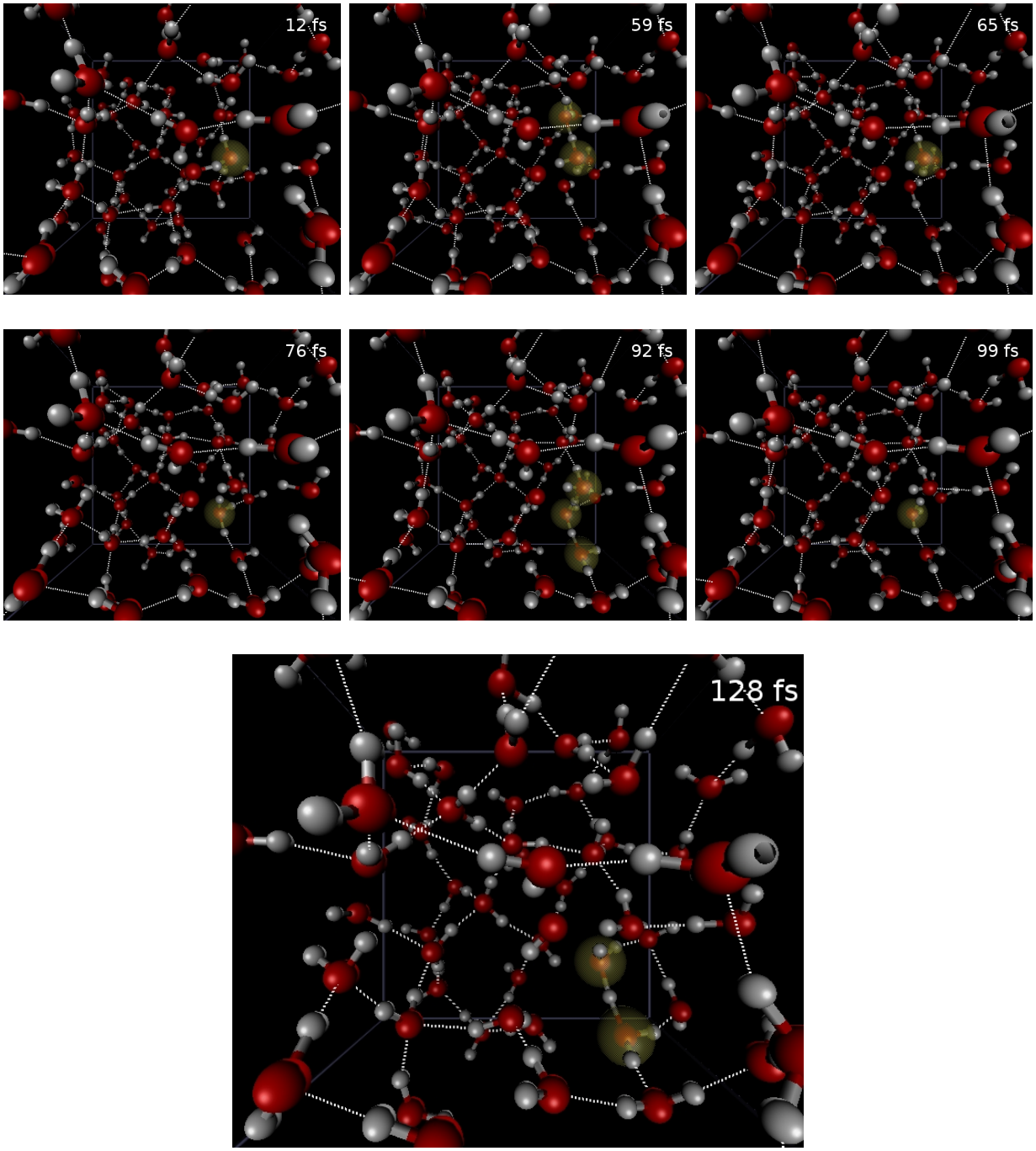

Figure 6.2: Upon excitation of a single water molecule (surrounded by a solvent shell) a fast proton transfer to a nearby water molecule occurrs (12 fs) (as indicated by a yellow sphere; representing the hydronium (H_3O^+)) followed by a localization on the molecule of about 53 fs, after which a full PT to a third water molecule is accomplished (76 fs) on which it becomes delocalized over a water chain for a very short period of time (92 fs), and again localizes on a third water molecule, followed by short delocalizations on a nearby lying forth water molecule (128 fs).

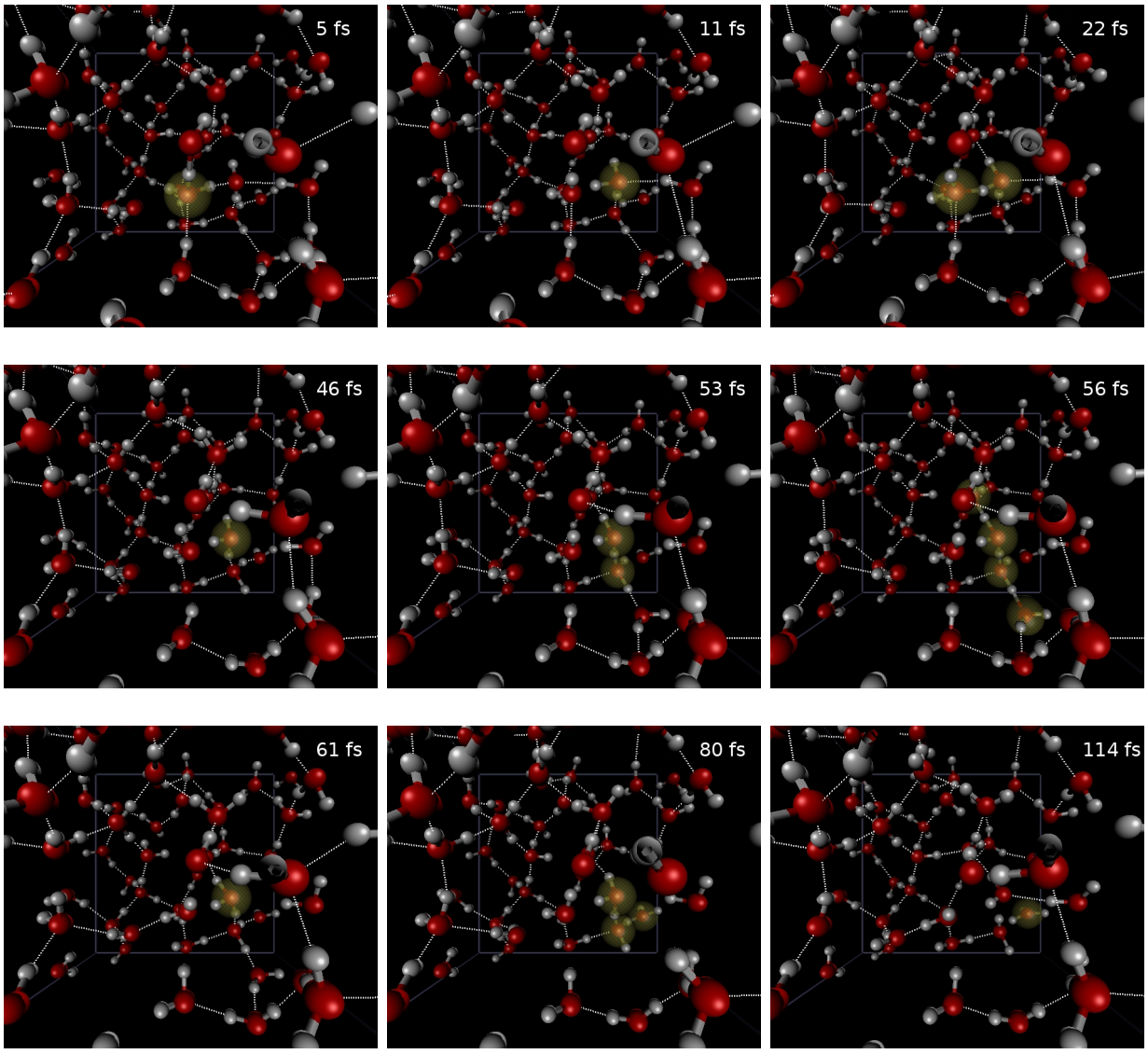

Figure 6.3: After the initial excitation an instantaneous PT from the first to the second and from the second to the third water molecule occurs within less than 11 fs in a Grotthuss-like fashion. Once the proton reaches the third molecule, after a while it becomes delocalized over the second and third molecule for a short time, after which it again becomes localized on the third molecule. However, due to sudden creation of a water wire, it delocalizes over 4 water molecules along a water wire for a short time (56 fs). After this massive delocalization, it again localizes on the third molecule, from which consecutive hops to a fourth and fifth molecules occur (114 fs).

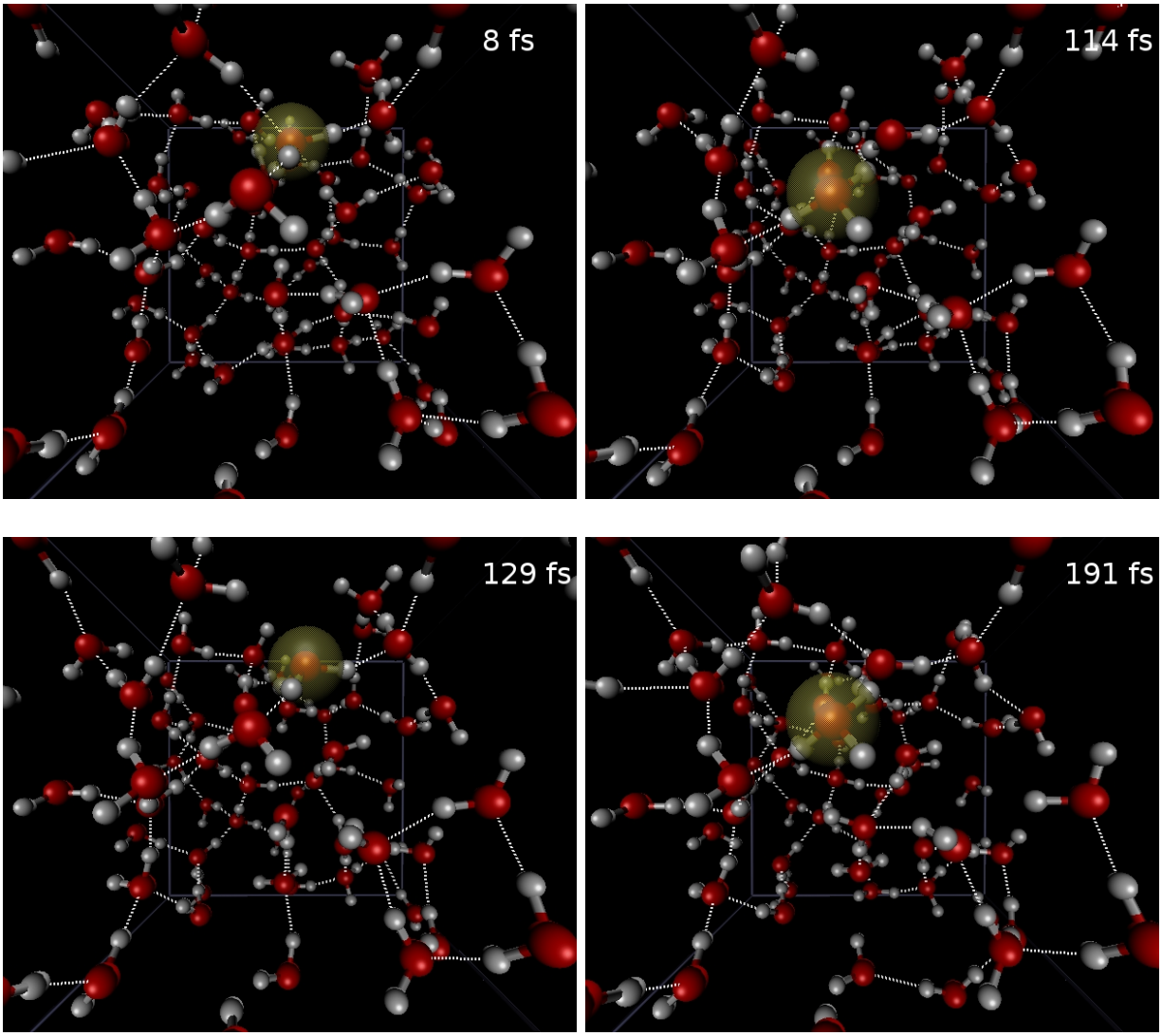

Figure 6.4: After a rapid PT to the neighboring water molecule (8 fs), the proton rests there for a relatively long period of time of about 106 fs, followed by forward and backward hops between the second and third molecule, until finally a full PT to a third molecule is accomplished (191 fs), from which it can further jump to a neighboring molecule.

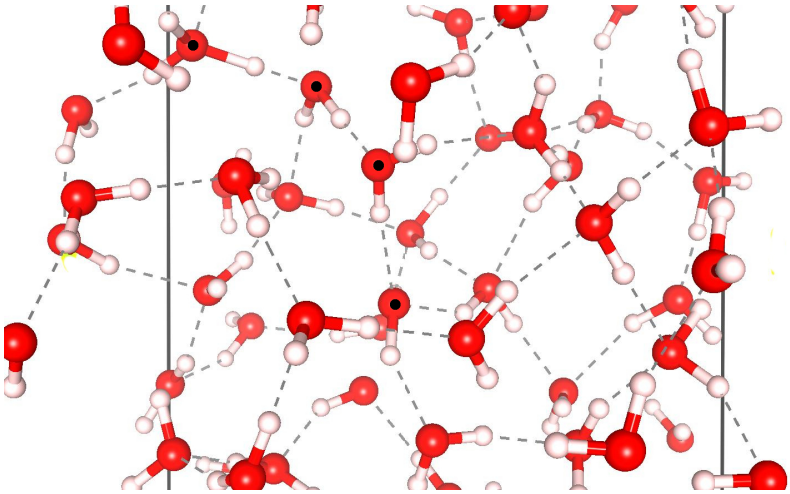

Figure 6.5: Visualization of a possible final trajectory of PT along a water chain marked by the black points on the oxygen atoms (red). The orientation of the water molecules toward each other is key for the type of PT, being either trapped on a molecule or becoming delocalized on a chain or rather fast proton transfers accompanied by back and forth hops.

on the solvation structure.

It is interesting to note that a similar type of proton transfer was also observed in the ground-state (S_0) of charged liquid water (adding an excess proton to the simulation box) by Hassanali et al. [21] on much larger timescales (ps) than in the present study (fs). Furthermore, it was shown by Hassanali that for an even larger box (128-water system) the observed complex proton dynamics is fully independent of the size of the box, and hence not artificial.

One further important aspect of the dynamics is the separation length between the initially excited and the last water molecule of the chain (the farest lying water molecule) which was measured experimentally and found to be 0.7±0.2 nm [22].

In the 30 water configurations the largest separation length (a possible path is shown in Fig. 6.5) in the S_1 excited-state runs was about 0.71 nm, in good agreement with the experimental data. Simultaneously, as the proton is transferred, the hydroxyl anion $(OH)^-$ is in a highly destabilized state, and consequently an electron is ejected to the solvent, leading to formation of a solvated electron and a hydroxyl radical (OH). The OH radical remains nearly rigid with extremely low diffusion during the entire proton transfer process. It also later exhibits no reactivity to the surrounding water molecules.

It should be mentioned that VandeVondele and Sprik [42] found that GGA functionals (such

as the one used for the production runs) are unable to correctly describe the OH radical in water due to the inherent self-interaction error. However, the OH radical and its solvation structure in water is irrelevant for the qualitative study of proton transfer in water, as the species (OH radical, H_3O^+, and e^-) are fully independent. For instance it was shown that the geminate recombination dynamics of the mentioned species can be perfectly described within the independent particle model by Monte Carlo methods [23].

Concerning the solvated electron density (calculated as doublet state for a 64-water box with an extra electron within the unrestricted KS formalism) again the self-interaction error leads to some delocalization of the spin density. However, as shown in Fig. 6.6, the solvated electron is to a large extent localized in a particular region of space (far from the remaining OH radical which is indicated by the yellow color) within the first solvent shell with some notable overlappings with the nearby water molecules and delocalizing tails extending the first and second solvent sphere. Therefore, the spatial extent of the solvated electron based on the PBE functional is a superposition of three densities; a localized part within a cavity, which contains the largest part of the total spin density, an enhanced density area on the neighboring water molecules, and a delocalizing density (in form of diffuse tails) which is the smaller part and distributed anisotropically mostly within the second and (to a lesser extent) third solvent sphere. The delocalization beyond the cavity is likely an artifact of the GGA functional. Moreover, artifacts resulting from periodic boundary conditions may give further error to the spin density distribution, in particular leading to artificial delocalization of the solvated electron.

However, the overall spin density distribution for the snapshot in Fig. 6.6 is in good agreement with the finding of Uhlig et al [34], where the authors also used a GGA-type functional for the open-shell solvated electron, combined with the QM/MM approach to mitigate PBC artifacts. In their paper, a detailed analysis of the radial distribution function of the spin density on the surrounding water molecules is given. The observed enhanced density on the nearby water molecules points at sizable overlap of electron density with the surrounding water molecules. This complex picture of spin distribution indicates at a mixed repulsive and attractive interaction between the solvated electron and the solvent shell. Consequently, the true spin distribution is highly sensitive to the details and interplay of repulsive and attractive interactions which can not be perfectly captured by density functional theory (DFT) due to its approximative nature.

One electron pseudo-potential (PP) cluster model calculations deliver no clear results for the solvated electron [30–32] since depending on the parameters in the construction of the electron-water pseudo-potential, the excess charge shows either a fully localized or an

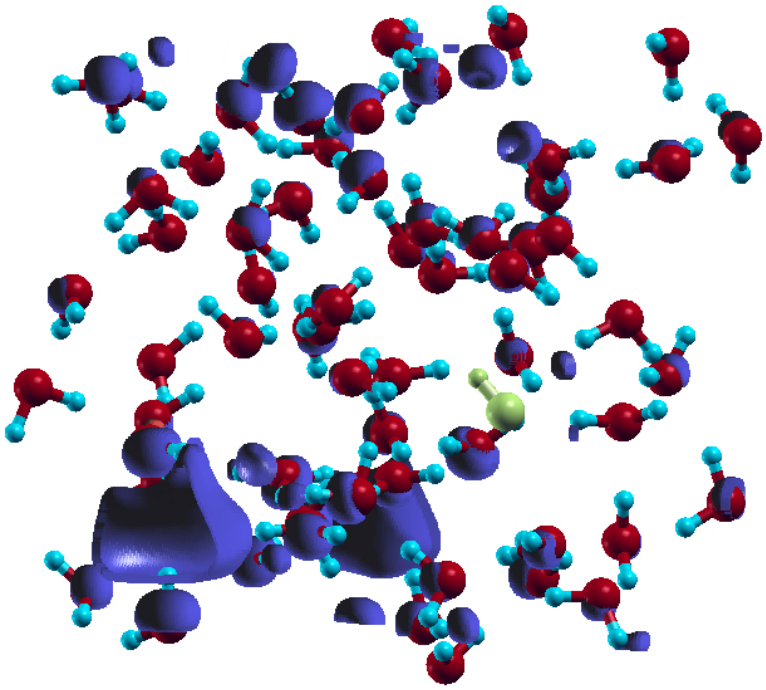

Figure 6.6: Spin density of the solvated electron (shown in blue) in the 64-water box at maximum propagation distance of the proton (after 115 fs) from the OH radical indicated by the yellow color in the box. The localized density coordinated to six water molecules can be seen in bottom left and in the background (periodic boundary conditions). The overlapping density on the water molecules around the localized part is obvious. The diffuse tails appear most in the upper half of the box.

enhanced delocalized behaviour, respectively, due to extreme sensitivity of interaction of solvated electron with water solvent and vice versa.

The separation length (also known as ejection length) between the OH radical (marked by the yellow color in the box) and the solvated electron (dominant blue) for the snapshot in Fig. 6.6 was found to be 0.86 nm (by direct distance measurement from the OH radical to the center of the solvated charge in the cavity) which is in good agreement with the experimentally measured OH – solvated electron distance of about 1 nm at ambient conditions [23]. Similar distances were also found for other snapshots.

6.2.3 Conclusions

By excited-state molecular dynamics simulations in the first singlet state of water it was found that a discrete proton transfer occurs. The propagation of the proton consists of multiple back and forth transitions with the possibility of becoming delocalized over several neighboring water molecules or being trapped by a water molecule for a relatively long

period of time due to a defected HBN. A pure Grotthuss mechanism for PT was not observed; however, it can not be ruled out, since a suddenly created water chain may provide an energetically favored defect free pathway for instantaneous consecutive hops to the neighboring water molecules. Simultaneously to PT, an excess charge is ejected from the hydroxyl (OH) to the liquid which becomes predominantly localized in a cavity-like environment with some delocalized parts beyond the first and second solvent sphere as a consequence of functional artifacts. The observed dynamics in S_1 strongly demonstrates the validity of PCET reaction (3), at least at an excitation energy of about 5 eV.

Bibliography

[1] W. Domcke, D. R. Yarkony, and H. Köppel, editors. Conical Intersections: Electronic Structure, Dynamics Spectroscopy, volume **15** of Advanced Series in Physical Chemistry. (2004).

[2] M. Born and J. R. Oppenheimer. Ann. Physik **84**, 457 (1927).

[3] M. Born and K. Huang. Dynamical Theory of Crystal Lattices. Oxford University Press, (1954).

[4] L. S. Cederbaum. In W. Domcke, D. R. Yarkony, and H. Köppel, editors, Conical Intersec- tions: Electronic Structure, Dynamics Spectroscopy, volume 15 of Advanced Series in Physical Chemistry, chapter 1, page 3. World Scientific, Singapore, (2004).

[5] V. May and O. Kühn. Charge and Energy Transfer Dynamics in Molecular Systems. Wiley-VCH, Weinheim, (2005).

[6] G. A. Worth and L. S. Cederbaum. Annu. Rev. Phys. Chem. **55**,127 (2004).

[7] K. Drukker. J. Comput. Phys. **153**, 225 (1999).

[8] I. Frank, J. Hutter, D. Marx, and M. Parrinello. J. Chem. Phys. **108**, 4060-4069 (1998).

[9] M. E. Casida. In D. P. Chong, editor, Recent Advances in Density Functional Methods, page 155. Singapore, World Scientific, 1995.

[10] M. A. L. Marques and E. K. U. Gross. In F. Nogueira, A. Castro, and M. A. L. Marques, editors, A Primer in Density Functional Theory, volume 620 of Lect. Notes. Phys., chapter 4, page 144. Springer, Berlin, 2003.

[11] J. C. Tully. J. Chem. Phys. **93**, 1061 (1990).

[12] Elles, C. G.; Jailaubekov, A. E.; Crowell, R. A.; Bradforth, S. E. J. Chem. Phys. **125**, 044515 (2016).

[13] Winter, B.; Weber, R.; Widdra, W.; Dittmar, M.; Faubel, M.; Hertel, I. V. J. Phys. Chem. A **108** , 2625 (108).

[14] Bernas, A.; Ferradini, C.; Jay-Gerin, J.-P. J. Photochem. Photobiol. A **117** , 171 (1998).

[15] Marsalek, O.; Uhlig, F.; VandeVondele, J.; Jungwirth, P. Acc. Chem. Res. **45**, 23 (2012).

[16] Marin, T. W.; Takahashi, K.; Bartels, D. M. **125** , 104314 (2006).

[17] Coe, J. V.; Earhart, A. D.; Cohen, M. H.; Hoffman, G. J.; Sarkas, H. W.; Bowen, K. H. J. Chem. Phys. **107**, 6023 (1997).

[18] Kratz, S.; Torres-Alacan, J.; Urbanek, J.; Lindner, J.; Vöhringer, P. Phys. Chem. Chem. Phys. **12**, 12169 (2010).

[19] Crowell, R. A.; Bartels, D. M. J. Phys. Chem. **100**, 17940 (1996).

[20] Thomsen, C. L.; Madsen, D.; Keiding, S. R.; Thogersen, J.; Christiansen, O. J. Chem. Phys. **110**, 3453 (1999).

[21] A. Hassanali et al. PNAS, **110**, 13723 (2013).

[22] Elles, C. G.; Shkrob, I. A.; Crowell, R. A.; Bradforth, S. E. J. Chem. Phys. **126**, 164503 (2007).

[23] Torres-Alacan, J.; Kratz, S.; Vöhringer, P. Phys. Chem. Chem. Phys. **13**, 20806 (2011).

[24] Engel, V.; Schinke, R.; Staemmler, V. J. Chem. Phys. **88**, 129 (1998).

[25] J. C. Tully, J. Chem. Phys. **93**, 1061 (1990).

[26] E. Tapavicza, I. Tavernelli, and U. Rothlisberger, Phys. Rev. Lett. **98**, 023001 (2007).

[27] E. Tapavicza, I. Tavernelli, U. Rothlisberger, C. Filippi, and M. E. Casida, J. Chem. Phys. **129**, 124108 (2008).

[28] I. Tavernelli, E. Tapavicza, and U. Rothlisberger, THEOCHEM **914**, (2009), http://dx.doi.org/10.1016/j.theochem.2009.04.020.

[29] I. Tavernelli, B. F. E. Curchod, A. Laktionov, and U. Rothlisberger, J. Chem. Phys. **133**, 194104 (2010).

[30] R. E. Larsen, W. J. Glover, B. J. Schwartz, Science **329**, 5987 (2010).

[31] L. D. Jacobson, and J. M. Herbert, Science **331**, 6023 (2011).

[32] L. Turi, À. Madaràsz, Science **331**, 6023 (2011).

[33] J. R. Casey, A. Kahros, and B. J. Schwartz, J. Phys. Chem. B **117**, (46), pp 14173–14182 (2013).

[34] F. Uhlig, O. Marsalek, and P. Jungwirth, J. Phys. Chem. Lett. **3**, (20), pp 3071-3075 (2012).

[35] N. Troullier and J. L. Martins, Phys. Rev. B **43**, 1993-2006 (1991).

[36] V. Garbuio, M. Cascellai, L. Reining, R. Del Sole and O. Pulci, Phys. Rev. Lett. **97**, 137402 (2006).

[37] V. Ziaei and T. Bredow, J. Chem. Phys. **145**, 064508 (2016).

[38] A. Bernas, C. Ferradini, and J.-P. Jay-Gerin, Chem. Phys. **222**, 151–160 (1997).

[39] CPMD, http://www.cpmd.org/, Copyright IBM Corp 1990-2015, Copyright MPI für Festkörperforschung Stuttgart 1997-2001.

[40] J. P. Perdew, K. Burke, and M. Ernzerhof, Phys. Rev. Lett. **77**, 3865-3868 (1996).

[41] C. Adamo, and V. Barone, J. Chem. Phys. **110**, 6158 (1999).

[42] J. VandeVondele and M. Sprika, Phys. Chem. Chem. Phys., **7**, 1363-1367 (2005).

Chapter 7

Summary and outlook

In this work, many-body perturbation theory within the Green's function formalism was applied to assess many-body effects in finite and periodic systems. In particular, the impact of electron-phonon coupling, GW self-consistency and higher-order correlation effects were calculated and discussed. Furthermore, it turned out that inclusion of excitonic effects or in other words inclusion of correlated motion of electron-hole pairs is of paramount importance to guarantee agreement with experimental spectra since such effects massively redistribute the spectral weights of the independent-particle spectra towards lower energies for both linear and non-linear spectra.

After it was shown that the GW approximation to the electron self-energy yields accurate band structures and that the Bethe-Salpeter equation describes excited states of solids accurately, the same methodology was applied on finite systems with localized basis sets. The results showed that GW/BSE theory is capable of accurate prediction of excited-state energies of large molecules with no empirical parameter involved. This was in particular shown for large charge-transfer molecules for which even advanced TD-DFT approaches fail to accurately predict the excitation energies due to the lack of the correct $\frac{1}{r}$ Coulombic attraction between the separated charges of the excited electron and hole. By contrast, this shortcoming is cured in the GW/BSE formalism through correct capturing of electron-hole interaction by means of a dynamically screened potential W. Therefore, this many-body method is extremely reliable when it comes to search for technologically relevant CT-molecules for light harvesting.

For small molecules however the GW/BSE accuracy considerably decreases. To solve this issue, a screening mixing ansatz was proposed in two different variants to considerably improve the BSE excitation energies. Furthermore, the proposed schemes in which one circumvents update of screening, can be extremely beneficial for calculation of excited-state properties of large molecules, as they decrease computational costs considerably. Further-

more, the schemes A and B are fully self-interaction free as HF orbitals are used as starting point. This is particularly important for those molecules with a more localized electronic structure for which DFT produces large self-interaction errors.

In the last part of this work, the results of a computational study of the ultrafast proton transfer dynamics in the first singlet excited state of liquid water are reported. The proton release and its short-time dynamics upon a 5 eV excitation were analysed by performing excited-state DFT-based molecular dynamics simulations. Two sets of simulations were performed. In the first one, a simulation box composed by only 8-water molecules was used to calculate non-adiabatic couplings between all states within S_{10} and S_0 to assess the decay time. It was found that after ultra-fast successive decays, the system remains in the S_1 state for considerably longer times, depending on the exchange-correlation functional. Based on this finding, a second set of short time scale simulations on S_1 was performed on much larger (and realistic) simulation boxes. From each of these second series an S_1 dynamics simulation was started. These simulations revealed a complex dissociation dynamics, with the proton often following a non-Grotthuss mechanism, as it carried out multiple back and forth movements or a long localization on a particular water molecule as a consequence of hydrogen bond defects, or even delocalization over several water molecules. Upon the proton transfer, an electron is injected into the liquid, it was found that the hydrated electron is mostly localized within a cavity-like environment with some enhanced densities on the surrounding water molecules, indicating at highly complex electron-solvent interaction.

In conclusion, the GW/BSE formalism can be regarded as a highly appealing alternative ab-initio approach to TD-DFT methods for calculation of static properties such as electronic, polaronic band structures, and excited states of large systems, as its approximated self-energy potential gives rise to a much more realistic and most importantly parameter-free quantification of many-body effects at much lower computational cost compared to coupled cluster based methods. The TD-DFT combined with ab-initio Born-Oppenheimer dynamics can be used for at least a semi-quantitative assessment of a range of complex phenomena, giving a unique access to the non-trivial dynamical processes in large chemical and biological systems.

Concerning the GW/BSE formalism unlike the TD-DFT methods there are still no gradients and Hessians for optimization and vibrational calculations, respectively. However this would be desirable as the GW method gives a precise description of the electronic structure of systems. Exploring the performance of the presented many-body method regarding geometrical and vibrational aspects of molecules and solids is an interesting future task. Aspects like exciton-phonon, exciton-magnon and exciton-magnon-phonon coupling in mag-

netic systems are further highly interesting subjects for future research, helping to gain a detailed understanding of material properties. So, this many-body approach coupled with other effects such as spin waves and lattice vibrations has the potential to provide a truly reliable theoretical tool to engineering materials of potential application in (nano)electronic, optoelectronic, catalysis and many other branches of science.

Appendix A

Convergence tests of liquid water

A.1 Convergence of the electronic band gap

In the following the convergence of the electronic band gap of liquid water is presented with respect to parameters : dielectric matrix cutoff, number of frequency points for sampling of the dielectric function, number of bands in the polarization and Green's function as well as exchange cutoff of the self-energy for one water snapshot. As can be seen a decent convergence can be reached for 400 bands, 50 Ry exchange cutoff, 5 Ry dielectric cutoff, 30 frequency points. Furthermore, for the 27-water box use of a 2x2x2 k-grid is mandatory to be able to accurately converge the spectral signatures with respect to the BZ sampling.

Table A.1: Convergence of the electronic band gap in eV with respect to dielectric matrix cutoff in Ry. Other parameters have been kept fixed at Bands = 400, Frequency = 30, and Exchange cutoff = 50 Ry.

G_0W_0@PBE approach				
$\epsilon(r, r', \omega)$	3	5	7	9
QP gap ($\Gamma - \Gamma$)	9.03	8.83	8.79	8.78

Table A.2: Convergence of the electronic band gap in eV with respect to number of frequency points to sample the dielectric function. Other parameters have been kept fixed at Bands = 400, dielectric matrix cutoff = 5 Ry, and Exchange cutoff = 50 Ry.

G_0W_0@PBE approach				
$\epsilon(r, r', \omega)$	10	30	50	70
QP gap ($\Gamma - \Gamma$)	8.50	8.83	8.79	8.79

Table A.3: Convergence of the electronic band gap in eV with respect to number of bands in the polarization and the Green's function. Other parameters have been kept fixed at dielectric matrix cutoff = 5 Ry, Exchange cutoff = 50 Ry, and Frequency = 30.

G_0W_0@PBE approach				
Bands	200	400	600	800
QP gap ($\Gamma - \Gamma$)	9.41	8.83	8.73	8.71

Table A.4: Convergence of the electronic band gap in eV with respect to exchnage cutoff of the self energy in Ry. Other parameters have been kept fixed at Bands = 400, dielectric matrix cutoff = 5 Ry and Frequency = 30.

G_0W_0@PBE approach				
Exchange Cutoff	50	75	100	125
QP gap ($\Gamma - \Gamma$)	8.83	8.83	8.83	8.83

Table A.5: Convergence of the electronic band gap in eV with respect to damping (in eV) in the Green's function. Other parameters have been kept fixed at Bands = 400, dielectric matrix cutoff = 5 Ry, Exchange cutoff = 50 Ry, and Frequency = 30.

G_0W_0@PBE approach				
damping	0.1	0.01	0.001	0.0001
QP gap ($\Gamma - \Gamma$)	8.83	8.83	8.83	8.83

Appendix B

GW/BSE with localized basis set

B.1 Visible and charge-transfer state of large synthesized PBI-macrocycle complex

---

Below excitation energies of the large PBE-macrocycle molecule **with** solvent effect (dichloromethane) for 20 excited states with SVP basis set using CAM-B3LYP are given :

```
Excitation energies and oscillator strengths with solvent effects :

 Excited State   1:      Singlet-A      2.6734 eV  463.77 nm  f=2.8215
     642 -> 652        0.48281
     643 -> 651        0.49129

 Excited State   2:      Singlet-A      2.6813 eV  462.40 nm  f=0.0017
     642 -> 651        0.48420
     643 -> 652        0.49268

 Excited State   3:      Singlet-A      3.1727 eV  390.78 nm  f=0.0000
     641 -> 657       -0.15123
     644 -> 660        0.15449
     649 -> 653        0.45595
     650 -> 654        0.46045

 Excited State   4:      Singlet-A      3.2047 eV  386.88 nm  f=0.0038
     644 -> 652       -0.21391
     650 -> 651        0.65793
```

```
Excited State   5:      Singlet-A      3.2050 eV  386.84 nm  f=0.0000
    644 -> 651       -0.21458
    650 -> 652        0.65881

Excited State   6:      Singlet-A      3.3363 eV  371.62 nm  f=2.6496
    641 -> 660        0.11299
    644 -> 657       -0.14842
    649 -> 654        0.43102
    650 -> 653        0.48718

Excited State   7:      Singlet-A      3.3510 eV  369.99 nm  f=0.0013
    641 -> 651       -0.16471
    649 -> 652        0.68020

Excited State   8:      Singlet-A      3.3515 eV  369.94 nm  f=0.0000
    641 -> 652       -0.16439
    649 -> 651        0.67952

Excited State   9:      Singlet-A      3.6878 eV  336.20 nm  f=0.0001
    645 -> 652        0.24270
    646 -> 652        0.42501
    647 -> 651        0.29111
    648 -> 651        0.40951

Excited State  10:      Singlet-A      3.6878 eV  336.20 nm  f=0.0000
    645 -> 651        0.24258
    646 -> 651        0.42537
    647 -> 652        0.29080
    648 -> 652        0.40949

Excited State  11:      Singlet-A      3.6956 eV  335.49 nm  f=0.0003
    645 -> 652        0.41654
    646 -> 652       -0.23811
    647 -> 651        0.41191
    648 -> 651       -0.29166

Excited State  12:      Singlet-A      3.6956 eV  335.49 nm  f=0.0000
```

```
    645 -> 651        0.41693
    646 -> 651       -0.23801
    647 -> 652        0.41195
    648 -> 652       -0.29137

Excited State  13:      Singlet-A      3.7466 eV  330.92 nm  f=1.6802
    641 -> 653       -0.30681
    644 -> 654       -0.29504
    646 -> 653        0.11993
    649 -> 657        0.36636
    650 -> 660       -0.32074

Excited State  14:      Singlet-A      3.8184 eV  324.70 nm  f=0.0002
    624 -> 651       -0.10785
    624 -> 652       -0.11405
    626 -> 651       -0.10264
    626 -> 652       -0.10503
    629 -> 651        0.22537
    629 -> 652        0.33399
    630 -> 651        0.38133
    630 -> 652        0.18632
    642 -> 661       -0.16379
    643 -> 661       -0.16502

Excited State  15:      Singlet-A      3.8184 eV  324.70 nm  f=0.0005
    623 -> 652        0.13063
    625 -> 652        0.12086
    629 -> 651        0.34484
    629 -> 652       -0.24843
    630 -> 651       -0.16540
    630 -> 652        0.36674
    642 -> 662       -0.16372
    643 -> 662        0.16510

Excited State  16:      Singlet-A      3.8314 eV  323.60 nm  f=0.0000
    641 -> 654       -0.20883
    644 -> 653       -0.31937
    645 -> 653        0.16645
```

```
    646 -> 654        0.19581
    649 -> 660       -0.25431
    650 -> 657        0.38452

Excited State  17:      Singlet-A      3.8587 eV  321.31 nm  f=0.0003
    645 -> 660       -0.20311
    646 -> 657        0.21316
    647 -> 654        0.37797
    648 -> 653        0.39821

Excited State  18:      Singlet-A      3.8672 eV  320.61 nm  f=0.2020
    645 -> 657        0.20575
    645 -> 665        0.10376
    646 -> 660       -0.20691
    647 -> 653        0.39739
    648 -> 654        0.38393

Excited State  19:      Singlet-A      3.8928 eV  318.50 nm  f=0.9435
    641 -> 653        0.10804
    644 -> 654        0.12090
    645 -> 654        0.37269
    646 -> 653        0.38492
    647 -> 660       -0.20578
    648 -> 657        0.21234
    648 -> 665        0.10478
    650 -> 671       -0.10194

Excited State  20:      Singlet-A      3.8974 eV  318.12 nm  f=0.0002
    644 -> 652        0.63568
    650 -> 651        0.23891
```

Below excitation energies of the large PBE-macrocycle molecule **without** solvent effect for 20 excited states with SVP basis set using CAM-B3LYP are given :

```
Excitation energies and oscillator strengths without solvent effects :

Excited State   1:      Singlet-A      2.7091 eV  457.66 nm  f=2.7046
    641 -> 651       -0.16590
    641 -> 652       -0.44707
    642 -> 651        0.46985
    642 -> 652       -0.15802

Excited State   2:      Singlet-A      2.7246 eV  455.06 nm  f=0.0019
    641 -> 651       -0.17875
    641 -> 652        0.46317
    642 -> 651        0.44126
    642 -> 652        0.18787

Excited State   3:      Singlet-A      2.8349 eV  437.35 nm  f=0.0243
    644 -> 652        0.20258
    650 -> 651       -0.19924
    650 -> 652        0.62757

Excited State   4:      Singlet-A      2.8351 eV  437.31 nm  f=0.0071
    644 -> 651       -0.20255
    650 -> 651        0.62737
    650 -> 652        0.19826

Excited State   5:      Singlet-A      2.9635 eV  418.37 nm  f=0.0001
    643 -> 651       -0.15289
    649 -> 651        0.63938
    649 -> 652       -0.24032

Excited State   6:      Singlet-A      2.9639 eV  418.31 nm  f=0.0003
    643 -> 652        0.15284
    649 -> 651        0.24067
    649 -> 652        0.63966
```

```
Excited State   7:      Singlet-A      3.1669 eV  391.51 nm  f=0.0002
    643 -> 659        0.15965
    644 -> 662        0.15969
    649 -> 653       -0.45715
    650 -> 654        0.45740

Excited State   8:      Singlet-A      3.3338 eV  371.90 nm  f=0.0000
    645 -> 651        0.21016
    646 -> 651        0.46120
    647 -> 651       -0.13172
    648 -> 651        0.47106

Excited State   9:      Singlet-A      3.3338 eV  371.90 nm  f=0.0000
    645 -> 652        0.16377
    646 -> 652       -0.44821
    647 -> 652        0.23540
    648 -> 652        0.46147

Excited State  10:      Singlet-A      3.3384 eV  371.38 nm  f=0.0000
    645 -> 652        0.44286
    646 -> 652        0.15241
    647 -> 652        0.46434
    648 -> 652       -0.24653

Excited State  11:      Singlet-A      3.3392 eV  371.29 nm  f=0.0000
    645 -> 651       -0.45803
    646 -> 651        0.20019
    647 -> 651        0.47534
    648 -> 651        0.14169

Excited State  12:      Singlet-A      3.4013 eV  364.52 nm  f=2.2748
    643 -> 662       -0.11553
    644 -> 659       -0.14927
    649 -> 654       -0.42974
    650 -> 653        0.48635

Excited State  13:      Singlet-A      3.5078 eV  353.46 nm  f=0.0001
    644 -> 651        0.64062
```

```
    650 -> 651        0.22698

Excited State  14:      Singlet-A      3.5079 eV  353.44 nm  f=0.0001
    644 -> 652        0.64155
    650 -> 652       -0.22706

Excited State  15:      Singlet-A      3.6201 eV  342.49 nm  f=0.0001
    643 -> 651        0.23141
    646 -> 651       -0.45847
    648 -> 651        0.47539

Excited State  16:      Singlet-A      3.6210 eV  342.40 nm  f=0.0001
    643 -> 652        0.23223
    646 -> 652        0.48531
    648 -> 652        0.44352

Excited State  17:      Singlet-A      3.6304 eV  341.51 nm  f=0.0000
    644 -> 651        0.10384
    645 -> 651        0.49058
    647 -> 651        0.49213

Excited State  18:      Singlet-A      3.6310 eV  341.46 nm  f=0.0000
    645 -> 652        0.52175
    647 -> 652       -0.46140

Excited State  19:      Singlet-A      3.6619 eV  338.58 nm  f=0.0011
    643 -> 652        0.62832
    646 -> 652       -0.19363
    648 -> 652       -0.15086
    649 -> 652       -0.15739

Excited State  20:      Singlet-A      3.6624 eV  338.54 nm  f=0.0007
    643 -> 651        0.62830
    646 -> 651        0.18424
    648 -> 651       -0.15901
    649 -> 651        0.15703
```

B3LYP optimized structure of the PBI-macrocycle complex in xyz format.

```
294
hybrid PBI-macrocycle complex

  H       7.873667     29.841346      3.473991
  H      -4.945039      7.886992     -7.184141
  H       6.291816     30.357399      4.059982
  H      -5.819564      9.411053     -7.459124
  H       6.149372     28.020301      3.194707
  C       7.107084     29.650576      4.230069
  H       8.512446     27.322980      3.650020
  C      -5.312659      8.803741     -6.712891
  H      -0.320769     11.659954     -5.244817
  H      -1.476075     12.958050     -5.623115
  O      -4.247897      9.602125     -6.221338
  H      -9.961478      1.948426     -4.812038
  C       6.615843     28.205302      4.169053
  H       9.415920     18.974910      0.785858
  H       7.544370     29.879936      5.205747
  O      -2.337246     11.153641     -5.422081
  H     -11.584037      1.780991     -4.103877
  H       6.762479     25.539554      3.378895
  H       8.615071     16.769106      0.096799
  C      -1.317245     12.059435     -5.032101
  C       7.724674     27.177233      4.399105
  H       9.121693     24.830653      3.800664
  C      -3.432638      9.076440     -5.270323
  O       9.605557     20.942508      2.268882
  H       7.953367     14.991903     -0.429942
  H      -6.020712      8.543276     -5.919654
  C     -10.523909      1.605220     -3.937997
  C      -2.378041      9.931798     -4.830319
  H       5.826159     28.056829      4.914159
  C       8.733184     18.425573      1.420343
  H      -4.359977      7.175991     -5.049895
  C       7.239042     25.727943      4.348412
  H       7.122085     12.773269     -1.041215
  C      -3.557223      7.820589     -4.723482
```

H	8.195488	27.367348	5.371469
C	8.269220	17.166751	1.039542
O	-10.388049	0.206394	-3.745448
H	7.286799	23.101847	3.613377
C	-1.501960	9.485057	-3.868217
C	8.351857	24.701495	4.571014
H	9.665151	22.424201	3.824092
H	-1.386268	12.310819	-3.969178
H	-10.199285	2.167064	-3.056412
C	7.279740	14.491664	0.250849
H	-0.707250	10.134250	-3.530463
C	8.844900	20.328444	2.996544
H	-8.033854	1.513177	-3.601329
H	-4.402393	5.015250	-4.347434
C	-2.666345	7.343613	-3.733385
C	6.813799	13.228081	-0.109215
C	8.329877	18.990277	2.613264
C	-9.147830	-0.295457	-3.509909
H	6.456693	25.581663	5.102465
C	-1.612835	8.195844	-3.295325
C	7.837908	23.259190	4.546950
H	-6.170472	2.761841	-3.239261
C	-7.989901	0.444732	-3.449808
H	-9.699705	-4.276811	-3.969667
O	-10.279309	-2.355898	-3.395902
H	8.838507	24.911220	5.528685
C	-3.680510	4.953091	-3.544663
C	7.393103	16.431940	1.832924
O	5.817403	10.667349	-0.736685
C	-2.793255	6.020211	-3.176471
H	-11.336904	-4.062364	-3.309748
C	8.953546	22.203282	4.616000
C	-9.087867	-1.708635	-3.317972
C	6.901836	15.104205	1.441872
C	-10.296572	-3.762269	-3.210193
N	8.422545	20.854702	4.230244
C	-5.354850	2.056713	-3.157097
C	-0.686081	7.728265	-2.295657

H	0.869494	9.310102	-2.115040
C	-6.731037	-0.153005	-3.204582
C	-3.475406	3.790497	-2.853958
H	11.494298	21.215340	5.153193
C	-1.905676	5.620241	-2.174675
C	0.501152	8.350006	-1.780001
C	5.953175	12.534906	0.717312
C	-4.063672	2.471306	-2.979502
H	7.129314	23.102780	5.361694
C	-5.524383	0.631289	-3.123758
C	7.439892	18.285418	3.450087
C	-7.872479	-2.307440	-3.079100
C	-0.875998	6.462345	-1.737433
H	10.185985	23.164297	6.049922
C	5.480478	11.190794	0.306172
C	6.959285	16.997044	3.069154
C	-6.670827	-1.563047	-3.012805
H	-7.825695	-3.377569	-2.939056
H	2.369498	9.975375	-0.097035
C	9.727343	22.176913	5.942471
S	-2.178078	3.976552	-1.660263
C	1.187890	7.590876	-0.874445
H	-9.934930	-4.041930	-2.215903
C	6.010797	14.408054	2.313561
C	-4.306574	-0.021102	-2.915722
C	10.830059	21.119391	6.019942
C	7.512912	20.210978	5.076329
S	-2.967551	1.089567	-2.798697
C	5.538695	13.113524	1.937951
S	0.357466	6.057502	-0.575040
C	2.941427	9.089011	0.144852
C	-5.400785	-2.194917	-2.758587
C	7.026370	18.869117	4.665513
C	2.463130	7.815525	-0.183833
C	-4.246124	-1.409485	-2.743431
H	10.389699	20.118570	5.956804
H	13.412063	20.217792	6.550277
H	-2.372306	-10.480169	-5.701030

N	4.610297	10.534896	1.196526
H	12.115959	22.207013	7.366490
H	9.037077	22.059405	6.778263
H	-3.151030	-12.688267	-6.411527
C	6.063682	16.305282	3.938050
C	4.143019	9.213353	0.829052
H	-5.851358	-4.338900	-2.361127
C	-5.100227	-3.565647	-2.453193
H	-3.849322	-14.436530	-6.983187
O	7.137094	20.728105	6.114004
C	5.576204	14.975578	3.549655
H	-4.663090	-16.653983	-7.620592
C	11.654601	21.213962	7.305214
C	3.233937	6.710244	0.187383
H	-11.941117	-22.395044	-10.027605
H	2.904639	5.726267	-0.116363
S	-2.814543	-2.340177	-2.397162
O	-2.144614	-8.540008	-4.150862
C	4.657682	12.407480	2.786982
C	12.742431	20.145235	7.415926
C	4.882919	8.106912	1.223573
C	6.153762	18.184814	5.486669
C	-3.777829	-3.813188	-2.212692
C	-2.993026	-11.073032	-5.042134
C	-3.443762	-12.332147	-5.434930
C	4.427616	6.822438	0.905705
C	4.161707	11.058761	2.425171
C	5.682467	16.922837	5.125458
C	-4.440625	-14.989823	-6.267872
H	-9.969411	-21.242002	-8.861620
H	12.281013	19.151719	7.357394
H	5.787150	8.246969	1.801798
H	15.355293	19.225612	7.974473
C	-4.897679	-16.252821	-6.643808
H	-13.947416	-23.879055	-9.934921
H	-4.422462	-6.459140	-2.728199
H	14.035369	21.227833	8.757130
H	10.983983	21.138579	8.169371

C	4.705638	14.240763	4.348879
C	-3.072466	-5.036636	-1.814124
H	5.841380	18.643147	6.415360
O	-5.870295	-18.791180	-7.310058
C	-12.324109	-22.722118	-9.054442
C	5.131167	5.599897	1.310555
C	-3.520328	-6.320132	-2.146494
C	4.251770	12.976552	3.976797
H	-12.992192	-21.924748	-8.710410
C	-2.842968	-9.215538	-3.423216
H	-7.943753	-20.128167	-7.692236
C	13.568973	20.237902	8.699637
S	4.165203	4.132273	1.521653
H	-12.491632	-24.820868	-9.609801
C	-3.332344	-10.560622	-3.806578
H	-1.558772	-3.944001	-0.774614
H	5.002671	16.427774	5.803983
C	-13.122825	-24.012434	-9.230844
O	3.410084	10.423968	3.136346
C	-1.881580	-4.926078	-1.091149
C	-4.243695	-13.118029	-4.611174
C	14.646956	19.161615	8.805393
C	-4.724913	-14.444132	-5.019572
C	-10.355176	-21.571105	-7.889545
H	4.359870	14.641421	5.290252
C	6.456049	5.349361	1.533295
H	7.208483	6.118808	1.422228
H	-11.025010	-20.774474	-7.545595
C	-2.773260	-7.426346	-1.765768
C	-5.655809	-17.011373	-5.775734
H	-10.488704	-23.656984	-8.420468
C	-6.122371	-18.356324	-6.199793
C	-11.157592	-22.859840	-8.074597
H	14.210259	18.159234	8.788026
H	3.576844	12.423580	4.616818
C	5.599188	3.197726	1.848976
H	-5.707284	-21.174926	-6.924868
H	12.899707	20.169313	9.564717

C	-1.103775	-6.030917	-0.733032
C	-8.397386	-20.411886	-6.741254
H	15.217386	19.256134	9.732407
N	-3.231208	-8.745506	-2.152726
H	-9.094117	-19.611643	-6.471648
C	6.756506	3.979388	1.841976
C	-1.572356	-7.303060	-1.079936
S	0.991382	-4.265296	-0.327121
S	4.315945	0.700914	1.925836
H	-13.549801	-24.347637	-8.281868
C	-4.139705	-11.320157	-2.931063
H	-8.531970	-22.514002	-7.250784
C	-4.596495	-12.615755	-3.321860
C	-9.190835	-21.711289	-6.906310
C	5.658717	1.809336	2.022620
H	11.284964	5.812824	1.218672
C	0.170376	-5.806156	-0.040399
C	-5.522377	-15.202555	-4.111935
S	3.518170	-2.180862	0.770161
H	-0.994220	-8.188505	-0.849600
H	9.187164	5.156149	1.980662
C	-5.973670	-16.499284	-4.500545
C	8.028876	3.344848	2.076689
H	-11.541381	-23.190456	-7.101815
N	-6.855852	-19.106311	-5.273939
H	-3.548671	-22.333281	-6.155794
C	2.229209	-4.673825	0.829081
C	-6.151600	-21.430694	-5.962413
C	9.233457	4.086072	2.121154
C	-7.318085	-20.482705	-5.648580
C	6.878589	1.154202	2.209167
C	5.412928	-0.682956	2.083529
C	0.863676	-6.570303	0.855845
C	3.255454	-3.830143	1.271227
H	-6.586273	-22.428335	-6.072292
C	-4.030599	-9.454422	-1.237157
C	4.823540	-2.001441	1.955946
C	8.088492	1.935046	2.269378

C	-4.489551	-10.797705	-1.665523
H	0.501696	-7.535919	1.181836
H	-9.578752	-22.029904	-5.931328
C	2.048246	-5.946217	1.375326
C	6.707281	-0.270905	2.241722
C	11.663437	5.534162	2.206968
C	-5.406509	-13.369879	-2.420094
C	-5.864347	-14.707591	-2.818011
H	-4.590804	-20.507264	-4.786103
C	10.451142	3.484166	2.339614
H	12.706188	5.831526	2.287397
C	4.150267	-4.235730	2.264222
C	-6.752977	-17.276417	-3.618768
C	5.036340	-3.168798	2.636016
H	-1.355740	-23.414253	-5.387072
O	11.645526	4.128224	2.395850
C	-5.068614	-21.487807	-4.883144
H	11.081582	6.051964	2.975854
C	-7.225994	-18.629330	-4.004234
C	-3.990305	-22.533177	-5.172335
C	9.349653	1.334060	2.493656
H	7.523127	-0.977557	2.306772
H	-7.795535	-20.838184	-4.738233
O	-4.319658	-8.974753	-0.159179
C	2.981229	-6.418390	2.366973
C	10.510495	2.071075	2.532477
H	-4.455089	-23.523598	-5.246222
C	4.031494	-5.564583	2.809821
H	5.764078	-3.235427	3.433135
H	9.393227	0.265729	2.646007
C	-5.275472	-11.544840	-0.812083
H	2.085389	-8.362918	2.588252
H	11.546266	-0.394016	2.061190
C	-5.723667	-12.810992	-1.185747
H	-2.418017	-21.581306	-4.045795
H	2.776555	-10.540438	3.004249
C	2.878511	-7.713174	2.928717
C	-6.634594	-15.511314	-1.982974

O	11.753173	1.565946	2.746907
C	-7.072793	-16.776684	-2.372692
C	-2.881529	-22.572629	-4.119826
C	-1.796914	-23.612286	-4.403586
O	-7.904494	-19.299090	-3.245065
H	-5.528971	-21.699022	-3.910760
C	4.928786	-6.046540	3.791656
H	5.729295	-5.400887	4.121468
H	-2.256951	-24.604314	-4.474520
H	-5.537318	-11.131521	0.152806
C	3.760451	-8.164520	3.883278
C	11.888552	0.166718	2.936799
H	7.399795	-6.766255	4.973961
H	-6.336265	-13.355512	-0.481748
C	4.812514	-7.308080	4.327193
H	-0.189418	-22.670693	-3.276539
H	-6.909936	-15.166919	-0.996995
C	2.710390	-10.298857	4.069628
H	-7.668750	-17.382518	-1.703171
H	12.951014	-0.012158	3.083267
O	3.727700	-9.391895	4.463999
H	0.065619	-24.389065	-3.581272
C	-0.693204	-23.638600	-3.348188
H	-3.323045	-22.771648	-3.135737
H	11.341242	-0.175126	3.820929
O	5.634147	-7.838626	5.270018
H	2.875508	-11.201957	4.652003
H	1.712956	-9.905862	4.289579
C	6.695560	-7.038879	5.766520
H	-1.095671	-23.872103	-2.358806
H	7.208224	-7.650607	6.505186
H	6.323833	-6.129097	6.247965

B.2 A many-body based screening ansatz for improvement of excitation energies

In the following the GW/BSE excitation energies of the first five lowest singlet states of 22 molecules are presented. The standard and the screening modified schemes are compared. Wherever computationally possible a larger basis set is used in the EOM-CCSD calculations to avoid basis set error biased results.

As discussed in the main text, the modified scheme reduces the typical overestimation of the HF based GW/BSE excitation energies through enhancement of the screening effects in the QP energies (scheme A) and in the BS equation (scheme B). This screening enhancement simulates the effect of vertex corrections in the dynamically screened interaction W.

This screening modified scheme can be extremely helpful in calculating excited states on top of the HF reference state at much lower computational cost for large molecular systems for which explicit computation of the vertex corrections is computationally intractable. Furthermore, this scheme avoids the self-consistency in the traditional self-consistent GW approaches.

BSE@ :	Standard G_nW_n@HF	Standard $\sigma(G_nW_n$@HF)	Scheme A G_0W_0@HF/LDA	Scheme A $\sigma(G_0W_0$@HF/LDA)	EOM-CCSD
H_2O (monomer) (aug-cc-pVQZ)					
S_1 (1B1)	08.242	0.487	07.795	0.040	07.755
S_2 (1A2)	09.920	0.414	09.446	0.059	09.506
S_3 (1A1)	10.536	0.473	10.071	0.008	10.063
S_4 (2B1)	10.922	0.238	10.420	0.263	10.684
S_5 (2A1)	11.429	0.294	10.904	0.230	11.135
mean absolute error		**0.381**		**0.120**	
H_4O_2 (dimer) (aug-cc-pVTZ)					
S_1 ($1A''$)	07.937	0.360	7.490	0.087	07.577
S_2 ($1A'$)	08.489	0.475	8.110	0.095	08.014
S_3 ($2A''$)	09.229	0.305	8.614	0.309	08.924
S_4 ($2A'$)	09.906	0.271	9.325	0.309	09.634
S_5 ($3A''$)	10.080	0.258	9.576	0.245	09.821
mean absolute error		**0.334**		**0.209**	

BSE@ :	Standard G_nW_n@HF	Standard $\sigma(G_nW_n$@HF)	Scheme A G_0W_0@HF/LDA	Scheme A $\sigma(G_0W_0$@HF/LDA)	EOM-CCSD
$H_{10}O_5$ (pentamer) (aug-cc-pVDZ)					
S_1 (1A)	7.345	0.464	6.852	0.028	6.881
S_2 (2A)	7.439	0.480	6.951	0.007	6.959
S_3 (3A)	8.369	0.797	7.704	0.132	7.572
S_4 (4A)	8.617	0.478	7.873	0.265	8.139
S_5 (5A)	8.666	0.479	7.915	0.271	8.187
mean absolute error		**0.540**		**0.141**	
$H_{12}O_6$ (hexamer) (cc-pVDZ)					
S_1 (1A)	09.292	0.273	08.885	0.133	09.019
S_2 (2A)	09.549	0.151	09.082	0.316	09.398
S_3 (3A)	09.902	0.324	09.455	0.122	09.578
S_4 (4A)	09.965	0.292	09.545	0.126	09.672
S_5 (5A)	10.520	0.505	09.816	0.198	10.015
mean absolute error		**0.309**		**0.179**	

BSE@ :	Standard G_nW_n@HF	Standard $\sigma(G_nW_n$@HF)	Scheme A G_0W_0@HF/LDA	Scheme A $\sigma(G_0W_0$@HF/LDA)	EOM-CCSD
NH_3 (monomer) (aug-cc-pVQZ)					
S_1 ($1A'$)	07.261	0.560	06.818	0.117	06.701
S_2 ($2A'$)	08.714	0.475	08.255	0.016	08.239
S_3 ($1A''$)	08.714	0.475	08.255	0.016	08.239
S_4 ($3A'$)	09.575	0.405	09.099	0.070	09.170
S_5 ($4A'$)	10.193	0.347	09.696	0.149	09.846
mean absolute error		**0.452**		**0.074**	
N_2H_6 (dimer) (aug-cc-pVTZ)					
S_1 ($1A'$)	6.914	0.469	6.495	0.050	6.445
S_2 ($2A'$)	7.340	0.512	6.939	0.111	6.828
S_3 ($1A''$)	8.057	0.355	7.600	0.101	7.702
S_4 ($3A'$)	8.230	0.415	7.686	0.128	7.815
S_5 ($4A'$)	8.700	0.366	8.198	0.135	8.334
mean absolute error		**0.423**		**0.105**	

BSE@ :	Standard G_nW_n@HF	Standard $\sigma(G_nW_n$@HF)	Scheme A G_0W_0@HF/LDA	Scheme A $\sigma(G_0W_0$@HF/LDA)	EOM-CCSD
H_2 (aug-cc-pVQZ)					
S_1 (1B3u)	12.861	0.334	12.529	0.002	12.527
S_2 (1 Ag)	13.258	0.294	12.917	0.046	12.964
S_3 (1B1u)	14.125	0.316	13.785	0.023	13.809
S_4 (1B2u)	14.125	0.316	13.785	0.023	13.809
S_5 (2B3u)	15.434	0.171	15.080	0.182	15.263
mean absolute error		**0.286**		**0.055**	
FURAN (aug-cc-pVTZ)					
S_1 (1A2)	6.422	0.299	6.171	0.048	6.123
S_2 (1B2)	6.703	0.278	6.560	0.135	6.425
S_3 (1B1)	6.929	0.264	6.687	0.022	6.665
S_4 (2A2)	7.102	0.261	6.828	0.012	6.841
S_5 (1A1)	7.404	0.630	7.167	0.393	6.774
mean absolute error		**0.346**		**0.122**	

BSE@ :	Standard G_nW_n@HF	Standard $\sigma(G_nW_n$@HF)	Scheme A G_0W_0@HF/LDA	Scheme A $\sigma(G_0W_0$@HF/LDA)	EOM-CCSD
ETHYLENE (aug-cc-pVTZ)					
S_1 (1B2u)	7.697	0.229	7.442	0.025	7.468
S_2 (1B1u)	8.253	0.152	8.092	0.008	8.101
S_3 (1B1g)	8.341	0.225	8.093	0.022	8.116
S_4 (1B3g)	8.410	0.224	8.130	0.055	8.186
S_5 (1 Ag)	9.037	0.143	8.798	0.095	8.894
mean absolute error		**0.194**		**0.041**	
ETHANE (aug-cc-pVTZ)					
S_1 (1Ag)	09.856	0.586	09.504	0.234	09.270
S_2 (1Bg)	09.856	0.586	09.504	0.234	09.270
S_3 (2Ag)	10.471	0.597	10.093	0.219	09.874
S_4 (1Au)	10.564	0.540	10.226	0.202	10.024
S_5 (1Bu)	10.564	0.540	10.226	0.202	10.024
mean absolute error		**0.570**		**0.218**	

BSE@ :	Standard G_nW_n@HF	Standard $\sigma(G_nW_n$@HF)	Scheme A G_0W_0@HF/LDA	Scheme A $\sigma(G_0W_0$@HF/LDA)	EOM-CCSD
CO_2 (aug-cc-pVTZ)					
S_1 (1 Au)	08.738	0.131	08.544	0.325	08.870
S_2 (2 Au)	09.010	0.065	08.780	0.164	08.945
S_3 (1B2u)	09.010	0.065	08.780	0.164	08.945
S_4 (1B1g)	09.487	0.618	09.118	0.249	08.869
S_5 (1B3g)	09.490	0.621	09.118	0.249	08.869
mean absolute error		**0.300**		**0.230**	
LiH (aug-cc-pVQZ)					
S_1 (1A1)	4.066	0.433	3.307	0.325	3.633
S_2 (1B2)	5.103	0.496	4.448	0.158	4.607
S_3 (1B1)	5.103	0.496	4.448	0.158	4.607
S_4 (2A1)	6.214	0.324	5.610	0.279	5.890
S_5 (3A1)	6.530	0.266	5.893	0.370	6.264
mean absolute error		**0.403**		**0.258**	

BSE@ :	Standard G_nW_n@HF	Standard $\sigma(G_nW_n$@HF)	Scheme A G_0W_0@HF/LDA	Scheme A $\sigma(G_0W_0$@HF/LDA)	EOM-CCSD
PH_3 (aug-cc-pVQZ)					
S_1 (1A)	6.833	0.592	6.543	0.302	6.241
S_2 (2A)	7.310	0.671	7.123	0.484	6.639
S_3 (3A)	7.310	0.671	7.123	0.484	6.639
S_4 (4A)	8.165	0.356	7.837	0.028	7.809
S_5 (5A)	8.165	0.356	7.837	0.028	7.809
mean absolute error		**0.529**		**0.265**	
CH_4 (aug-cc-pVQZ)					
S_1 (1A1)	11.217	0.567	10.859	0.209	10.650
S_2 (1B1)	11.218	0.568	10.859	0.209	10.650
S_3 (1B2)	11.218	0.568	10.859	0.209	10.650
S_4 (2A1)	12.412	0.522	12.022	0.132	11.890
S_5 (2B1)	12.412	0.522	12.022	0.132	11.890
mean absolute error		**0.549**		**0.179**	

BSE@ :	Standard G_nW_n@HF	Standard $\sigma(G_nW_n$@HF)	Scheme A G_0W_0@HF/LDA	Scheme A $\sigma(G_0W_0$@HF/LDA)	EOM-CCSD
BF (aug-cc-pVQZ)					
S_1 (1A1)	7.022	0.561	6.814	0.353	6.461
S_2 (1B1)	7.022	0.561	6.814	0.353	6.461
S_3 (1B2)	8.789	0.406	8.323	0.059	8.383
S_4 (2A1)	8.993	0.252	8.654	0.086	8.741
S_5 (2B1)	9.220	0.098	8.781	0.340	9.122
mean absolute error		**0.376**		**0.238**	
Vynil bromide (aug-cc-pVTZ)					
S_1 (1A$''$)	6.563	0.346	6.314	0.097	6.217
S_2 (1A$'$)	6.599	0.331	6.390	0.122	6.268
S_3 (2A$''$)	7.161	0.350	6.898	0.087	6.811
S_4 (3A$''$)	7.344	0.505	7.026	0.187	6.839
S_5 (4A$''$)	7.354	0.324	7.091	0.061	7.030
mean absolute error		**0.371**		**0.111**	

BSE@ :	Standard G_nW_n@HF	Standard $\sigma(G_nW_n$@HF)	Scheme A G_0W_0@HF/LDA	Scheme A $\sigma(G_0W_0$@HF/LDA)	EOM-CCSD
Na_2 (aug-cc-pVTZ)					
S_1 (1B1u)	2.190	0.325	1.894	0.029	1.865
S_2 (1B2u)	2.815	0.342	2.744	0.271	2.473
S_3 (1B3u)	2.815	0.342	2.744	0.271	2.473
S_4 (1 Ag)	3.171	0.538	2.994	0.361	2.633
S_5 (1B3g)	3.410	0.561	3.287	0.438	2.849
mean absolute error		**0.422**		**0.274**	
Na_4 (aug-cc-pVDZ)					
S_1 (1A)	1.030	0.097	0.792	0.140	0.933
S_2 (2A)	1.715	0.297	1.579	0.161	1.418
S_3 (3A)	2.066	0.258	1.843	0.035	1.808
S_4 (4A)	2.360	0.460	2.165	0.265	1.900
S_5 (5A)	2.429	0.424	2.354	0.349	2.005
mean absolute error		**0.307**		**0.190**	

Table B.1: Excitation energies of the first 5 singlet states in eV based on BSE@G_nW_n@HF, BSE@G_0W_0@HF/LDA, and EOM-CCSD.

BSE@ :	Standard G_nW_n@HF	Standard $\sigma(G_nW_n$@HF)	Scheme A G_0W_0@HF/LDA	Scheme A $\sigma(G_0W_0$@HF/LDA)	EOM-CCSD
Si_2H_6 (aug-cc-pVTZ)					
S_1 (1Ag)	8.211	0.577	7.848	0.214	7.634
S_2 (1Au)	8.244	0.626	8.078	0.460	7.618
S_3 (1Bu)	8.244	0.626	8.078	0.460	7.618
S_4 (2Bu)	8.635	0.651	8.271	0.287	7.984
S_5 (2Ag)	8.885	0.654	8.568	0.337	8.231
mean absolute error		**0.627**		**0.352**	
COS (aug-cc-pVQZ)					
S_1 (1A2)	6.264	0.499	6.144	0.379	5.765
S_2 (1A1)	6.519	0.688	6.384	0.553	5.831
S_3 (2A2)	6.519	0.688	6.384	0.553	5.831
S_4 (1B1)	8.198	0.661	7.936	0.399	7.537
S_5 (1B2)	8.199	0.662	7.936	0.399	7.537
mean absolute error		**0.640**		**0.456**	